Tuning the chiroptical properties of Goldhelices through their nanostructure optimization and hierarchical organization

Jie Gao

université de BORDEAUX

THÈSE PRÉSENTÉE

POUR OBTENIR LE GRADE DE

DOCTEUR DE

L'UNIVERSITÉ DE BORDEAUX

ÉCOLE DOCTORALE DES SCIENCES CHIMIQUES

SPÉCIALITÉ : CHIMIE PHYSIQUE

Par Jie GAO

Tuning the chiroptical properties of Goldhelices through their nanostructure optimization and hierarchical organization

Sous la direction de : Reiko ODA

Soutenue le 19 Septembre 2019

Membres du jury :

M. Avarvari, Narcis	Directeur de Recherche, CNRS, UMR 6200, Angers	Rapporteur
M. Artzner, Franck	Directeur de Recherche, CNRS, UMR 6251, Rennes	Rapporteur
M. Pauly, Matthias	Maitre de Conférences, CNRS, UPR 22, Strasbourg	Examinateur
M. Battie, Yann	Maitre de Conférences, LCP-A2MC, Metz	Examinateur
Mme. Drisko, Glenna	Charge de Recherche, CNRS, UMR 5026, Bordeaux	Examinateur
Mme. Tréguer-Delapierre, Mona	Professeur, Université de Bordeaux	Examinateur
Mme. Oda, Reiko	Directeur de Recherche, CNRS, UMR 5248, Bordeaux	Directrice de thèse
Mme. Emilie, Pouget	Charge de Recherche, CNRS, UMR 5248, Bordeaux	Co-encadrante
M. Buffeteau, Thierry	Directeur de Recherche, CNRS, UMR 5255, Bordeaux	Invité

-Acknowledgement-

This work was performed in the laboratory of Chimie et Biologie des Membranes et des Nanoobjets (CBMN), and Institut Européen de Chimie de Biologie (IECB). I would like to thank the directiors from both institutions, Sophie Lecomte and Rémi Fronzes.

I really appreciate all the jury members, specially Dr. Franck Artzner (Université Rennes) and Dr. Nacris Avarvari (Université Angers) who spent their precious time reviewing this manuscript.

I would like to express most sincere gratitude to my supervisors Dr. Reiko Oda and Dr. Emilie Pouget, who whose countless guidance in both academic and life constituted my achievement in Bordeaux. I believe no matter where I will be and what I will do, their invaluable way of thinking and experience will always be my lighthouse.

Of course, I cannot have my thesis like this without all the collaborations. In the past four year, I had four most important collaborations. With the help of Dr. Jacques Leng, I acquired the knowledge of microfluidics, which is one approach to arrange silica helices. Dr. Glenna Drisko, who always encourages me and provided support of her expertise in Dip-coating and I really hope her little angel become well soon. Dr. Matthias Pauly shared vital insights in our discussions, and he managed to reverse all the characterization instruments that we needed when I was working in Strasbourg. Dr. Yann Battie, whom I am fortunate to know and collaborate with, he provided his expertise in simulations and theorical calculation fields, which leads to a clear application of our materials.

This thesis is consisted by numerous helps, and there are a number of people who shared their knowledge, kindness and expertise with me. I would like to thank all of them in particular: Dr. Thierry Buffeteau who helped me corrected the manuscript and measured VCD and IR spectra, Dr. Brice Kauffman who did X-ray scattering characterization , Mr. Armel Bezault who did Cryo-TEM characterization, Mr. Julien Hunel who helped me with AFM, Mr. Sisareuth Tan and Dr. Marion Decossas-Mendoza who helped and trained me with TEM characterization, Dr. Michel Martineau and Dr. Philippe Legros who helped me with SEM characterization, Miss Laethtia Minder who trained and helped me with CD spectra characterization, Dr. Virginie Ponsinet, Dr.

Philippe Barois, and Dr. Dario Bassani who gave useful advices after my Amadeus presentation. Dr. David Gonzalez-Rodriguez who predicted the silica helices deposition by dip-coating.

I would like to my lovely colleagues in my group: Antoine Amestoy, Antoine Scalabre, Dr. Balamurgugan Kuppan, Jianqiao Jiang, Dr. Kyohei Yoshida, Peizhao Liu, Dr. Shaheen Pathan and Wijak Yospanya. In particular, I would like to thank previous group members: Dr. Jiaji Cheng and Dr. Yutaka Okazaki who inspired me in science and helped me in life, Dr. Gregory Kemper who taught to start the synthesis at beginning, and Dr. Mariam Attoui with whom we share 3.5 years together, as close friends we discussed the research projects together and share our life with each other.

And I would like to thank all my friends in Bordeaux, who shared the impressive moments and offered me food: Dr. Jinhua Wang, Dr. Xiang Wang, Dr. Wu Cheng, Chenhao Yao, Jia Li, Junjie Hao, Yuling Yin, Wencan He, Dr. Bosi Mao and Xiaozhou Ma. Specially, I would like to express my appreciations to my French teachers: Dr. Thierry Maligne and Mr. Junping Zhou.

Last but not least, the unconditional love from my family support me go through all the unfavorable conditions. Mon cher, Jason, thank you for always by my side, I cannot image how to survive all these ups and downs without you. I am so lucky to have you.

Tuning the chiroptical properties of Goldhelices through their nanostructure optimization and hierarchical organization

Chiral materials can have strong influence on the propagation of light and have attracted attention in the nano-science community. Gold nanoparticles (GNPs), stable plasmonic materials in the visible range (400-800 nm), are attractive objects as building blocks for optical materials. We have designed and obtained Goldhelices by grafting GNPs on silica nano-helical structures. The work presented in this thesis aims at developing tunable Goldhelices and organizing them in order to enhance, modify, reduce or even eliminate the chiroptical properties. The details of the nanostructures as well as the kinetics of formation of organic self-assembly which is used as templates for the formation of Goldhelices are fully studied. The hierarchical organization of the Goldhelices is investigated by the use of three techniques, the microfluidics, the dip-coating and the grazing incident spraying. Finally, the effect of the organization on their optical properties are characterized by chiral spectroscopies and Mueller matrix polarization ellipsometry. We demonstrate that such a system can be used for the creation of linear or circular polarizer where such polarization is solely tunable by the organization of the Goldhelices.

Key words: self-assembly, chirality, silica helices, Gold nanoparticles, alignment

Ajustement des propriétés chiroptiques de Goldhelices via l’optimisation de leur nanostructure et leur organisation hiérarchique

Les matériaux chiraux peuvent avoir une forte influence sur la propagation de la lumière et ont attiré l'attention de la communauté des nanosciences. Les nanoparticules d'or, matériaux plasmoniques stables ayant une activité dans le visible (400 à 800 nm), sont des objets attrayants en tant que blocs de construction pour la formation de matériaux optiques. Précédemment, nous avons conçu et obtenu des Goldhelices en greffant des nanoparticules d’or sur des nano structures hélicoïdales de silice. Le travail présenté dans cette thèse vise à développer et à organiser les Goldhelices de manière à améliorer, modifier, réduire, voire même éliminer les propriétés chiroptiques. Les détails des nanostructures ainsi que la cinétique de formation de l'auto-assemblage organique utilisé comme support pour la formation de Goldhelices sont étudiés. Des Goldhelices sont ensuit organisées hiérarchiquement à l’aide de trois techniques : la microfluidique, le « dip coating » et le « Grazing Incidence Spraying ». Enfin, l’effet de ces organisations sur les propriétés optiques sont caractérisées par spectroscopies chirales et ellipsométrie. Nous démontrons qu'un tel système peut être utilisé pour la création de polariseur linéaire ou circulaire où une telle polarisation est uniquement dépendant par l'organisation des Goldhelices.

Mots clés : auto-assemblage, chiralité, hélices de silice, nanoparticules d’or, alignement

Outline

General Introduction

The refractive index (indicated by *n*) of a material is a dimensionless number that describes how fast light propagates through a material, and it determines how much the path of light is bent upon entering the material. According to the Maxwell equations, the refractive index is defined as $n = \sqrt{\varepsilon\mu}$, where ε and μ are the permittivity and permeability of the material. In chiral media, the chirality parameter *K* will influence this propagation giving two different refractive indices $n_+ = \sqrt{\varepsilon\mu} + K$ and $n_- = \sqrt{\varepsilon\mu} - K$ for the right-handed and left-handed circularly polarized waves. Thus, a chiral system gives an additional opportunity to control the refractive index. However, it remains challenging to fabricate chiroptical materials in the visible range (400-700 nm). The reason is that the dimension of the materials should be much smaller than the wavelength of the exciting electromagnetic field. This means that for visible light, nanoscale materials are required. While chiral meta-surfaces can be obtained via top-down lithography techniques, only the bottom-up approach, typically based on the self-assembly of colloids, offers an approach to the large-scale creation of such nano systems. Simple plasmonic nanoparticles e.g. gold nanoparticles (GNP) can be assembled on organic scaffold such as DNA or peptides. If these hybrid structures can give interesting chiroptical properties, they generally suffer from chemical, mechanical or thermal perturbation. The objective of this thesis is to achieve stable nanoobjects with tunable chirality and arrays of these nanoobjects with a controlled orientation at the macroscopic level. Our strategy is to synthesize chiral inorganic (silica) nanostructures with tunable chirality that can be used as scaffolds for the grafting functional optical materials such as gold nanoparticles (GNPs).

Previously, the Chiral Molecular Assemblies (CMA) group developed a series of surfactant-counterion complexes that could self-assemble into helical supramolecular structures (called nanohelices). These organic chiral structures can be replicated by silica to obtain silica nanohelices with tunable morphology. Finally, the grafting of GNPs on these silica templates gives hybrid structures named “Goldhelices” with chiroptical properties. This is the starting point of the present work. In order to enhance and modulate these chiroptical properties, two strategies are developed: 1. Tuning the twist degree of the helical substrate. 2. Organizing the Goldhelices on different levels.

The chirality of the silica substrate originates from the organic supramolecular template. The self-assembling process is therefore studied to obtain various helices with controlled curvatures (helical or twisted), handedness and dimensions in terms of diameter, width and pitch. In particular, the effect of the enantiomeric excess on the supramolecular structural formation will be explained in Chapter 3.

The Goldhelices previously reported by the group are based on the electrostatic grafting of the GNP on silica helices. Here, we investigated the optimization of such hybrid structures by creating a strong covalent bond between GNPs and the silica surface making these hybrids more robust against the solvent nature, the temperature or the drying of the structures. The synthesis and the chiroptical properties of these new Goldhelices are developed in the Chapter 4. These more robust structures can then be used to create organized structures such as oriented films or 3D compact structures while retaining the chiroptical properties.

In the Chapter 5, three techniques are used to organize the silica nanohelices and the Goldhelices into specific orientations on a large scale: two techniques based on the evaporative forces: one within microfluidic channels and another on substrates by dip-coating; and a third technique based on the shear flow forces, the Grazing Incident Spraying. As preliminary tests, the bare silica helices are organized by the three techniques to examine if these methods are suitable for the orientation of nanometric elongated chiral materials. We then used Goldhelices for the most suitable technique, the Grazing Incident Spraying. Finally, the characterization of these new organized materials by Mueller matrix polarimetry with an ellipsometer was performed, revealing the modulated optical properties related to the organization of films.

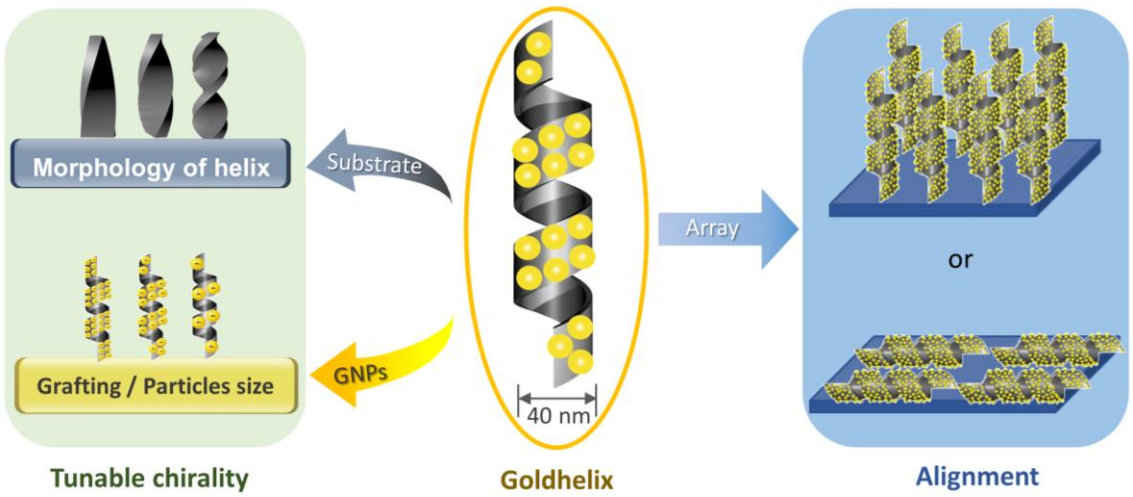
Morphology of helix
Substrate
Grafting / Particles size
GNPs
40 nm
Array
or
Tunable chirality
Goldhelix
Alignment

Chapter 1. Literature review

Chapter 1: Literature review

Contents

1. Introduction

Chirality is a property of an object or system which is distinguishable from its mirror image. A chiral object and its mirror image are called enantiomorphs (Greek opposite forms) or when referring to molecules, enantiomers.[1] Chiral molecules attracted researchers' interest since the first chiral molecule reported by Louis Pasteur in 1848.[2] Chiral molecules are omnipresent in our world: more than 80% of active compounds used by pharmaceutical companies are chiral,[3] the amino acids that make up various proteins in the human body are chiral, and fragrance molecules of fruits and spices are chiral. For example, enantiomers can give differences in odor like orange and lemon (chiral limonene), or mint and caraway (chiral carvone). Moreover, genetic information is carried by chiral nucleotides, and only D nucleotides exist in nature. A submicron scale chiral structure can be constituted through chiral molecules and chirality can be detected at different dimensions. For example, DNA which consists of nucleotides occurs only in the right-handed helical shape. Starting from chiral molecules, different levels of chiral structures (even macroscopic levels) can be built, which means that chiral information is transmissible. For instance, the presence of an asymmetric carbon in a molecule induces chirality at the molecular level, and this chirality can be expressed at a supramolecular level if molecules self-assemble ("Self-assembly" is a phrase which can be used widely but, in this thesis, means molecular self-assembly in the solvent)[4]. An important class of structures showing chiral morphology based on molecular assembly are fibrils, for example helices. A chiral structure could help achiral molecules or particles arrange in a chiral structure, by which, chiral information can be induced to achiral molecules. Achiral molecules in nature or spherical particles can show chiral properties through this approach and generate vast novel characteristics.

Thanks to the chiral transmissibility, various functional materials could be synthesized and applied in asymmetric catalysis,[5] chiral recognition,[6,7] sensing,[8] and light manipulation.[9] Among these applications, we are interested in manipulating light propagation in the visible range. Chiral materials can be used in optics, since the refractive index of materials can be modified through chirality without changing the permittivity or permeability.[10]

Matter structure on a length scale smaller than the wavelength of light can exhibit unusual optical properties and organization at the dimensions of 1/10 of the wavelength of the incident light, suggesting that the propagation of light can be tuned.[11,12] To fabricate optical materials affecting visible light propagation (wavelengths between 400 and 800 nm), structures around 40-70 nm are needed. The bottom up approach has some advantages with respect to top down techniques, mainly in that large amounts of nanometric scale structures can be obtained at lower cost. When a chiral system is built, various plasmonic particles can be grafted onto the chiral substrate. If there are interactions between the nanoparticles (NPs) upon inducing a chiral arrangement, the originally achiral particles can receive the chiral information from the substrate and can have a chiral response according to their absorbance. The chiral morphological control of the template can be used to tune the chiroptical response of the final plasmonic structures.

Furthermore, orientated and/or densely packed plasmonic materials may lead to a further increase in the chiral optical response.[13] Even though in-depth study has been done on chiral nanomaterials, due to the limited stability and yield, few materials can be really converted into macroscopic 2D or 3D materials. To realize real macroscopic materials, and potentially gain new properties, the chiral nanometric materials need to be densely packed and organized. Different techniques which allow nanomaterial alignment will be introduced.

In this chapter, a literature review will be presented about molecular self-assembly with a focus on chirality transmission from chiral molecules to supramolecular structures at nanometric or micrometric scales. Secondly, we will present the advantages of plasmonic particles and some representative articles about metallic nanoparticles which are already or can potentially be applied to optics. The third part is about techniques to organize anisotropic or fiber-like nanomaterials, in order to obtain macroscopic materials and to enhance or create new optical properties.

2. Chirality transmission

Chirality can be propagated from one atom to the whole molecule, from a molecule to several molecules, from several molecules to a supramolecular assembly, from a nano-substrate to particles, and also from organic structures to inorganic ones. In this section, two categories of chiral transmission will be presented, which are from chiral molecules to supramolecular structures, from chiral organic structures to inorganic materials.

2.1 From chiral molecules to chiral supramolecular structures

Molecular self-assembly is the process by which molecules adopt a defined arrangement without guidance or management from an external source. In both intra- and intermolecular self-assembly, assembly of molecules is directed through noncovalent interaction, such as hydrogen bonding, hydrophobic forces, van der Waals forces, π-π stacking or electrostatic interactions.[14,15] Over the last several decades, various structures derived from molecular self-assembly have been reported, and these structures include spherical micelles, vesicles, cylinders, lamellas, gyroids, or helical structures through the self-assembly of lipids, polymers or amphiphiles.[16,17,18] Among these supramolecular structures, only chiral structures formed by chiral molecules will be discussed in this thesis. Over the last thirty years,[19] chiral self-assembly to form supramolecular structures has continuously attracted researchers' attention.[20]

In 1984, Yamada et al.[19] synthesized the compound, double-chain alkyl amphiphiles with an oligo-L-amino acid (glutamic acid)-head group ($2C_mGlu_n$, m is 12 or 16, n is 14, as shown in Figure 1.1), and reported that this compound could form helical super structures from molecular bilayers in water at pH 8-9. This study provided one of the first examples of a superstructure constituted by synthetic bilayers. Circular dichroism (CD) spectra of the superstructures of $2C_{12}Glu_{14}$ and $2C_{16}Glu_{14}$ were different from the random coil. Random coil samples (5.0×10^{-4} M) show the same spectra as diluted samples of $2C_{12}Glu_{14}$ and $2C_{16}Glu_{14}$ ($\approx 10^{-6}$ M) or in the presence of an anionic surfactant which could break the superstructures. Therefore, the unusual CD signal of $2C_{12}Glu_{14}$ and $2C_{16}Glu_{14}$ were attributable to the structures formed in water. From this article, we know that the CD spectra of the superstructure and the random coil formed from the same compound can be

different, which means supramolecular structure may have special chiral properties in comparison with the individual molecule.

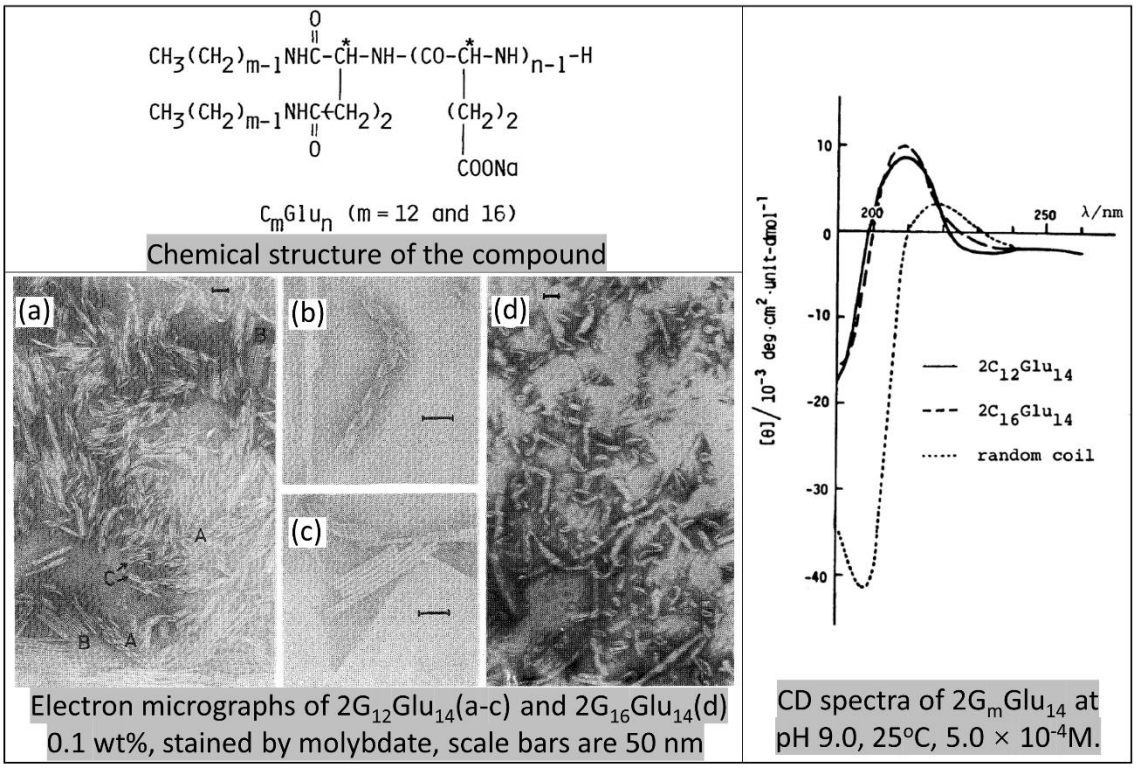

Figure 1.1 Chemical structure of the compound reported by Yamada et al., electron micrographs of superstructures formed in water, and CD spectra of the superstructures and the random coil.[19]

In the 1980s, J. Fuhrhop's group[21,22,23] reported a series of lipid bilayer fibers formed by diastereomeric and enantiomeric N-octylaldonamides. Dihelical fibers were formed by spontaneous aggregation of octyl L-and D-gluconamides (**1a** and **2**),[22] as shown in Figure 1.2. However, in the racemic mixture (**1a** and **2**, mixed in a 1:1 ratio), only non-twisted platelets were found on the electron micrographs, which agreed with the macroscopic observation that the racemate did not form a clear gel. Only white precipitates were formed when the hot solution of racemate was cooled. An important difference between the thermograms (Figure 1.2) of the D-enantiomer gel and of the racemic platelets was observed after aging 8-16 h. Moreover, different DSC thermograms were obtained for the gel of **1a** which was freshly prepared (within 1 h) and aged for several hours. This example exhibited that the self-assemblies of octyl L-and D-gluconamides in aqueous solution are right- and left- handed twisted structures. The racemate self-assembled into a different structure from the enantiomer in terms of size and design. The morphological

difference resulting from deviations in molecular packing resulted in the variation in the differential scanning calorimetry (DSC) thermograms.

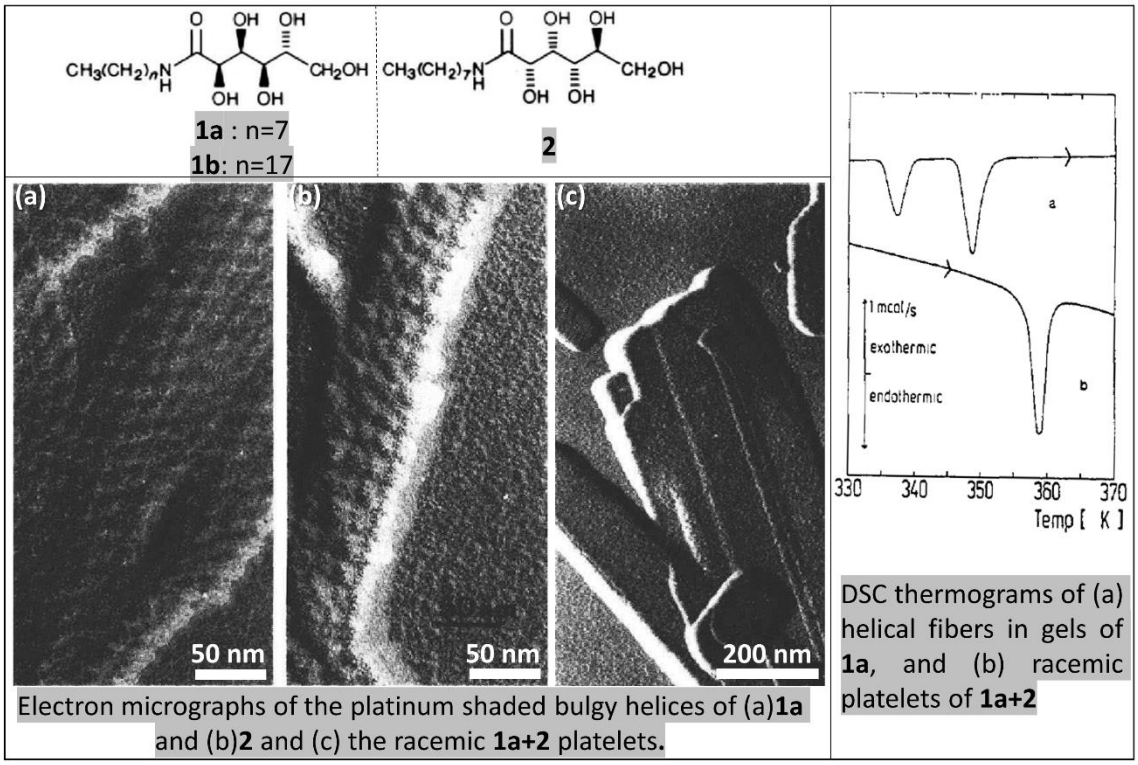

Figure 1.2 Chemical structure of the compound used by Fuhrhop[22], electron micrographs of gels formed by the compounds, and DSC thermograms of the compound 1a, and mix of 1a+2.

In general, chiral molecules self-assemble into helical structures, and the chiral supramolecular structure depends on the molecular enantiomers. When two enantiomers are mixed with equimolar quantities, flat twisted ribbons are formed. But when the two enantiomers are mixed with one in excess, which kind of structure will be formed? In the 1990's, Oda's group reported the chiral structure of amphiphiles in aqueous solution[24] and studied the conformation formed by the mixture of two enantiomers.[25] Specifically, chirality of the self-assembled twisted ribbons could be tuned by varying the enantiomeric excess (e.e., calculated with $(\varphi_L - \varphi_D)/(\varphi_L + \varphi_D)$) of 16-2-16 tartrate gemini (n=16, $2X^-$ = L-tartrate and D-tartrate, in Figure 1.3). T/W (periodical length / width of ribbons) were used to indicate the twisted degree of the structure. The smaller is the e.e. value of 16-2-16 tartrate gemini, the larger the T/W ratio will be for the twisted ribbons (as shown in the table in Figure 1.3). Experimental observation and theoretical modelling both confirmed

that an effective way to control the morphology of twisted ribbons is to vary the enantiomeric excess of 16-2-16 tartrate gemini.

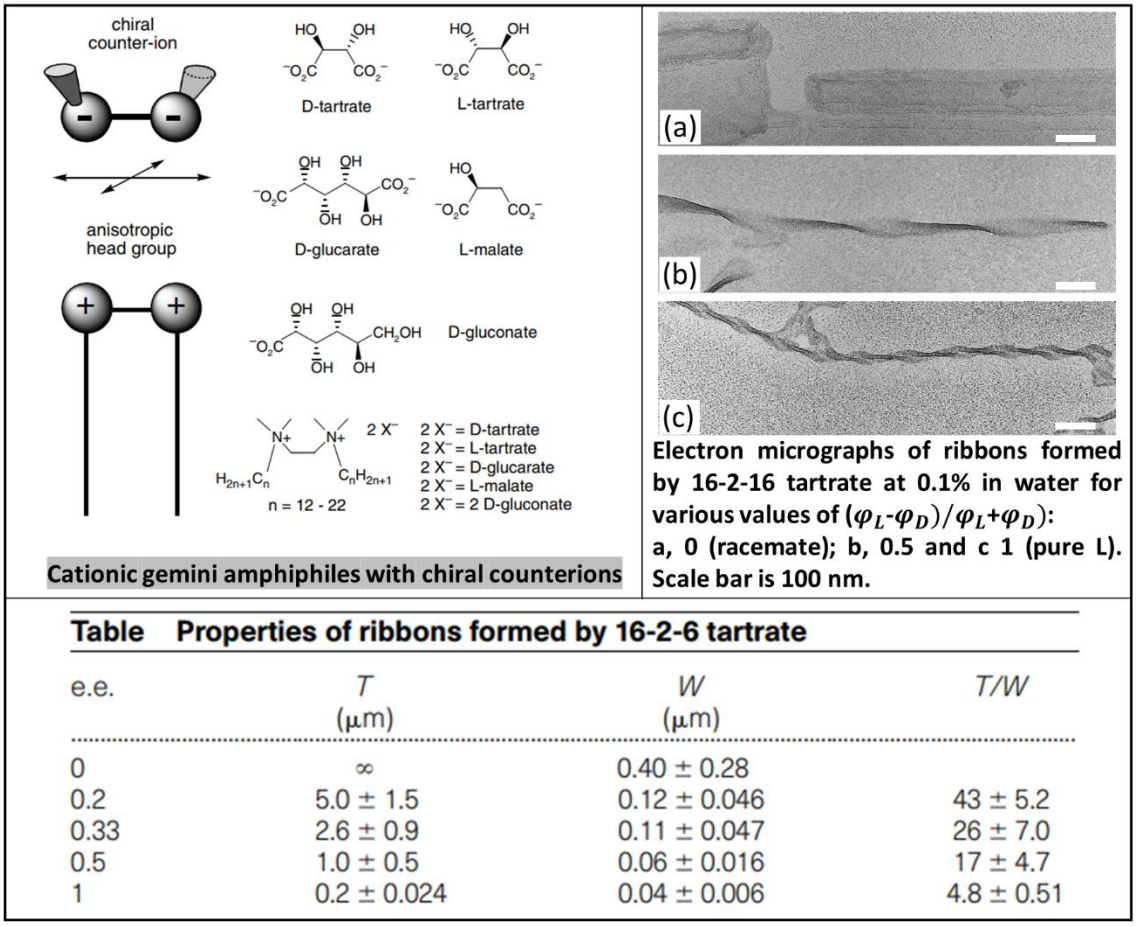

Table Properties of ribbons formed by 16-2-6 tartrate

e.e.	*T* (μm)	*W* (μm)	*T*/*W*
0	∞	0.40 ± 0.28	
0.2	5.0 ± 1.5	0.12 ± 0.046	43 ± 5.2
0.33	2.6 ± 0.9	0.11 ± 0.047	26 ± 7.0
0.5	1.0 ± 0.5	0.06 ± 0.016	17 ± 4.7
1	0.2 ± 0.024	0.04 ± 0.006	4.8 ± 0.51

Figure 1.3 Chemical structure of the compound used by Oda[25], electron micrographs of the twisted ribbons formed by the compounds, and a table listing the dimensions of the twisted ribbons.

In many systems, when the quantities of two enantiomers are unequal, the chirality of the system is determined by the enantiomeric excess of the species by following a majority rule.[26] The chiral supramolecular structures can be adjusted by controlling the e.e. values of chiral molecules, and correspondingly, optical activity can be tuned.[27, 28, 29] However, very recently, there is a special case reported by Liu's group:[20] they found one system in which the alkyl chain length prevails over the enantiomeric excess. As Figure 1.4 shows, pure L-lipid and pure D-lipid respectively formed P-helical and M-helical structures. If the number of carbons of 2-methylene were equivalent in the L- and D-lipids, the mixture of the two enantiomers (n = m) followed the majority rule. However, when the alkyl chain length was unequal (n ≠ m), the lipid with the longer chain would rearrange its

molecule conformation (Figure 1.4 d) to match that of the shorter lipid. The final chirality of the tubes was exclusively determined by the short lipid chirality. Both theoretical simulation and experimental observation supported the mechanism they proposed.

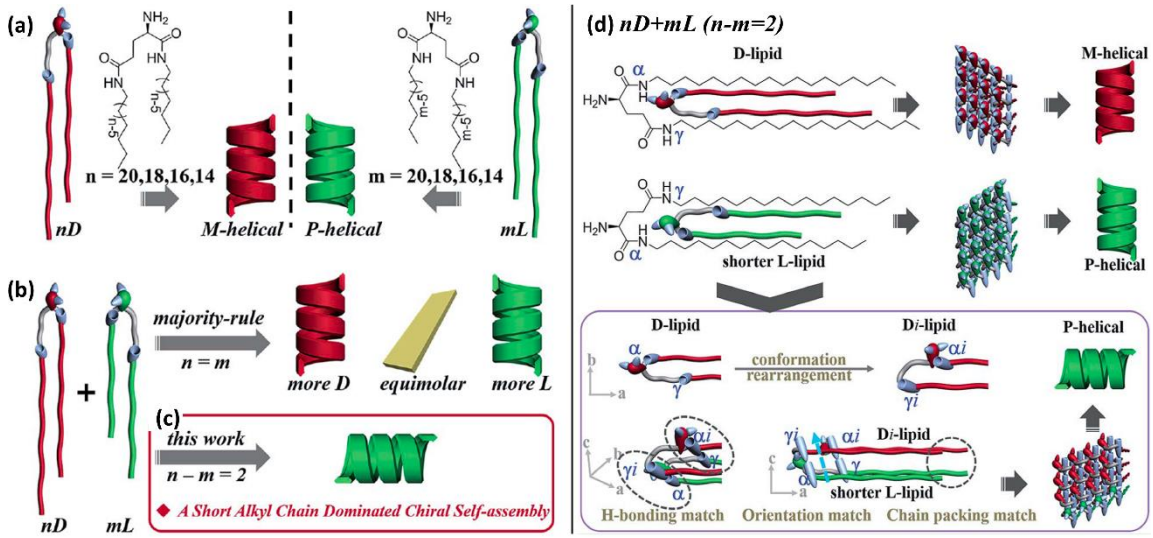

Figure 1.4 Self-assembly of chiral lipids. (a) enantiomerically pure D- and L- lipids respectively form M- and P-helices. (b) Mixing racemates follows the majority rule if n=m. (c) Mixing two heterochiral lipids with a mirror image chiral head, but a 2-methylene discrepancy in alkyl chain length, leads to homochiral composite nanotube, whose helical sense is determined by the chirality of the lipid with the shorter alkyl chain, regardless of their mixing ratios. (d) Mechanism of homochiral nanotubes formed from heterochiral lipids.[20]

There are more and more compounds with chiral molecules discovered and synthesized to form helical structures in aqueous or organic solvents.[30,31 32] Various systems have been studied to investigate how and why chiral supramolecular structures form and to study their optical properties. Regardless of the nature of the molecules (amino acid, surfactant, or copolymer) self-assembly rules follow two main principles: one is the majority rule principle as introduced, [26,27,28,29] and the second is called the sergeants and soldiers principle.[33,34,35] The sergeants-and-soldiers rule covers the interaction between chiral sergeants and achiral soldiers and states that the chirality of the whole system follows the chirality of the sergeant. Some systems followed a special mechanism, like conformational rearrangement.[20] The main forces driving self-assembly vary from one system to another, which gives each system its own features.

2.2 From chiral organic to inorganic structures

Even though flexible and fine tunable supramolecular structures can be formed by chiral molecular self-assemblies, the formation of chiral nanometric structures is in either aqueous solution or organic solvent. Despite high solvent boiling points, self-assemblies only exist at relatively low temperatures, and can be destroyed by heating the solution. Moreover, the interactions which keep the self-assembly are weak,[36] so supramolecular structures can be easily destroyed by changing the solvent, pH or ionic concentration of the solution. The structures can also evolve with time, which means aging time can change the structures at the molecular level and/or supramolecular level.[22,25,37,38] Therefore, the chiral nanometric structures formed in solution are unstable both thermodynamically and kinetically. In order to take advantage of these chiral supramolecular structures, we need to stabilize these fragile and sensitive structures. One effective strategy is to solidify the self-assembly within an inorganic matrix. Since inorganic materials are generally more robust than the organic equivalent, inorganic replication freezes the morphology in a certain kinetic stage of the self-assembly process.

In 1993, Archilald et al.[39] tried to control the formation of tubular inorganic-organic composites by using self-assembled lipid tubules as templates for the crystallization of inorganic oxides. The idea was to first modify assembled tubes (formed by galactocerebroside) to give microstructural anionic sites for the electrostatic binding of Fe (III) polyhydroxy cationic species. At that time, they were successful in promoting inorganic nucleation on the external surface of the lipid microstructure, but they were not able to reproducibly synthesize tubule-based composites. They offered the possibility to transcribe the organic structure by inorganic materials.

Later Y. Ono et al. [40] prepared hollow fibers of silica based on organic gels templates in 1998. They showed the formation of fibers by use of two different compounds (as shown in Figure 1.5 a). Because the oligomeric silica species were only absorbed on the cationic (quaternary ammonium) gelator fibrils (formed by compound ***2***), the fibers containing $NMe_3^+Br^-$ could be transcribed by the silica (Figure 1.5 b). In contrast, the organic gelator fibrils of ***1*** without the cation cannot absorb oligomeric silica, only granular silica structures were observed.

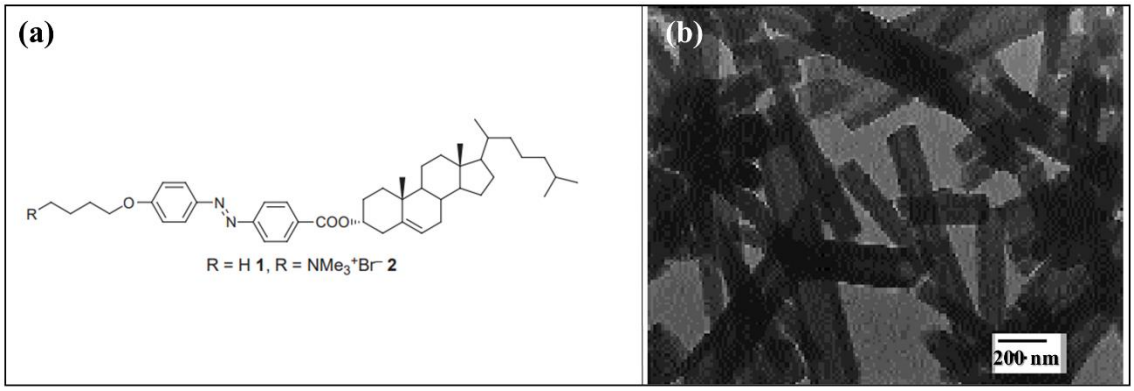

Figure 1.5 (a) Chemical structure of the compound *1* and *2*, with -H and NMe_3Br^- respectively. (b) Electron micrographs of hollow silica tubes.[40]

In 2001, J. D. Hartgerikn et al.[41] reported hydroxyapatite crystals grown along the long axes of collagen fibrils, by which they created mineralized nanofibers. The exact mechanism of this control is not clear, yet it may be due to specific arrangements of the acidic group that promoted the growth of crystals in an orientation by an epitaxial mechanism.[42]

To transmit chiral structures from organic to inorganic matter, silica is a good candidate. Indeed, numerous reports have been produced fabricating porous silica or tubular silica materials.[43,44,45] To sum up the extensive literature on this silicification process, an electrostatic interaction between the organic assembly and the silanol precursors is necessary to make the inorganic transcription possible. Due to the inorganic morphology replicating the organic structure, the chiral property of organic self-assembly could be propagated into inorganic silica materials. Yang et al.[46] reported helical silica and hybrid silica nanofibers in 2006 via the sol-gel polymerization using a chiral cationic gelator. At the beginning of 21st century, S. Shinkai's group published several articles reporting chiral silica structures produced by the sol-gel transcription of organic fibers.[47,48,49] Later, in 2004, S. Che et al.[50] reported the synthesis of chiral mesoporous silica based on the self-assembly of chiral anionic surfactants and inorganic precursors by using amino silane or quaternized amino silane as a co-structure-directing agent. R. Oda and S. Shinkai collaborated to obtain tunable chiral silica structures, in which the morphologies of the self-assemblies depend on the enantiomeric excess of the organic gemini surfactants.[51] Then several publications by Oda's group were produced regarding silica chiral structures: T. Delcolos, et al.[52] obtained helical silica structures from an

organic template, and later Y. Okazaki et al. [53] improved the silica helice preparation in terms of the necessary duration and the homogeneity of the suspension. To date, the chiral silica structure is confirmd only by microscopic images.

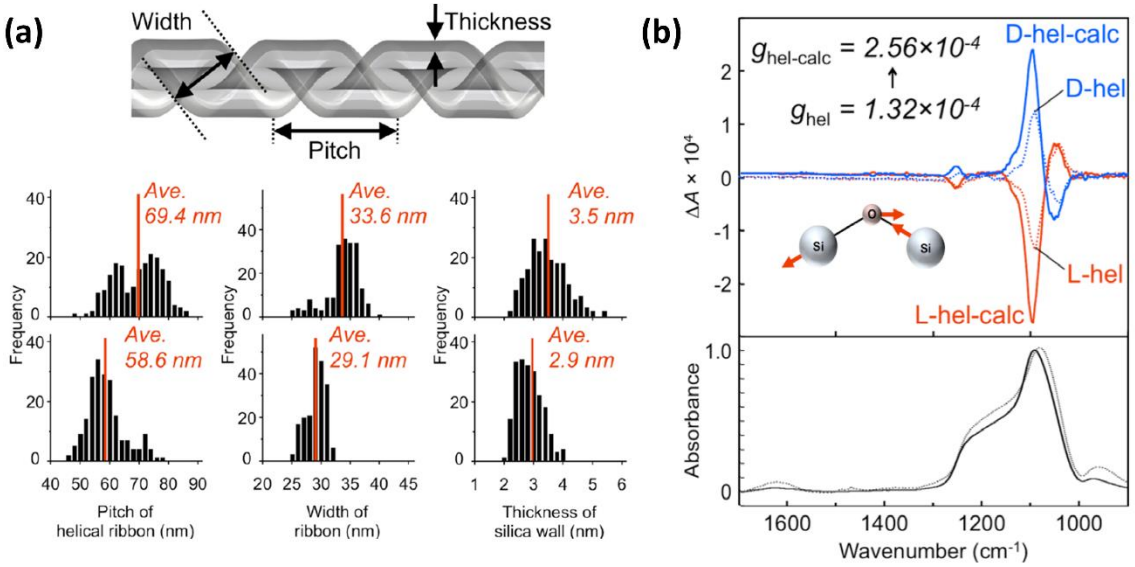

Figure 1.6 (a) Morphological characterization of silica-lipid hybrid helical ribbons before and after calcination, schematic illustration of a silica helical ribbon and the quantitative evaluation of the morphological change. (b) Infrared spectrum and vibration circular dichroism spectrum of silica helical ribbons before (dotted line) and after (solid line) calcination.

Y. Okazaki et al.[54] were the first to report chiral signals from a siloxane network forming right-handed and left-handed helical nanostructures. The chirality of amorphous silica originates from a chiral siloxane network expressed from the chiral organization of Si-O-Si bonds, which is strong evidence that chirality can be transmitted from organic molecules to inorganic materials, through sol-gel transcription and polycondensation of silanols. The vibrational circular dichroism spectrum of L-helical ribbons presented a strong negative-positive (from long to short wavenumbers) Cotton effect for the transverse optical mode at 1090 cm^{-1}, and a much weaker negative Cotton effect for the longitudinal optical mode at 1240 cm^{-1} of the Si-O-Si asymmetric stretching vibration. The D-helical ribbons gave an opposite signal. In parallel, they calcined the silica helical structure at 600 ^{o}C. After calcination, 25% of silanol groups had been dehydrated, more than three-fold siloxane rings had been formed via an endothermic reaction during heating. The helical pitch, width and thickness of the silica helices all decreased, and the vibrational

circular dichroism spectra showed stronger signals at 1090 cm^{-1} and 1240 cm^{-1}. This was the first report of chiral signals from a siloxane network.

3. Plasmonic nanoparticles

The term *plasmon* was used in the 1950s by D. Pines [55] to describe high frequency collective oscillations in metals. When incident light hits a metal nanoparticle, its electric field pushes the electron cloud of the particle towards one side of the particle. This means that negative charges of electrons accumulate on that side, leaving behind a positive charge on the other side of particle. These negative and positive charges attract one another; if the negative charge were suddenly released, then, it would oscillate back and forth at a certain frequency. When the frequency of incident light matches this metal nanoparticle resonance frequency, it will produce a large oscillation of all the free electrons in the metal. Because so many electrons are simultaneously oscillating, large electric fields are produced in the immediate vicinity of the particle. These fields themselves act on the electrons, reinforcing the oscillation. This coupled excitation, consisting of oscillating charges inside the particles and oscillating electromagnetic fields immediately outside of the particle, is known as a *plasmon resonance*, or *localized surface plasmon*, or a *particle plasmon*.[56]

3.1 Metal materials in optics

When an electric field is applied to a metal, electrons move on the order of femtoseconds, which is instantaneous compared to the period of microwaves and radio waves. The metal therefore can be treated as prefect conductors. However, at near infrared and optical frequencies, the response time becomes comparable to the period of the electromagnetic wave; this matching of time scales leads to a strong coupling between the electromagnetic field and electron motion, that we refer to as plasmons. Plasmons move across metal surfaces with phase velocities that can be very different from those of freely propagating light waves. When the dimensions of metal objects are comparable to or larger than the optical wavelength, this phase mismatch means that incident light does not naturally excite plasmons with high efficiency. Only nanoscale objects whose dimensions are small compared to the optical wavelength offer a strong coupling between light and plasmon resonances.[56]

Metal nanoparticles with resonance in the visible range can be used as functional materials to manipulate light. More specifically, Group 11 metals of the periodical table have plasmonic resonance at visible frequencies. Copper, for example, can support plasmon resonance at optical frequencies, but these resonances are weak due to the rapid dissipation by losses in the metal.[57,58] Silver has the lowest losses and strongest plasmon resonance of all known materials.[59,60,61] Gold has plasmon resonance in the visible range and it is one of the most used as it is more chemically and physically stable than silver.[62,63] Other materials can produce plasmon resonance in other frequency ranges: aluminum supports plasmons at ultraviolet frequencies,[64,65] and highly doped semiconductors and oxides support plasmons at infrared frequencies.[66] For the purpose of manipulating visible light, modern plasmonic materials are focused on gold and silver.[56,67]

3.2 Chiral metal nanoparticles

The resonant interaction between surface charge oscillation and the electric field of light constitutes gives rise to the unique properties of metal nanoparticles.[68] Among the various nanoscale metal devices in optics, a particular class is chiral plasmonic nanoparticles. Chiral metal nanoparticles are important materials for applications in catalysis,[69,70] sensing,[71,72] and photonics.[73]

When nanoparticles are chiral, they can give a chiral optical response in the plasmonic wavelength, which can be characterized by circular dichroism spectroscopy. Circular dichroism (CD) is dichroism involving circular polarized light, and circular polarization of an electromagnetic wave is a polarization state in which, at each point, the electric field of the wave has a constant magnitude, but its direction rotates with time at a steady rate in a plane perpendicular to the direction of the wave.[74] A circularly polarized wave can be in one of two possible states, right circular polarization and the left circular polarization, in which the electric field vector rotates in a right-hand and left-hand sense with respect to the direction of propagation respectively. As a chiral molecule has different absorption when it is illuminated with left- or right-hand circularly polarized light,[75] the electronic CD spectroscopy can measure this difference. Chiral metal nanoparticles have this property in the plasmonic range (if the metal is silver or gold, it affects the visible range). Furthermore, chiral materials can also vary light propagation via the refractive

index of the materials.[76,77] However, the control of metal chirality is difficult to achieve. As summarized by C. Gautier and T. Burgi [78] in 2008, three categories of chiral metal nanoparticles can be distinguished (Figure 1.7): in the first (a) the optical activity arises from an intrinsically chiral inorganic core shape, in the second (b) the inorganic core can be achiral and the optical activity is induced by a chiral environment like a chiral organic shell or chiral electrostatic field, and in the third (c), chiral ligands are used to stabilize the nanoparticles creating a chiral footprinton the surface of the metal. This classification is based on the source of the chiral optical activity: the particle structure, environment or surface.

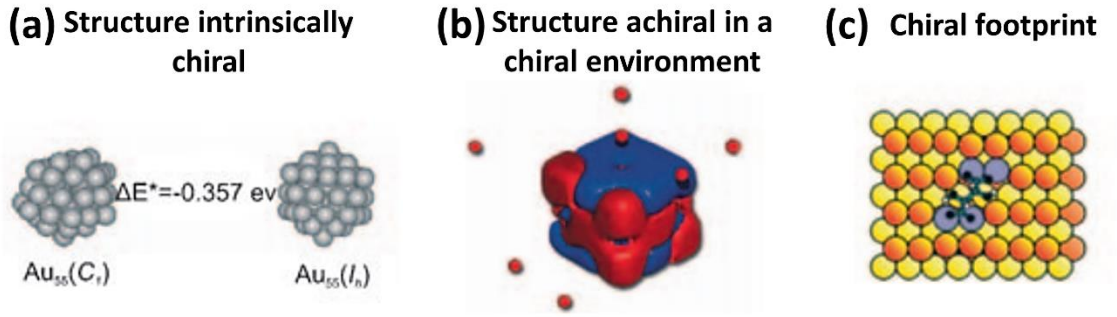

Figure 1.7 Possible origins of chiroptical activity observed for metal particles.[77]

Later, in 2017, N. A. Kotov et al[79] described four types of chemical and physical origins of chirality for nanoparticles based on the differences in the formation process of the chiral particles as shown in Figure 1.8. Type *a*: the inorganic core of metal of the NP itself has a chiral shape. Type *b*: NPs with a chiral surface on an inorganic core, which is normally induced through the adsorption of chiral molecules. Type *c*: NPs with a chiral pattern of surface ligands. Type *d*: polarization effects in the inorganic core, which can be induced by chiral molecules or assemblies of nanoparticles.

There are some overlap and differences between the classifications of Burgi and Kotov. The second classification will be adopted here, as it allows us to directly image the nanoparticle preparation approach, and this thesis is an experimental work. More details about these four types of chirality will be discussed based on Kotov's classification.[79]

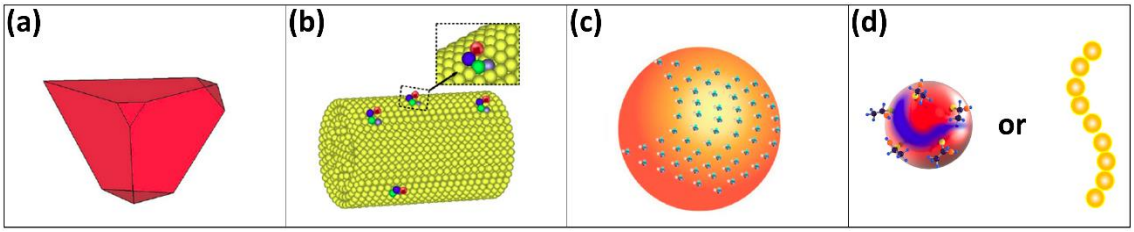

Figure 1.8 (a) Type *a* chirality: the inorganic core has a chiral shape. (b) Type *b* chirality: the chiral surface on an inorganic core. (c) Type *c* chirality: a chiral pattern of surface ligands. (d) Type *d* chirality: polarization effects in the inorganic core, which can be induced by chiral molecules or nanoparticle assemblies.[79]

Type *a* chirality is associated with an asymmetric nanoparticle inorganic core, for example, nanoparticles in the shape of tetrahedrons with variable truncations [80] or nanoparticles with a chiral core. A large amount of work in nanomaterials with asymmetric structures has been reported,[79] and a few representative examples will be illustrated in this section (Figure 1.9 a).

In 2007, A. Lechtken et al. [81] studied Au_{34}^- possible structures using density functional theory (DFT) calculations. The lowest-energy structure found for Au_{34}^- is chiral, whose chirality is apparent in the helical arrangement of the edge atoms.

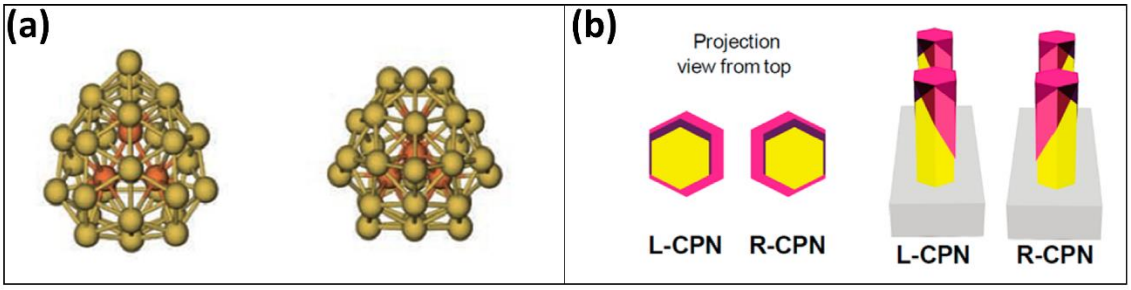

Figure 1.9 (a) Selected energy-minimum structure found for a Au_{34}^- cluster using DFT calculations.[81] (b) Chiral plasmonic nanostructures (CPN): two layers of gold shells (pink and yellow color indicating first and second gold layers, respectively) on ZnO nanopillars. [82]

Kotov's group managed to obtain the chiral signal of gold, by depositing two layers of gold shell on achiral ZnO pillars.[82] The gold shells did not fully cover the substrate, and there was a shift between the first and second layer of gold shell, by 90 ^oC and -90 ^oC for L- and D- chiral plasmonic nanostructures (Figure 1.9 b). At the same time, they dissolved the ZnO nanopillar and kept the bilayered gold shells in an aqueous suspension. This gold shell suspension still showed chiral optical activity in the visible range.

In 2014, A. Ben-Moshe et al., reported a tellurium nanostructure with a chiral shape using thiolated chiral biomolecules.[83] Te precursors were reduced in the presence of a large concentration of thiolated chiral biomolecules such as glutathione, where the thiol group strongly binds to Te. This chiral Te nanostructure worked as a template for the gold and silver telluride nanostructures. Gold nanostructures could be achieved by galvanic replacement of the Te nanocrystal, and silver telluride could be easily obtained by reacting with silver ions. Gold and silver telluride (Figure 1.10 f and g) showed chiral signals in the visible range (Figure 1.10 h). The chirality of these nanostructures of gold and silver telluride are from the asymmetric geometry.

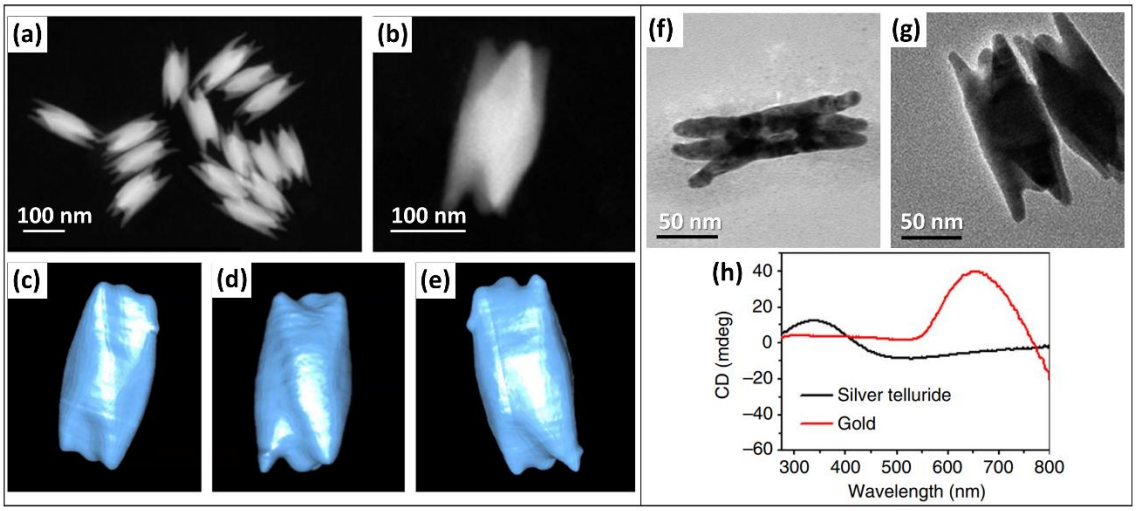

Figure 1.10 (a,b) Dark-field scanning transmission electron microscope (STEM) images of Te nanostructures, (c-e) tomographic reconstruction of the particle in b, (f) and (g) transmission electron microscope (TEM) images of gold nanostructures and silver telluride nanocrystals, (h) CD spectra of nanostructures in f and g.[83]

J. Yeom et al.[80] synthesized CdTe chiral nanostructures by circularly polarized light irradiation. Right- (left-) handed circularly polarized light at the wavelength of 543 nm induced the formation of right- (left-) handed twisted ribbons of thioglycolic acid-capped CdTe NPs with an enantiomeric excess exceeding 30%. However, linearly polarized light or dark conditions led to straight nanoribbons. CD spectra of purified nanoribbons were measured in aqueous dispersions and revealed distinct chiroptical bands at 490, 590 and 700 nm. Therefore, the chiroptical property could be induced by the chiral shape of the twisted ribbons.

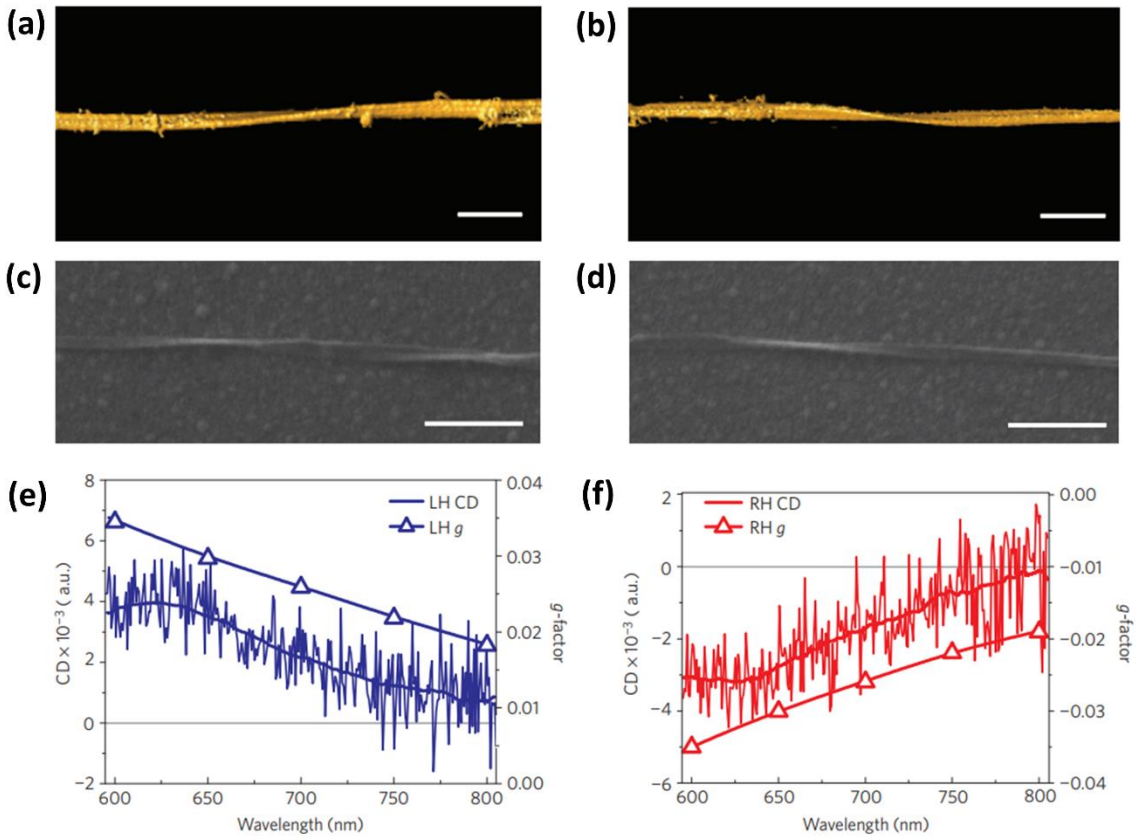

Figure 1.11 Chirality of single nanoribbons. (a,b) Surface rendering of the 3D TEM tomographic reconstruction of a L-(a) and R-(b) handed nanoribbons, scale bars 100 nm. (c,d) SEM images of single L-(c) and R-(d) handed nanoribbons, scale bars 500 nm. (e,f) CD spectra and calculated g-factor spectra of signal single L-(e) and R-(f) handed nanoribbons respectively.[80]

All these chiral nanostructures have Type *a* chirality, i.e. based on an intrinsic chiral morphology for the materials itself, which can be induced by chiral atomic steric arrangement, chiral molecule, special physical or mechanical control, or circularly polarized light illumination.

In Type *b* chirality, NPs are associated with asymmetries on the NP surface, which manifests distortions and displacements of the atoms of the NP core in response to the presence of the stabilizers. The work of R. Raval's group[84] shows that (R, R)- or (S, S)-tartaric acid molecules were adsorbed on the Cu (110) surface, which could work as a heterogeneous enantioselective catalyst. They showed that the active phase consists of extended supramolecular assemblies (bitartrate) of adsorbed (R, R)-tartaric acid, which destroys existing symmetry elements of the metal and directly bestows chirality to the surface. Through low-energy electron diffraction patterns, surface infrared and scanning

tunneling microscope images (Figure 1.12), they demonstrated that it is possible to create a chiral surface sustaining a single handedness across the entire surface. Later, this group observed and analyzed the chiral induction by adsorption of the enantiomer tartaric acid on the defined Ni (110) surface. [85]

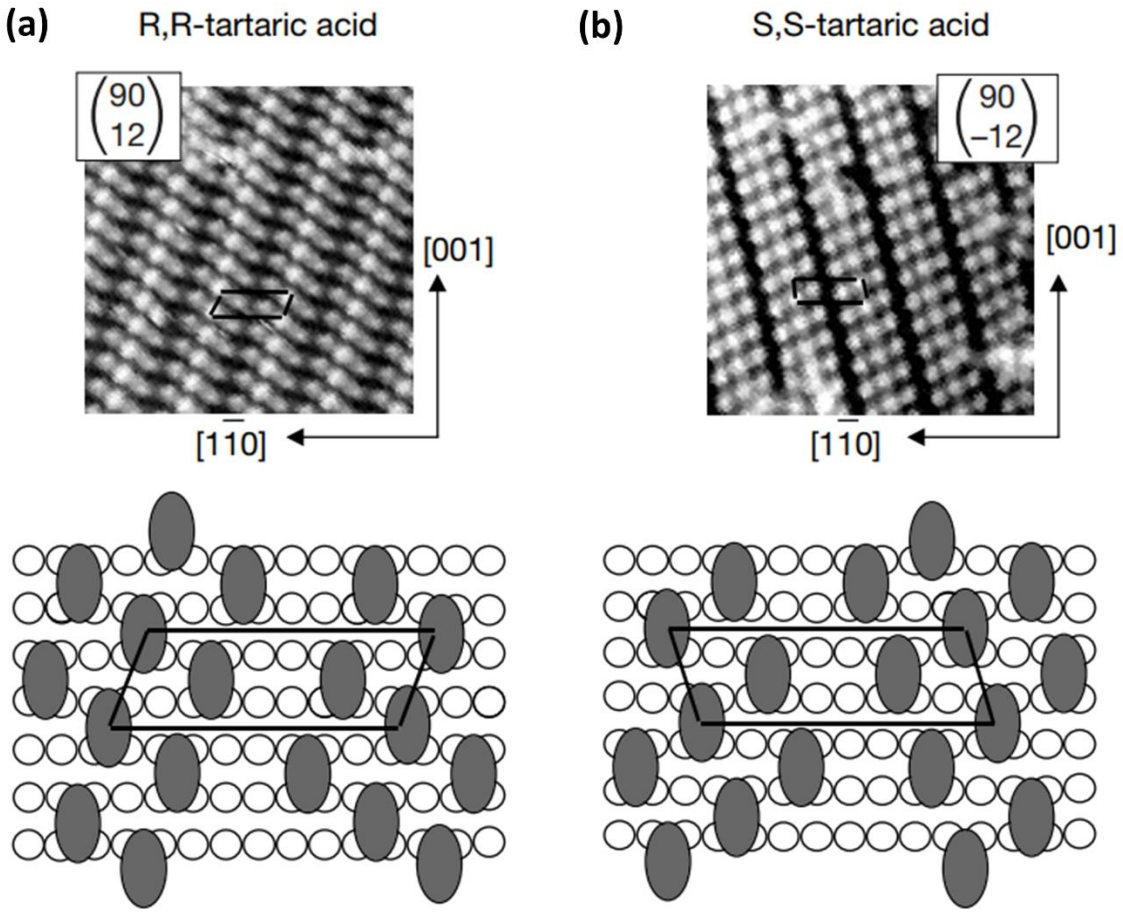

Figure 1.12 Scanning tunneling microscope (STM) images showing mirror chiral surfaces created by (R, R)- and (S, S)-TA absorbed on Cu (110). Shown are 108 Å × 108 Å STM images of (90, 12) (R, R)-TA bitartrate phase (a) and the (90, -12) (S, S)-TA bitartrate phase (b). Below each STM image is a schematic diagram displaying the position of the molecular features observed relative to the Cu (110) surface.

C. Gautier and T. Burgi studied chiral *N*-isobutyryl-cysteine protected gold nanoparticles through their optical activity in UV-vis and infrared. [86] Through the vibrational circular dichroism spectra investigations (experimentally and theoretically), they concluded that the carboxyl group was interacting with gold particles, and the chiral molecules (thiol group and carboxyl group) on the particles may induce a chiral footprint. Later, in 2008, they studied chiral inversion of gold nanoparticles by ligand exchange with

the opposite enantiomer.[87] The optical activity of the metal-based electronic transitions is reversed although the patterns of CD spectra remain largely unchanged. The optical activity is dictated by the chiral thiol, which is adsorbed on the surface of gold nanoparticles. There are also other chiral nanoparticles that belongs to Type *b* chirality, such as thiol capped CdTe nanocrystals.[88]

Type *c* chirality is due to the chiral pattern of the surface ligands. The molecules absorbed on the surface control and regulate the surface interactions. These molecules or self-assemblies of molecules can be heterogeneously distributed on the surface of the nanoparticles.[89] For example, I. Dolamic et al.[90] reported gold clusters modified with an achiral ligand, 2-phenylethylthiol. $Au_{38}(SCH_2CH_2Ph)_{24}$, had no electronic CD signal initially, but after the $Au_{38}(SCH_2CH_2Ph)_{24}$ suspension was passed through chiral high-performance liquid chromatography, two enantiomers of gold clusters appeared. These two enantiomers showed opposite CD spectra at 600 nm wavelength, which proved that with an achiral ligand (-$SHCH_2CH_2Ph$), chiral gold clusters can be obtained, and this chirality stems only from the asymmetric arrangement of achiral adsorbates on a surface. Type *c* chirality has been identified by X-ray diffraction.[91]

Type *d* chirality is the chiral field effect, the polarized effects in the inorganic core which can induce dissymmetric adsorbates or arrangements. When this polarization of metal clusters was induced by chiral molecules, it is difficult to judge if this chiral system belongs to Type *b* or Type *d* chirality, unless the related simulation or calculation resolves the atomic positions within the metallic cluster.[92] Actually, multiple chiral factors can be included and should be considered in one practical system.[79,93,94] When the polarization of the inorganic core is induced by structural arrangement, without other chiral molecules, this kind of chirality was assigned to Type *d*. This phenomena attributes to the metal plasmonic property: when one metallic nanoparticle is placed next to another one, the particle plasmon resonance of the two nanoparticles can be coupled. Indeed, the additional enhancement is expected due to the electromagnetic interactions between the two metallic nanoparticles. When the distance between the two nanoparticles is less than the particle diameter, an extremely high field confinement called *hot spots* can be created. Hot-spot-induced chiroptical activity is enhanced in assemblies of NPs, due to the resonance between

the polarization oscillations in the adjacent plasmon.[95] The chiral optical property of metal nanoparticles can be obtained according to the assemblies of NPs, which is proved experimentally[96, 97, 98]and theoretically.[99]

Z. Li et al.[96] could control the assembly and disassembly of Au nanorods (Au NR) via DNA. Au NR were modified by DNA containing four extra bases, and Au NRs with DNA remained separate in the solution if the temperature was above its melting temperature, 50 ^{o}C. Because the sticky ends of DNA can further be complementary, when the temperature is cooled to 20 ^{o}C, spontaneous aggregation of Au NRs were formed. CD spectra and UV-vis spectra of the Au NR with DNA were performed under 60 ^{o}C and 20 ^{o}C. Evidently, the change of UV-vis absorption at different temperatures was much smaller than that of CD spectra, with respect to both the spectral patterns and the peak intensity. The reason is that the plasmonic CD response is much more sensitive to transformations in the nanostructure configuration, as well as to electronic transitions. The chirality of this Au NR belongs to Type *b* at 60 ^{o}C where the Au NR with DNA were dispersed individually. However, at 20 ^{o}C, Au NR assembled through DNA spacers, and the CD spectra at 20 ^{o}C indicated chiral optical property of the assembles of Au NRs, which consists of Type *b* and Type *d* chirality.

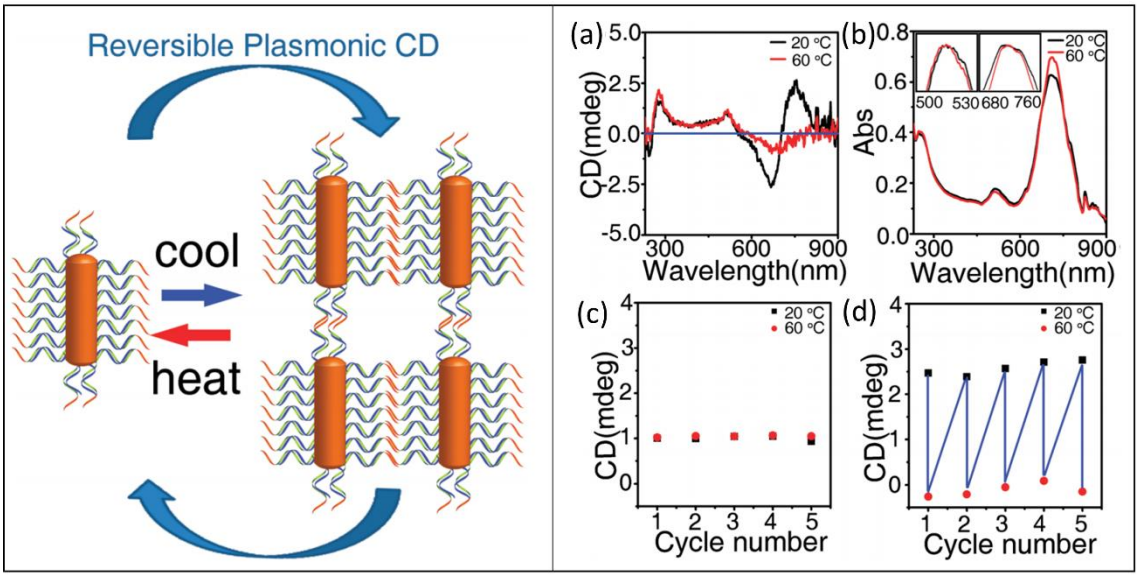

Figure 1.13 Left side: the scheme of reversible plasmonic CD responses based on the dynamic assembly and disassembly of double-strand DNA modified Au NRs (yellow column) at different temperatures. Au NRs are modified with single-strand DNA (blue curves) and its complementary DNA (green curves) with the sticky end (red curves). Right side: reversible plasmonic CD spectra (a) and corresponding

UV-vis absorption spectra (b) of DNA modified Au NRs at 20 °C (black line) and 60 °C (red line). The insets are the enlarged UV spectra. CD intensity at 512 nm (c) and 750 nm (d) cycled at 20 °C (black dots) and 60 °C (red dots).[96]

W. Yan et al.[97] designed pyramidal structures of nanoparticles using DNA. These nanoparticles consisted of three types of Au NPs (Au_1, Au_2, Au_3 diameters: 10 nm, 15 nm, 25 nm respectively) modified with DNA, Ag NPs and quantum dots (QDs). Through delicately designed DNA strands, various pyramids could be achieved (Type1 to Type 6), and their CD spectra were shown in Figure 1.14 (b, c, d). Even if DNA is a chiral molecule, the chiral optical response when they are attached on the NPs is negligible (Type 1). Interestingly, when the pyramids were composed by more than two kinds of NPs, strong CD signals appeared, indicating the assembled NP structure forms a polarized environment. Type 5(*R*-enantiomer) and Type 6(*S*-enantiomer) assemblies showed nearly perfectly opposite CD spectra in terms of their peak position and their intensity. This work revealed that CD spectra could be controlled by the pyramidal assemblies of NPs, and the size or elements of NPs could affect the CD signals in terms of intensity and pattern. Z. Fan and A. O. Govorov,[99] created pyramid models of NPs. The simulated chiroptical properties agreed with the experimental results.

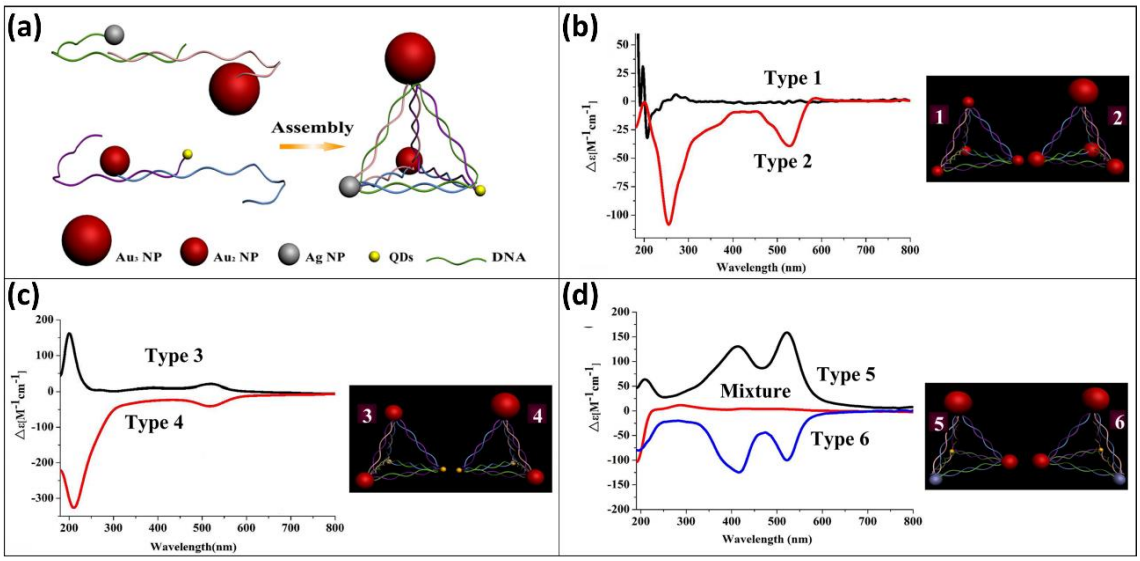

Figure 1.14 Schematic illustration of synthesis of a chiral NP pyramid (a), CD spectra of pyramids made from (b) four Au_1 (Type1) and three Au_2+Au_3 (Type 2); (c) two Au_2 + two QDs (Type 3), and Au_2 + Au_3 + two QDs (Type 4); and (d) Au_2 + Au_3 + Ag + QD as S-(Type 5) and R-enantiomers (Type 6).

Chiral nanoparticles could express special chiroptical properties, but due to various chiral factors and a complex experimental environment, there are normally more than one

type of chirality in a system. In order to effectively control chirality, it is important to understand how the various chiral factors contribute to the system. However, it is practically impossible to separate the multiple chirality types within a system. Therefore, the system with a singal chirality type is the ideal model for investigating chirality control.

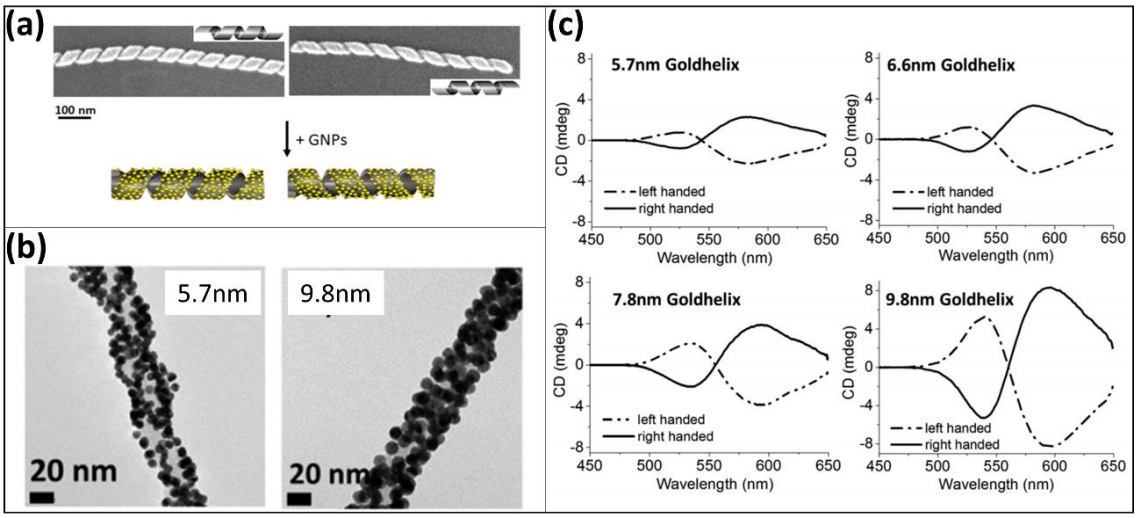

Figure 1.15 (a) Schematic illustration to form GoldHelix: GNPs were grafted on a helical silica structure. (b) TEM images of the GoldHelix with different diameters of GNPs, 5.7 nm and 9.8 nm. (c) CD spectra of the GoldHelix with four diameters of GNPs, 5.7 nm, 6.6 nm, 7.8 nm and 9.8 nm.[98]

In the CMA group of the CBMN Institute, J. Cheng et al.[98] prepared helical structures of gold NPs named Goldhelices. Various GNPs with different diameters were grafted on silica helical nanostructures, as shown in Figure 1.15 (a). In this case, GNPs were reduced and stabilized by tannic acid and tri-sodium citrate, and free GNPs did not show any CD signal. Left- and right-handed silica helical structures were used as a template to support GNPs of various diameter, as TEM images show in Figure 1.15 (b). Depending on the handedness of the silica structures, left- and right-Goldhelices were produced with opposite CD spectra (Figure1.15 (c)), and the intensity of the CD signal increased with the diameter of GNPs, which confirmed that the larger the nanoparticles, the stronger the surface plasmon resonance response. In this system, the chirality of the Goldhelices came from the helical assembly of achiral GNPs. Since there are no other chiral molecules in the system, the unique chiral source belongs to Type *d* chirality, i.e. the polarization induced by the helicoidal organization of the GNPs. This system is the only one showing such good chiral induction with a controlled handedness via an inorganic template. This makes it

particularly suitable for specific applications as long as it can resist various solvents, high temperatures and pressures.

4. Alignment techniques

If nanoparticles show unexpected and unprecedented properties, their 2D or 3D organization would enhance these properties. Moreover, properties related to direction are induced through particle alignment. With oriented or densely packed nanomaterials, a further increase in electromagnetic response may be achieved.[71] Therefore, particle synthesis and various methods to align/organize the particless must be pursued. The controlled alignment of anisotropic nanoscale objects is one key prerequisite in material science. Anisotropic properties refer to a material's physical properties (for example absorbance, refractive index, conductivity, and tensile strength) for the case in which these properties differ when measured along different directions in space.[100] Because there are many techniques that can be used to align nanoobjects,[100,101,102] it is impossible to introduce them individually. We will present here some of these techniques that we think could be useful for nanohelice alignment. Most of the techniques to align the nanomaterials rely on these principles: electric field, [103,104,105] magnetic field,[106,107] mechanical stretching,[108,109] spatial confinement,[110, 111,112] and shear forces.[100,113,114]

4.1 Alignment based on an electric field

Electrospinning has been applied to prepare uniaxially aligned nanofibers made of ceramics, polymer/ceramic composites, carbon nanofibers and TiO_2.[115] The principle of this approach is to use a collector consisting of two pieces of electrically conductive substrates separated by a gap in which width can vary from hundreds of micrometers to several centimeters. As driven by electrostatic interactions, the charged nanofibers were stretched to span across the gap and thus become uniaxially aligned arrays over large areas. Because the nanofibers were suspended over the gap, they could be conveniently transferred to the surface of other substrates for subsequent treatment and various applications.

D. Li et al.[115] aligned inorganic nanofibers made of carbon, TiO_2/PVP, TiO_2, and Sb-doped SnO_2 through electrospinning (Figure 1.16 (d-g)). Figure 1.16 (a) schematically

illustrates the setup used for these electrospinning experiments. Figure 1.16 (b) shows a cross sectional view of the calculated electric field strength vectors between the needle and the ground. Figure 1.16 (c) illustrates the electrostatic forces acting on a charged nanofiber spanning the gap. To prepared inorganic nanofibers, the solution (which consists of polymer or the polymer with titanium tetra-isopropoxide or polymer with tin isopropoxide and antimony(III) isopropoxide), were electrospun under various spinning voltages, and calcination processes were followed for carbon nanofibers, TiO_2, and SbO_2-doped SnO_2 (Figure (d, f, g)). To summarize, the polymer solution and compounds containing inorganic elements are processed into nanofibers using electrospinning. Through calcination, the extra carbonate is removed under air, and well-organized nanofibers of inorganic oxide are obtained.

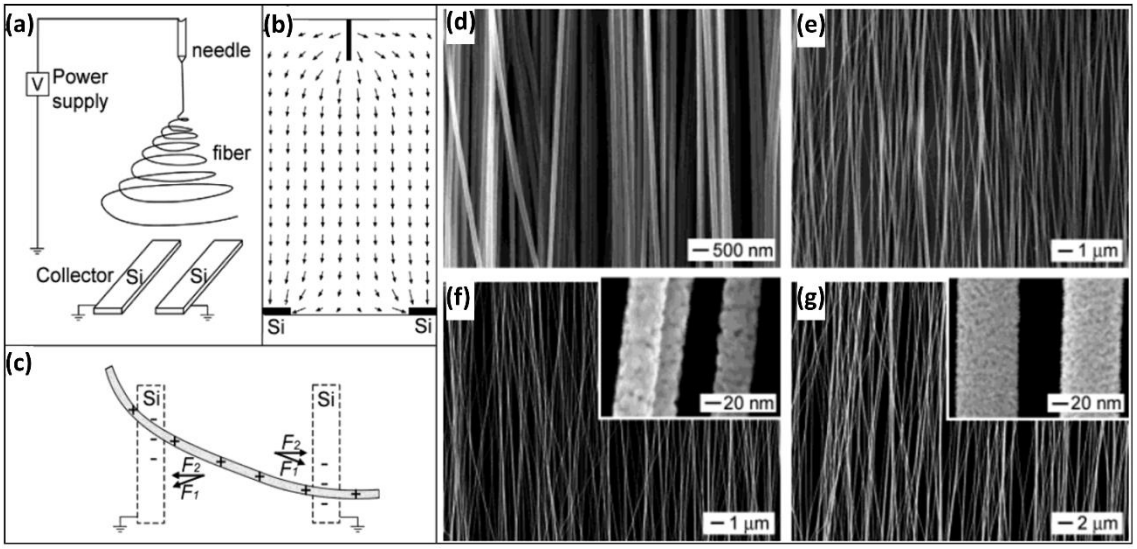

Figure 1.16 Left side: (a) Schematic illustration of the electrospinning setup that was used to generate uniaxially aligned nanofibers. The collector contained two pieces of conductive silicon stripes separated by a gap. (b) Calculated electric field strength vectors in the region between the needle and the collector. The arrows denote the direction of the electrostatic field lines. (c) Electrostatic force analysis of a charged nanofiber spanning the gap. The electrostatic force (F_1) resulting from the electric field and the Coulomb interactions (F_2) between the positive charges on the nanofiber and the negative image charges on the two grounded electrodes. Right part is a SEM image of uniaxially aligned nanofibers made of various materials: (d) carbon nanofibers, (e) TiO_2/PVP, (f) TiO_2, and (g) Sb-doped SnO_2. The insets show enlarged SEM images of these ceramic nanofibers.[115]

Dielectrophoresis (DEP) allows the materials to be directly integrated into prefabricated electrodes at selected positions within circuits and does not require post-etching or transfer printing. DEP has been used to prepare high density alignment of carbon

nanotubes.[103, 116] Shekhar et al. reported 2D aligned single-wall carbon nanotube (SWNT) arrays *via* AC-DEP (Figure 1.17a) using stable, surfactant-free SWNT suspensions.[116] They could control the density of nanotubes by tuning the concentration of the SWNT solution, which is of great importance to fabricate high-quality nanoelectronic devices. The alignment of SWNTs was uniform throughout the channel width (Figure 1.17 (d)), which could be attributed to the uniform electric field lines in a parallel plate arrangement (Figure 1.17 (b)).

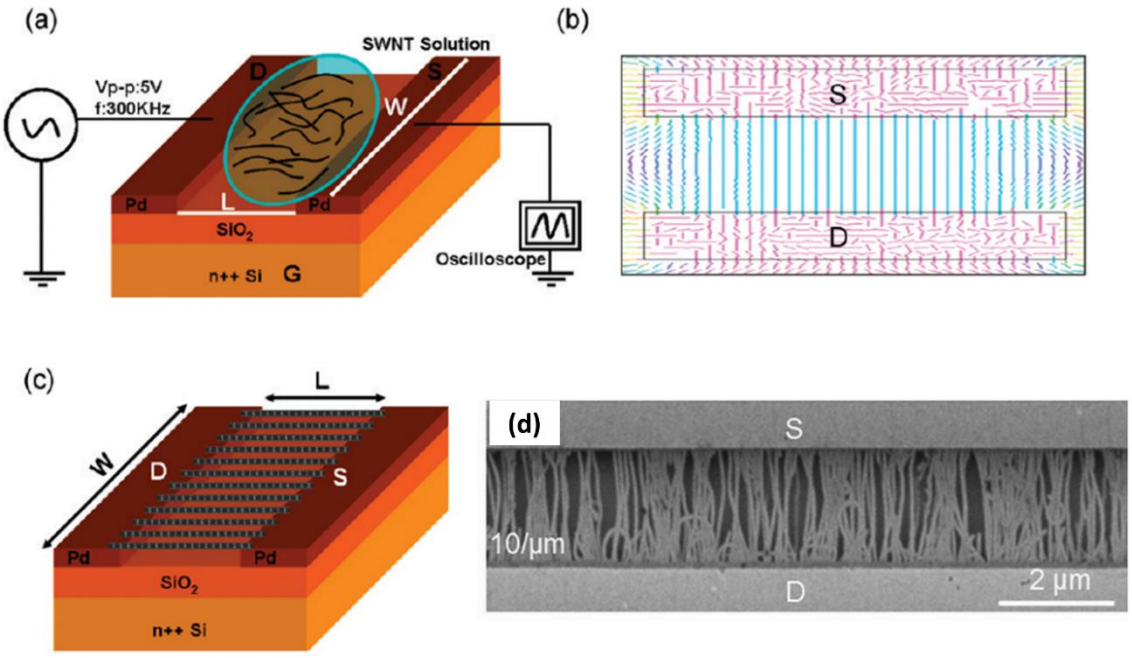

Figure 1.17 (a) Schematic of the DEP assembly. (b) Two-dimensional simulated electric field around the electrode gap. S and D indicated Pd source and drain electrodes. (c) Cartoon of the aligned nanotubes after the DEP process. (d) SEM image for a typical DEP assembly of carbon nanotubes (10 SWNT/μm, L = 2 μm and W = 25 μm).[116]

4.2 Alignment based on a magnetic field

Magnetic alignment is reported as an easy technique for assembling nanowires. By integrating the ferromagnetic ends of nanostructures and using the magnetic interaction between ferromagnetic ends and electrodes, Hangarter et al.[117] manipulated the nanowire assemblies, positioning and spatially manipulating the ferromagnetic nanostructures. Nanowires made of Ni/Au/Ni nanowires and Ni/Bi/Ni were prepared and the contrast between Ni and Au or Bi were observed by SEM (Figure 1.18 a and b). Well-aligned nanowires were observed under a magnetic field, forming high-density arrays. This

alignment platform can also give rise to more complex structures by allowing the rotation of the substrate orientation with respect to the magnetic field. The magnetic field controls the nanowire direction, achieving angles from 45° to 135° with respect to the electrodes as demonstrated in Figure1.18 (c-e).

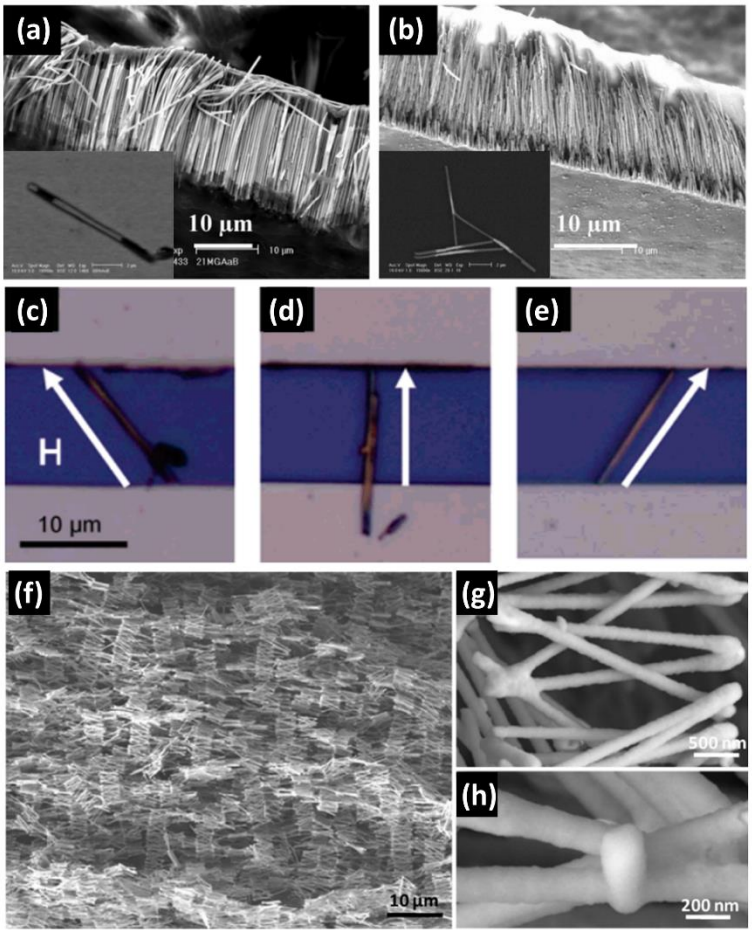

Figure 1.18 Secondary electron (Se^-) SEM images of templated Ni/Au/Ni nanowires (a) and Ni/Bi/Ni nanowires (b), the inserts show single Ni/Au/Ni and Ni/Bi/Ni nanowires. Optical images of magnetically aligned Ni/Au/Ni nanowires at 45º (c), 90º (d) and 135º (e) with respect to the ferromagnetic lines. SEM images of large-scale 3D nanowire networks formed in a liquid reflow with the aid of an external magnetic field.[117] (f) Overview of well aligned nanowire networks composed of Sn-Au-Ni-Au-Sn nanowires, (g) 'head-to-head' bonding by tin solder and (h) 'head-to-tail' bonding by tin solder.[118]

With external magnetic field control, nanowires made of Sn, Au and Ni were assembled on a large scale.[118] At first, nanowires with Sn, Au, Ni and tin solder at both ends were prepared, and these nanowires were successfully assembled and joined together via the solder reflow process. By using the magnetic field assisted method, the nanowires were self-assembled into large-scale 3D network structures (Figure 1.18 (f)), which were

conductive due to the low contact resistance of the solder joints formed. Figure 1.18 (g) and (h) are higher magnification SEM images of a local area showing two types of joints (head-to-head and head-to-tail) between nanowires. Due to the unique network structures, both bonds were present and contributed to the formation of the conductivity. Overall the nanowire structures were very well maintained and good solder joints were formed between the nanowires. Nanowire alignment over large areas were achieved under magnetic field.

4.3 Alignment based on mechanical stretching

Mechanical stretching has been applied to align elongated nanomaterials since 1998.[108] L. Jin et al, suspended multiwalled carbon nanotubes (MWCNT) and a thermoplastic polymer (polyhydroxyaminoether) in chloroform. After sonication and drying, a black thin film was formed, and the polymer-MWCNT composite was cut into 5×3 mm strips. The strips were mechanically stretched by applying a constant load at 100 ^{o}C. The final length of the strips was 5 times that of the initial strips without fracture. During this stretching process, the MWCNTs were very well aligned in the polymer matrix along the stretching direction (Figure 1.19 (a)).

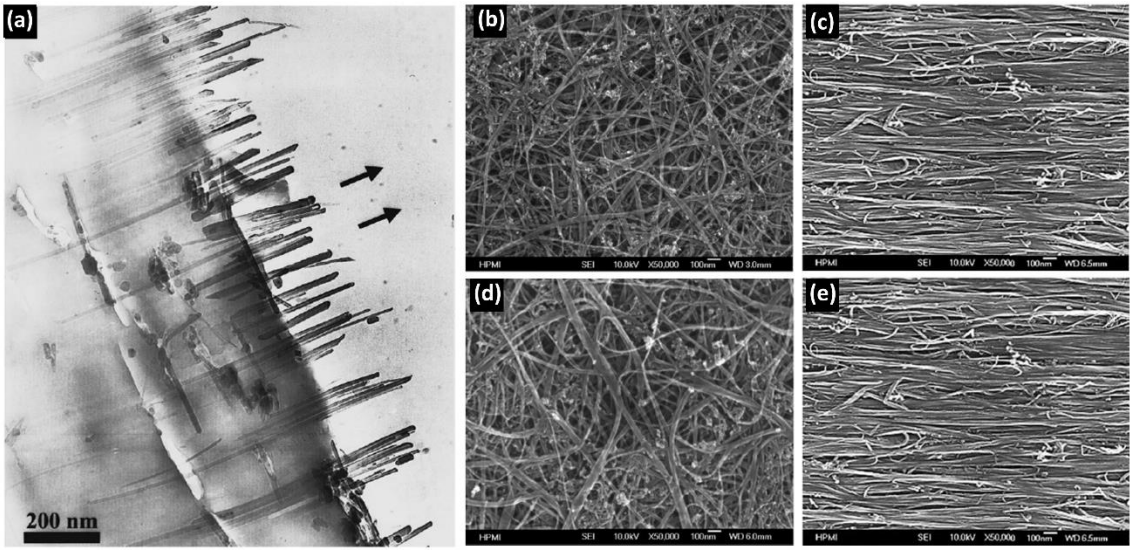

Figure 1.19 (a) TEM image of an internal fracture surface of composite after being sliced parallel to the stretching by a microtome. SEM images of neat MWCNT networks at strains of 0%.[108] (b) and 30% (c). SEM images of resin treated MWCNT networks at strains of 0% (d) and 40% (e).[119]

In 2015, R. Downes[119] treated MWCNT with an uncured resin, which led to an intense increase in the degree of alignment and final mechanical properties of the CNT networks. Sheets of random MWCNTs were cut into strips and placed on a tensile testing machine. Figure 1.19 (b) and (c) show SEM images of neat MWCNT at 0% (b) and 30% (c) strain. MWCNT with the resin could be aligned at strains of 40% (Figure 1.19(e)). MWCNT within the resin were able to withstand up to 40% strains and showed increased orientation and crystallization within the necking region. Therefore, well-aligned MWCNT materials could be obtained via uniaxial strains, the stretching process was highly scalable and the resultant materials have great potential for high-performance composite applications.

4.4 Alignment based on spatial confinement

A large group of alignment techniques are based on confinement, in which entropy plays a crucial role, for example, nematic-like phases in the concentrated and confined zones. These techniques are normally assisted with other factors, such as hydrophobicity, pre-etched substrates and evaporation. Langmuir-Blodgett films, capillary tubes, dip-coating or microfluidic techniques[120] can be included in this section.

The Langmuir-Blodgett technique was used to produce ultrathin organic films, aligning molecules within the film.[121,122] Later this technique was extended to align nanoscale anisotropic materials, if the material was partly hydrophobic. P. Yang's group reported uniform $BaCrO_4$ nanorods organized into 3D-nematic phases by the Langmuir-Blodgett technique *via* the compression of the barriers (illustrated in Figure 1.20).[123,124] Initially, these aggregates were dispersed at the subphase surface in a mostly isotropic organization (Figure 1.20 (a)). When the monolayer was compressed to a surface pressure of ~30 mN/m with continuous compression, a monolayer of nanorods in a nematic arrangement were first obtained, as the nanorods being qualitatively aligned in the direction of the barrier (Figure 1.20 b). With further compression (surface pressure about ~35 mN/m), nanorod assemblies with 2D-smectic arrangement were obtained (Figure 1.20 (c)). When the surface pressure reached above ~38 mN/m, a transition from a monolayer to a multilayer was observed and the system eventually resumed a disordered 3D-nematic configuration (Figure1.20 (d)). With the Langmuir-Blodgett technique, not only the surface

pressure is important to achieve the alignment of nanostructure, but also the surface functionality of these nanostructures played significant roles in regulating the attractive and repulsive interactions among these individual units.

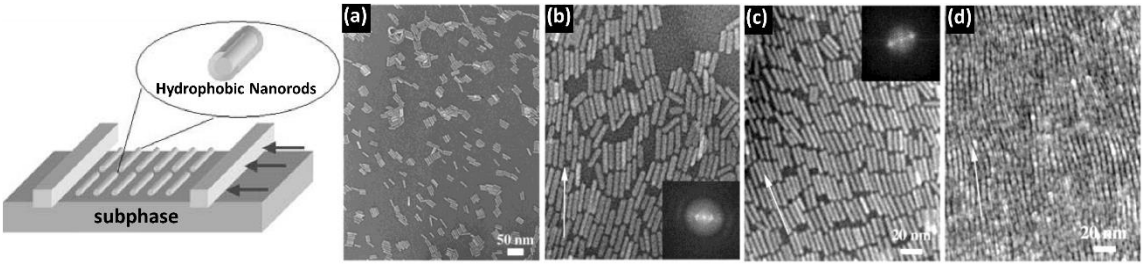

Figure 1.20 Schematic illustration of the Langmuir - Blodgett apparatus for nanorod assembly. Nanorods are generally rendered hydrophobic through surface functionalization.[124] TEM images of the nanorod assemblies at the water/air interface at different stages of compression: (a) isotropic distribution at low pressure; (b) monolayer with partial nematic arrangement; (c) monolayer with smectic arrangement; and (d) nanorod multilayer with nematic configuration. Insets in panels (b) and (c) are the Fourier transform of the corresponding image.[123]

A capillary tube was used to organize rod-like bio nanoparticles (tobacco mosaic virus, TMV particles) by Y. Lin et al.[125]. The tube not only provided a confined space, but also created a curved surface with multiple forces at the contact line to control the self-assembly process. Irregular aggregations of TMV were formed in the capillary tube at a TMV concentration of 0.01 mg/mL in pure water (Figure 1.21 (c)). At a TMV concentration of 0.1 mg/mL, the air-liquid interface was saturated with randomly packed viral particles; therefore, TMV randomly deposited on the substrate and formed a loose multilayer structure (Figure 1.21 (d)). A further increase in the TMV concentration increased the volume fraction of TMV at the interface, leading to an intensification in the dipole-dipole repulsion between TMV rods until they were forced to orient perpendicular to the air-liquid interface (Figure 1.21 (e)). By packing head to head and forming lines, the rod-like particles not only relieved the strong dipole-dipole repulsion, but also effectively minimized the interfacial energy, and gained entropy in the system.

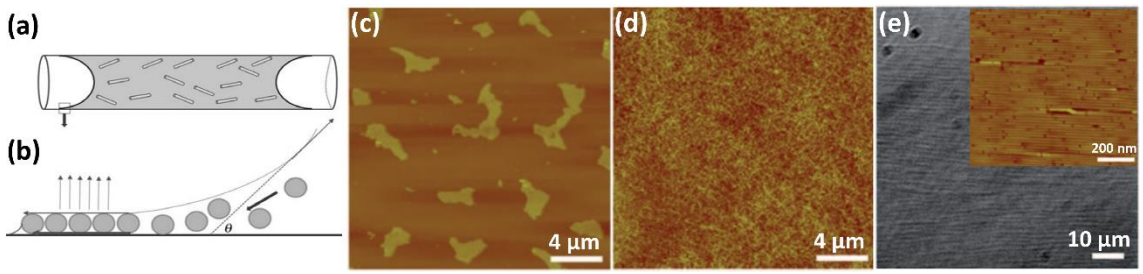

Figure 1.21 (a) Schematic representation of a capillary tube containing the TMV solution, (b) schematic illustration of the thin meniscus formed at the contact line, as indicated in a small square on left bottom of (a). Theta is the contact angle between water and the substrate and the arrow on the right labels the moving direction of TMV particles caused by convective force. Atomic force microscopy (AFM) images of the drying TMV solution in the capillary tube at a TMV concentration of 0.01 mg/mL (c) and 0.1 mg/mL (d). Optical image (e) of a drying 26 mg/mL TMV solution in the capillary tube. The insert is an AFM image.[125]

Dip-coating is one technique without sophisticated operations, which has been widely used in industry and the laboratory. H. Shimoda et al.[126] reported that SWNTs could be aligned on a glass surface (Figure 1.22 (a)). The nematic like SWNT structures formed were aligned on the surface of substrate (Figure 1.22 (b)). With dip-coating, the meniscus itself constrains nanoobjects in the suspension. For a better understanding about this technique, more examples and the mechanism of organization will be presented in Chapter 4.

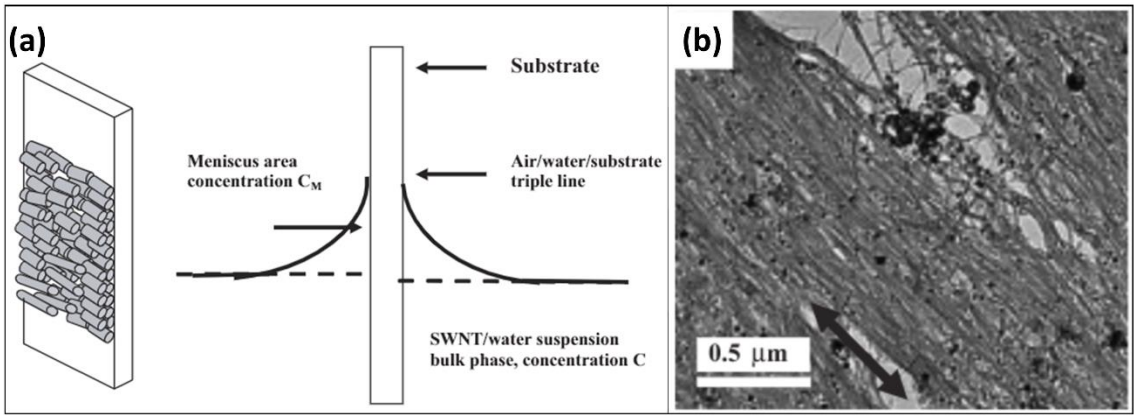

Figure 1.22 (a) Schematic illustration of the self-assembly process. The substrate was vertically immersed in a suspension of SWNTs. With the evaporation of water, SWNT bundles assembled on the glass substrate around the air/water/substrate triple line, as showed on the left. (b) TEM image of a self-assembled SWMT membrane.[126]

4.5 Alignment based on shear force

Shear induced alignment can be used for a wide range of materials compared to the magnetic or electric field techniques, and it theoretically can work with all elongated materials, independent of their chemical properties.

J. Kim et al. fabricated uniformly aligned nanorod films of lanthanum phosphate ($LaPO_4$) structures by blade coating (Figure 1.23 e).[127] A phase-tuned nanorod suspension was deposited on a substrate moving at a constant speed (500 μm/s) under the coating blade

with a controlled gap width (50 μm). The blade was designed to have a large drag area parallel to the substrate. During the blade dragging the suspension, a constant shear rate (γ) was applied generating a couette flow in the gap, thus uniformly shearing the suspension. After passing the blade, the substrate was heated to evaporate the solvent and solidify the film (Figure 1.23 (c)). If a thixotropic gel was used, the geometry of the rods in each section of the coating steps in Figure 1.23 (e) correspond to the schematic snapshots in Figure 1.23 (a-d). Figure 1.23 (f) shows an SEM image of the $LaPO_4$ nanorod film's surface and cross section.

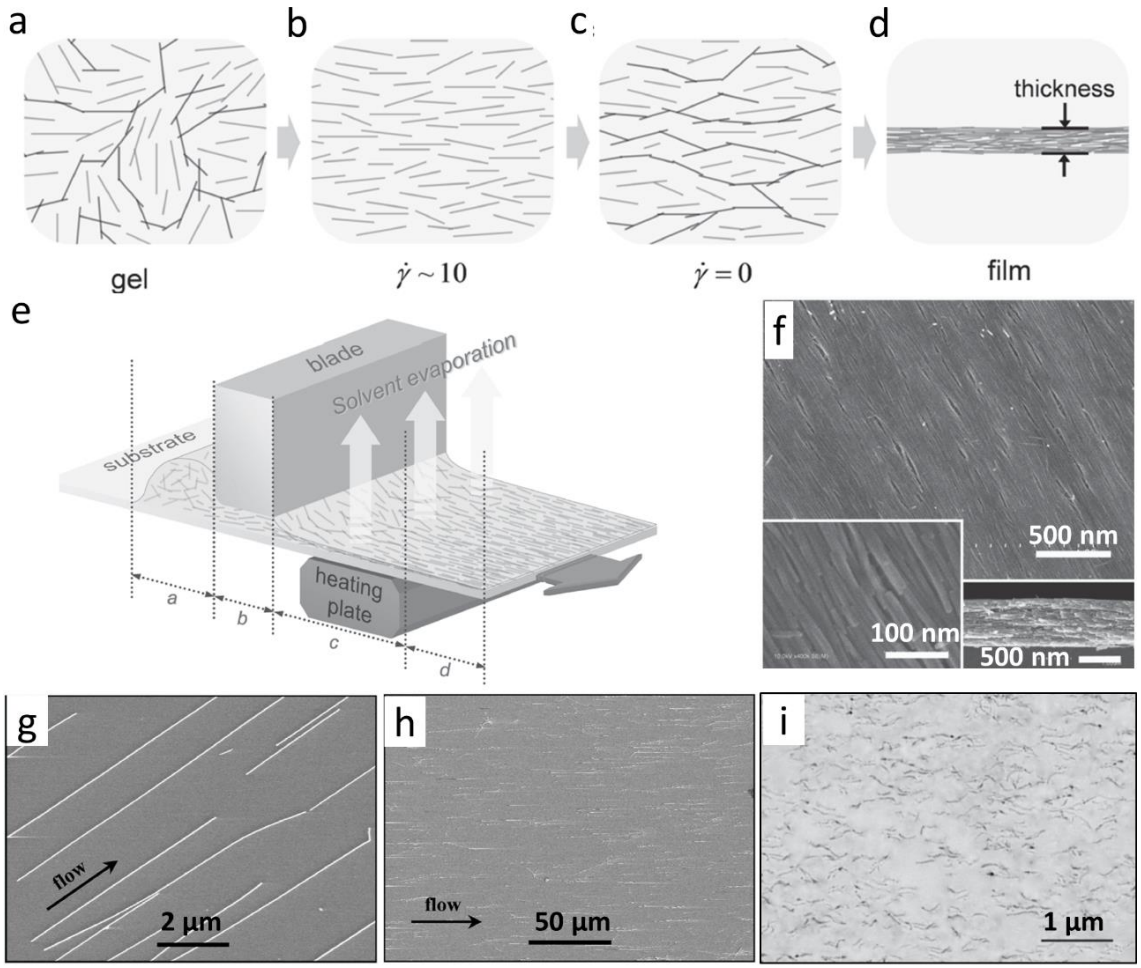

Figure 1.23 Snapshots of nanorods in the thixotropic suspension at each step of the coating process: (a) gel with random networks, (b) sheared sol where the networks break down, (c) gel with aligned networks after shear, and (d) aligned film after solvent evaporation. (e) Schematic illustration of the fabrication of aligned nanorod thin films by the blade-coating process. (a-d) are indicated in the scheme (e). (f) SEM images of an aligned $LaPO_4$ nanorod film surface and cross section.[127] (g) and (h) SEM images of parallel arrays of InP NWs aligned by channel flow.[113] (i) TEM image of aluminum oxide nano wire (NW) alignment.[128]

There are other works based on shear force with a pre-designed channel to increase this effect.[113,128] Y. Huang et al. aligned indium phosphide (InP) nanowires (NW) through microfluidic channel structures formed between a polymer mold and a flat substrate (Figure 1.23 (g,h)). D. E. Yunus et al. aligned short nanofibers of aluminum oxide in 3D printed polymer composites (Figure 1.23 (i)).[128]

Cellulosic nanofibers (CNFs) can be aligned by the grazing incidence spraying technique (Figure 1.24), which is developed by G. Decher.[129] In recent years, in addition to CNFs, monolayer of silver nanowires (AgNWs)[130] and gold nanorods (Au NR)[131] have been deposited with one orientation through this spray device. Furthermore, multilayers of orientated elongated materials could be obtained using the layer-by-layer technique, which will be illustrated in the Chapter 5.

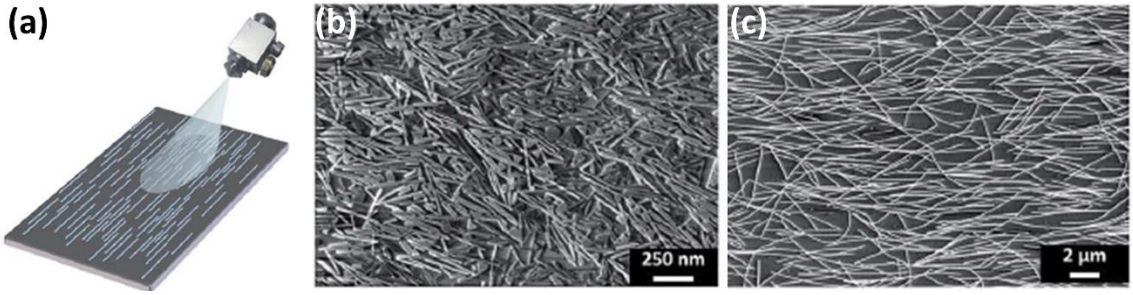

Figure 1.24 Schematic representation of the grazing incident spray approach (a), SEM images of a deposited monolayer of long Au NRs (b) and Ag NWs (c). [131]

5. Conclusions

In this chapter, chirality at different levels has been introduced, from chiral molecules to supramolecular structures, from organic supramolecular structures to inorganic materials, from chiral substrates to achiral particles. At each step, the transmission of chirality is the key. Once the chiral control is mastered, materials with chiral properties could be used in various applications, and in this thesis, I will focus on optics in the visible range. Plasmonic nanoparticles with special electromagnetic properties will prove to be promising candidates for the design of optical materials. Furthermore, oriented and densely packed nanomaterials may lead to a further increase in electromagnetic manipulation. In order to fabricate devices with anisotropic physical properties, the controlled alignment of nanoscale objects is one key prerequisite for

materials science. To convert nanoobjects in suspension to macroscopic 2D or 3D materials, highly stable and well-defined nanoobjects are required, which can withstand complex forces during alignment. Various alignment techniques based on different organization principles have been presented in this chapter.

References

1. Wikipedia, https://en.wikipedia.org/wiki/Chirality.

2. M. L. Pasteur, Mémoire sur la relation qui peut exister entre la forme cristalline et la composition chimique, et sur la cause de la polarisation rotatoire, C. R. T. Académie des science, 1848, 26, 535-539.

3. H. Yamamoto and T. Kato, Molecular Technology, Volume 3 Materials Innovation, chapter 6, pp: 107-137.

4. G. M. Whitesides and B. Grzybowski, Self-assembly at all scales, Science, 2002, 295, 2418-2421.

5. S. Hashiguchi, A. Fujii, J. Takehara, T. Ikariya and R. Noyori, Asymmetric transfer hydrogenation of aromatic ketones catalyzed by chiral ruthenium (II) complexes, J. Am. Chem. Soc., 1995, 117, 7562-7563.

6. L. Pu, Fluorescence of organic molecules in chiral recognition, Chem. Rev., 2004, 104, 1687-1716.

7. Y. Kubo, S. Maeda, S. Tokika and M. Kubo, Colorimetric chiral recognition by a molecular sensor, Nature, 1996, 382, 522-524.

8. Z. Chen, Q. Wang, X. Wu, Z. Liu and Y. Jiang, Optical chirality sensing using macrocycles synthetic and supramolecular oligomers/polymers, and nanoparticle based sensors, Chem. Soc. Rev., 2015, 44, 4249-4263.

9. Y. Xia, Chiral inorganic nanoparticles: origin, optical properties and bio applications, Nanoscale, 2011, 3, 1374-1382.

10. J. B. Pendry, A chiral route to negative refraction, Science, 2004, 306, 1353-1355.

11. J. K. Gansel, M. Thiel, M. S. Rill, M. Decker, K. Bade, V. Saile, G. Von Freymann, S. Linden and M. Wegener, Gold helix photonic metamaterial as broadband circular polarizer, Science, 2009, 5947(325): 1513-1515.

12. Y. Liu and X. Zhang, Metamaterials: a new frontier of science and technology, Chem. Soc. Rev., 2011, 40, 2494-2507.

13. A. Kuzyk, R. Schreiber, Z. Fan, G. Pardatscher, E. Roller, A. Hogele, F. C. Simmel, A. O. Govorov and T. Liedl, DNA-base self-assembly of chiral plasmonic nanostructures with tailored optical response, Nature, 2002, 483, 311-314.

14 . J. -M. Lehn, Supramolecular chemistry-scope and perspectives molecules, supermolecules, and molecular devices, Angew. Chem., 1988, 27(1), 89-112.

15. X. Zhang and C. Wang, Supramolecular amphiphiles, Chem. Soc. Rev., 2011, 40, 94-101.

16. C. V. Kulkarni, Lipid self-assemblies and nanostructure emulsions for cosmetic formulations, Cosmetics, 2016, 3, 37.

17. A. Blanazs, S. P. Armes and A. J. Ryan, Self-assembled block copolymer aggregates: from micelles to vesicles and their biological applications, Macromol. Rapid Commun., 2009, 30, 267-277.

18. C. Huang, D. Quinn, Y. Sadovsky, S. Suresh and K. J. Hsia, Formation and size distribution of self-assembled vesicles, PNAS, 2017, 114(11), 2910-2915.

19. K. Yamada, I. Hirotaka, I. Toshio, F. Takanori and H. Chuichi, Formation of helical super structure from single-walled bilayers by amphiphiles with oligo-L-Glutamic acid-head group, Chem. Lett., 1984, 1713-1716.

20. X. Zhu, Y. Jiang, D. Yang, L. Zhang, Y. Li and M. Liu, Homochiral nanotubes from heterochiral lipid mixtures: a shorter alkyl chain dominated chiral self-assembly, Chem. Sci., 2019, 10, 3873-3880.

21. J. Fuhrhop, D. M. Krull and G. Buldt, Precipitates with β-pleated sheet structure by mixing aqueous solutions of helical poly(D-lysine) and poly(L-lysine), Angew. Chem. Int. Engl., 1987, 26 (7), 699-700.

22. J. Fuhrhop, P. Schnieder, J. Rosenberg and E. Boekema, The chiral bilayer effect stabilizes micellar fibers, J. Am. Chem. Soc., 1987, 109, 3387-3390.

23. J. Fuhrhop, P. Schnieder, E. Boekema and W. Helfrich, Lipid bilayer fibers from diastereomeric and enantiomeric N-Octyladonamides, J. Am. Chem. Soc., 1988, 110, 2861-2687.

24. R. Oda, I. Huc and S. J. Candau, Gemini surfactants as new low molecular weight gelators of organic solvents and water, Angew. Chem. Int. Ed., 1998, 37(9), 2689-2691.

25. R. Oda, I. Huc, M. Schmutz, S. J. Candau and F. C. Mackintosh, Tuning bilayer twist using chiral counterions, Nature, 1999, 399, 566-569.

26. M. M. Green, B. A. Garetz, B. Munoz, H. Chang, S. Hoke and R. G. Cooks, Majority rules in the copolymerization of mirror image isomers, J. Am. Chem. Soc, 1995, 117, 4181-4182.

27. H. Cao, and S. D. Feyter, Amplification of chirality in surface-confined supramolecular bilayers, Nat. Commun., 2018, 9, 3416.

28. W. Jin, T. Fukushima, M. Niki, A. Kosaka, N. Ishii and T. Aida, Self-assembled graphitic nanotubes with one-handed helical arrays of a chiral amphiphilic molecular graphene, 2005, 102(3), 10801-10806.

29. J. Kumar, H. Tsumatori, T. Kawai and T. Nakashima, Self-discriminating termination of chiral supramolecular polymerization: tuning the length of nanofibers, 2015, 54, 5943-5947.

30. C. C. Lee, C. Grenier, E. W. Meijer and A. P. H. J. Schenning, Preparation and characterization of helical self-assembled nanofibers, Chem. Soc. Rev., 2009, 38, 671-683.

31. C. Wang, Z. Wang and X. Zhang, Amphiphilic building blocks for self-assembly: from amphiphiles to supra-amphiphiles, Acc. Chem. Res., 2012, 45(4), 608-618.

32. E. Yashima, K. Maeda, H. Lida, Y. Furusho and K. Nagai, Helical polymers: synthesis, structures and functions, Chem. Rev., 2009, 109, 6102-6211.

33. M. M. Green, and M. P. Reidy, Macromolecular stereochemistry: The out of proportion influence of optically active comonomers on the conformational characteristics of polyisocyanates. The sergeants and soldiers experiment, J. Am. Chem. Soc., 1989, 111, 6452-6454.

34. A. R. A. Palmans, and E. W. Meijer, Amplification of chirality in dynamic supramolecular aggregates, Angew. Chem. Int. Ed., 2007, 46, 8948-8968.

35. W. Makiguchi, S. Kobayashi, Y. Furusho and E. Yashima, Formation of a homo double helix of a conjugated polymer with carboxy groups and amplification of macromolecular helicity by chiral amines sandwiched between the strands, Angew. Chem. Int. Ed., 2013, 52, 5275-5279.

36. C. F.J. Faul, and M. Antonietti, Ionic self-assembly: facile synthesis of supramolecular materials, Adv. Mater., 2003, 15(9), 673-683.

37. T. Shimizu, M. Masuda and H. Minamikawa, Supramolecular nanotube architectures based on amphiphilic molecules, Chem. Rev., 2005, 105(4), 1401-1444.

38. E. Yashima, N. Ousaka, D. Taura, K. Shimomura, T. Ikai and K. Maeda, Supramolecular helical systems: helical assemblies of small molecules, foldamers, and polymers with chiral amplification and their functions, Chem. Rev., 2016, 116, 13752-13990.

39. D. D. Archlbald, and S. Mann, Template mineralization of self-assembled anisotropic lipid microstructures, Nature, 1993, 364, 430-433.

40. Y. Ono, K. Nakashima, M. Sano, Y. Kanekiyo, K. Inoue, S. Shinkai, M. Sano and J. Hojo, Organic gels are useful as a template for the preparation of hollow fiber silica, Chem. Commun., 1998, 14, 1477-1478.

41. J. D. Hartgerink, E. Beniash and S. I. Stupp, Self-assembly and mineralization of peptide-amphiphile nanofibers, Science, 2001, 294, 1684-1688.

42. S. Mann, J. P. Hannington and R. J. P. Williams, Phospholipid vesicles as a model system for biomineralization, Nature, 324, 565-567.

43. C. J. Brinker, K. D. Keefer, D. W. Schaefer and C. S. Ashley, Sol-gel transition in simple silicates, J. Non-Cryst. Solids, 1982, 48, 47-64.

44. D. Zhao, J. Feng, Q. Huo, N. Melosh, G. H. Fredrickson, B. F. Chmelka and G. D. Stucky, Triblock copolymer syntheses of mesoporous silica with periodic 50 to 300 angstrom pores, Science, 1998, 279, 548-552.

45. D. Zhao, Q. Huo, J. Feng, B. F. Chmelka and G. D. Stucky, Nonionic triblock and star deblock copolymer and oligomeric surfactant syntheses of highly ordered, hydrothermally stable, mesoporous silica structures, J. Am. Chem. Soc., 1998, 120, 6024-6036.

46. Y. Yang, M. Suzuki, H. Fukui, H. Shirai and K. Hanabusa, Preparation of helical mesoporous silica and hybrid silica nanofibers using hydrogelator, Chem. Mater., 2006, 18, 1324-1329.

47. J. H. Jung, Y. Ono, K. Hanabusa and S. Shinkai, Creation of both right-handed and left-handed silica structures by sol-gel transcription of organogel fibers comprised of chiral diaminocyclohexane derivatives, J. Am. Chem. Soc., 2000, 122, 5008-5009.

48. J. H. Jung, H. Kobayashi, M. Masuda, T. Shimizu and S. Shinkai, Helical ribbon aggregation composed of a crown-appended cholesterol derivative which acts as an amphiphilic gelator of organic solvents and as template for chiral silica transcription, J. Am. Chem. Soc., 2001, 123, 8785-8789.

49. S. Tamaru, M. Takeuchi, M. Sano and S. Shinkai, Sol-gel transcription of sugar-append porphyrin assemblies into fibrous silica: unimolecular stacks versus helical bundles as templates, Angew. Chem. Int. Ed., 2002, 41, 853-856.

50. S. Che, Z. Liu, T. Ohsuna, K. Sakamoto, O. Terasaki and T. Tatsumi, Synthesis and characterization of chiral mesoporous silica, Nature, 2004, 429, 281-284.

51. K. Sugiyasu, S. Tamaru, M. Takeuchi, D. Berthier, I. Huc, R. Oda and S. Shinkai, Double helical silica fibrils by sol–gel transcription of chiral aggregates of gemini surfactants, Chem. Comm., 2002, 1212-1213.

52. T. Delclos, C. Aime, E. Pouget, A. Brizard, I. Huc, M. Delville and R. Oda, Individualized silica nanohelices and nanotubes: tuning inorganic nanostructures using lipidic self-assemblie, Nano Lett., 2008, 8 (7), 1929-1935.

53. Y. Okazaki, J. Cheng, D. Dedovets, G. Kemper, M. Delville, M. Durrieu, H. Ihara, M. Takafuji, E. Pouget and R. Oda, Chiral colloids: Homogeneous suspension of individualized SiO2 helical and twisted nanoribbons, 2014, 8 (7), 6863-6872.

54. Y. Okazaki, T. Buffeteau, E. Siurdyban, D. Talaga, N. Ryu, R. Yagi, E. Pouget, M. Takafuji, H. Ihara and R. Oda, Direct observation of siloxane chirality on twisted and helical nanometric amorphous silica, Nano Lett., 2016, 16, 6411-6415.

55. D. Pines, D. Bohm, A collective description of electron interaction: II collective *vs* individual particle aspects of the interaction, Phys. Rev., 1952, 85(2), 338-353.

56. M. Pelton, G. Bryant, Introduction to metal-nanoparticle plasmonics, 2013, Vol.5.

57. P. Aebi, et al., Secondary-electron and energy-loss spectra of copper, Surf. Sci. Lett., 1991, 264, 181-186.

58. Q.-C. Sun, Y. Ding, S. M. Goodman, H. H. Funke and P. Nagpal, Copper plasmonics and catalysis: role of electron-phonon interactions in dephasing localized surface plasomons, Nanoscale, 2014, 6, 12450-12457.

59. D. L. Jeanmaire, and R. P. Vanduyne, Surface raman spectroelectrochemistry part 1. heterocyclic, aromatic and aliphatic amines adsorbed on the anodized silver electrode, J. Electroanal. Chem., 1977, 84, 1-20.

60. M. D. Malinsky, K. L. Kelly, G. C. Schatz and R. P. Van Duyne, Nanosphere lithography: effect of substrate on the localized surface plasmon resonance spectrum of silver nanoparticles, J. Phys. Chem. B, 2001, 105, 2343-2350.

61. L. J. Sherry, R. Jin, C. A. Mirkin, G. C. Schatz and R. P. Van Duyne, Localized surface plasmon resonance spectroscopy of single siliver triangular nanoprisms, Nano Lett., 2006, 6(9), 2060-2065.

62. S. Link and M. A. El-Sayed, Size and temperature dependence of the plasmon absorption of colloidal gold nanoparticles, J. Phys. Chem. B, 1999, 103, 4212-4217.

63. S. K. Ghosh and T. Pal, Interparticle coupling effect on the surface plasmon resonance of gold nanoparticles: from theory to applications, Chem. Rev., 2007, 107, 4797-4862.

64. P. M. Lundquist, W. P. Lin, Z. Y. Xu, G. K. Wong, E. D. Rippert, J. A. Helfrich and J. B. Ketterson, Ultraviolet second harmonic generation in radiofrequency sputterdeposited aluminum nitride thin film, Appl. Phys. Lett., 1994, 65(9), 1084-1087.

65. R. LaVilla and H. Mendlowitz, Optical constants of aluminum in vacuum ultraviolet, Phys. Rev. Lett., 1962, 9(4), 149-150.

66. M. Shahzad, G. Medhi, R. E. Peale, W. R. Buchwald, J. W. Cleary, R. Soref, G. D. Boreman and O. Edwards, Infrared surface plasmons on heavily doped silicon, J. Appl. Phys, 2011, 110, 12305.

67. M. E. Stewart, C. R. Anderton, L. B. Thompson, J. Maria, S. K. Gray, J. A. Rogers and R. G. Nuzzo, Nanostructured plasmonic sensors, Chem. Rev., 2008, 108, 494-521.

68. W. L. Barnes, A. Dereux and T. W. Ebbesen, Surface plasmon subwavelength optics, Nature, 2003, 424, 824-830.

69. K. Sawai, R. Tatumi, T. Nakahodo and H. Fujihara, Asymmetric Suzuki-Miyaura coupling reactions catalyzed by chiral palladium nanoparticles at room temperature, Angew. Chem. Int. Ed., 2008, 47, 6917-6919.

70. T. Mallat, E. Orglmeister and A. Baiker, Asymmetric Catalysis at chiral metal surfaces, Chem. Rev., 2007, 107(11), 4863-4890.

71. Y.-J. Kang, J.-W. Oh, Y.-R. Kim, J. S. Kim and H. Kim, Chiral gold nanoparticle-based electrochemical sensor for enantioselective recognition of 3,4-dihydroxyphenylalanine, Chem. Comm., 2010, 46, 5665-5667.

72. Z. Chen, Q. Wang, X. Wu, Z. Li and Y. Jiang, Optical chirality sensing using macrocycles, synthetic and supramolecular oligomers/polymers, and nanoparticles based sensors, Chem. Soc. Rev., 2015, 44, 4249-4263.

73. W. L. Barnes, A. Dereux and T. W. Ebbesen, Surface plasmon subwavelength optics, Nature, 2003, 424, 824-830.

74. Wikipedia, https://en.wikipedia.org/wiki/Circular_dichroism

75. Y. Tang, A. E. Cohen, Optical chirality and its interaction with matter, Phys. Rev. Lett., 2010, 104, 163901.

76. J. B. Pendry, A chiral route to negative refraction, Science, 2004, 306, 1353-1356.

77. A. Kuzyk, R. Schreiber, Z. Fan, G. Pardatscher, E. Roller, A. Hogele, F. C. Simmel, A. O. Govorov and T. Liedl, DNA-based self-assembly of chiral plasmonic nanostructure with tailored optical response, Nature, 2012, 483, 311-314.

78. C. Gautier and T. Burgi, Chiral gold nanoparticles, Chem. Phys. Chem., 2009, 10, 483-492.

79. W. Ma, L. Xu, A. F. de Moura, X. Wu, H. Kuang, C. Xu and N. A. Kotov, Chiral inorganic nanostructures, Chem. Rev., 2017, 117, 8041-8093.

80. J. Yeom, B. Yeom, H. Chan, K. W. Smith, S. Dominguez-Medina, J. H. Bahng, G. Zhao, W. Chang, S. Chang, A. Chuvilin, D. Melnikau, A. L. Rogach, P. Zhang, S. Link, P. Kral and N. A. Kotov, Chiral templating of self-assembling nanostructures by circularly polarized light, Nat. Mater., 2014, 14, 66-72.

81. A. Lechtken, D. Schooss, J. R. Stairs, M. N. Blom, F. F. Priv.-Doz, N. Morgner, O. Kostko, B. von Issendorff and M. M. Kappes, Au_{34}^- : a chiral gold cluster, Angew. Chem. Int. Ed., 2007, 46, 2944-2948.

82. B. Yeom, H. Zhang, H. Zhang, J. il Park, K. Kim, A. O. Govorov and N. A. Kotov, Chiral plasmonic nanostructures on achiral nanopillars, Nano Lett., 2013, 13, 5277-5283.

83. A. Ben-Moshe, S. G. Wolf, M. B. Sadan, L. Houben, Z. Fan, A. O. Govorov and G. Markovich, Enantioselective control of lattice and shape chirality in inorganic nanostructures using chiral biomolecules, Nat. Commun., 2014, 5, 4302.

84. M. O. Lorenzo, C. J. Baddeley, C. Muryn and R. Raval, Extended surface chirality from supramolecular assemblies of absorbed chiral molecules, Nature, 2000, 404, 376-379.

85. V. Humblot, S. Hag, C. Muryn, W. A. Hofer and R. Raval, From local adsorption stresses to chiral surface: (R, R)- tartaric acid on Ni (110), J. Am. Chem. Soc., 2002, 124, 503-510.

86. C. Gautier and T. Burgi, Chiral N-isobutyryl-cysteine protected gold nanoparticles: preparation, size selection, and optical activity in the UV-vis and infrared, J. Am. Chem. Soc., 2006, 128, 11079-11087.

87. C. Gautier and T. Burgi, Chiral inversion of gold nanoparticles, J. Am. Chem. Soc., 2008, 130, 7077-7084.

88. T. Nakashima, Y. Kobayashi and T. Kawai, Optical activity and chiral memory of thiol-capped CdTe nanocrystals, J. Am. Chem. Soc., 2009, 131, 10342-10343.

89. C. Singh, P. K. Ghorai, M. A. Horsch, A. M. Jackson, R. G. Larson, F. Stellacci and S. C. Glotzer, Entropy-mediated patterning of surfactant-coated nanoparticles and surfaces, Phys. Rev. Lett., 2007, 99, 226106.

90. I. Dolamic, S. Knoppe, A. Dass and T. Burgi, First enantioseparation and circular dichroism spectra of Au_{38} clusters protected by achiral ligands, Nat. Commun., 2012, 3, 798.

91. Q. Chen, D. J. Frankel and N. V. Richardson, Chemisorption induced chirality: glycine on Cu (110), Surf. Sci., 2002, 497, 37-46.

92. M.-R. Goldsmith, C. B. George, G. Zuber, R. Naaman, D. H. Waldeck, P. Wipf and D. N. Beratan, The chiroptical signature of achiral metal clusters induced by dissymmetric absorbates, Phys. Chem. Chem. Phys., 2006, 8, 63-67.

93. C. Noguez and I. L. Garzon, Optically active metal nanoparticles, Chem. Soc. Rev., 2009, 38, 757-771.

94. W. Ma, H. Kuang, L. Xu, L. Ding, C. Xu, L. Wang and N. A. Kotov, Attomolar DNA detection with chiral nanorod assemblies, Nat. Commun., 2013, 4, 2689.

95. I. Lieberman, G. Schemer, T. Fried, E. M. Kosower and G. Markovich, Plasmon-resonance-enhanced absorption and circular dichroism, Angew. Chem. Int. Ed., 2008, 47, 4855-4857.

96. Z. Li, Z. Zhu, W. Liu, Y. Zhou, B. Han, Y. Gao and Z. Tang, Reversible plasmonic circular dichroism of Au nanorod and DNA assemblies, J. Am. Chem. Soc., 2012, 134, 3322-3325.

97. W. Yan, L. Xu, C. Xu, W. Ma, H. Kuang, L. Wang and N. A. Kotov, Self-assembly of chiral nanoparticle pyramids with strong R/S optical activity, J. Am. Chem. Soc., 2012, 134, 151114-15121.

98. J. Cheng, G. Le Saux, J. Gao, T. Buffeteau, Y. Battie, P. Barois, V. Ponsinet, M. Delville, O. Ersen, E. Pouget and R. Oda, GoldHelix: gold nanoparticles forming 3D helical superstructures with controlled morphology and strong chiroptical property, ACS Nano, 2017, 11, 3806-3818.

99. Z. Fan and A. O. Govorov, Plasmonic circular dichroism of chiral metal nanoparticle assemblies, Nano Lett., 2010, 10, 2580-2587.

100. R. Blell, X. Lin, T. Lindstrom, M. Ankerfors, M. Pauly, O. Felix and G. Decher, Generating in-plane orientational order in multilayer films prepared by spray-assisted layer-by-layer assembly, ACS Nano, 2017, 11, 84-94.

101. J.-W. Liu, H.-W. Liang and S.-H. Yu, Macroscopic-scale assembled nanowire thin films and their functionalities, Chem. Rev., 2012, 112, 4770-4799.

102. C. Bower, W. Zhu, S. Jin and O. Zhou, Plasma-induced alignment of carbon nanotubes, Appl. Phys. Lett., 2000, 77, 830-834.

103. J. Xie, X. Li and Y. Xia, Putting electrospun nanofibers to work for biomedical research, Macromol. Rapid Commun., 2008, 29, 1775-1792.

104. B. Wang, Y. Ma, N. Li, Y. Wu, F. Li and Y. Chen, Facile and scalable fabrication of well-aligned and closely packed single-walled carbon nanotube films on various substrates, Adv. Mater., 2010, 22, 3067-3070.

105. B. K. Sarker, S. Shekhar and S. I. Khondaker, Semiconducting enriched carbon nanotube aligned arrays of tunable density and their electrical transport properties, ACS Nano, 2011, 5 (8), 6297-6305.

106. C. Hangarter, Y. Rheem, B. Yoo, E.-H. Yang and N. V. Myung, Hierarchical magnetic assembly of nanowires, Nanotechnology, 2007, 18, 205305.

107. I. O. Shklyarevskiy, P. Jonkheijm, P. C. M. Christianen, A. P. H. J. Schenning, A. Del Guerzo, J.-P. Desvergne, E. W. Meijer and J. C. Mann, Magnetic alignment of self-assembled anthracene organogel fibers, Langmuir, 2005, 21, 2108-2112.

108. L. Jin, C. Bower and O. Zhou, Alignment of carbon nanotubes in a polymer matrix by mechanical stretching, Appl. Phys. Lett., 1998, 78(9), 1197-1199.

109. S. Zhang, X. Liu, S. F. Barreto-Ortiz, Y. Yu, B. P. Ginn, N. A. DeSantis, D. L. Hutton, W. L. Grayson, F.-Z. Cui, B. A. Korgel, S. Gerecht and H.-Q. Mao, Creating polymer hydrogel microfibres with internal alignment via electrical and mechanical strentching, Biomaterials, 2014, 35, 3243-3251.

110. M. C. Petty, Possible applications for Langmuir-Blodegett films, Thin Solid Films, 1992, 210, 417-426.

111. J. Huang, R. Fan, S. Connor and P. Yang, One-step patterning of aligned nanowire arrays by programmed dip coating, Angew. Chem. Int. Ed., 2007, 46, 2414-2417.

112. W. Han and Z. Lin, Learning from “coffee rings”: ordered structures enabled by controlled evaporative self-assembly, Angew. Chem. Int. Ed., 2012, 51, 1534-1546.

113. Y. Huang, X. Duan, Q. Wei and C. M. Lieber, Directed assembly of one-dimensional nanostructures into functional networks, Science, 2001, 630-633.

114. H. Hu, M. Pauly, O. Felix and G. Decher, Spray-assisted alignment of layer-by-layer assembled silver nanowires: a general approach for preparation of highly anisotropic nano-composite films, Nanoscale, 2017, 9, 1307-1314.

115. D. Li, Y. Wang and Y. Xia, Electrospinning of polymeric and ceramic nanofibers as uniaxially aligned arrays, Nano Lett., 2003, 3(8), 1167-1171.

116. S. Shekhar, P. Stokes and S. I. Khondaker, Ultrahigh density alignment of carbon nanotube arrays by dielectrophoresis, ACS Nano, 2011, 5(3), 1739-1746.

117. C. M. Hangarter, N. V. Myung, Magnetic alignment of nanowires, Chem. Mater., 2005, 17(6), 1320-1324.

118. F. Gao and Z. Gu, Nano-soldering of magnetically aligned three-dimensional nanowire networks, Nanotechnology, 2010, 21, 115604.

119. R. Downes, S. Wang, D. Haldane, A. Moench and R. Liang, Strain-induced alignment mechanisms of carbon nanotube networks, Adv. Eng. Mater., 2015, 17(3), 349-358.

120. J. Angle, A. Lazzolino, J.-B. Salmon, J. Leng, S. P. Chandran, V. Ponsinet, A. Desert, A. Le Beulze, S. Mornet, M. Treguer-Delapierre and M. A. Correa-Duarte, Microfluidic-induced growth and shape-up of three-dimensional extended arrays of densely packed nanoparticles, ACS Nano, 2013, 7(8), 6465-6477.

121. K. B. Blodgett and I. Langmuir, Built-up films of barium stearate and their optical properties, Phys. Rev., 1937, 51, 964-982.

122. D. K. Schwartz, J. Garnaes, R. Viswanathan and J. A. Zasadzinski, Surface order and stability of Langmuir-Blodgett films, Science, 1992, 257, 508-511.

123. F. Kim, S. Kwan, J. Akana and P. Yang, Langmuir-Blodgett nanorod assembly, J. Am. Chem. Soc., 2001, 123, 4360-4361.

124. P. Yang and F. Kim, Langmuir-Blodgett assembly of one-dimensional nanostructures, Chem. Phys. Chem., 2002, 3, 503-506.

125. Y. Lin, E. Balizan, L. Andrew Lee, Z. Niu and Q. Wang, Self-assembly of rodlike bio-nanoparticles in capillary tubes, Angew. Chem., 2010, 122, 880-884.

126. H. Shimoda, S. J. Oh, H. Z. Geng, R. J. Walker, X. B. Zhang, L. E. McNeil and O. Zhou, Self-assembly of carbon nanotubes, Adv. Mater., 2002, 14(18), 899-901.

127. J. Kim, J. Peretti, K. Lahlil, J.-P. Boilot and T. Gacoin, Optically anisotropic thin films by shear-oriented assembly of colloidal nanorods, Adv. Mater., 2013, 25, 3295-3300.

128. D. E. Yunus, W. Shi, S. Sohrabi and Y. Liu, Shear induced alignment of short nanofibers in 3D printed polymer composites, Nanotechnology, 2016, 27, 495302.

129 .G. Decher, Fuzzy nanoassemblies: toward layered polymeric multicomposites, Science, 1997, 277, 1232-1237.

130. H. Hu, M. Pauly, O. Felix and G. Decher, Spray-assisted alignment of Layer-by-Layer assembled silver nanowires: a general approach for the preparation of highly anisotropic nano-composite films, Nanoscale, 2017, 9, 1307-1314.

131. S. Sekar, V. Lemaire, H. Hu, G. Decher and M. Pauly, Anisotropic optical and conductive properties of oriented 1D-nanoparticle thin films made by spray-assisted self-assembly, Faraday Discuss., 2016, 191, 373-389.

Chapter 2. Research design and methodology

Contents

1. Research design

The chiral molecules are known to interact with the light differently depending on the enantiomer (making light turning left or right). During the last two decades, the chirality is studied not only related to the molecular level but also to the nanometric objects and the macroscopic level. Chiroptical materials at all the dimensions have attracted human's attention because they can affect the propagation of light. Plasmonic metal particles are good candidate because they have surface plasmonic resonance (SPR) at the same range as the visible light. On the other hand, in terms of visible light whose wavelength is between 400-700 nm, manufacturing materials that interact with light in a controllable way is challenging as it must be structured on a length scale smaller than the wavelength of the exciting electromagnetic field, i.e. with a characteristic scale of tens of nanometers for applications in the visible range.[1,2,3] Regarding the difficulty to create chiral plasmonic nanoparticles, a common strategy is the induction of chirality from a template or a molecule to the nanoparticle. Particularly, the helicoidal organization of non-chiral plasmonic particles induces strong chiroptical properties.

In the present work, to build up the plasmonic chiral nanomaterials, we start from a chiral amphiphile self-assembly. The CMA group has reported methods on synthesizing organic right- and left-handed helical nanostructures via chiral self-assembling of a complex of a Gemini 16-2-16 surfactant complexed with a tartrate counter-ion. The chirality L or D of tartrate counter-ion induces the right- or left-handed helicoidal direction.[4] Through sol-gel process, these chiral helical nanostructures can be transcribed into silica materials.[5] Meanwhile, spherical gold nanoparticles (GNPs) stabilized by tannic acid and citric acid are synthesized and can be attached on the chiral silica helical structures through electrostatic interaction.[6] Such structures named Goldhelices show chiroptical properties. The optical property comes from the plasmonic nature of the GNPs and the chirality comes from the helicoidal assembly. Based on these previous works, we aim in this manuscript at increasing and modulating the chiroptical properties focusing on three points (as shown in Figure 2.1): 1) the tunability of the morphology of the organic self-assembly and so the silica templates, 2) a better grafting of the GNPs to increase the stability of the Goldhelices and 3) the organization in 2 or 3 dimensions of these nano

objects. Only the achievement of these 3 points could make the Goldhelices interesting materials for concrete applications like the creation of circular and linear polarizers with tunable properties.

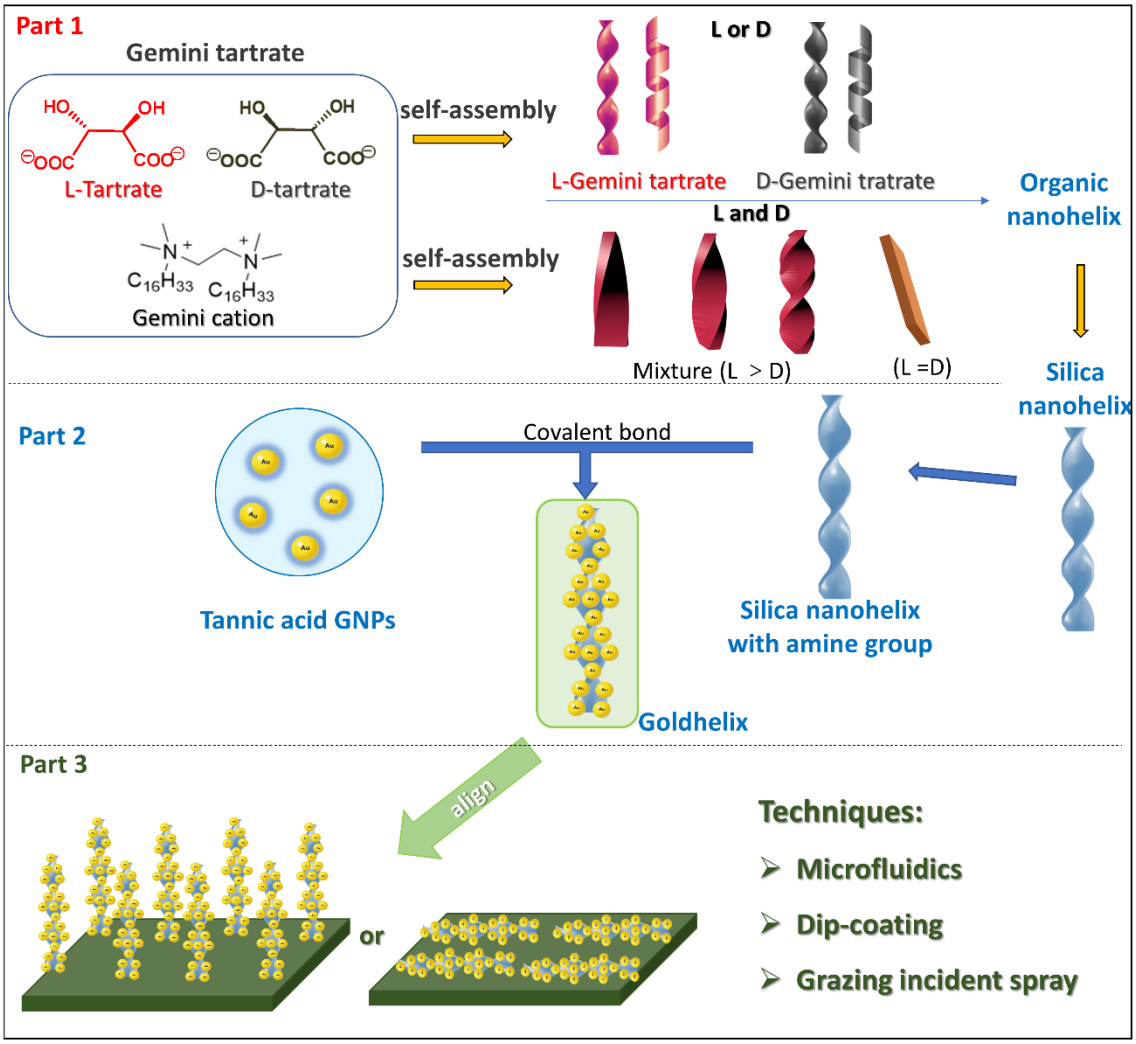

Figure 2.1 Scheme of the three experimental parts in this thesis.

Firstly, in order to adjust the morphology of the chiral substrate, we need to start from the amphiphile self-assembly morphologies tuning. Through studying the supramolecular structure formed by different enantiomeric excess of the tartrate counter-ion, the mechanism of self-assembly process is studied and unveiled in Chapter 3. X-ray diffraction, transmission electron microscopy and scanning electron microscopy were used to observe the structure and morphology of the self-assembly. Electronic circular dichroism

and vibrational circular dichroism spectra were carried on comparing the chirality of the supramolecular structures.

If the Goldhelices presented by Cheng et al.[6] are interesting for fundamental science, their real use is not possible as the electrostatic bond between the GNPs and the silica surface is a weak bond and suffer from vulnerability while changing the environment, for example under different solvent, temperature, or even dry status. To build the solid chiral nanomaterial, we develop a strong covalent grafting of the GNPs on the silica structures (Figure 2.1, Part 2). This study is described in Chapter 4. Transmission electron microscopy and electronic circular dichroism were used to investigate the morphology and chirality of the Goldhelices.

If one-dimensional nanoscale building blocks can be ordered and rationally assembled into appropriate two- or three-dimensional architectures, they will offer fundamental scientific opportunities to investigate the influence of their collective optical, magnetic, and electronic properties with a directionality, particularly important for technological applications. [7, 8] To do so, grazing incident spray, dip-coating and microfluidic techniques were used to organize the anisotropic nanomaterials (Part 3). These studies are detailed in Chapter 5. Optical microscopy, atomic force microscopy and scanning electron microscopy were used to observe the organization of the building blocks, and the optical property of the materials was measured and analyzed by electronic CD spectra and ellipsometry.

2. Methodology

2.1 Optical microscopy

The optical microscope is a type of microscope that commonly uses visible light and a system of lenses to magnify images of small objects. In this thesis, A Nikon DXM 1200 camera and Lucia G software with an objective magnification of ×10 were used to collect optical microscopy images with a resolution of 1.1 μm.

2.2 Atomic force microscopy (AFM)

AFM is a type of scanning probe microscope with demonstrated resolution on the order of fractions of a nanometer. The information is gathered by "touching" the surface with a mechanical probe. AFM analysis of the topology of the samples was performed on a Dimension Icon ScanAsyst from Bruker in intermittent contact mode (or tapping mode). The morphologies and patterns of samples were measured precisely using an AFM with a silicon nitride probe, and general overview of the sample was collected by an optical microscope which is coupled with AFM device. The parameters for measurement were a PeakForce® frequency of 2 kHz and a scan tip rate of 0.125 Hz. The probe used has a tip radius of 5.0 nm and a constant stiffness of 0.4 N/m.

2.3 Transmission electron microscopy (TEM)

2.3.1 Equipment description

TEM is a microscopic technique in which a beam of electrons is transmitted through a specimen to form an image formed from the interaction of the electrons with the sample.[9] A sophisticated system of electromagnetic lenses focuses the scattered electrons into an image or diffraction pattern (Figure 2.2 a). The beam of electrons from the electron gun is focused into a small, thin, coherent beam by using the condenser lens. The beam then strikes the specimen and parts of it are transmitted depending upon the thickness and electron transparency of the specimen. This transmitted portion is focused by the objective lens into an image on fluorescent screen or charge coupled device (CCD) camera. The image strikes the fluorescent screen and light is generated, allowing users to see the images. The image then passed down the column through the intermediate and projector lenses, is enlarged all the way. TEMs can reveal the finest details of internal structure - in some cases as small as individual atom. [10]

TEM was performed at room temperature on a Philips EM 120 electron microscope operating at 120 kV, and the images were collected by a 2k × 2k Gatan ssCCD camera.

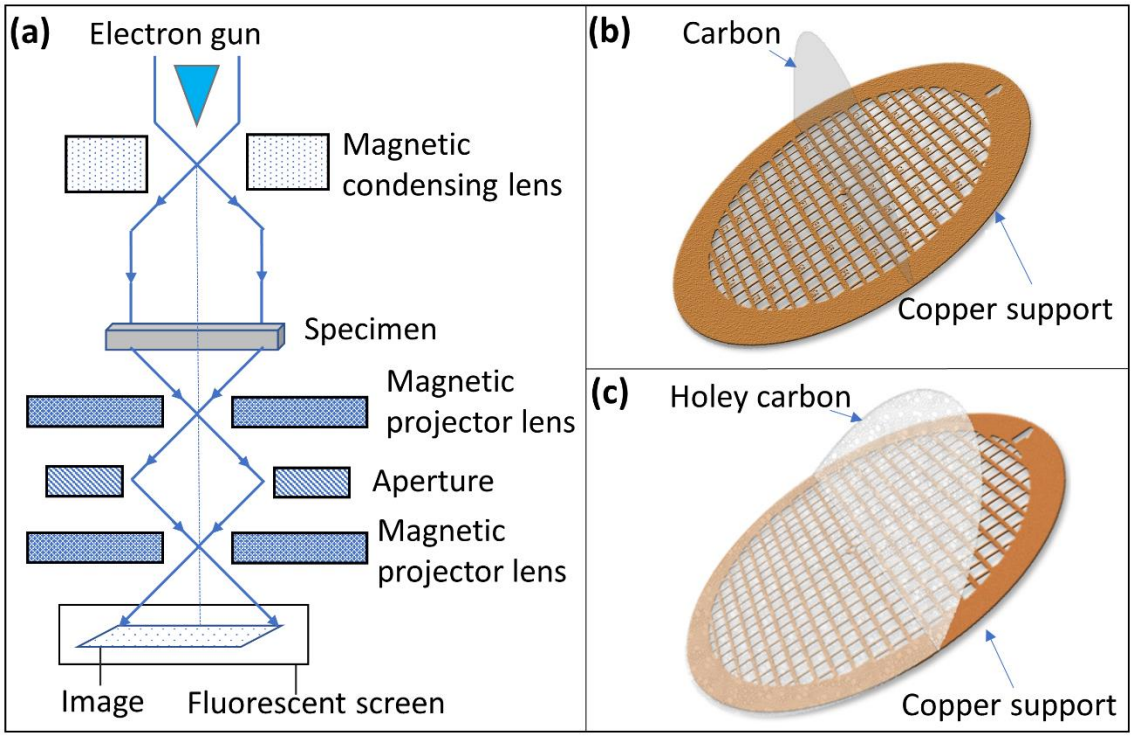

Figure 2.2 (a) Schematic illustration of TEM working principle. Grids on which sample deposited for TEM observation (b) and Cryo-TEM observation (c).

2.3.2 Sample preparation

To prepare TEM sample of inorganic nanomaterials, 400 meshes copper grids covered by a thin carbon film are used (Figure 2.2 b) When the solvent of the suspension is organic solvent, one drop of the liquid sample (~20 µL) can be deposited on grid. When the solvent is water, before dropping the aqueous solution, the carbon film should be treated by UV/Ozone cleaner (purchased from Bioforce/ Nanoscience). With this treatment, the carbon surface becomes hydrophilic. This induce a better wettability of the solution and avoid the aggregation due to the drying. After the suspensions of nanoobjects are dropped on the surface of carbon film around 40 seconds, to avoid the agglomeration of nanomaterials, filter papers are used to blot the liquid drop until only thin layer of liquid film remained on the surface of the grid. 30 mins are needed to let the remaining liquid evaporate.

To observe the morphology of the organic gemini/tartrate samples, the use of an external stainer is needed as the organic material is not dense enough to the electrons. To do so, the sample is first deposited on the hydrophilic TEM grid and the excess of liquid is

blotted. Before a complete drying of the sample, one drop of stainer is dropped on the grid for 40 s, then the stainer is removed by filter paper. The stainer will accumulate at the surface of the organic objects, inducing a better contrast and so revealing their morphologies. In the thesis, stainer is 1% wt uranyl acetate in aqueous solution.

2.4 Cryo-Transmission electron microscope (Cryo-TEM)

2.4.1 Equipment description

Cryo-TEM is an electron microscopy technique in which aqueous suspensions are observed in their native state (no drying) thanks to the cryogenic freezing of the sample. During the observation, the specimen holder of Cryo-TEM maintains the specimen at liquid nitrogen temperature.

The Cryo-EM utilized in the work is Talos Arctica 200 kV-FEG under 200 kV. With its innovative design to increase stability of samples, it enables us to quickly observe supramolecular structure with time dependence. TEM mode was used to observe the self-assembly structures of chiral amphiphiles, which were frozen in the ice on the surface of grid.

2.4.2 Sample preparation

To prepare Cryo-TEM samples, 200 meshes copper grids covered with holey carbon films (Figure 2.2 c) are used. At first, the grid was treated by oxygen plasma atmosphere to make it hydrophilic. Then, one drop of sample was deposited on the grid and after 10 seconds the drop was blotted by filter paper keeping a very thin slide of the specimen (the grids with thin liquid film remaining). The grid is immediately plunged into a liquid ethane bath to vitrify the water solvent and freeze the sample.

It is very important that the process of freezing the sample is very quick. This prevents the crystalline ice formation around the specimen sample. If ice is formed, it readily absorbs the electron beam, which in turn obscures the sample.[11]

2.5 Scanning electron microscopy (SEM)

2.5.1 Equipment description

SEM is a powerful tool for materials surface characterization. At first, electrons are generated at the top of the column by the electron source. Lenses are used to control the path of the electrons. The condenser lens defines the size of the electron beam (which defines the resolution), while the main role of the objective lens is to focus the beam onto the sample, as shown in Figure 2.3 (a). In this thesis, only secondary electron detector was used. However, overall, the interaction of electrons with a sample can result in the generation of many different types of electrons, photons, or irradiations.[12]

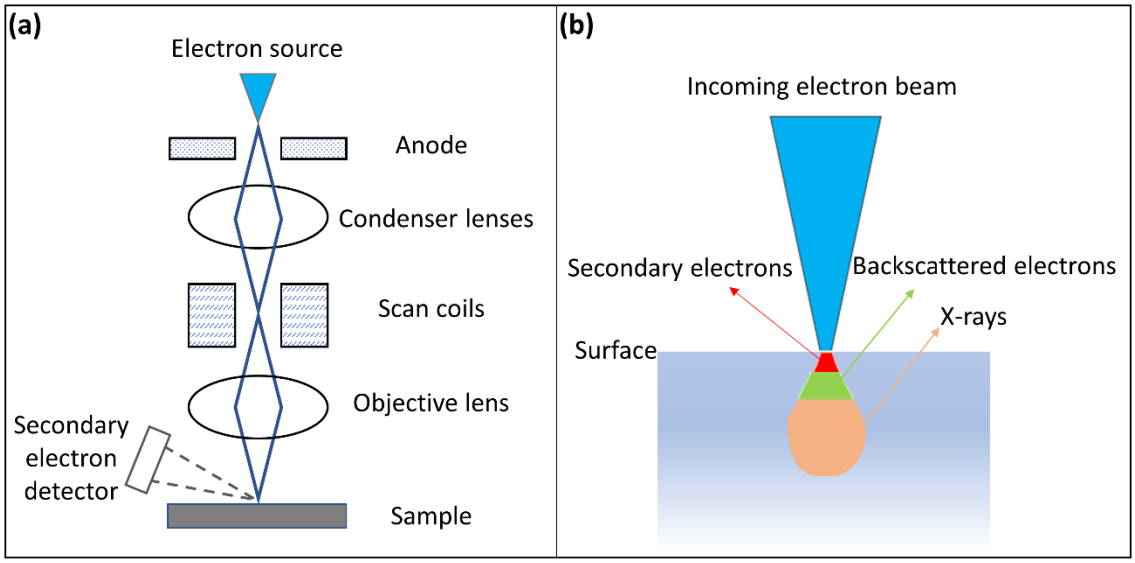

Figure 2.3 (a) Schematic representation of basic SEM components and (b) different types of signals which are detected in SEM.

In the case of SEM, there are these types of signals that can be detected: secondary electrons (SE), backscattered electrons (BSE), and X-ray (Figure 2.3 b). SE are produced when an incident electron excites an electron in the sample and loses some of its energy in the process. The excited electron moves towards the surface of the sample and, if it still has sufficient energy, it excites the surface and is called a secondary electron. Alternatively, when the electron beam strikes the sample, some of the electrons are scattered (deflected from their original path) by atoms in the specimen in an elastic fashion (no loss of energy). These elastically scattered primary electrons (high-energy electrons) that rebound from the

sample surface are called BSE. X-rays generated from the electron-matter interaction is used to analyze elements of the sample due to the specific energy of each element.

Two models of SEM have been used for the observation: SEM-FEG JSM 6700F JEOL, and SEM-FEG Hitachi SU-70. The measurement condition of Hitachi SU-70 is under 1 kV, and distance is 3 mm. The measurement with 6700F JEOL is under 5kV voltage, with a distance of 6-8 mm.

2.5.2 Sample preparation

The silicon slides are fixed with double face carbon tape on a classical SEM stub. For the observation with Hitachi SU-70, this SEM sample could be directly inserted into machine. Sample metallization with Au/Pt plasma is required for 6700F JEOL observation. When the substrate and sample both are insulator materials, carbon conductive glue is applied on the margin of samples.

3. Spectroscopic techniques

3.1 X-ray scattering techniques

X-ray scattering techniques are a family of non-destructive analytical techniques which reveal information about the crystal structure. When X-rays are incident on an atom, they make the electronic cloud move, as does any electromagnetic wave. The movement of these charges re-radiates waves with the same frequency, blurred slightly due to a variety of effects; this phenomenon is known as Rayleigh scattering (or elastic scattering). The properties and functions of materials largely depend on the crystal structures and therefore X-ray scattering has been widely used as an indispensable mean in materials research, development and production.[13, 14, 15]Two process may occur: 1) the beam may be absorbed with an ejection of electrons from the atom, or 2) the beam may be scattered.[16] These techniques are based on observing the scattered intensity of an X-ray beam hitting a sample as function of incident and scattered angle, polarization and wavelength or energy.[17] These re-emitted wave fields interfere with each other either constructively or destructively, producing a diffraction pattern on a detector or film. The resulting wave interference pattern is the basis of diffraction analysis, which is called Bragg diffraction.[18] As shown in

Figure 2.4, when the beams traverse a crystalline solid, constructive interference occurs when this length is equal to an integer multiple of the wavelength of the radiation, therefore we have the equation:

$$2dsin\theta = n\lambda$$

where d is interplanar distance of lattice planes of a crystalline, θ indicates the scattering angle, n is a positive integer, and λ is the wavelength of the incident wave. With the scattering angle and interference wavelength, the crystalline interplanar distance can be caculated.

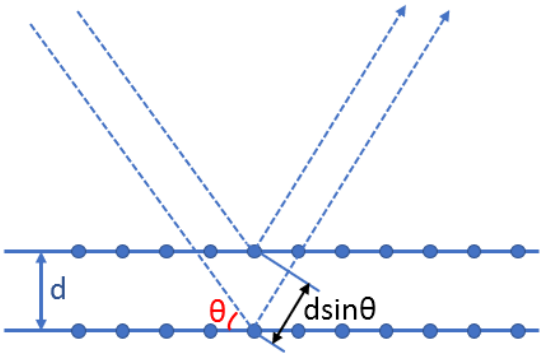

Figure 2.4 Scheme of Bragg diffraction. Two beams with identical wavelength and phase approach a crystalline solid and are scattered off two different atoms within it. The lower beam traverses an extra length of 2dsinθ.

The experiments in the thesis were done with Rigaku Nano viewer, Microfocus rotating Cu anode 3kW. X-ray scattering spectrum is performed under room temperature, and with 16 min exposure time.

3.2 Ultraviolet-visible (UV-vis) spectroscopy

UV-*vis* spectroscopy is routinely used in analytical chemistry to detect the absorbance of the molecules in the range of 190-750 nm (UV wavelength: 190-380 nm, visible light wavelength: 380-750 nm).[19] It is most often used as a quantitative way to determine concentrations of an absorbing species, through Beer-Lambert law[20]:

$$A = log_{10}(I_0/I) = \varepsilon cL$$

Where A is the measured absorbance, I_0 is the intensity of the incident light at a given wavelength, I is the transmitted intensity, ε is the molar absorptivity, c is the concentration of absorbing species, L is the path length through the sample in centimeters.

3.3 Electron circular dichroism spectroscopy

Circular dichroism (CD) spectroscopy is dichroism involving circularly polarized light, the differential absorption of left- and right- handed light. Circularly polarized light of an electromagnetic wave is a polarization state in which, at each point, the electric field of the wave has a constant magnitude, but its direction rotated with time at a steady rate in a plane perpendicular to the direction of the wave. As shown in Figure 2.6, a circularly polarized wave can be in one of two possible states: right circular polarization or left circular polarization in which the electric field vector rotates in a right- or left-hand sense with respect to the direction of propagation.[21]

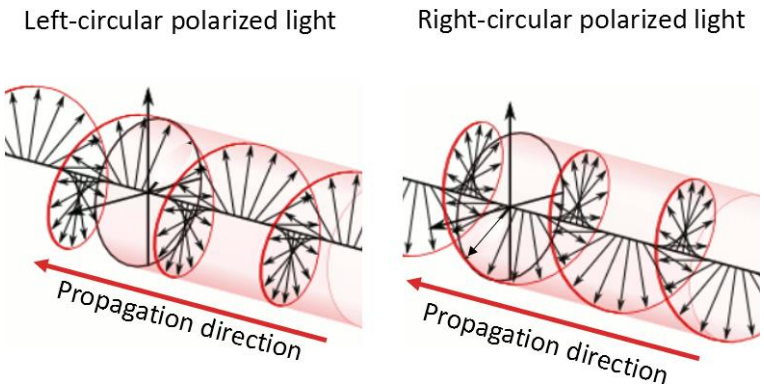

Figure 2.6 Schema of the electric field vectors of a traveling circularly polarized electromagnetic wave, left-circular polarized light and right-circular polarized light. (reprint from wikipedia)

The chiral molecules or materials with chiral properties have different absorptions for left- and right-handed light. The electronic CD spectroscopy is usually measured as the differential absorbance of left (A_{LCP}) and right (A_{RCP}) circularly polarized light, and so be expressed as:

$$\Delta A = A_{LCP} - A_{DCP}$$

With Beer Lambert law inducing the concentration of sample and pathlength of the incident light, the equation can be transformed as:

$$\Delta\varepsilon = \varepsilon_{LCP} - \varepsilon_{DCP} = \Delta A/(c \cdot L)$$

where ε_{LCP} and ε_{DCP} are the molar absorptivity for left and right polarized light. The output results of CD spectra are indicated with the degree of ellipticity θ, which is defined as tangent of the ratio of the minor to major elliptical axis. As Figure 2.7 shown, the angle θ

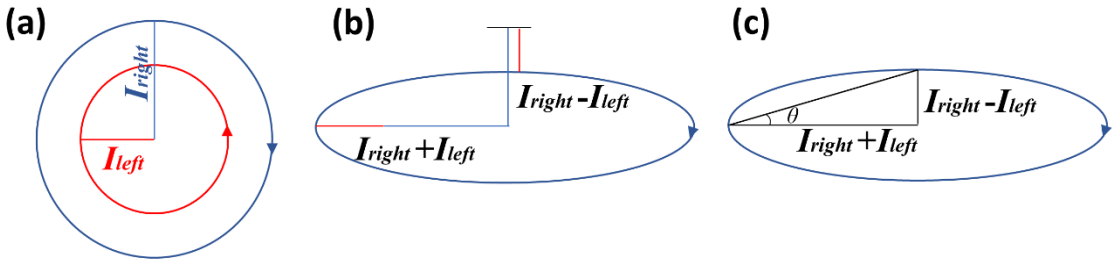

Figure 2.7 When the right and left circular polarized light have different magnitude (a), they can be merge together to form elliptically polarized light (b), and the angle of ellipticity θ indicated in (c) is used to describe this explicitly. *Iright* and *Ileft* are the intensities of right and left circularly polarized light.

Electronic CD spectra is measured with a Jasco J-815 spectrometer, and wavelength range is between 183 to 800 nm. Temperature can be controlled within 4 to 90 ^{o}C. While the CD measurement is performing, UV spectra can be recorded simultaneously.

3.4 Vibrational circular dichroism

3.4.1 Infrared spectroscopy

Infrared spectroscopy (IR) is a technique detecting the interaction of infrared radiation with matter, and IR spectra is recorded by passing a beam of infrared light through the sample.[19] The entire wavelength range is measured using a Fourier transform instrument and then a transmittance or absorbance spectrum is generated using a dedicated procedure. When the frequency of the IR is the same as the vibrational frequency of a bond or collection of bonds, absorption occurs, which means the peaks in IR spectra indicate vibrational mode of the bonds.

3.4.2 Vibrational circular dichroism spectroscopy (VCD)

Vibrational circular dichroism (VCD) consists in measuring the difference of the absorbance spectra recorded with left and right circularly polarized light in infrared range. The main principle is the same than the electronic CD spectroscopy, except the wavelength range of incident electromagnetic wave which covers the Infrared range. The VCD makes

it possible to determination the configuration and conformation of chiral molecules. VCD spectra offers different chiral information of chiral material in terms of bond vibrations instead of electron excitation.

The VCD spectra were collected with an optical bench, which consists of polarization vibrational dichroism by polarization modulation (PM-VCD spectroscopy) and NEXUS 670 spectrometer (Thermo Optek).[22] The pathlength of cell for VCD measurement is 50 μm, and the resolution is of 4 cm^{-1}.

3.5 Muller matrix polarimetry

3.5.1 Spectroscopic ellipsometry

Ellipsometry is an optical technique to investigate the refractive index and the thickness of the thin film. The principle of the ellipsometry is to analyze the light polarization changes through the sample. The ellipsometric studies are done in collaboration with Yann Battié at the University of Lorraine. An UVISEL Horiba phase modulated ellipsometer is used. The Figure 2.8 represents the components of the ellipsometry, a polarization of incident light is controlled by the first blue polarizer, and the polarized light pass through the sample. Then, the reflected light is collected by the detector. After passing through the sample, this polarized beam passes through photoelastic modulator, an analyzer, polarizer, then reaches the detector which allows to acquire the polarization change of the beam.[23]

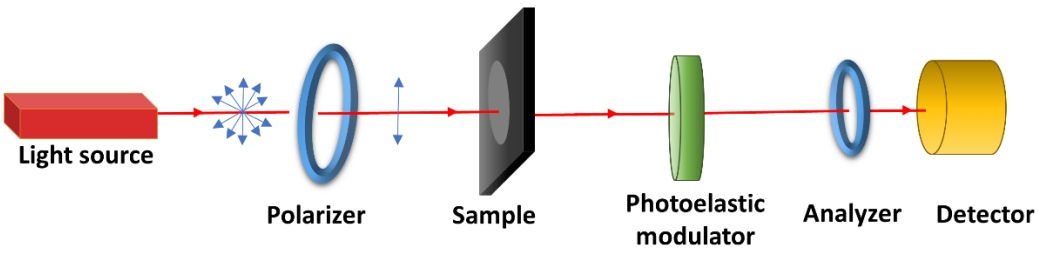

Figure 2.8 The configuration of the UVISEL phase modulated ellipsometer.

3.5.2 Muller matrix polarimetry

Muller matrix provides the most general and complete description of the response of a medium to excitation by polarized light. And it characterized the optical properties of the sample by interaction of polarized light with matter in the absence of non-linear effects. Muller matrix M of a sample is defined by the linear relationship:

$$S_r = MS_i$$

where S_r and S_i are the Stokes vectors of the incident and the reflected beam.[24] Muller matrix is marked as:

$$M = (m_{ij})_{1 \le ij \le 4}$$

a 4 × 4 real matrix which characterizes the sample. Based on the Muller matrix, circular birefringence (CB), circular dichroism (CD), linear birefringence (LB) and linear dichroism (LD) can be calculated through the transform of $M = e^L$, then matrix L can be written as:

$$L = \begin{bmatrix} 0 & -LD & -LD' & CD \\ -LD & 0 & CB & LB' \\ -LD' & -CB & 0 & -LB \\ CD & -LB' & LB & 0 \end{bmatrix}$$

In this thesis, the first 3 columns of the Mueller matrix are accessible since this system can only perform linear polarization incident light. 12 elements of the Mueller matrix are accessible by performing ellipsometry measurements under different orientations of the polarizer and the photoelastic modulator. It offers the information of circular birefringence, circular dichroism, linear birefringence and linear dichroism for a sample.

In summary, to characterize the morphology of the created organic and inorganic nanoobjects and evaluate their chiral properties, an association of microscopic and spectroscopic techniques is necessary. As Figure 2.9 summarizes, morphology and alignment are observed with different microscopies: the TEM reveal the individual object morphology at the nanometric scale. The SEM gives a 3D information of these morphologies at the nanoscale (particularly the handedness of the helices) and also a more

global organization at scales going from 100 nm to 10 µm. The microscopic organization is revealed by the optical microscopy techniques. Electron circular dichroism and vibration circular dichroism detects the self-assembly of the Gemini tartrate. X-ray scattering helps to analysis the molecular structures. Mueller matrix indicates the optical properties of non-oriented and oriented Goldhelices.

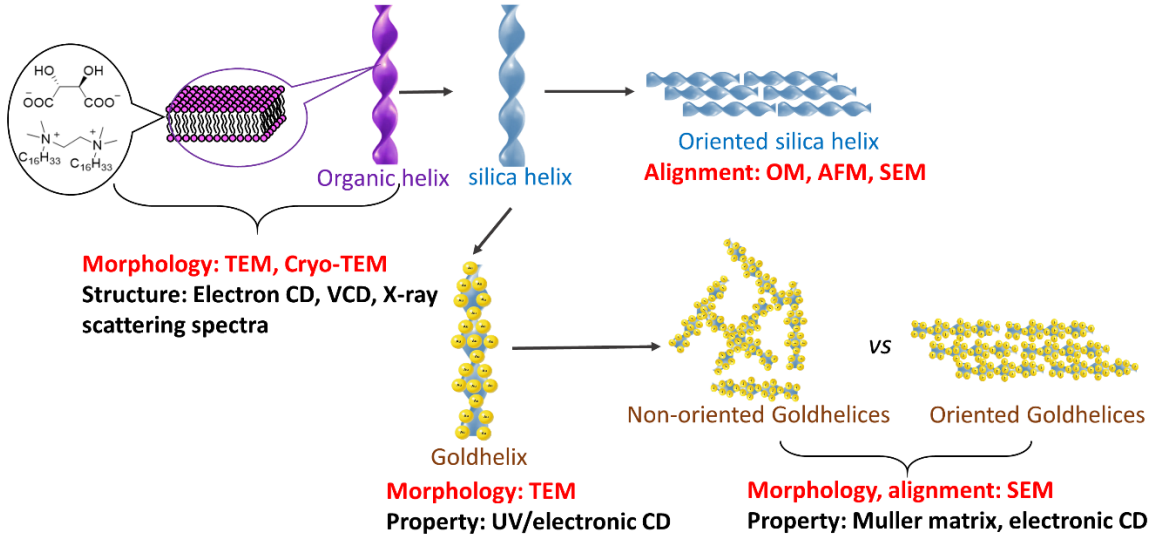

Figure 2.9 Scheme to show the samples synthesized in the thesis and their corresponding characterization techniques.

4. Alignment techniques

4.1 Grazing incident spray

4.1.1 Grazing incident spray set up

The grazing incidence spray (GIS) is used for the purpose of producing oriented deposits of anisotropic nanoparticles.[25] As the Figure 2.10 (a) shows, the computer is the center to set the values of liquid rate and air flow, and the spray duration with the LabVIEW software. Then air and liquid pass through the nozzle together and generate the spray flow. The liquid which consists of anisotropic nano object suspensions is sprayed and the nanoobjects are deposited on the substrate. Due to the shear force generated by the air flow and liquid flow, the nano objects can be oriented with the direction of the spray flow.

Liquid flow can be controlled by the pump 1 (Figure 2.10 b) automatically, and air flow need to be adjusted manually by the knob (Figure 2.10 c). With the proper parameters

of air flow and liquid rate, continuous spray flow can be generated. The sprayed shape on the substrate can be controlled by the distance between the nozzle and edge of substrate (d, in Figure 2.10 a), and the angle between nozzle and substrate plane (θ, in Figure 2.10 a). All the tubes in this system are fluoroethylene propylene tube, which are purchased from Interchim Company. The model of the pomp to control liquid is M50 syringe-free liquid handling pump from Valco Instruments Company. The nozzle type is AZ9344CX, with needle (Figure 2.10 d) 1.02 mm from AZTEK company.

These experiments are done in collaboration with Matthias Pauly from ICS in Strasbourg.

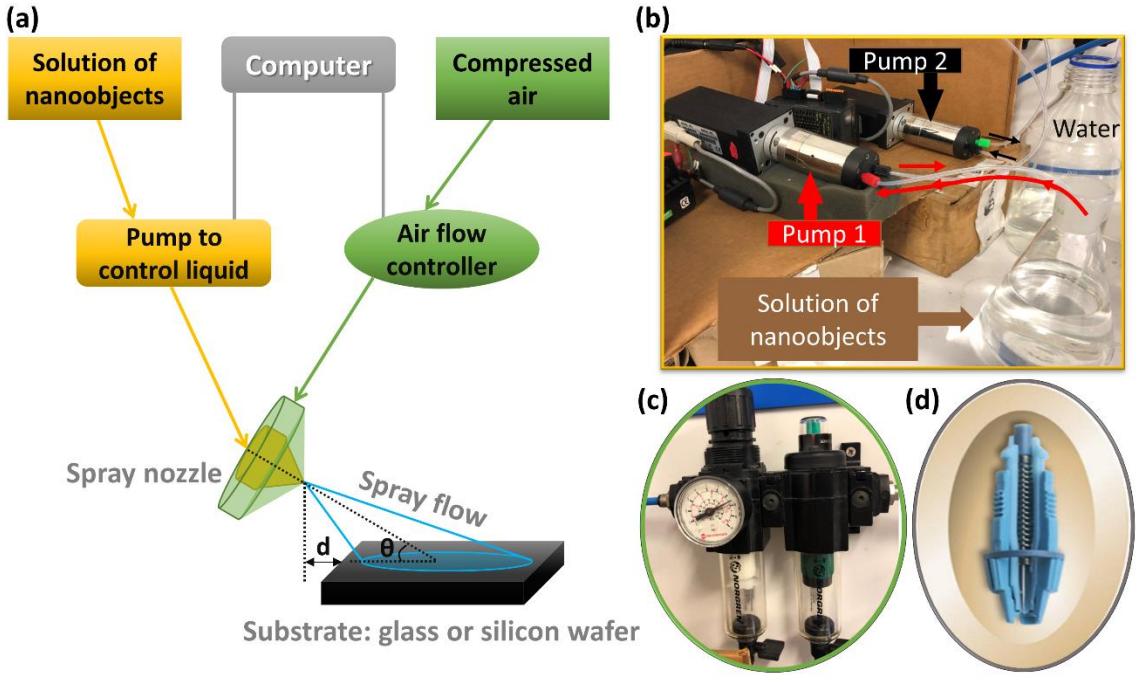

Figure 2.10 (a) Schematic illustration of GIS system. Photographs of pump to control liquid rate (b), air flowmeter (c), and internal structure of spray nozzle (d).

4.1.2 Suspension preparation and substrate treatment

The nano objects solutions have to be stable and homogenous to ensure a continuous spray flow. In the thesis, short silica nanohelices (length around 500 nm) were well dispersed in ultrapure water. Also, suspensions of GoldHelix were prepared in ultrapure water and ethanol solvants. More information can be found in Chapter 5.

Glass or silicon wafer are commonly used as substrates in the lab. The treatments of substrate are identical for both glass and silicon wafer: at first, the 2.5 × 2.5 cm slide was immersed in ethanol for 5 mins and in a diluted Hellmanex III solution for another 5 mins, the beakers containing the solutions are placed in ultrasonication bath. Then the slide was rinsed with ultrapure water and followed with compressed air drying. Primarily cleaned slide was place in the chamber of oxygen plasma generator. After 3 mins oxygen plasma atmosphere treatment, the surface of the slide became hydrophilic and contained more active SiOH groups. Finally, a polyethylenimine (PEI, M_w, ~60 000 g/mol) solution was spray for 6 s on the glass surface and followed by 10 s ultrapure water rinsing and dried. After all these treatments, the glass surface is a slightly positively charged due to the PEI coverage. The charge of the slide surface can be modified negatively by spraying the poly sodium 4-styrenesulfonat (PSS, M_w, ~70 000g/mol), and the thickness of polymer can be controlled by spraying several cycles of cation and anion polymers thanks to the lay-by-lay technique. [26]

4.2 Dip-coating

4.2.1 Dip-coating set up

Dip-coating is an industrial coating process which has been applied to prepare films[27] and hybrid materials.[28] It is also commonly used in academic research and more recently it is used to deposit nanoobjects on a surface.[29]

Dip-coating technique is to dip the substrate into one solution, and withdrawal the substrate with certain speed. The materials which were in solution can be deposited on the substrate when then solvent evaporated. The whole dip-coating process is schematically explained in Figure 2.11. At first, the silicon substrate and the nanoobject suspension are placed on their position, and the temperature of the chamber is adjusted. Once the temperature is ideal and stable, the sample holder is lifted till the suspension cover the major surface of the substrate. To avoid reflecting surface, the sample holder stays for 30 s. Then, the sample holder declines on a constant speed between 2.5 μm/s and 3 cm/s until the separation of suspension and the substrate.

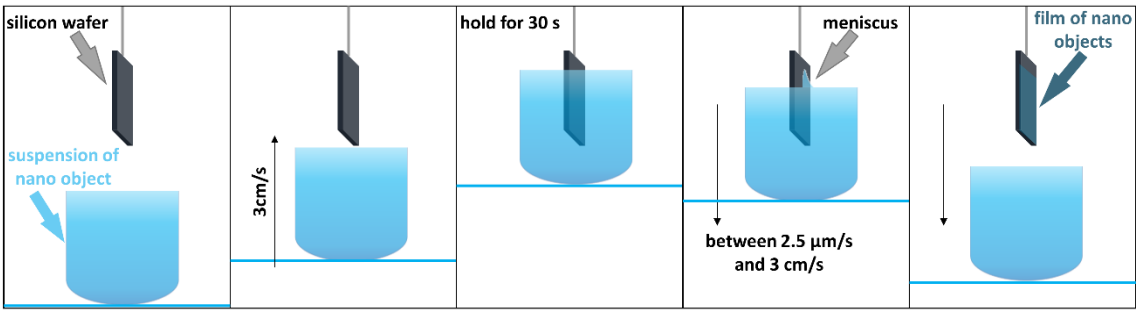

Figure 2.11 Fives steps for one dip-coating process. Instead of the immersing and withdrawal substrate, in this system, the mobile part is sample holder which supports suspension of nanoobject.

Dip coating experiments were performed on an ACEdip 2.0 dip-coater from SolGelWay. Note that, even if the substrate is silicon, there is always a thin silica layer on the surface of silicon. In this thesis, thickness of the silica layer is around 7 nm. The withdrawal speed can be controlled between 1µm/s and 30 000 µm/s. The chamber temperature (25 °C to 50 °C) were controlled using the software ACEdip 2.0 SOLGELWAY without cooling system.

4.2.2 Suspension preparation and substrate treatment

Suspension used for dip-coating should be stable and homogeneous solution to assure a uniform and reproducible coating on the substrate surface. Long silica helices were fragmented by tip-sonication inducing well-dispersed short silica helices suspensions in mixture of isopropanol and ethanol (1:1).

Substrates for dip-coating in this work are silicon wafer: boron doped prime CZ silicon wafers with (100) orientation, obtained from Sil'tronix. The wafers with rectangular form (1 × 5 cm) were rinsed with absolute ethanol and wiped dry with a Kimwipe paper and compressed air.

4.3 Microfluidics

4.3.1 Microfluidic devices

Microfluidics deals with the behavior of fluids that are geometrically constrained to a small, typically sub-millimeter scale, channel in which capillary penetration governs mass transport. It can be used to design chips with various shapes, useful for many

applications ranging from high-throughput screening applications to the design of new liquid display technology.[30, 31]

The microfluidic evaporator was prepared with the collaboration of Jacques Leng, using the devices and instruments supported by Solvay/Lab of Future. For commercial confidential reasons, only the design and principle of the preparation of evaporator chip will be mentioned. As Figure 2.12 (a) shown, the evaporator chip includes inlets and channels without outlets. Since the channels are made of polydimethylsiloxane (PDMS), which is porous and allows the gas passing through, when syringe containing nanoobjects suspension is pushed strongly, the gas insides the channels is driven out, and nanoobjects can be injected into channels. The evaporator chip channel patterns are obtained according to the mask design in Figure 2.12 (b), and the photo of the evaporator is shown in Figure 2.12 (c), which includes eight individual evaporators.

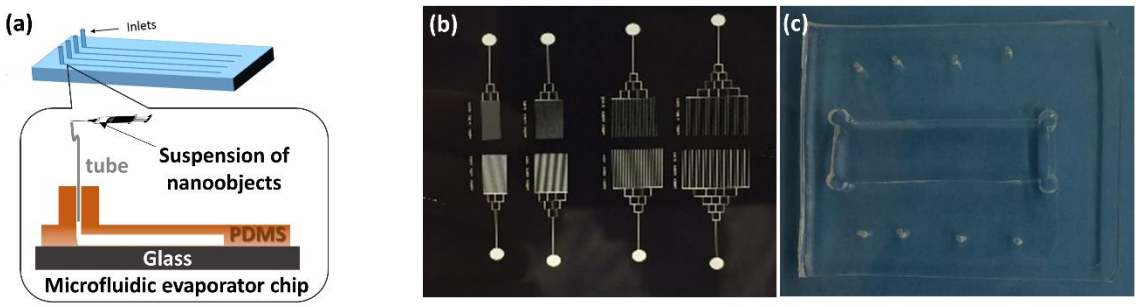

Figure 2.12 (a) Schema of microfluidic evaporator, photographs of the mask used in this work(b) and evaporator chip (c).

4.3.2 Preparation of microfluidic chip

The preparation of microfluidic evaporator procedures is shown in Figure 2.13. The main principle is to use photoresist transcript the mask patterns (Figure 2.12 b), then the PDMS is combined with photoresist. At high temperature, PDMS forms crosslinking, and the PDMS block can be separated from the photoresist while the PDMS block contains the pattern of photoresist. Then it can be attached to a new flat substrate, which is evaporator with the design of mask.

The process of microfluidic chip preparation is briefly described: at first, a lay of negative photoresist was coated on the silicon wafer surface and the thickness of photoresist defined the height of the channel. Various duration of UV treatment was

exposed to the photoresist through the mask (the mask is shown in Figure 2.12 b, it contains eight independent micro evaporator channels, the difference between upper 4 evaporators and the bottom ones is the width of channel). Followed with removing the unexposed photoresist, therefore, the pattern of mask is kept by the exposed UV photoresist. Then, PDMS is poured on the silicon wafer with mask pattern, and thickness of PDMS should be more than the height of the photoresist. After this combination is kept in 90 ^{o}C for several hour, the PDMS and the silica wafer with photoresist can be separated by peeling off the PDMS membrane. Silica wafer with photoresist can be recycled and kept for another PDMS membrane (Figure 2.13, grey arrow).

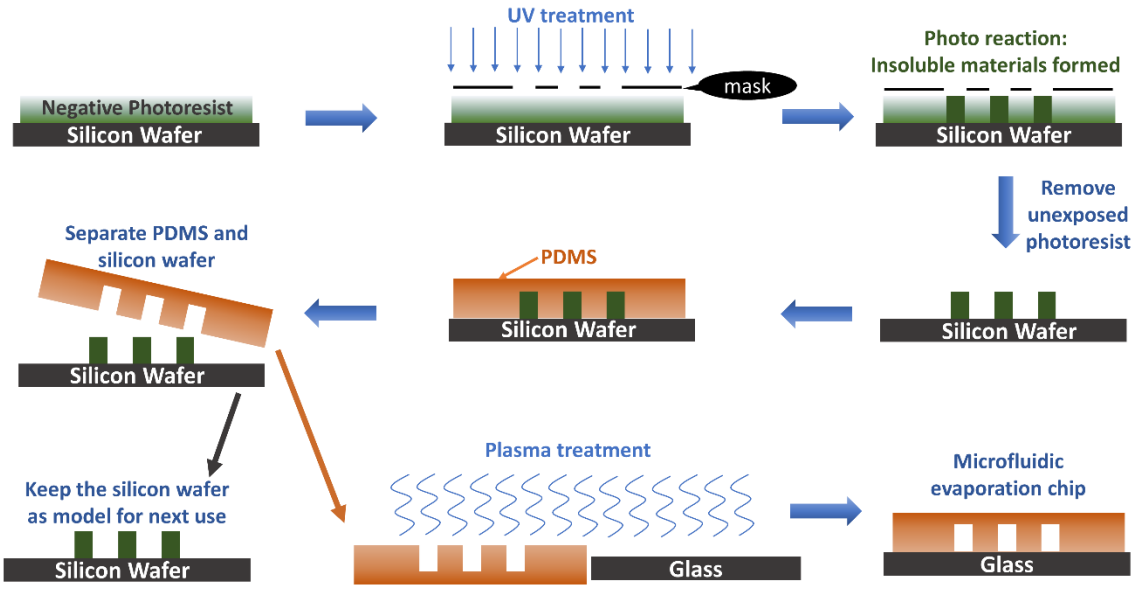

Figure 2.13 Schematically procedures for preparation of microfluidic evaporation chip.

When the PDMS was peeled off from the silica wafer (Figure 2.13, yellow arrow), it will be treated under oxygen plasma and same treatment is applied on the glass surface. After 10 mins oxygen plasma treatment, the chemical groups on surfaces of glass and PDMS are activated. They can be attached together manually, and their combination is reinforced by keeping them in the oven with 90 ^{o}C for overnight. The final microfluidic evaporator is completed.

References

1. R. Schreiber, N. Luong, Z. Fan, A. Kuzyk, P. C. Nickels, T. Zhang, D. M. Smith, B. Yurke, W. Kuang, A. O. Govorov and T. Liedl, Chiral plasmonic DNA nanostructures with switchable circular dichroism, Nat. Commun., 2013, 4, 2948.

2. R. Noyori and M. Kitamura, Enantioselective addition of organometallic reagents to carbonyl compounds: chirality transfer, multiplication and amplification, Angew. Chem. Int. Ed. Engl., 1991, 30, 49-69.

3. V. Mujica, Chirality transfer takes a jump, Nat. Chem., 2015, 7, 543-544.

4. R. Oda, I. Huc, M. Schmutz, S. J. Candau and F. C. Mackintosh, Tuning bilayer twist using chiral counterions, Nature, 1999, 399, 566-569.

5. T. Delclos, C. Aime, E. Pouget, A. Brizard, I. Huc, M. Delville and R. Oda, Individualized silica nanohelices and nanotubes: tuning inorganic nanostructures using lipidic self-assemblies, Nano Lett., 2008, 8 (7), 1929-1935.

6. J. Cheng, G. Le Saux, J. Gao, T. Buffeteau, Y. Battie, P. Barois, V. Ponsinet, M. Delville, O. Ersen, E. Pouget and R. Oda, Goldhelix: Gold nanoparticles forming 3D helical superstructures with controlled morphology and strong chiroptical property, ACS Nano, 2017, 11, 3806-3818.

7. F. Kim, S. Kwan, J. Akana and P. Yang, Langmuir-Blodgett nanorod assembly, J. Am. Chem. Soc., 2001, 123, 4360-4361.

8. J. K. Gansel, M. Thiel, M. S. Rill, M. Decker, K. Bade, V. Saile, G. von Freymann, S. Linden and M. Wegener, Gold helix photonic metamaterials as broadband circular polarize, Science, 2009, 325, 1513-1515.

9. D. B. Williams and C. B. Carter, Transmission electron microscopy, Springer Science, 1996.

10.https://warwick.ac.uk/fac/sci/physics/current/postgraduate/regs/mpagswarwick/ex5/techniques/structural/tem/

11. https://www.microscopemaster.com/cryo-electron-microscopy.html

12. https://blog.phenom-world.com/what-is-sem

13. B. J. Reardon and C. R. Hubbard, A review of XRD data of phases present in the CaO-SrO-PbO system, Power Diffr., 1992, 7 (2), 96-98.

14. M. Kahle, M. Kleber and R. Jahn, Review of XRD-based quantitative analyses of clay minerals in soils: the suitability of mineral intensity factors, Geoderma, 2002, 109, 191-201.

15. A. B. Garg and R. Rao, Copper delafossites under high pressure-a brief review of XRD and raman spectroscopic studies, Crystals, 2018, 8, 255.

16. B. E. Warren, X-ray diffraction, Pan American International Corporation, 1990.

17. Wikipedia, https://en.wikipedia.org/wiki/X-ray_scattering_techniques

18. W. H. Bragg and W. L. Bragg, The reflection of X-rays by crystals, Proc. Royal Soc. Lond. A, 1913, 88 (605), 428-438.

19. J. Workman and A.W. Springsteen, Applied spectroscopy: a compact reference for practitioners, United Kingdom Edition by Academic Press, 1998, section I, pp: 29-36.

20. M. N. Berberan-Santos, Beer's law revisited, J. Chem. Educ., 1990, 67, 757-759.

21. N. Berova, K. Nakanishi and R. W. Woddy, Circular dichroism principles and applications, second edition, Wiley-VCH, 2000.

22. T. Buffeteau, F. Lagugne-Labarthet and C. Sourisseau, Vibrational circular dichroism in general anisotropic thin solid films: measurement and theoretical approach, C. Appl. Spectrosc., 2005, 59, 732-745.

23.http://www.horiba.com/fileadmin/uploads/Scientific/Downloads/OpticalSchool_CN/TN/ellipsometer/Overview_of_Phase_Modulation_Technology.pdf

24. Wikipedia, https://en.wikipedia.org/wiki/Mueller_calculus

25. R. Blell, X. Lin, T. Lindstrom, M. Ankerfors, M. Pauly, O. Felix and G. Decher, Generating in-plane orientational order in multilayer films prepared by spray-assisted layer-by-layer assembly, ASC Nano, 2017, 11, 84-94.

26. G. Decher, Fuzzy nanoassemblies: toward layered polymeric multicomposites, Science, 1997, 277, 1232-1237.

27. Y. Lu, R. Ganguli, C. A. Drewien, M. T. Anderson, C. J. Brinker, W. Gong, Y. Guo, H. Soyez, B. Dunn, M. H. Huang and J. I. Zink, Continuous formation of supported cubic and hexagonal mesoporous films by sol-gel dip-coating, Nature, 1997, 389, 364-368.

28. M. Jokinen, M. Patsi, H. Rahiala, T. Peltola, M. Ritala and J. B. Rosenholm, Influence of sol and surface properties on in vitro bioactivity of sol-gel-derived TiO_2-SiO_2 films deposited by dip coating method, J. Biomed. Mater. Res., 1998, 42, 295-302.

29. A. Gans, E. Dressair, B. Colnet, G. Saingier, M. Z. Bazant and A. Sauret, Dip-coating of suspension, Soft Matter, 2019, 15, 252-261.

30. T. Thorsen, S. J. Maerkl and S. R. Quake, Microfluidic large-scale integration, Science, 298, 580-584.

31. A. Merlin, J.-B. Salmon and J. Leng, Microfluidic-assited growth of colloidal crystals, Soft Matter, 2012, 8, 3526-3537.

Chapter 3. Kinetic evolution of nanohelices formation based on 16-2-16 gemini surfactant self-assemblies

Contents

1. Introduction

Chiral molecules could propagate the chirality information at intra- and inter-molecular levels, and nanoscale supramolecular level. On the other hand, the surfactants can self-assemble to various structures in solvents due to their amphiphilic properties and their morphologies depend on the concentration, temperature and the nature of the solvent have been widely studied. In 1993, R. Zana et al.[1] reported that bis (quaternary ammonium) gemini surfactants showed very low critical micellar concentration compared to the corresponding monomeric surfactants. In 1997, Oda et al.[2] reported a series of surfactants C_2H_4-α,ω-($Me_2N^+C_mH_{2m+1}$)($Me_2N^+C_nH_{2n+1}$)Br^{2-} *n-2-m* (n, m indicated the numbers of carbon in the alkyl chain, as shown in Figure 3.1 a) with bromide. With the study of different self-assemblies of the surfactants with various *n* and *m*, effects of chain length (*n* = *m*, 6-18) and the dissymmetry (n ≠ m) was investigated in aqueous solutions. We learned that both decreasing the chain length and decreasing the symmetry resulted in larger spontaneous curvatures. The tubular/lamellar phases are more stable for longer chain lengths (Figure 3.1 b).

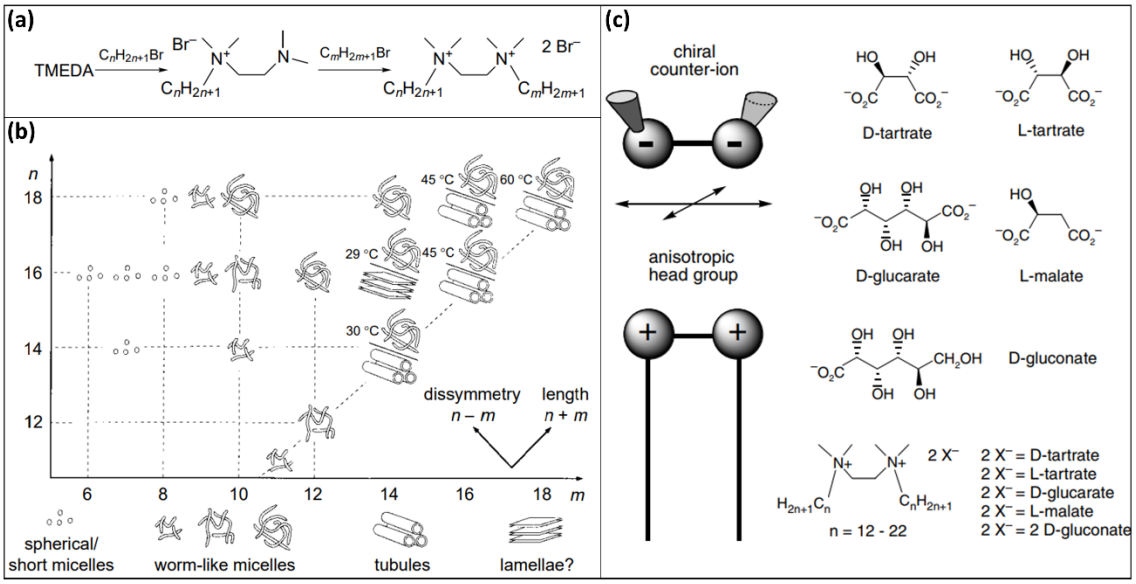

Figure 3.1 (a) Synthesis proceeds of the various bromide gemini surfactant, where TEMD is the abbreviation of N,N,N',N'-tetramethylethylenediamine , (b) Phase observed in aqueous solutions of *n-2-m* surfactants as a function of n and m. Worm-like micelles were divided into three categories according to their overlap concentrations: (*i*) lower than 0.5% w/w for the longer micelles; (*ii*) between 0.5 and 2%; (*iii*) between 2 and 10%.[2] (c) Cationic gemini amphiphiles having chiral counterions instead of bromide.[3]

In 1999, they studied the original self-assembled structures formed by cationic gemini amphiphiles with chiral counterions [3] (shown in Figure 3.1 c). With chiral counterions tartrate twisted nano ribbons were observed by TEM, the pitch and width of which depended on the length of hydrocarbon chains. Interestingly, with other anions, such as Malate (dianion as tartrate, but only one hydroxyl group), gluconate or glucarate (dianion or monoanion with several hydroxyl groups), the same gemini cationic surfactant did not form twisted ribbons, indicating that a very delicate balance of the molecular structure is required for the expression of chiral molecular assemblies based on cooperative intermolecular interaction. Among various hydrocarbon chain lengths which were studied, 16-2-16 tartrate Gemini was particularly investigated, and pure 16-2-16 L-tartrate consistently formed twisted ribbons with right handedness, while the pure 16-2-16 D-tartrate formed left-handed twisted ribbons. When the two enantiomers were mixed with various ratios, twisted ribbons with a continuous variation of twist period and width were obtained, instead of a mixture of twisted ribbons with opposite handedness. An increase of the enantiomeric excess (ee) caused a decrease of twist pitch from infinite (flat ribbons for ee=0, i.e. same amount of L and D counter-ion) to 200 nm for ee = 1 (Figure 3.2).

e.e.	*T* (μm)	*W* (μm)	*T*/*W*
0	∞	0.40 ± 0.28	
0.2	5.0 ± 1.5	0.12 ± 0.046	43 ± 5.2
0.33	2.6 ± 0.9	0.11 ± 0.047	26 ± 7.0
0.5	1.0 ± 0.5	0.06 ± 0.016	17 ± 4.7
1	0.2 ± 0.024	0.04 ± 0.006	4.8 ± 0.51

Figure 3.2 showed the values of e.e. and the mean values and standard deviation of ribbon period (T), width (W) and period/width. e.e. is defined as the relative concentration difference ($\varphi_L - \varphi_D$)/ ($\varphi_L + \varphi_D$), from 0(racemic) to 1(pure L-tartrate).[3]

Chiral amphiphilic molecules often assemble in solution to from aggregates with high aspect ratios such as rods, tapes, or tubes, suggesting that the chirality is intimately associated with the growth and stability of self-assembled fibers of small organic molecules.[4, 5] 16-2-16 L-tartrate Gemini formed twist or helical ribbons and tubules as reported by our group in 2007.[6] The formations of these supramolecular structures were studied with various concentration. For concentrations: 5 mM, 10mM and 20 mM solution

of 16-2-16 L-tartrate gemini hydrogel formation was observed after about 3h, 1h and 10 min, respectively, which indicated that higher concentration lead to quick kinetic processes. As Figure 3.3 shows, the morphologies of the aggregates formed by 16-2-16 L-tartrate Gemini evolved with the aging time: with 3 h and 36 h, helical ribbons and tubes were observed respectively.

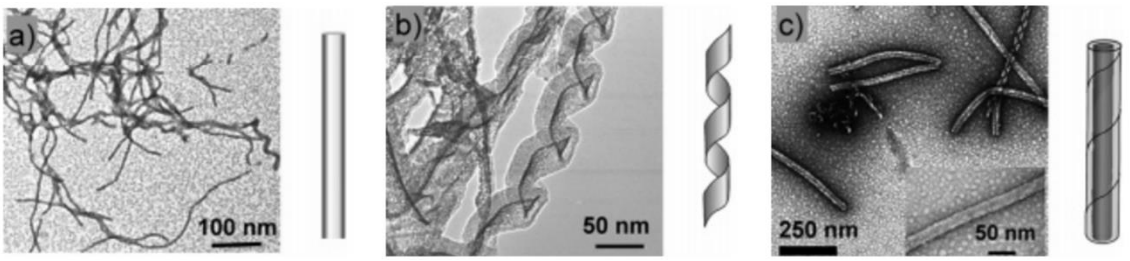

Figure 3.3 TEM micrographs and schematic representation of the evolution of the morphologies of fibrous structures of 16-2-16 L-tartrate Gemini (10mM in H_2O) with time (a) ill-defined fibers after 2h, (b) helical ribbons after 3h, and (c) tubes after 36h.[5]

Not only the nanoscale supramolecular level morphologies of 16-2-16 tartrate Gemini were studied, but also the detailed molecular organization was studied. According to IR spectra of 16-2-16 L-tartrate Gemini in water [6], CH_2 antisymmetric and symmetric stretching vibration shifted from 2924 to 2919 cm^{-1} and from 2853 to 2849 cm^{-1} when micelles transform to helical ribbons which indicated that the alkyl chain had orthorhombic crystalline ordering.[7] Through combining crystallographic analysis of 16-2-16 LD-tartrate Gemini by X-ray scattering and molecular modeling, the three-dimensional organization of the molecules were elucidated.[8] Molecular packing of racemic 16-2-16 tartrate gemini (Figure 3.4 a) gave the best fit between experimental and simulated powder diffraction patterns. The precise locations of tartrate, gemini and water molecules are all clearly indicated. The gemini dications are achiral intrinsically but they are pro-chiral and adopt two mirror-imaged conformations with the presence of L and D tartrate counterions. According to the planer chiral shape of the ethylene spacer observed from top view, these conformations will be noted Z and backward-Z (Figure 3.4 b). The white square in Figure 3.4 (a) is one minimal period unit, and it contains four 16-2-16 gemini tartrate molecules, which belongs to four leaflets separately. And water molecules which are involved in the self-assembly appear inside one bilayer (transparent blue in Figure 3.4 a) and between two

bilayers (opaque blue in Figure 3.4 a). The periodical unit is also elucidated schematically by black dash rectangular in Figure 3.4 (c).

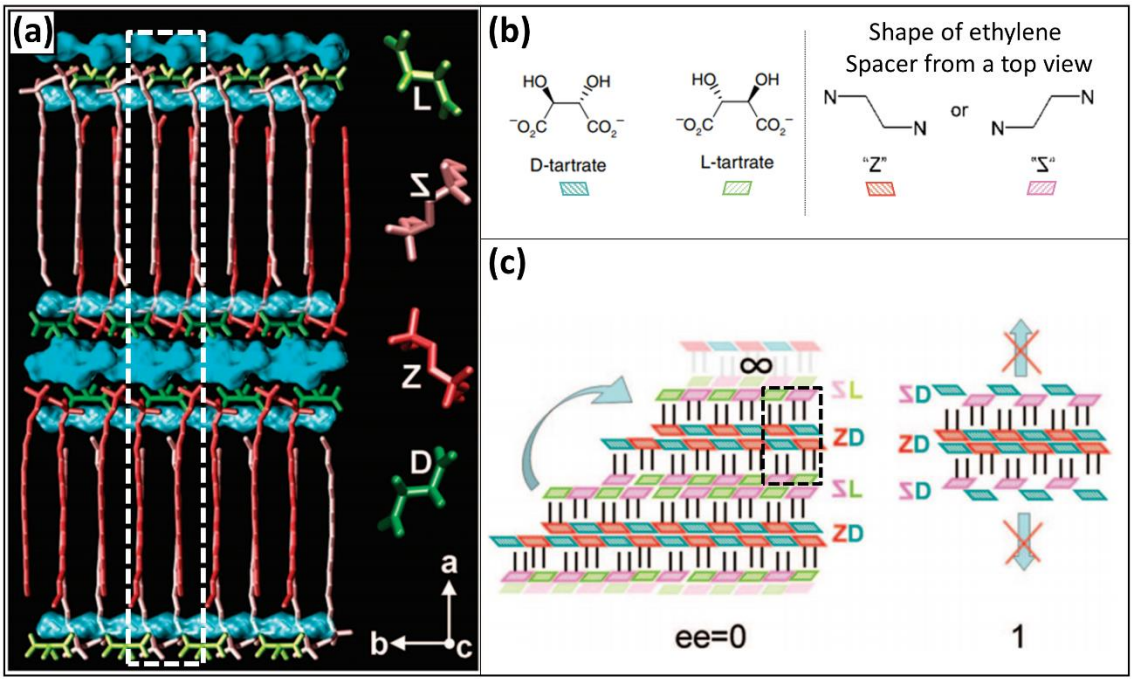

Figure 3.4 (a)Molecular packing of 16-2-16 gemini tartrate, view from the sides, along the *c* axis, and color code used to represent D- and L-tartrate as well as two enantiomeric conformers of gemini head group. (b) structure and symbols of tartrate and gemini. (c) Schema of ee = 0 and 1 16-2-16 gemini tartrate structure. In the racemate (ee = 0), the contact layer between two consecutive gemini bilayers is always homochiral. This packing is possible with a pure enantiomer only for the internal adjacent leaflets.[8]

Both electrostatic interaction between chiral counterions and gemini surfactant and the hydrophobic effect between gemini surfactant are crucial for determining the crystalline molecular organization in this structure with long range cooperative chirality induction. When the multilayer supramolecular structure was formed with 16-2-16 gemini tartrate amphiphiles, the two conformation of gemini, Z conformation (denoted by red parallelogram) and backward-Z conformations (denoted by purple parallelogram) form selective ion-pair with either L or D tartrate. The conformation of the gemini surfactant as well as the tartrate on one side of bilayer is homo-chiral, and the other side of the same bilayer (also homo-chiral) is the mirror image of the first layer (two monolayers are hetero-chiral). The two adjacent bilayers are mirror image of each other. As such the periodic unit, (unit cell) is made of two bilayers. While ee = 0, these double bilayers can stack infinitely, and formed thick and flat ribbons, as shown in Figure 3.4 (c). In contrast, following this rule,

only two bilayers can stack for pure enantiomer, separated by a domain with a D-Z-D-Z (for instance) array of headgroups and tartrate ions. In the external leaflets of these double-bilayer ribbons, the heterochiral bilayer packing requires that the gemini conformation is opposite that in the inner leaf, backward-Z, and obviously, the only available tartrate (D) cannot be accommodated within the chiral cavity where D-tartrates are expected. The minority of enantiomer limits the bilayer number, and according to the packing rule, the number of bilayers of the assembly can be expected to follow the relationship: *n* (bilayers) = 2/ee.[9] For ee = 0 the bilayers number is infinite, for ee = 0.5 four bilayers will be formed, and only one double bilayers are formed with ee = 1. In all the cases, left or right handedness of the twisted ribbons can be determined depending of the D or L nature of the majority of the counter-ion. This packing principle agreed the previous result in which with ee = 0.5 larger twisted ribbons than ee = 1 were formed[3]. The thickness of the twisted ribbons consists of the multiplayers of self-assembly with 16-2-16 gemini tartrate, which is larger in ee = 0.5 (4 bilayers) than ee = 1 (2 bilayers).

The morphologies of 16-2-16 gemini tartrate can be controlled by temperature, enantiomeric excess and aging time [6, 8], and the molecular organization of the self-assembly has been clearly investigated. Furthermore, the handedness of nanometrical helices could be inverted with an excess solution of opposite enantiomers.[10] Briefly, pure L-tartrate gemini was dissolved in ultrapure water with 10 mM concentration. Then various equivalents (1, 2, 4 and 20 eq.) of D-tartrate were added in the L-tartrate gemini gel and followed with ultrapure water rinsing. It was clearly observed that this helix inversion is the cooperative result of various transitions, from the molecular to mesoscopic scale, with different kinetics: the chirality inversion of tartrate anions occurred very quickly, and CD signals of tartrate ions were inverted (except, 1 eq., ee=0). The counterion exchange is immediate when the aggregates are in contact with the opposite enantiomers. However, the morphological helicity inversion process is slow, of the order of days. For the first time the multi-step mechanisms in the chirality inversion of molecular aggregates were reported.[10]

In summary, the effect of an important number parameters on the morphologies of 16-2-16 gemini tartrate has been investigated since 20 years: the morphology of the self-assemblies of pure enantiomers 16-2-16 gemini tartrate can be tuned from twisted ribbons,[8]

helical ribbons to tubules[6] with the various aging time (Figure 3.5 ee = 1, vertically illustrated) or a very little quantity of additives (~1-5%), and size of twisted ribbons can be tuned with various enantiomeric excess of 16-2-16 gemini tartrate (Figure 3.5, ee from 0 to 1, horizontally illustrated). However, further investigation is required to elucidate how such large twisted ribbons formed with ee = 0.2, 0.33 and 0.5, and how the small twisted ribbons with ee = 1 evolve to helical ribbons. During my thesis, I have studied the morphologies of chiral ribbons and their kinetic evolution in the whole range of the enantiomer excess.

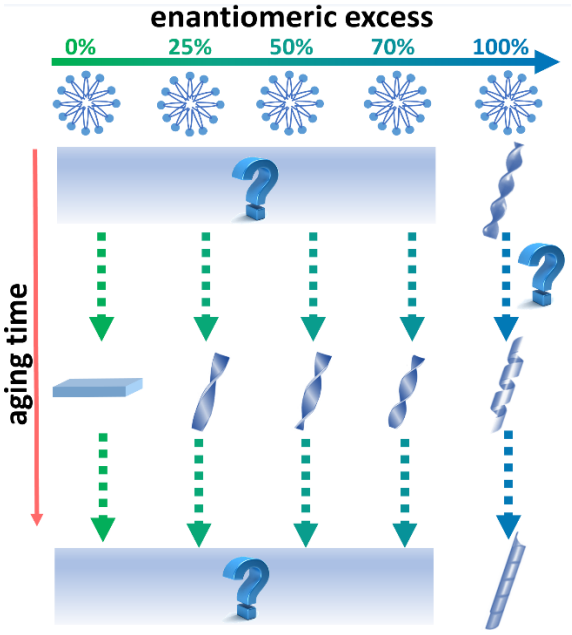

Figure 3.5 A evolution table of the 16-2-16 gemini tartrate in the whole range of enantiomeric excess. Three question marks indicate the unsolved mechanism.

In this thesis, nano twisted ribbons and nano helical ribbon are collectively called as nano helices.

2. Evolution of 16-2-16 gemini tartrate with 0.9 ≤ ee ≤ 1

2.1 Morphologic kinetic evolution

Morphologies formed by 16-2-16 gemini tartrate with ee =1 (L-gemini tartrate) values were followed by TEM images under 20°C. Figure 3.6 showed that the twisted ribbon formed by ee = 1 (16-2-16 L-gemini tartrate) evolved into helical ribbons, and tubules with barber's pole in agreement with the previous reports. But to understand why

the morphology developed from the twisted ribbons into helical ribbons, more details about these structures are needed, and the intermediate state containing both twisted ribbons and helical ribbons should be studied. The TEM images in Figure 3.6 was obtained with uranyl acetate staining (details in chapter 2). This staining technique shows the interest of being very quick, but the organic structure can be damaged by these dyes which are basically non-chiral ions. This is why cryo-TEM images were collected for twisted ribbons and helical ribbons to confirm the morphology observed.

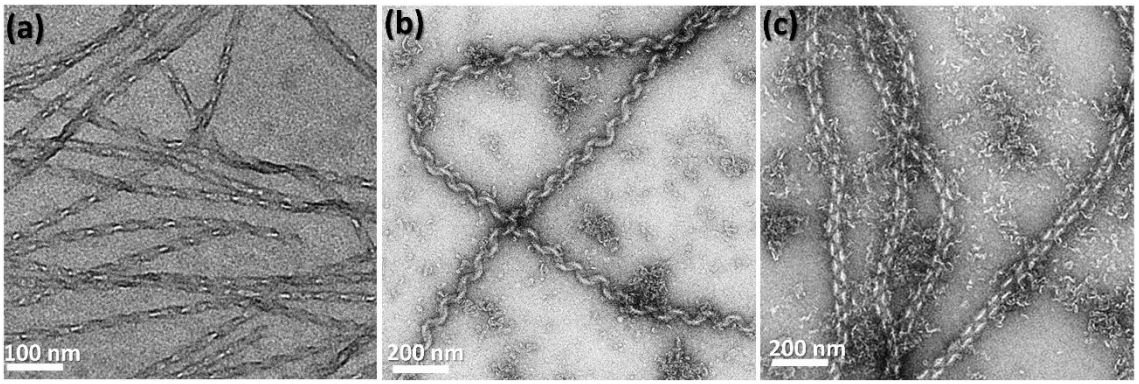

Figure 3.6 TEM images of 16-2-16 gemini tartrate (ee = 1, at 1 mM concentration) aged under 20°C with different time (a) 2h, (b) 2d, and (c) 4d.

Figure 3.7 (a) to (d) are representative Cyro-TEM images of twisted ribbons and helical ribbons formed by ee =0.9 and 1 16-2-16 gemini tartrate (1 mM). The pitch and width are statistically measured on the Cryo-TEM images. The Figure 3.7 (f) schematically indicated the method to count pitch and width of twisted and helical ribbons. According to the Table 3.1, for all the twisted ribbons, the pitch lengths remained at around 108 nm, but the width increased with time : 12 (2h) to 19 (5h) nm, and 13.5 (2h) to 21 (5h) nm for ee = 0.9 and 1 respectively. When the aging time is 5h, both 16-2-16 gemini tartrate with ee = 0.9 and ee =1 had the mixture of twisted ribbons and helical ribbons.

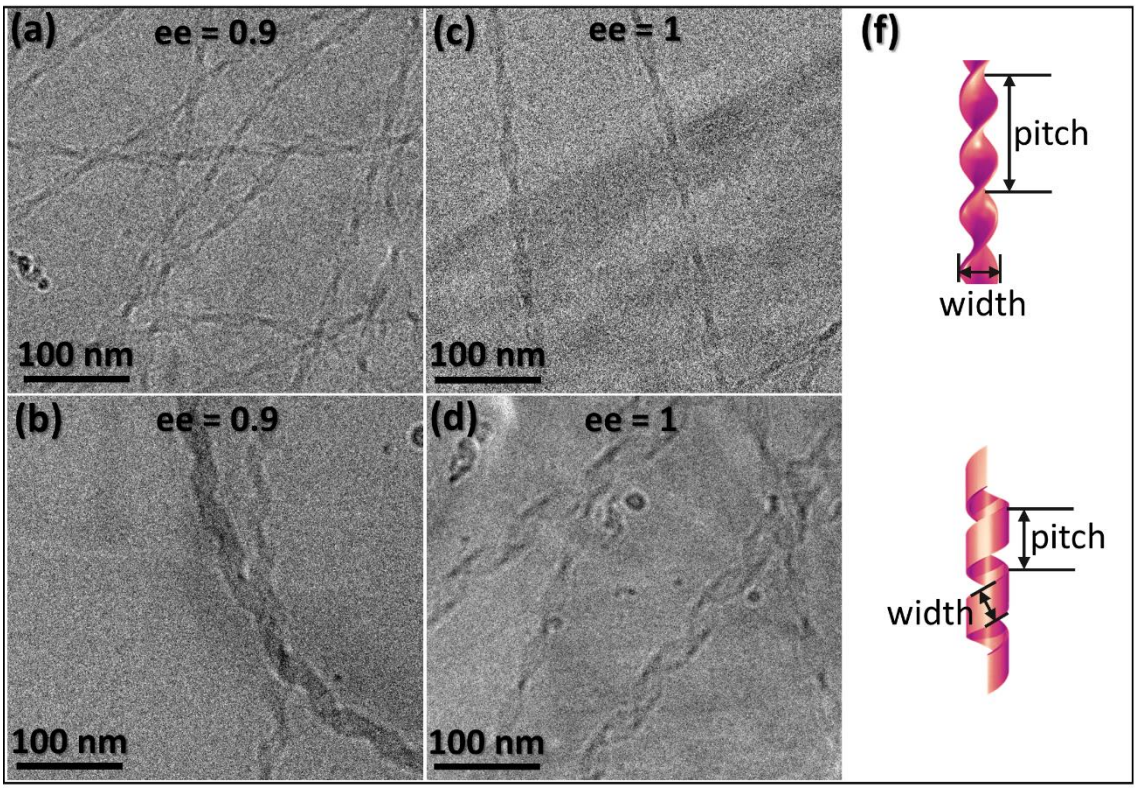

Figure 3.7 Cryo-TEM images of twisted ribbons and helical ribbons formed by 16-2-16 gemini tartrate with ee = 0.9 aging 2 h (a) and aging 5 h (b), ee = 1 aging 2h (c) and aging 5 h (d). (f) scheme of twisted ribbons and helical ribbons.

ee	Aging time	Morphology	Pitch/nm	Width/nm
0.9	2h	Twisted ribbons	108.23 ± 14.23	11.94 ± 1.52
	5h	Twisted ribbons	109.75 ± 7.01	19.23 ± 2.46
		Helical ribbons	77.53 ± 5.01	26.93 ± 2.62
1	2h	Twisted ribbons	108.32 ± 7.61	13.53 ± 2.48
	5h	Twisted ribbons	108.43 ± 5.31	20.40 ±3.42
		Helical ribbons	79.39 ± 7.63	27.92 ± 5.50

Table 3.1 Pitch length and width of twisted ribbons and helical ribbons formed with high ee values (ee >0.8) 16-2-16 gemini tartrate. The statistics were done with cryo-TEM images, 100 helices were counted for each sample.

Comparing the TEM images with uranyl acetate staining and Cryo-TEM images, we observed the morphology of twisted ribbons and helical ribbons clearly. TEM images with staining showed the morphology, but the border of the twisted ribbons is not clear

enough to do statistics. With cryo-TEM images, higher resolution helps to distinguish the width of the ribbons unambiguously, and with time only width of twisted ribbons increased. The width of helical ribbons is larger than twisted ones.

2.2 Mechanism of transition between twisted and helical ribbons

Introducing a twist into a flat ribbon implied that the area per molecule should be higher for a molecule close to the long edges of the ribbon than in the middle of the ribbon. This is why a simple way to increase the surface area while preserving molecular organization and crystalline chain-packing is to introduce a molecular tilt.[8] As Figure 3.8 (a) shows, the organization of the gemini molecules is the same everywhere but the gemini molecules on the edge of twisted ribbons tilted in the (x, y) plane, perpendicular to z (Figure 3.8 b). While the width of ribbons increased with time, the tilt of the molecules at the edge increases. Nevertheless, such tilt encounters a limit: when the width is large enough and the edge molecules reached to the upper limit beyond which bilayer integrity does not hold, the morphology will transit into helical ribbons (Figure 3.8 c) where the area per molecule at the center of the ribbons is the same as that at the edge of the ribbons. Thus, increasing the width of helical ribbons does not require energy, and they are wider than twisted ribbons for the range of ee 0.9-1 (Table 3.1). This twisted ribbon to helical ribbon evolution mechanism has been theoretically proposed by Oda's group,[8] but these measurements are the first that could experimentally confirm this increase of width. This observation agreed well and verified the mechanism proposed in 2008.

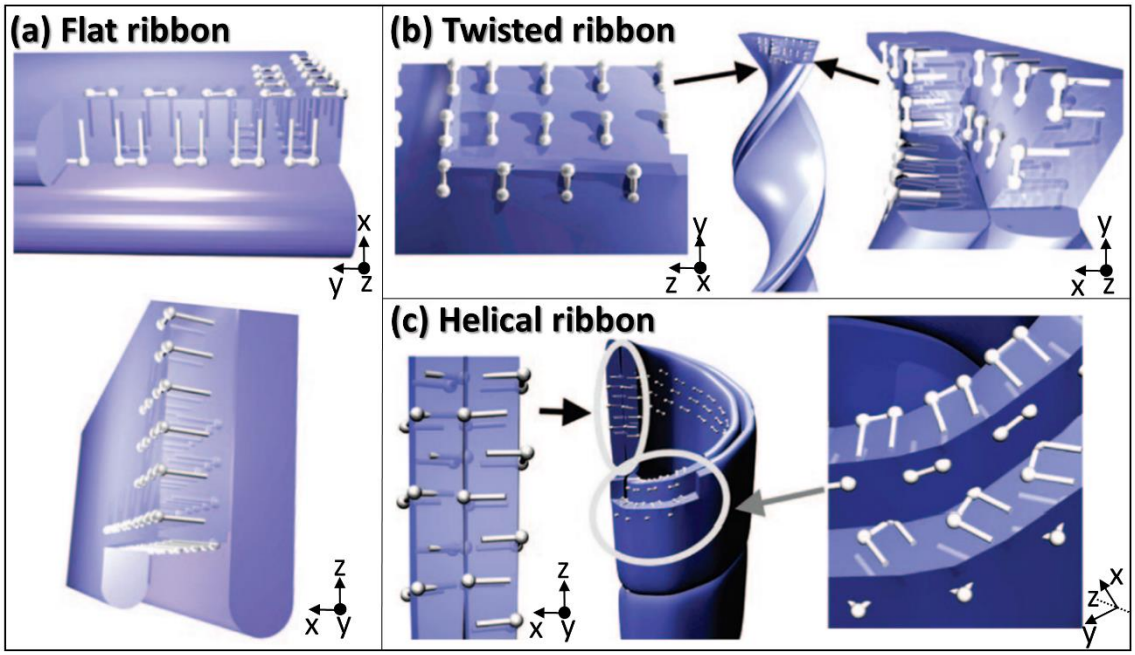

Figure 3.8 Schematic representation of the orientation of gemini molecules with respect to ribbons in (a), twisted(b) and (c) helical structures.[8] Three-dimensional coordination system on the right bottom of each scheme indicated the view direction of section.

2.3 Kinetic evolution at the molecular level

Since the evolution trend is the same for ee = 0.9 and ee = 1, only pure 16-2-16 L-gemini tartrate self-assembly was studied. In order to investigate the molecular level organization, electronic circular dichroism (ECD) spectra, vibrational circular dichroism (VCD) and X-ray scattering techniques were used to characterize the self-assembled structures of 16-2-16 L-gemini tartrate. Depending on the technique, the detection limitation in term of concentration varies. Therefore, in total three concentrations (1 mM, 10 mM and 50 mM) of 16-2-16 L-gemini tartrate were prepared in pure water. 50 mM 16-2-16 L-gemini tartrate solution with opaque white color brought too much scattering and saturated UV absorbance. Electronic CD spectra can only measure the 1 mM and 10 mM 16-2-16 L-gemini tartrate solution with 1 mm pathlength. However, VCD can only measure 10 mM and 50 mM 16-2-16 L-gemini tartrate, since 1 mM is too diluted to collect the signal. 50 mM 16-2-16 L-gemini tartrate was also used for X-ray scattering investigation.

2.3.1 Characterizations of supramolecular structure by electronic CD spectra

The solution of 16-2-16 L-gemini tartrate (dissolved in water at around 50°C) is cooled down to 20 °C, then the ECD was investigated as a function of aging time at 190-250 nm which corresponds to the absorption region of the carboxylate chromophores.[9,11]

ECD spectra have been recorded along the self-assembly process of 1mM and 10 mM 16-2-16 L-gemini tartrate after being cooling down to 20°C up to 10 hours aging. As Figure 3.9 shows, the evolution of the electronic CD spectra of 1 mM and 10 mM of 16-2-16 L-gemini tartrate indicated that the evolution trend (spectra pattern) is concentration independent, whereas the kinetics strongly depends on the concentration. At both concentrations, the evolution is the following: at the beginning of the aging, there were two negative bands, which resulted from n-π* transition of carboxylate group. After about one hour, the electronic CD spectra showed a strong cotton effect between the carboxylates with a positive peak and a negative one. This Cotton effect reveals the chiral arrangement of the tartrate molecules. For 1 mM 16-2-16 L-gemini tartrate, it took 70 min for the ECD spectra to reach the equilibrium. For the CD spectra of 10 mM 16-2-16 L-gemini tartrate, the equilibration time was shorter, around 40 mins. After this transition (40, 70 min for 1,10 mM), there is no more changes according to electronic CD observation, in which CD spectrum of 10 h aging is the same as the one of 2 h.

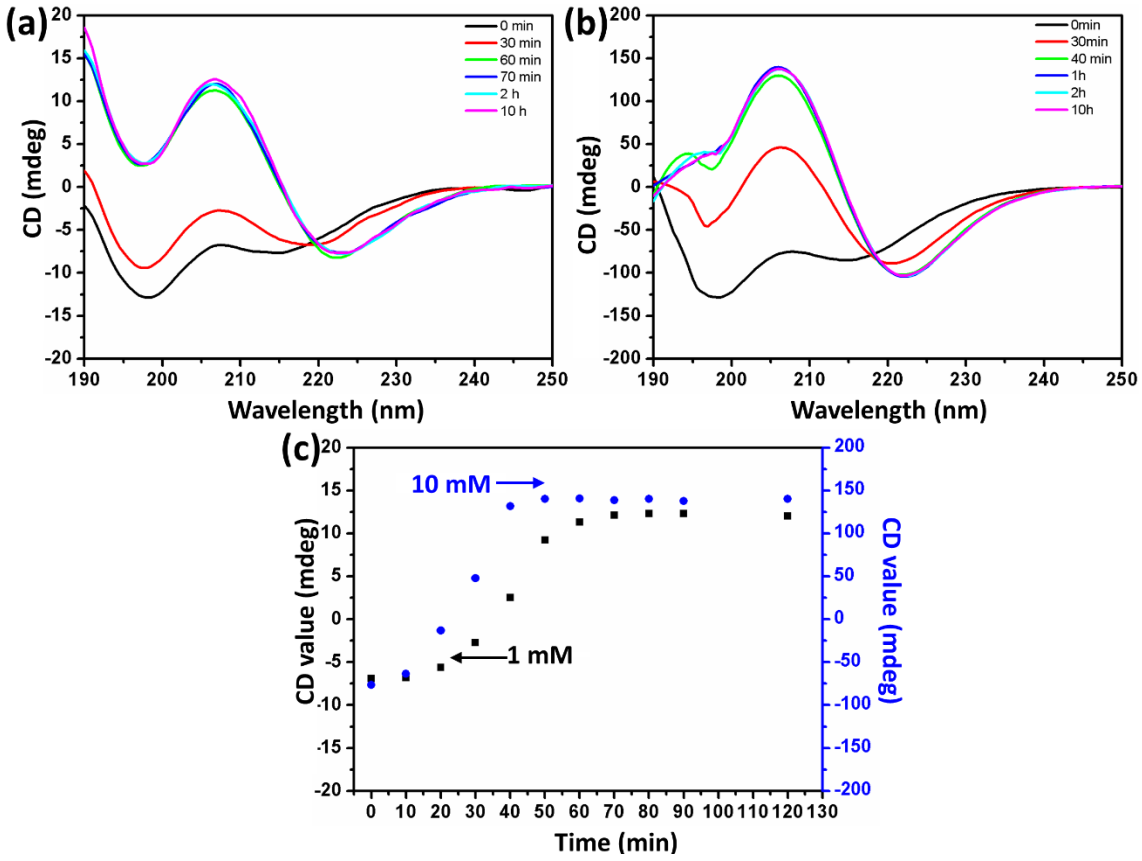

Figure 3.9 CD spectra of 16-2-16 L-gemini tartrate with 1 mM (a) and 10 mM (b) with various aging time at 20°C, (c) showed the CD values at 206 nm, which indicated the evolution of peaks directly.

2.3.2 Characterizations of supramolecular structure by VCD

In order to further investigate the molecular chirality, vibrational circular dichroism (VCD) was utilized to detect the vibration of CO_2^- in tartrate molecules. For the VCD measurement, the solution of 10 mM and 50 mM 16-2-16 gemini tartrate were characterized.

According to IR spectra, there is a strong antisymmetric stretching of the carboxylate groups ($\nu_a CO_2^-$) of tartrates at 1610 cm^{-1} (Figure 3.10 a), and VCD spectrum of 16-2-16 L-gemini tartrate exhibited a negative couplet (positive at higher wavenumber and negative at lower wavenumber). Here, we introduced the g factor, a dimensionless factor to evaluate the chirality of $\nu_a CO_2^-$, which is calculated as follows:

$$g = \frac{\Delta A}{A}$$

Figure 3.10 (b) illustrated the g factor of $\nu_a CO_2^-$ evolving with time. These two samples showed the same tendency regarding the g evolution. In the beginning, g values showed a fast increase, and then decreased until reaching a constant value around 0.0004 (same for the two concentrations). 20 h and 10 h were needed to reach the equilibrium value for 10 mM and 50 mM 16-2-16 L-gemini tartrate solution. The g-value variation was attributed to the transformation from micelle to twisted ribbon (in the first hour), then to helical ribbons (20 and 10h), with the evidence provided by TEM images (Figure 3.11).

From the VCD results, the g-factor evolution trend is concentration independent, but the speeds are different, which agrees well with the conclusion from electronic CD spectra. However, for VCD, the kinetic process lasts for at least 14 hours and 10 hours for 10 mM and 50 mM 16-2-16 L-gemini tartrate to reach the equilibrium, which was not observed with ECD (reached at equilibrium within 1 hour). Also, interestingly, the maximum which was observed with VCD at the very early hours was not observed with ECD which showed constant increase until reaching the equilibrium values. There is similar multi steps conversion of chirality reported with this system.[10] Electronic CD spectra detected molecular levels, which is much faster than the morphology. VCD could detect the vibration of carboxylate group, which reflected to both the molecular and supramolecular levels.

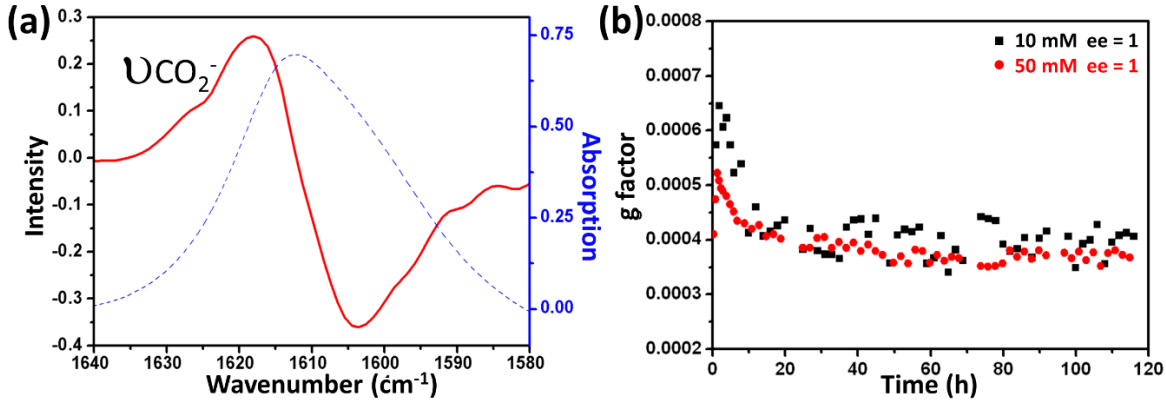

Figure 3.10 (a) Representative VCD and IR spectra of tartrate ions in 10 mM 16-2-16 L-gemini tartrate aging 2 hours. (b) g factor comparison of 10 mM and 50 mM 16-2-16 L-gemini tartrate.

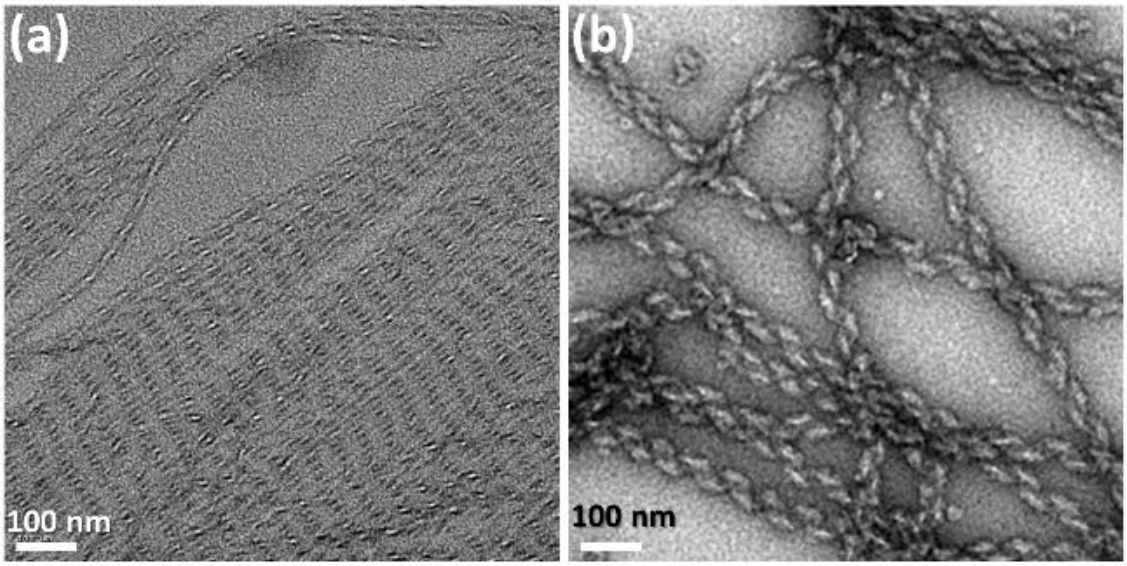

Figure 3.11 TEM images of 10 mM 16-2-16 L-gemini tartrate aging 2h (a) and 14h (b) with uranyl acetate negative staining.

2.3.3 Characterizations of supramolecular structure by X-ray scattering

Previously, X-ray scattering elucidated the molecular structures of the twisted ribbons and helical ribbons formed by pure 16-2-16 L-gemini tartrate in water (10% w/w which is about 17 mM), and it was shown that the experimental and the theoretical diffraction patterns were identical.[8] Briefly, according to modeling, the water molecules which are involved in the self-assembly of the 16-2-16 L-gemini tartrate were observed by X-ray scattering. The number of water molecules has particular large influence on the intensities of peaks at 2θ = 2.7°(2,0,0), 5.4°(4,0,0), 8.1°(6,0,0), 9.38°(2,0,1) and 10.82°(8,0,0).[8] θ could be transformed into Q values, with the equation:

$$Q = \frac{4\pi/\lambda}{sin\,\theta}$$

where θ is the scattering angle, and λ is 1.54 for Copper anode. The corresponding Q values are 0.2, 0.4, 0.58, 0.68 and 0.78, in Figure 3.12.

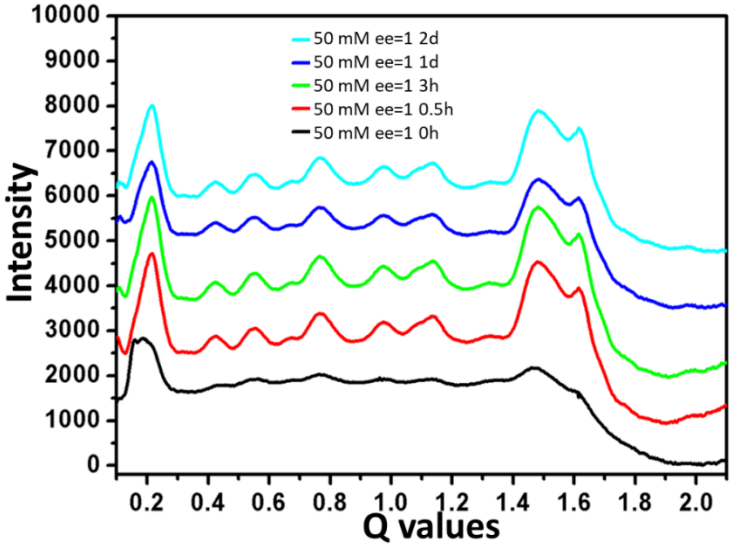

Figure 3.12 X-ray scattering patterns of 50 mM 16-2-16 L-gemini tartrate with various aging time.

Since the same evolution tendency was exhibited based on VCD spectra for the 10 mM and 50 mM samples, only 50 mM 16-2-16 L-gemini tartrate sample was prepared for X-ray scattering measurement. Following the time dependent evolution (Figure 3.12), we observed that the intensity of the peaks increased from 0 h to 30 min, when they reached the equilibrium values, without any further evolution afterwards, which means that the water molecules involved in the self-assembly are already crystalline within 30 min. After 30 min, there was no other changes from X-ray scattering patterns, which indicated no obvious difference between twisted and helical ribbons.

3. Evolution of 16-2-16 gemini tartrate with ee < 0.8

3.1 Morphologic kinetic evolution

Morphologies of the chiral ribbons formed by 16-2-16 gemini tartrate with various ee values were followed by TEM images under 20°C. As an illustration of all the ee studied in this part, Figure 3.13 showed that the twisted ribbons formed by ee = 0.25 16-2-16 tartrate (1 mM) formed twisted ribbons with a large range of the pitch, but grew globally into larger twisted ribbons with time. The pitch of the twisted ribbons (marked by two-way arrow in Figure 3.13) increased from around 1 μm to 4 μm between the aging time from 6 hours to 6 days. To study the morphology formed by ee = 0.25 16-2-16 gemini tartrate, the pitch length of twisted ribbons is plotted by the black squares in Figure 3.14 (a) for the

different aging time. We observed that pitch lengths reached the equilibrium value at around 5 days. The evolution of pitch length was also compared with gels with 10 mM and 50 mM 16-2-16 gemini tartrate (still ee = 0.25) (Figure 3.14 (a)). From these three samples of ee = 0.25 with various concentrations, we could conclude that the twisted ribbons grew into larger dimensions with time, but with the maximum pitch length around 4 μm for ee = 0.25 16-2-16 gemini tartrate. Higher the concentration of 16-2-16 gemini tartrate is, faster the twisted ribbons reach to the maximum (5d for 1mM, 3d for 10 mM and only 2d for 50 mM). The evolution includes two process: in first stage when the aging time is shorter than 10 h, the pitch length of twisted ribbons increased; and in second stage after 10 h aging, the increase of pitch length slowed down until it reaches the plateau (4 μm).

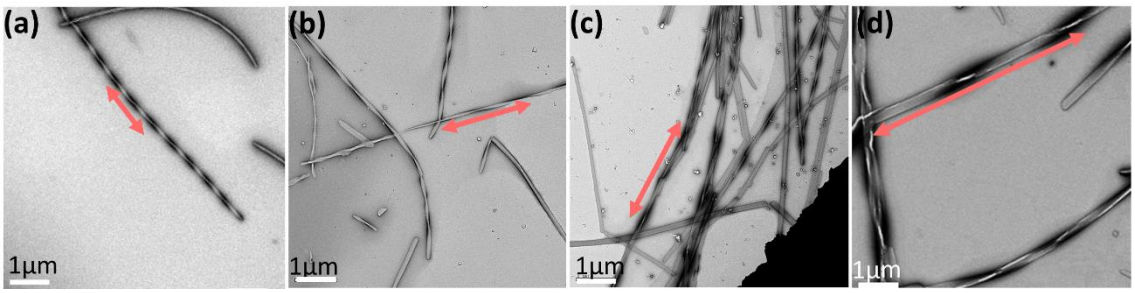

Figure 3.13 TEM images of 16-2-16 gemini tartrate (ee = 0.25, at 1 mM concentration) aged under 20°C with different time (a) 6h, (b) 1d, (c) 3d, and (d) 6d.

16-2-16 gemini tartrate with ee = 0.33 and 0.5 at 1 mM concentration also formed large twisted ribbons, and we also observed the increase of pitch length with time as Figure 3.14 (b) shows. The final pitch length decreased with larger ee value (4 μm, 3.2 μm and 2.5 μm for ee = 0.25, 0.33 and 0.5 16-2-16 gemini tartrate respectively). Widths of the twisted ribbons were also measured. Figure 3.14 (c) showed the relationship of the width and pitch length of twisted ribbons formed by various ee of 16-2-16 gemini tartrate. We found that no matter how long the aging time was and what ee value was, the pitch length is always proportionally related to the width of twisted ribbons.

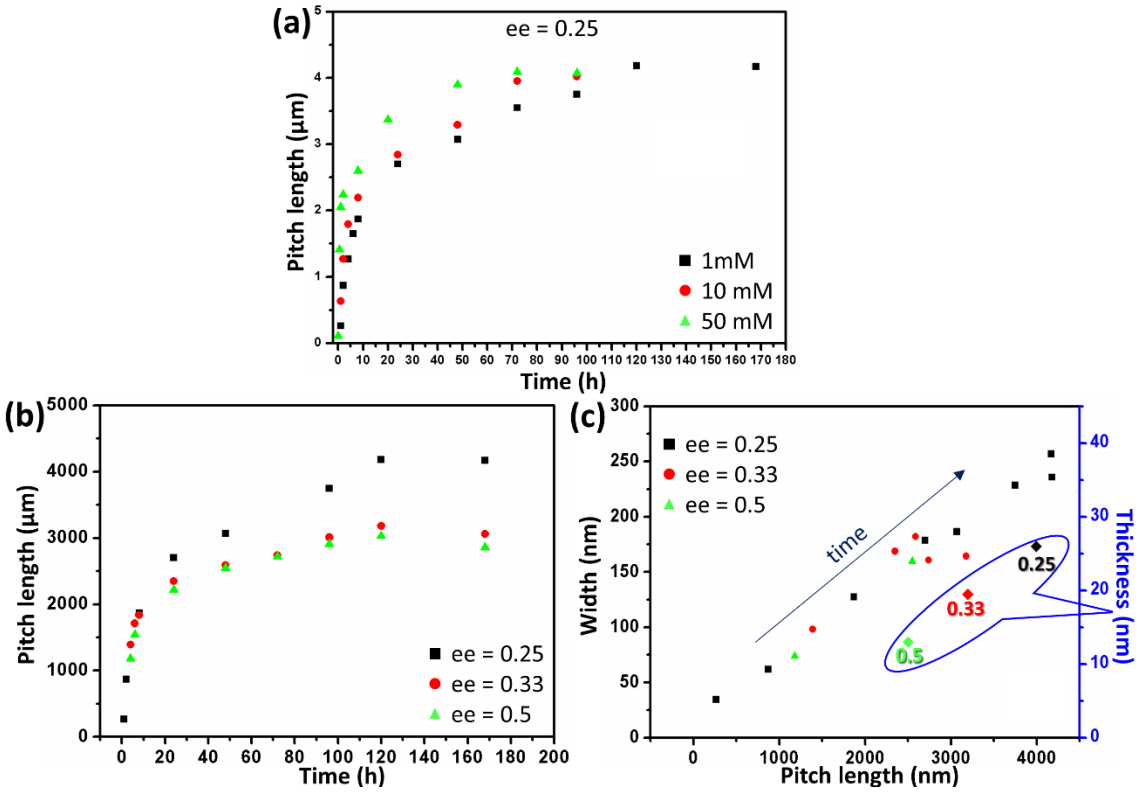

Figure 3.14 (a) Relation of pitch length and aging time of ee = 0.25 16-2-16 gemini tartrate with various concentration, (b) relation of pitch length and aging time of ee = 0.25, 0.33 and 0.5 with 1 mM concentration, (c) relation of width and pitch for ee = 0.25, 0.33 and 0.5 with various aging time.

According to the previous reports, the thickness of a self-assembled ribbon can be estimated as 3.25 × 2/ee nm.[7,8] When the pitch length reached to the maximum size, the estimated thickness was calculated for ee = 0.25, 0.33 and 0.5 (diamonds marked in Figure 3.14 c related to blue axis) to be 26 nm, 17 nm and 13 nm respectively. It is clearly shown that, the final pitch length, width and thickness have linear correlation. Before this work, we knew that by controlling ee values of 16-2-16 gemini tartrate, the twisted ribbons' morphology can be tuned. Now, we know how 16-2-16 gemini tartrate of various ee values can evolve to larger twisted ribbons with different dimensions, and at the same time, this morphology tuning can be realized by the aging time.

3.2 Evolution mechanism of 16-2-16 gemini tartrate with ee < 0.8

To understand how the small twisted ribbons grow into large twisted ribbons in the case of ee = 0.25, 0.33 and 0.5, 16-2-16 gemini tartrate, we propose two possible mechanisms which go through small twisted ribbons and generate large twisted ribbons in

the end, as shown in Figure 3.15. Let's take ee = 0.25 as an example, where 16-2-16 L-gemini tartrate (62.5%) and D-gemini tartrate (37.5%) are mixed in the solution (details shown in experimental section). As schematized in the figure 3.15, the first possibility is that the majority of mixture (16-2-16 L-gemini tartrate) formed double bilayers cluster-like structures primarily. With time, other free 16-2-16 gemini tartrate molecules packed on the double bilayer structures and eventually multi bilayers are formed (ideally 8 bilayers in the case of ee=0.25). During this process the pitch, width and thickness of the twist ribbons grow with time. The second mechanism is that cluster-like double bilayers of 16-2-16 L-gemini tartrate and D-gemini tartrate are formed separately and simultaneously. Then with time, tartrate ions exchange and as the grey double arrows show (second approach in Figure 3.15). In the end, multilayers formed with merging double bilayers. In this case, one should observe the mixture of right- and left- handed helices at the early stage, which then merge with time toward large pitch helices with only one handedness.

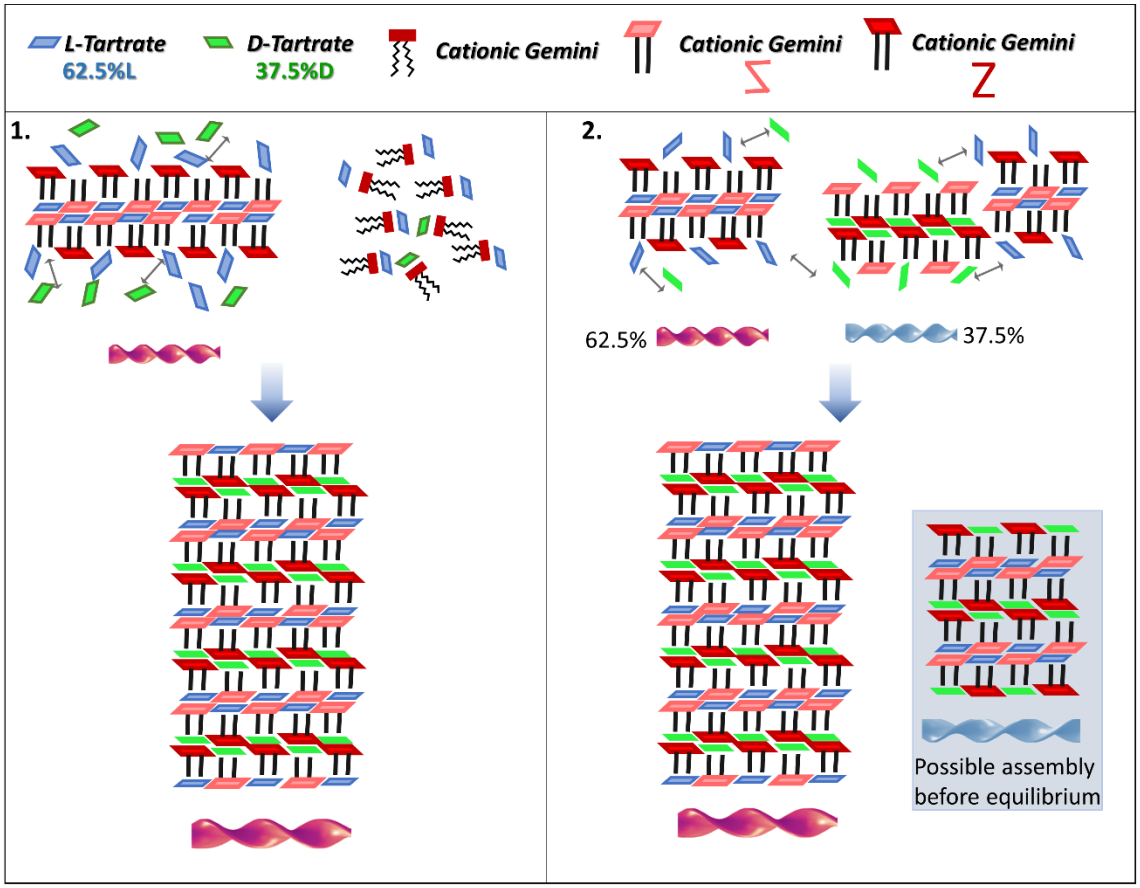

Figure 3.15 Schematic illustration of two possible approaches of forming big twisted ribbon.

To figure out with which mechanism, the 16-2-16 gemini tartrate twisted ribbons form and grow in size, during the self-assembly process, the differences of two means are listed: 1) number of twisted ribbons should be less in first mechanism than the second one; 2) there is only one right-handed twisted ribbons in first approach, but both right- and left-handed twisted ribbons at beginning. However, it turned out that it is impossible to quantify the numbers of the twisted ribbons, and also it is hard to tell the handedness of twisted ribbons with the TEM images as we observe the samples in transmission model.

Since it is not easy to prove the mechanism with the ee = 0.25 sample, we decided to study the extreme situation, which is racemic16-2-16 gemini tartrate. If the first mechanism works, only flat ribbons will be present, but with a thickness increasing with time. If the second mechanism is true, we should observe twisted ribbons with the two handednesses at the beginning of the self-assembly and flat ribbons for longer aging time. Therefore, 1 mM racemic 16-2-16 gemini tartrate was observed for various aging times (Figure 3.16). With 2h aging time, only twisted ribbons were observed with racemic 16-2-16 gemini tartrate. The pitch length and width of twisted ribbons became larger with time, by comparing Figure 3.16 (a), (b) and (c). The flat ribbons were present with 6d aging time as shown in Figure 3.16 (d). This experimental observation seems to confirm the second self-assembly process.

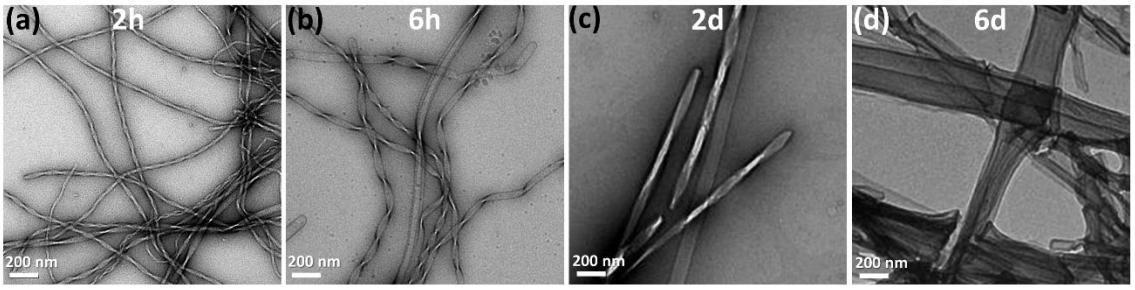

Figure 3.16 TEM images of racemic 16-2-16 gemini tartrate (ee = 0, at 1 mM concentration) aged under 20°C with different time (a) 2h, (b) 6h, (c) 2d, and (d) 6d.

To further confirm the second mechanism, efforts were given to be able to distinguish the handedness of twisted ribbons. A technique to give the information on the 3D relief of the ribbons' morphologies was then needed: because the technique is already used frequently in the group, we decided to stabilize the organic structures thanks to a silica layer (see details in chapters 4).[12, 13] These rigid 16-2-16 gemini tartrate / silica structures

could be observed by SEM after a metallization of the surface (see chapter 2). Silica transcript structures of 2h aged racemic 16-2-16 gemini tartrate was thus observed with TEM and SEM. TEM images of the silica twisted ribbons in Figure 3.17 a showed a good agreement with the original organic structure (Figure 3.16 a). With help of SEM images, we could reveal coexistence of left- and right- handed twisted ribbons in the same sample, as marked by blue and red arrows in Figure 3.16 (b). Furthermore, we check the ee = 0.25 16-2-16 gemini tartrate organic TEM images cautiously (Figure 3.13 d), two opposite handedness twisted ribbon are observed (labeled in Figure 3.17 c) although it is less obvious than with the SEM images on silica ribbons.

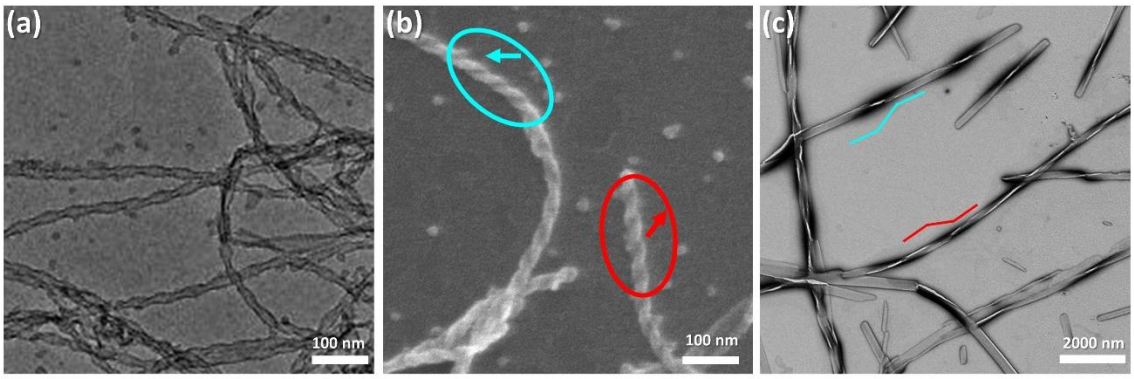

Figure 3.17 TEM image (a) and SEM image (b) of silica stabilized structure from racemic 16-2-16 gemini tartrate (ee = 0, at 1 mM concentration) aged 2h under 20°C. (c) TEM image images of gemini tartrate (ee = 0.25, at 1 mM concentration) aged 6d under 20°C, which is the same image of Figure 3.13 (d).

The ensemble of the above mentioned results confirm that in the mixture of 16-2-16 L-gemini tartrate and D-gemini tartrate, initially, left- and right- handed twisted ribbons coexist at beginning, with time these small twisted ribbons merge into one-handed larger ribbons. This finding showed that the formations of these chiral ribbons are first entropy driven at their early stage, by coexistence of two small chiral ribbons with opposite handedness, which is metastable. With time, the stacking of the multi-bilayers occur driven by the favored interaction between the tartrate and one of the conformations of gemini on the external leaflet of the bilayers, leading to their growth in the thickness, width, and the periodicity, which can be considered as enthalpy driven.

3.3 Kinetic evolution at the molecular level

In order to investigate the molecular level organization, electronic CD, VCD and X-ray scattering techniques were used. Since the evolution trend is the same for ee = 0, 0.25, 0.33 and 0.5 16-2-16 gemini tartrate, the sample ee = 0.25 gemini tartrate was chosen to represent gemini tartrate with ee < 0.8 category. Like for the study for ee > 0.8, the detection limits regarding the concentration of the samples differ with the different techniques. Previously, the evolution of the morphology for three concentrations (1 mM, 10 mM and 50 mM) were followed by TEM in Part 3.1, and all of them showed the same tendency. Therefore, the most suitable concentration will be adopted for each technique: 1 mM for electronic CD spectra, and 50 mM for VCD and X-ray scattering.

3.3.1 Characterization of ee = 0.25 16-2-16 gemini tartrate evolution by electronic CD

Figure 3.18 (a) showed the evolution of 1 mM ee = 0.25 16-2-16 gemini tartrate ECD spectra from t = 0 to 3h aging time. Originally, electronic CD spectrum of 0 min had the same pattern (but with lower intensity) as the enantiomer 16-2-16 L-gemini tartrate with two negative peaks attributing to tartrate ions in micelles.[9] And final ECD pattern aging time had similar shape than 16-2-16 L-gemini tartrate, which consists of positive peak at high wavenumber and negative peak at low wavenumber indicating to bilayer structures.[9] CD values at 207 nm was plotted as a function of aging time in Figure 3.18 (b). It increased very quickly at first, decreased a bit, and kept stable after 100 min. This change in Figure 3.18 b is more complex than the pure 16-2-16 L-gemini tartrate (Figure 3.9 c). The reason is probably that the evolution speed of 16-2-16 L- and D- gemini tartrate are different due to different concentrations, and what is measured is the sum of these two enantiomers signals in ee = 0.25 16-2-16 gemini tartrate (in which we could consider that the concentration of the L and D gemini tartrate are 0.625 mM and 0.375 mM respectively.

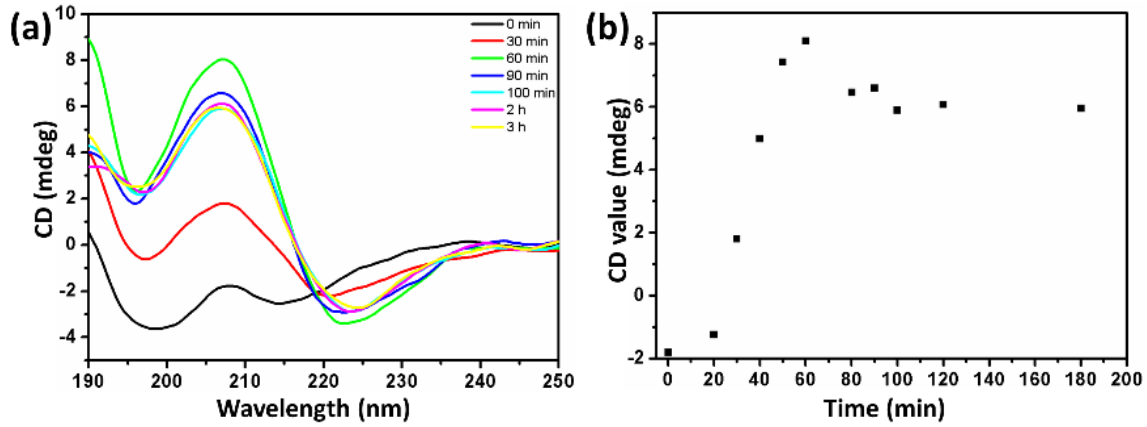

Figure 3.18 (a) CD spectra of ee = 0.25 16-2-16 gemini tartrate with 1 mM various aging time at 20°C, and (b) showed the CD values at 206 nm, which indicated the evolution of peaks directly.

3.3.2 Characterization of ee = 0.25 16-2-16 gemini tartrate evolution by VCD

50 mM ee = 0.25 16-2-16 L-gemini tartrate assembly was investigated by VCD. The antisymmetric stretching of the carboxylate groups ($\nu_a CO_2^-$) of tartrates at 1610 cm^{-1} shows strong VCD signal with cotton coupling (positive peak at 1620 cm^{-1} and negative peak at 1615 cm^{-1}) (Figure 3.19 (a)). Interestingly, the intensity of the signal increased slowly, but strongly with time. The g factor of ee = 0.25 16-2-16 gemini tartrate increases continuously with aging time till 6 days, showing surprisingly slow evolution process.

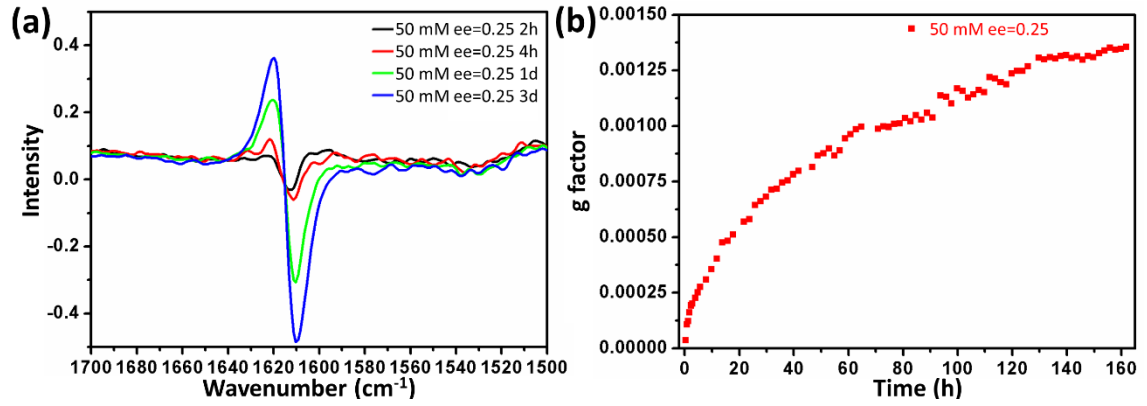

Figure 3.19 (a)VCD spectra of ee = 0.25 16-2-16 gemini tartrate in 50 mM aging various duration, and (b) g factor of peak of $\nu_a CO_2^-$ evolution with time.

3.3.3 Characterization of ee = 0.25 16-2-16 gemini tartrate evolution by X-ray scattering

X-ray scattering patterns of ee = 0.25 16-2-16 gemini tartrate expressed identical peaks as the ee = 1 samples and the full width at half maximum (FWHM) of these peaks kept unchanged after 1 h (as showed in Figure 3.20 b). However, unlike ee = 1, the peaks

in ee = 0.25 slowly increased with time. as shown in Figure 3.20 (a) and Figure 3.20 (b). This result reveals that the crystallinity of self-assembly increased, which may indicate that multi-bilayers are formed with time in ee = 0.25, which corresponds to the increase in thickness of the ribbons.

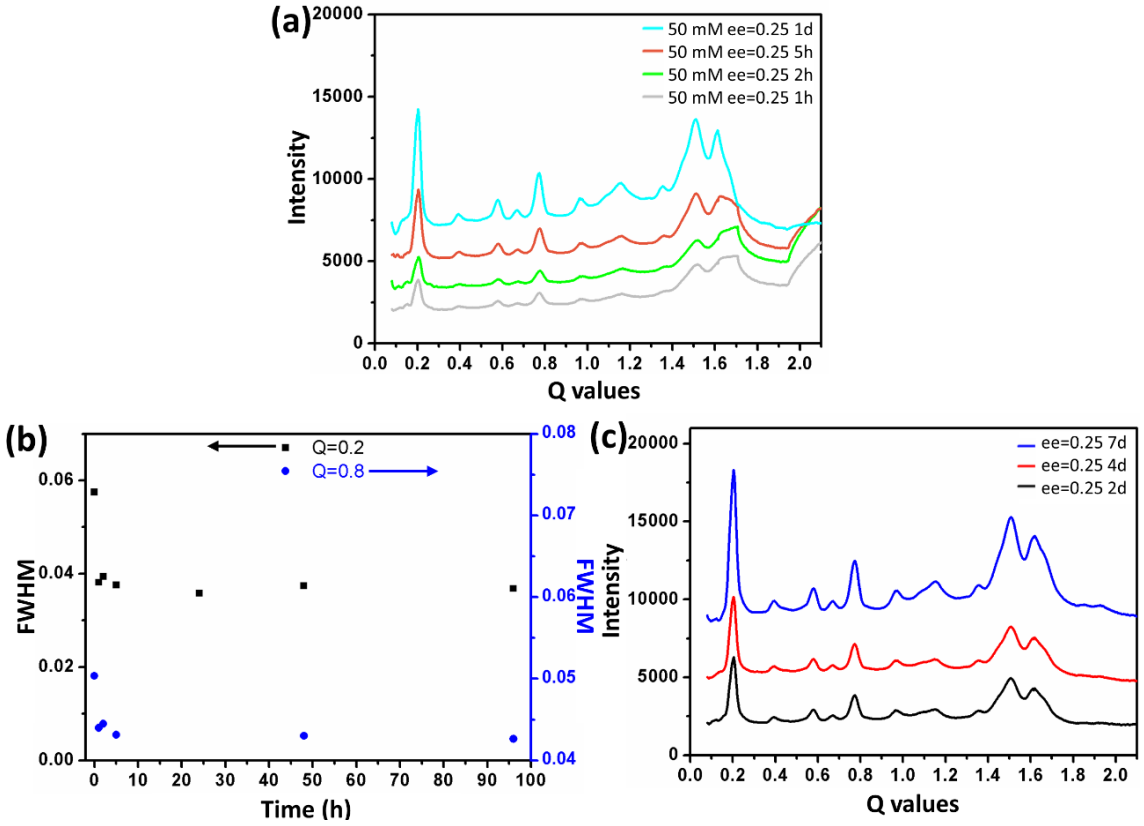

Figure 3.20 (a) X-ray scattering patterns of ee = 0.25 16-2-16 gemini tartrate in 50 mM aged with various duration, (b) Full width at half maximum indicated sharpness of peak, (c) X-ray scattering patterns of ee = 0.25 16-2-16 gemini tartrate aging with 2d to 7d. Please note that, after 2 days, the gel formed with 50 mM ee = 0.25 16-2-16 gemini tartrate broken, so the X-ray scattering measurement was performed with the solid part for 2d, 4d and 7d instead of the whole homogenous gel.

4. Comparison of two evolutionary processes

According to the characterization and analysis of the 16-2-16 gemini tartrate under various conditions performed by TEM, electronic CD, VCD, and X-ray scattering techniques, two interesting processes are observed depending on the ee values of 16-2-16 gemini tartrate.

4.1 Morphology comparison of 16-2-16 gemini tartrate with various ee

Figure 3.14 showed the details of how the pitches, width and morphologies evolve with time as function of ee values: when ee < 0.8, the ribbons becomes wider and larger (longer pitch) with time until a limit where the pitch and width are stabilized. For ee > 0.8, twist ribbons evolve with time to form helices and tubes. Figure 3.21 (a) showed that for ee > 0.8, the width increased with time while the pitch did not vary at the beginning. Figure 3.21 (b) plotted width of the twisted ribbons as a function of pitch for ee = 0.25, 0.33 and 0.5 after different aging times. There is a strong correlation between the pitch length and width of twisted ribbons, and they all fall in a line regardless the ee and aging time of the 16-2-16 gemini tartrate, shown in Figure 3.14 (b). When ee < 0.8, and twisted ribbons never transformed into helical ribbons, which may be due to the fact that the thicker ribbons with higher bending modulus cost more energy to form helical shape.

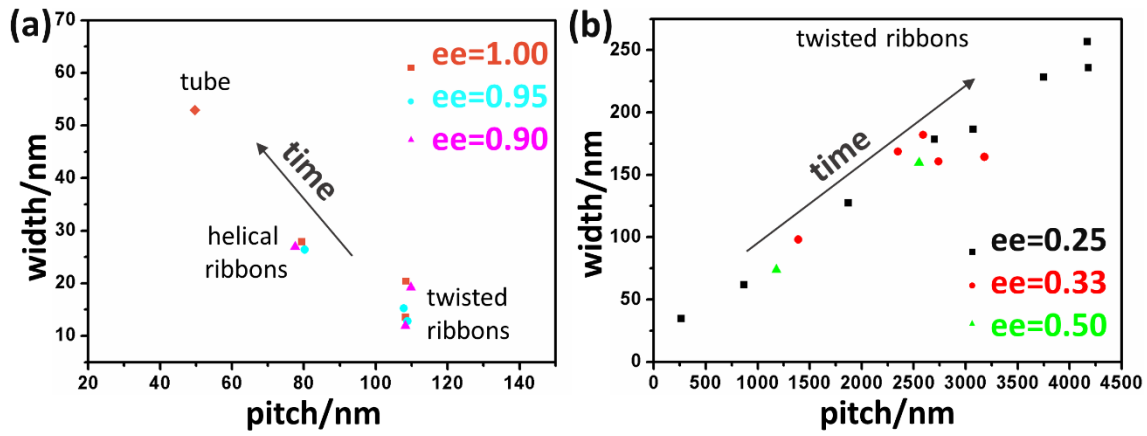

Figure 3.21 (a) and (b) ribbons width as a function of pitch for (b) ee = 0.9, 0.95, 1 and (c) ee = 0.25, 0.33, 0.5.

4.2 Chirality comparison of 16-2-16 gemini tartrate with various ee

According to the VCD spectra of ee = 0.25 and 1 16-2-16 gemini tartrate as representative samples for ee < 0.8 and ee > 0.8, g-factors of $\nu_a CO_2^-$ were plotted in Figure 3.22 (a) as a function of the aging time. Right after they are heated to micellar phase and cooled down (t = 0.5 h), the g-factor is the higher for ee = 1, and decreases as decreasing ee as expected (Figure 3.22 b black line). However, with time, the g factor of ee > 0.8 decreased while g factor increased for ee < 0.8 (Figure 3.22 b). For ee > 0.8, the twist to helical morphology change seems to coincide the decrease of g-value, which may be

related to the nature of the curvature, Gaussian vs cylindrical curvature. Indeed for the molecules organized in Gaussian curvature, the molecules are under twist in both orthogonal direction whereas for those in cylindrical curvature, they are twisted only in one direction. For ee < 0.8, it is multilayer molecules packing which results in more chirality of $\nu_a CO_2^-$, and the final equilibrium g factor values is much more pronounced than the g-values for ee > 0.8 in agreement with our previous report.[9]

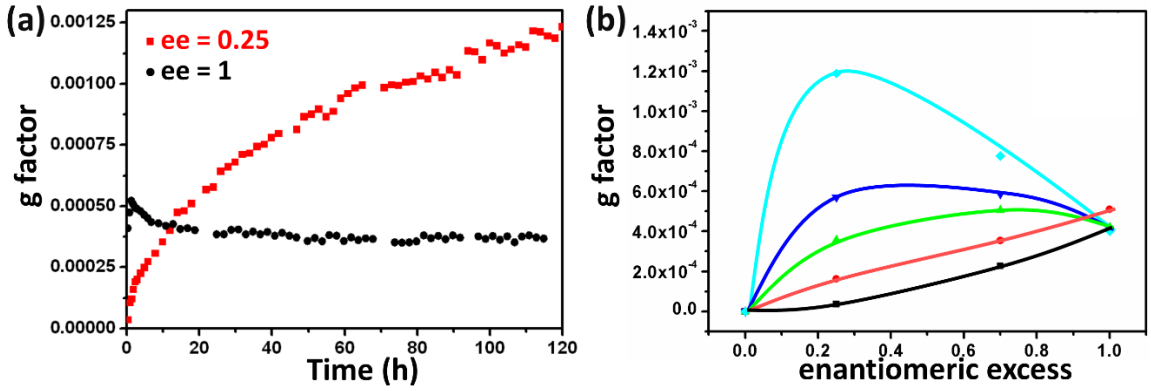

Figure 3.22 (a) The g factors of ee = 0.25 and 1 as function of aging time. And (b) the g factors obtained from as a function of ee at various aging time, and lines from black to blue are corresponding to black-0.5h, red-2h, green-10h, blue-20h, and lightblue-120h.

4.3 Conclusion

There are many factors which affect the self-assembly process of 16-2-16 gemini tartrate, like solvent, temperature, addition of achiral ions and concentration. In the thesis, we only studied the effect of the concentration and ee of 16-2-16 gemini tartrate.

In general, higher concentration of 16-2-16 gemini tartrate with same ee showed faster evolution, but the final morphology at equilibrium is the same for all the concentrations. Therefore, concentration changes the self-assembly kinetics, not the morphology of the assemblies.

With the various ee 16-2-16 gemini tartrate, there are two types of evolution. For ee > 0.9, double bilayer structure transformed from twisted to helical ribbons with time as confirmed by TEM images. The VCD signal for the twisted ribbons shows higher g-values with respect to those for the helical ribbons. For ee < 0.8, only twisted ribbons can be formed as revealed by TEM images. But the molecular structure evolves with time from

double bilayers to multi-bilayers, which is verified by VCD spectra and X-ray scattering. Both left- and right-handed twisted ribbons are present initially, since the double bilayers are formed randomly. But with time, the majority of the twisted ribbons' handedness depends on the majority of 16-2-16 gemini tartrate, and only homo handedness of twisted ribbons should be present at equilibrium state.

Experimental section

Synthesis of 16-2-16 gemini tartrate

The synthesis steps of 16-2-16 gemini tartrate is schematically illustrated in Figure 3.23. At first, the product ***a*** 16-2-16 Gemini Bromide was obtained according to the procedures developed by R. Zana et al.[14,15,16] with tetramethyl ethylenediamine (TEMDA) and 1-bromohexadecane in acetonitrile. Then, compound ***b*** 16-2-16 gemini acetate was synthesized from 16-2-16 Gemini bromide by ion exchange reaction with silver acetate as previously reported. [17] Finally, the acetate can be replaced with tartrate ions with presence of 2 eq. tartaric acid, and the product ***c*** 16-2-16 gemini tartrate can be obtained.[2,6,18]

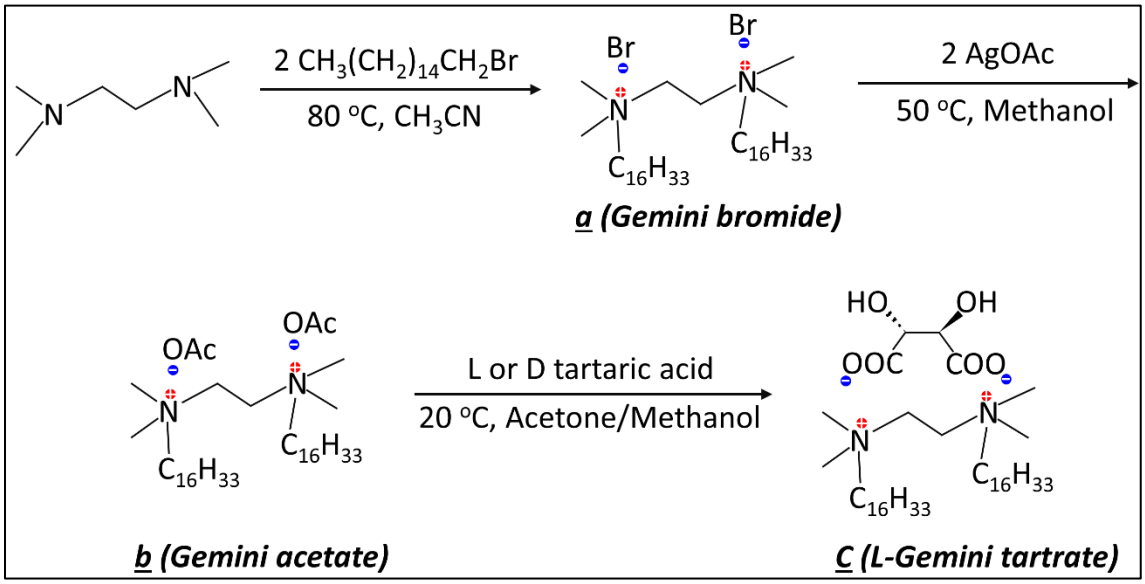

Figure 3.23 Synthesis steps of 16-2-16 gemini tartrate and depending on the L or D tartrate acid from compounds *b* to *c*, 16-2-16 L- or D- gemini tartrate can be obtained.

Typically, the first step is: 2.47 mL of TEMDA was mixed to 15 g 1-bromohexadecane in 150 mL of acetonitrile (molar ratio of two reactants is 1:3) and stirred

at 400 rpm at 80 °C for 48h. When the reaction was finished, the reaction mixture was stored at 4°C for 2 hour and Gemini bromide was precipitated as white solid. The product was collected by filtration and washed by acetonitrile 3-5 times at 80 °C to remove the unreactive reactants. After the washing, the Gemini bromide was filtered, rinsed with acetone and dried under vacuum overnight. The yield of final product ***a*** was around 7 g (67%).

Step 2: Gemini acetate: 2.01 g of 16-2-16 Gemini bromide and 1.38 g of silver acetate (molar ratio of two reactants is 1:3) were mixed in 100 mL methanol in a round-bottom flask covered with aluminum foil. The mixture was heated up to 50 °C for 24 h. Then the suspension was filtered on Celite to remove silver bromide and unreacted silver acetate and the transparent liquid after filtration was collected. The solvent methanol was removed by rotor evaporator, while solid came out in the flask. 3 drops of methanol was added to dissolve the product at 60 °C and 100 mL of acetone was added in the flask. The mixture was kept at 4°C overnight inducing the precipitate of the Gemini acetate as a fine white powder. The Gemini acetate was filtered, rinsed with a mixture of methanol/chloromethane (1:9), and dried under vacuum overnight. The yield of product ***b*** was around 1.2-1.5 g (63-78%).

500 mg of 16-2-16 Gemini acetate and 220 mg of L or D tartaric acid (molar ratio of two reactants is 1:2) were dissolved in two portions of 10 mL mixture of methanol/ Acetone (1:9) separately. Tartaric acid solution was added into 16-2-16 Gemini acetate solution drop by drop while stirring. When the mix was finished, the final ration of Gemini acetate and tartaric acid is 1:2, and the mixture was kept at 25°C with string for 1h. The 16-2-16 gemini tartrate was precipitated as white powder, and the product was collected by filtration. And 2 times washing with mixture of MeOH/acetone and 5 times washing with cold ultra-pure water was followed. The Gemini acetate was filtered, rinsed with acetone, and dried under vacuum for overnight. The yield of the third step is about 70% (with compound ***c*** 16-2-16 L- or- D gemini tartrate around 360 mg).

16-2-16 gemini tartrate with various ee

To obtain 16-2-16 gemini tartrate with various ee, pure 16-2-16 L- and D- gemini tartrate were mixed with different ratios, according to the definition of ee.

$$\text{ee} = \frac{n_L - n_D}{n_L + n_D}$$

where n_L and n_D are the moles of 16-2-16 L- and D- gemini tartrate respectively. To make sure two enantiomers are mixed homogenously in water during the self-assembly process, organic solvent is used to dissolve the 16-2-16 gemini tartrate at first. Take ee = 0.25 16-2-16 gemini tartrate as an example: 6.75 mg of 16-2-16 L-gemini tartrate and 3.25 mg of 16-2-16 D-gemini tartrate were dissolved in 1-2 mL methanol. Then the mixture was kept under vacuum to remove the methanol, and white powder was present on the bottom of the container. At this time, a certain amount of ultrapure water was added according to the desired concentration and the solution was heated up to 60°C to dissolve the 16-2-16 gemini tartrate. After 15 min, the 16-2-16 gemini tartrate could be totally dissolved in water and the solution was transferred into a cabinet with a controlled temperature to exactly 20°C. Aging time started to be counted when the sample was placed at 20°C.

References

1. R. Zana and Y. Talmon, Dependence of aggregate morphology on structure of dimeric surfactant, Nature, 1993, 362, 228-230.

2. R. Oda, I. Huc and S. J. Candau, Gemini surfactants, the effect of hydrophobic chain length and dissymmetry, Chem. Commun., 1997, 2105-2106.

3. R. Oda, I. Huc, M. Schmutz, S. J. Candau and F. C. Mackintosh, Tuning bilayer twist using chiral counterions, Nature, 399, 566-569.

4. H. Ihara, M. Takafuji and T. Sakurai, In encyclopedia of nanoscience and nanotechnology, H. S. Nalwa Ed., American scientific publisher: 2004, Vol 9, PP: 473-495.

5. A. Bizard, R. Oda and I. Huc, Chirality effects in self-assembled fibrillar networks, Top. Curr. Chem., 2005, 256, 167-218.

6. A. Brizard, C. Aime, T. Labrot, I. Huc, D. Berthier, F. Artzner, B. Desbat and R. Oda, Counerion, temperature, and time modulation of nanometric chiral ribbons from Gemini-tartrate amphiphile, J. Am. Chem. Soc., 2007, 129, 3754-3762.

7. R. G. Snyder, Vibrational spectra of crystalline n-Paraffins II. Intermolecular effects, J. Mol. Spectrosc.1961, 7, 116-144.

8. R. Oda, F. Artzner, M. Laguerre and I. Huc, Molecular structure of self-assembled chiral nanoribbons and nanotubules revealed in the hydrated state, J. Am. Chem. Soc., 2008, 130, 14705-14712.

9. A. Brizard, D. Berthier, C. Aime, T. Buffeteau, D. Cavagnat, L. Ducasse, I. Huc and R. Oda, Molecular and supramolecular chirality in Gemini-tartrate amphiphiles studied by electronic and vibrational circular dichroisms, Chirality, 2009, 21, 153-162.

10. R. Tomato, N. Daugey, T. Buffeteau, B. Kauffmann, M. Fakafuji, H. Ihara and R. Oda, *In situ* helicity inversion of self-assembled nano-helices, Chem. Commun., 2015, 51, 3518-3521.

11. D. Berthier, T. Buffeteau, J.-M. Leger, R. Oda and I. Huc, From chiral counterions to twisted membranes, J. Am. Chem. Soc., 2002, 124, 13486-13494.

12. T. Delclos, C. Aime, E. Pouget, A. Brizard, I. Huc, M. Delville and R. Oda, Individualized silica nanohelices and nanotubes: tuning inorganic nanostructure using lipidic self-assemblies, Nano Lett., 2008, 8 (7), 1929-1935.

13. Y. Okazaki, J. Cheng, D. Dedovets, G. Kemper, M. Delville, M. Durrieu, H. Ihara, M. Takafuji, E. Pouget and R. Oda, Chiral colloids: homogeneous suspension of individualized SiO2 helical and twisted nanoribbons, ACS Nano, 2014, 8 (7), 6863-6872.

14. M. Frindi, B. Michels, H. Levy and R. Zana, Alkanediyl-α,ω-bis (dimethylalkylammonium bromide) surfactants. 4 Ultrasonic absorption studies of amphiphile exchange between micelles and bulk phase in aqueous micellar solution. Langmuir, 1994, 10(4), 1140-1145.

15. R. Zana, Gemini (dimeric) surfactants, Curr. Opin. Colloid Interface Sci., 1996, 1(5), 566-571.

16. M. In and R. Zana, Phase behavior of gemini surfactants, J. Disper. Sci. Technol., 2007, 28 (1), 143-154.

17. S. Manet, Y. Karpichev, D. Bassani, R. Kiagus-Ahmad and R. Oda, Counteranion effect on micellization of cationic gemini surfactants 14-2-14: Hofmeister and other counterions, Langmuir, 2010, 26(13), 10645-10656.

18. A. Brizard, R. Kiagus-Ahmad and R. Oda, Control of nano-micrometric twist and helical ribbon formation with gemini-oligoalanine via interpeptidic beta-sheet structure formation, Chem. Commun., 2007, 22, 2275-2277.

Chapter 4. Synthesis of Goldhelices: chiral arrangement of achiral GNPs for chiroptical properties

Contents

1. Introduction and state of the art

Since several centuries B.C., gold, as one type of malleable noble metal, attracted interests of people from all over the world. Although gold is one of the most ancient topic, there still remain mysteries on their properties, which leads to an exponentially increasing number of publications, especially in the context of emerging nanoscience and nanotechnology with Gold Nano Particles (GNP) and Self-Assembled Monolayers (SAM). [1] D.A. Weitz first reported fractal structure formed by kinetic aggregation of aqueous gold colloids in 1984. [2] An extremely large number of publications reported the use of GNPs, especially in the field of sensor [3] and biomedical applications [4]. Since GNPs or gold nanorods (GNR) exhibit rich surface plasmon resonance-derived properties, the surface plasmonic resonance intensity and relative optical property can be controlled by surface functionalization or tuned arrangement of GNPs. Here we will focus on chiral gold clusters which can potentially be used for the applications such as the development of sensors,[5] ultra-thin quarter wave plates, electromagnetic nano-devices [6] and asymmetric catalysis[7, 8].

Both top-down and bottom-up approaches can be used to achieve complex gold nanostructures. J. K. Gansel et al [9] fabricated gold helix photonic metamaterials as broadband circular polarizer through three-dimensional direct laser writing into a photoresist followed by electrochemical deposition of gold, in which laser writing is the key step to control the morphology. As such, top-down approach is a powerful mean to explore a wide range of structures with fine control. However, they are expensive, limited in the sample size, and slow to perform. Thus, it remains challenging to produce and engineer nanometric materials. Bottom-up processes, in contrast, are based on the chemical deposition and/or molecular self-assemblies, the properties of which depend strongly on the chemical properties of single unites. Sophisticated structures can be obtained based on the precise chemistry control with bottom-up strategy. In the chiral gold cluster field in particular, complex nanomaterials were created with controllable chiral optical properties. We will first present the literature which describe the controlled synthesis and organization of GNRs or GNPs with tunable chiroptical properties using the bottom-up approach.

Fu Zhu et al.[10] synthesized end to end assemblies of GNRs which can be used as sensors to detect the configuration of cysteine or glutathione. They found that GNRs with

aspect ratio of 3.1 in aqueous cetyltrimethylammonium bromide CTAB solution gave opposite CD signals at the wavelength of 500-850 nm when they were mixed with L-Cysteine ($_{L}$-Cys) and D-Cysteine ($_{D}$-Cys), as shown in Figure 4.1 (A). The intensity of the CD spectra varied with the pH of the solution. While the pH is 5.02, at the isoelectric point of Cys, strongest induced CD was observed from GNRs. This is due to the assemblies of GNRs in the presence of $_{L}$-Cys or $_{D}$-Cys leading to the cooperative effect, and the enhancement of CD signals. Furthermore, the GNRs response to Cys is linearly relative to the concentration of Cys (1-5μM). Such type of GNRs could work as a sensor for detecting enantiomer and quantification of the glutathione. Both glutathione and Cys contain thiol group and amine group, which could interact strongly with each other via covalent bonding with Au at a certain pH. They concluded that the induction of chirality could be assigned to the induced assembly of GNRs in the presence of Cys. An interesting observation reported in this paper reflects the property of GNRs or GNPs in general that the CD signals of Cys (around 200 nm in Figure 4.1 (a) and (b)) are modified when they are mixed with GNRs suspension. This is due to the enhancement of the CD signals, which is attributed to the surface plasmon resonance of the gold or silver particles[11].

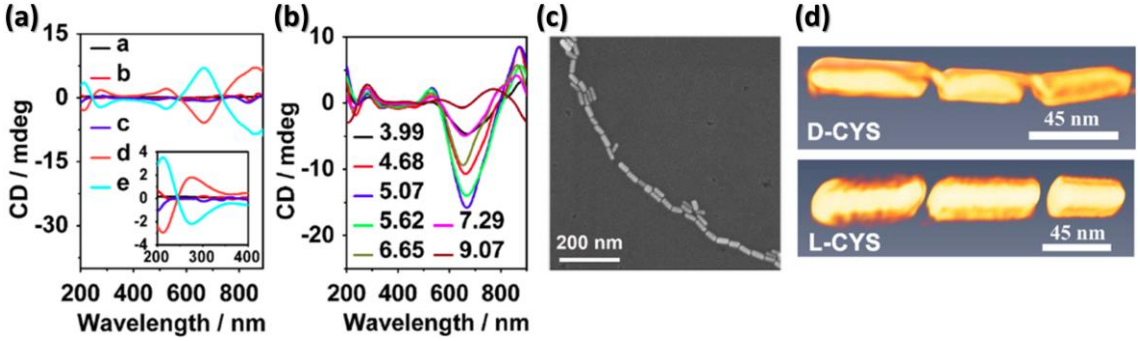

Figure 4.1 (a) CD spectra of Au nanorod alone *a*, L-Cys *b* or D-Cys alone *c*, and mixture of Au nanorods and L-Cys *d* or D-Cys *e*. (b) CD spectra of the mixture of L-Cys and Au nanorods at various pH. (c) SEM image of Au nanorods after addition of L-Cys at pH 5.07. (d) Cryo TEM tomography images for Cys-induced end-to-end assembly of Au nanorod. [10]

Wenjing Liu et al. reported the gold nanorod@chiral mesoporous silica core-shell nanoparticles (GNRs@CMS) with unique optical properties in 2013.[12] They prepared GNRs stabilized by CTAB at first, and then coated them with mesoporous silica shell with the addition of tetraethyl orthosilicate (TEOS) and N-palmitoyl-L (or D or DL)-phenylalanine (C_{16}-$_{L/D/DL}$-Phe). Unlike the previous assemblies of GNRs showing CD

signal, single GNRs@CMS showed CD signals with C_{16}-L-Phe or C_{16}-D-Phe in Figure 4.2(i). Position of the peak in CD spectra varied with the aspect ratio of GNRs@CMS, because with an increase of aspect ratios of GNR cores, the absorption peaks at around 700 nm related to longitudinal LSPR of GNRs are red shifted. This GNRs@CMS could be used as sensors to examine the enantiomer of Cys as well. When GNRs@CMS templated with C_{16}-L-Phe were mixed with L-Cys, a novel peak at 730 cm^{-1} appeared in Raman spectrum, as in Figure 4.2 (j).

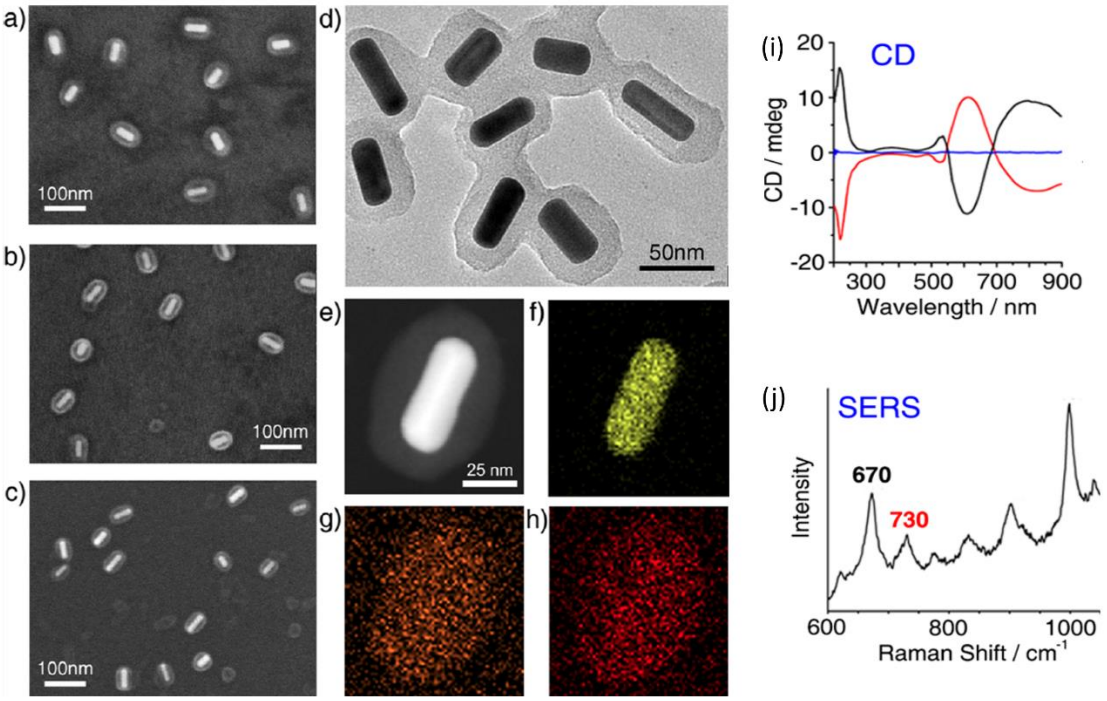

Figure 4.2 SEM images of the GNR@CMS NPs synthesized with three different chiral surfactants: (a) C_{16}-L-Phe; (b) C_{16}-D-Phe; (c) C_{16}-DL-Phe. (d) TEM image of GNR@CMS NPs. (e) HAADF-STEM image. HAADF-STEM-EDS mapping images of core-shell NPs: (f) Au mapping; (g) Si mapping; (h) O mapping, and(i) CD spectra of them. (j) SERS spectra of L-Cys loaded into GNR@CMS NPs with C_{16}-L-Phe. [12]

When we discuss about the chirality and asymmetric structures, DNA cannot be forgotten as it can be designed into two- and three- dimensional shapes[13,14]. Anton Kuzyk et al.[15] succeeded in chiral plasmonic nanostructures assisted by DNA-based self-assembly with tailored optical response. GNPs with 10 nm diameter are attached on the sites offered by DNA origami as schema shown in Figure 4.3 (a) and corresponding TEM image in Figure 4.3 (b). CD spectra (Figure 4.3 (c)) showed opposite signals for left-handed and right-handed helical arrangements, with a good agreement with theoretical calculation.

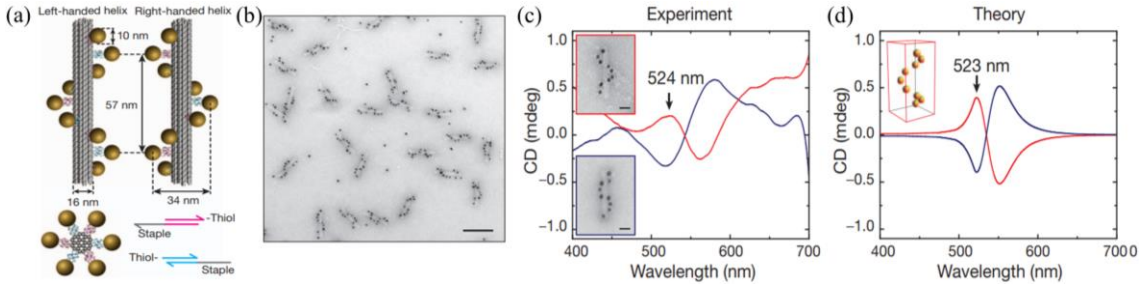

Figure 4.3 (a) Left- and right-handed nanohelices (diameter 34 nm, helical pitch 57 nm) are formed by nine gold nanoparticles each of diameter 10 nm that are attached to the surface of DNA origami 24-helix bundles (each of diameter 16 nm). (b) TEM image of assembled left-handed gold nanohelices (scale bar, 100 nm). (c) Experimental and (d)theoretical CD spectra of left-handed (red lines) and right-handed (blue lines) helices of nine gold nanoparticles.[15]

By increasing the diameter of GNPs to 16 nm and arranging them on the DNA origami by the thiol sites, they could control the wavelength at which CD was observed as well as their intensity. Peak position in CD spectra for both left and right-handed helices of GNPs with 16 nm red-shifted to 545 nm with higher signal than the CD signal which was observed with 10 nm GNPs (at 524 nm) in good agreement with the theoretical calculations based on classical electrodynamic. According to dipole theory[16], CD signal becomes stronger when the particles are either larger or arranged in a tighter helix. On the other hand, they also plated silver onto pre-assembled 10 nm gold particle helices (about 3 nm shell of silver), and the recorded CD spectra was blue shifted due to the plasmonic resonances in silver occurrence at a shorter wavelength.

Even though there are many reports on the control of CD spectra by the size of the particles and the metals[17, 18], most of the reported nanostructures obtained with bottom up approach are based on organic scaffolds, which is generally vulnerable to the chemical, mechanical and thermal perturbations. Moreover, the handedness of the organic self-assembly is not always controlled.

Among many reports on fabrication of the chiral plasmonic particles by bottom-up approaches one typical approach is to prepare stabilized nanoparticles by chiral molecules[19]. Another effective method is to use chiral template as a substrate to support metal nanoparticles[20] or to use chiral hollow structure holding and constraining the metals structure [21, 22]. However, when the chiral sources are concerned, one system may include several types of chirality. As mentioned in chapter 1, there are several types of chirality for

nanoparticles (NPs). For example, a) the asymmetric geometry of NPs, or b) achiral NPs arranged in a chiral way, or c) achiral NPs coat by achiral stabilizer non-uniformly, or d) achiral NPs which are stabilized by chiral ligand uniformly.

Previously, in our group, silica nanohelices were obtained through a sol-gel transcription of organic helices[23] , which are more stable and perdurable in aqueous or organic suspensions. The pure right- and left- handed silica helices in nanometric scales offer homo chiral environment for the achiral particles or molecules. GNPs with various diameters from 5 to 10 nm were grafted on the silica substrate by electrostatic interactions[24], as shown in Figure 4.4 (a). In this manuscript, we named the silica helices decorated by GNPs as Goldhelices. CD signals with opposite signs were detected for left- and right-handed Goldhelices (Figure 4.4 (b)). We calculated the g factors to evaluate and compare the chirality of the Goldhelices with different GNPs diameters. With an increase of GNPs diameter, stronger coupling between GNPs and g factor increases, which agree with the article [17], and our simulated results based on the coupled dipole method.

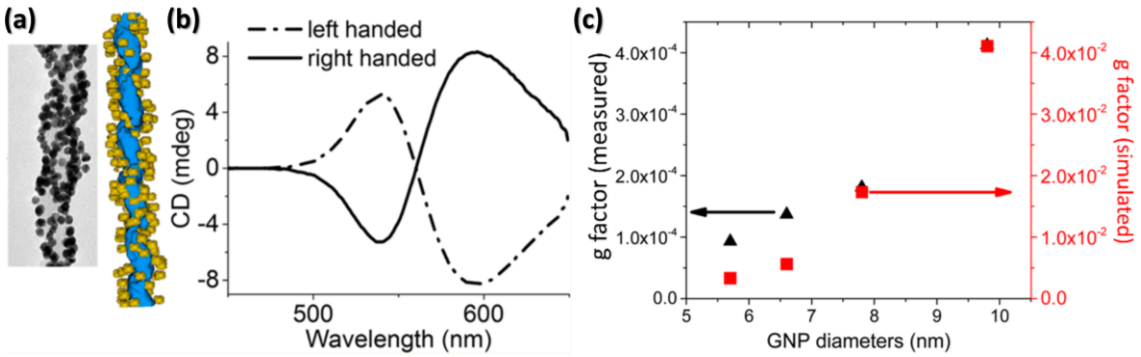

Figure 4.4 (a) TEM image and the reconstructed model based on tomography of gold helix, (b) Left- and right-handed gold helices (GNPs diameter 10nm) , (c) experimental and simulated g factor of CD spectra of gold helices with different diameters of GNPs.

Now, let us go back to the four articles (Cys, core-shell, DNA and Silica nanohelices) and consider how the non-chiral spherical or rod-like GNP or GNR can show CD signals. In the first article[10], the chiral source is L-Cys or D-Cys, but the CD signals expressed both the assemblies of GNRs and conjugation of GNRs and Cys. There are two possible origins of chirality: one is the chiral arrangement of GNRs, the other one is the chiral Cys coated GNRs. In the second article[12], there are also two possibilities about chiral signal of the GNRs@CMS. One is from the direct interaction between GNRs and C_{16}-L-

Phe or C_{16}-$_D$-Phe, another possible chiral source is the mesoporous silica which is chiral due to C_{16}-$_L$-Phe or C_{16}-$_D$-Phe. In general, GNRs or GNPs covered or linked with chiral ligand can lead to induced chirality on the optical properties of these particles, if the system contains one more reagent, or if these GNRs or GNPs are arranged with chiral organization, chirality enhancement or cooperative chirality can be observed. In the third article[15], chiral source is the DNA origami, CD signal of GNPs is only due to their helical arrangement. But to be very strict, GNPs covered by nucleic acid should be examined to exclude the (c) and (d) type chirality.

In the articles presented by our group, there are no chiral molecules in the system, but the nanometric helical morphology of the silica helices is the only chiral source, clearly demonstrating that the chiral response of GNPs resulted solely from their helical arrange.

Despite the considerable amount of work on chiral plasmonic nanoparticles, there still exist two limits which are very challenging to overcome. First, it is not easy to control the intensity of the chiroptical response due to the multiple chiral factors in one system. Secondly, with the development in nanoscience and nanomaterials fields which have as ultimate objectives as the designing of devices, it is now crucial to perform hierarchical organization of nanoobjects towards 2D or 3D materials. The stability of many nanoobjects may depend strongly on their environment, thus making them less universal in terms of applicability. To overcome the first handicap, our previous Goldhelix[24] is a perfect candidate, since in this system, we could control the sign and the intensity of G factors through helix handedness and the GNPs diameter respectively. For the stability of the nanomaterials, one of the crucial factors is the link between two elements. In this chapter, we will discuss how to design hybrid gold-silica nanomaterials with steady and durable covalent bonds between gold and silica. The chiroptical properties of the samples will then be presented.

2. Synthesis and characterization of the Goldhelices

2.1 Synthesis, fragmentation and functionalization of silica helices

In 2001, in collaboration with the group of P. Shinkai from Kyushu University, our group has succeeded in transcribing the organic self-assembly of nanometric helices to

silica structures via sol-gel polycondensation technique in pyridine.[25] This was then optimized later by Delclos et al.[26], who developed a method to do the transcription in water[27] in 2008, as shown in Figure 4.5. However, with this method, it took 20 days to get silica helical ribbons and also these nanoribbons are long and entangled (Figure 4.6 (a) and (b)). In 2014, Okazaki[28] et al. further optimized the parameters for the silica transcription via acidic catalysis, and shortened process from 20 days to 15 hours. In parallel they have shown how to create colloidal and well-dispersible silica helices with controlled length by cutting them with high power sonication. Based on the previous members hard work, a routine process to fabricate silica twisted and helical ribbons is now established. The twisted and helices silica nanoribbons are collectively named under the generic name silica helices.

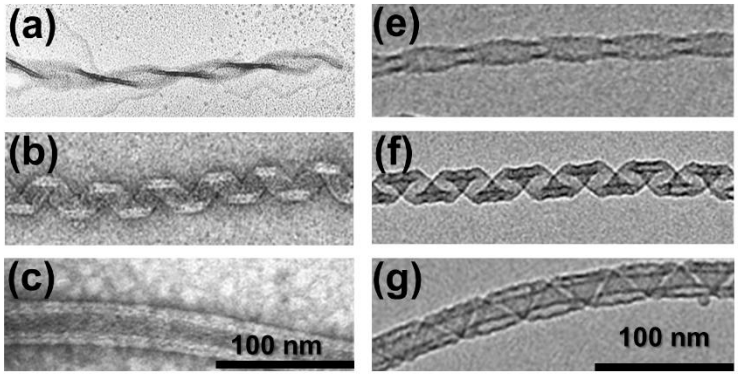

Figure 4.5 TEM images of organic self-assembly structure stained by uranyl acetate (a) twisted ribbon, (b) helical ribbon and (c) tube. TEM images of silica structures transcripted from organic tamples (e) silica twisted ribbon, (f) silica helical ribbon and (g) silica tube.

The synthesis process of the silica helices and their suspension into colloidal suspensions are detailed in the two following paragraphs.

Synthesis process of silica helices: 1 mM Gemini tartrate are solubilized in ultrapure water (3.58 mg of 16-2-16 L-Gemini tartrate powder, dissolved into 5 mL of water), and then the solution of Gemini tartrate was heated up above the Krafft temperature for 15min, (typically 60 ^{o}C for 16-2-16 L-Gemini tartrate). Next, the solution was transferred into a 20 ^{o}C incubator, and aged for 2 hours and 3 days respectively for organic twisted ribbons and helical ribbons. Meanwhile, pre-hydrolysis of TEOS was performed: 500 µL of TEOS was added to the 10 mL of 0.1 mM aqueous solution of L-tartaric acid (pH 3.8) and pre-hydrolyzed at 20°C by stirring on the roller-mixer for 7 hours. These two

solutions were mixed by volume ratio of 1:1, and the mixture was kept at 20°C overnight. To stop the silica transcription and avoid the formation of isolated SiO_2 nanoparticles, several washings are needed. In the present case, we washed the suspension with isopropanol 4 times using centrifugation (10 min, 2000 G), by which both the excess of TEOS and the organic Gemini tartrate inside the silica structures were removed. Then we performed 2 washings with ethanol. Final product was dispersed in ethanol.

As it was shown in previous work [28], the organic nanohelices are entangled and form gels (Figure 4.6 (a) and (b)) so the inorganic counterpart is also formed by entangled helices. In order to obtain short and individual silica nanohelices in solution, 1 mL suspension of as-prepared silica helices dispersed in a mixture of ethanol and isopropanol (ratio 1:1) with a concentration of 1 mg/mL was treated by tip-sonication under 130 W. Sonication time was 10 min, with a pulse of 1s separated by 1s pause. During the sonication, the suspension was kept in a water-ice bath. After this fragmentation process, well-dispersed short silica helices are obtained, as indicated by Figure 4.6 (c) and (d).

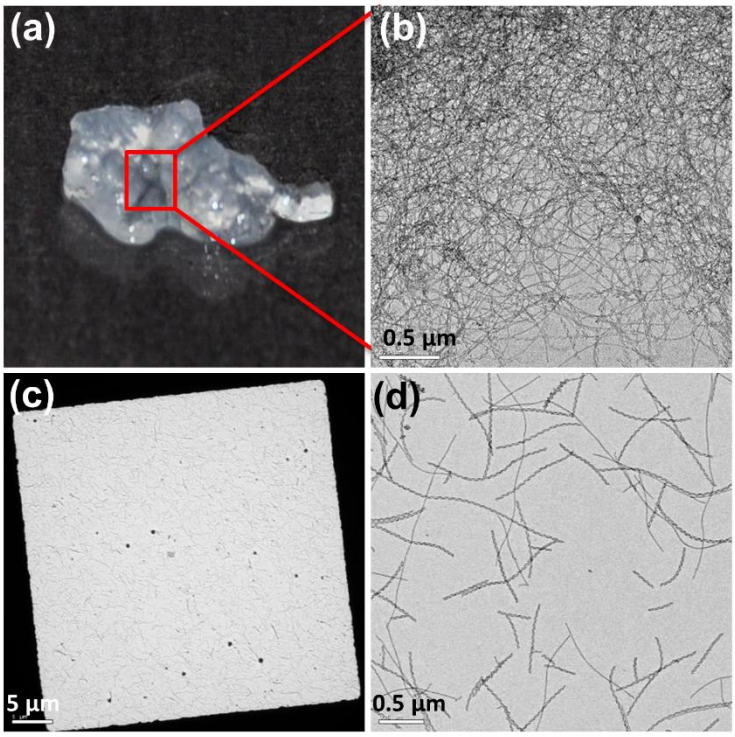

Figure 4.6 Typical entangled silica nanohelices images of optical microscope (a) and TEM image (b), TEM images of well-dispersed silica helices after tip-sonication in low magnification (c) and high magnification (d).

Well-defined silica helices present the similar surface chemical environment as other porous silica materials. There are four types of silanol on the helix surface (Figure 4.7), and without high temperature dihydroxylation, isolated, vicinal, geminal silanol are the majority of the total silica sites[29].

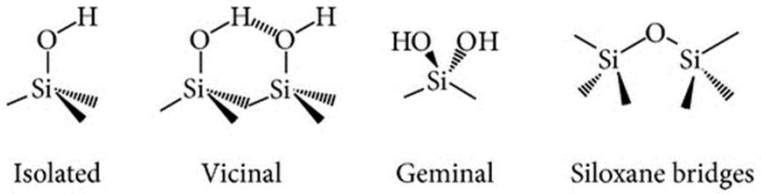

To functionalize silica surface, there are three available approaches[30].

$$\equiv Si - OH + Cl - SiR_3 \rightarrow \equiv Si - OSiR_3 + HCl \cdot base \quad (1)$$

$$\equiv Si - OH + R'O - SiR_3 \rightarrow \equiv Si - OSiR_3 + HOR' \quad (2)$$

$$2 \equiv Si - OH + HN(SiR_3)_2 \rightarrow \equiv 2 \equiv Si - OSiR_3 + NH_3 \quad (3)$$

Inspired by the method *(2)*[31], the previous members of our group developed an approach to functionalize silica surface by (3-aminopropyl) tri-ethoxy silane (APTES).[32] 2 µmol of APTES were added to 0.5 mg of short silica nanohelices dispersed in 1 mL mixture of ethanol and isopropanol. The reaction mixture was homogenized in a sonication bath for 5 minutes and then kept at 80 ˚C overnight (16h) followed by washing twice by centrifugation with isopropanol. This functionalization step can be repeated. In general, the amine coverage density is more or less around 0.5~1 NH_2/nm^2 as reported in Cheng et al [24] regardless of the number of functionalization steps.

2.2 Synthesis of GNPs and surface ligand exchange

GNPs can typically be obtained by reducing the aqueous solution of gold salt, followed by addition of stabilizers. Depending on the type of the reducing agent and stabilizers, different diameters of GNPs are obtained. In this thesis, GNPs were reduced and stabilized by both tannic acid and tri-sodium citrate[33]. To make 100 mL of GNPs colloid solution, two separated solutions were prepared. Solution A: 1mL 1wt% aqueous gold chloride and 80 mL ultrapure water were mixed and heated up to 60 ^oC. Solution B: 4 mL 1% tri-sodium citrate, 16 mL ultrapure water and 0.1 mL of 1% tannic were mixed

and heated up to 60 °C. After solution A and solution B were kept at 60 °C for 15 mins, the two solutions were mixed into one flask and heated up to 100 °C under reflux. The reaction was finished after one hour and the final product was cooled by ice bath. The solution contained GNPs with diameter of 10 nm which are named in this manuscript as TA-GNPs-10nm as the nanoparticles are stabilized with a mixture of citric acid and tannic acid (TA). Starting from these particles, the surface ligands can be exchanged with more suitable ligands. This ligand exchange reaction[24] was done by using O-(2-Carboxyethyl)-O'-(2-mercaptoethyl) heptaethylene glycol (noted as PEG in this manuscript) or 11-mercaptoundecanoic acid (MUA). Both PEG ($SHCH_2CH_2$-$[OCH_2CH_2]_8$-COOH) and MUA (SH CH_2-$[CH_2]_9$-COOH) end with thiol group and carboxyl group. MUA, which is 100 time cheaper than PEG, was used for optimizing experimental parameters. The typical preparation is shown in Figure 4.7: 8mL of as-synthesized TA-GNPs-10 nm was centrifuged at 21000G for 30 mins, followed by removing 6 mL of supernatant. Then, 2 mL of a 10 mM solution of MUA in ethanol was added in to 2 mL TA-GNPs-10 nm. The solution was sonicated for 10 min and placed on shaker with 400 rpm overnight at 4°C. The mixture is washed three times by centrifugation and redispersion in ultrapure water. A final centrifugation was performed to obtain four times concentrated gold solution, marked as TA-GNPs-10 nm-MUA. Same experiment could be done replacing MUA by PEG.

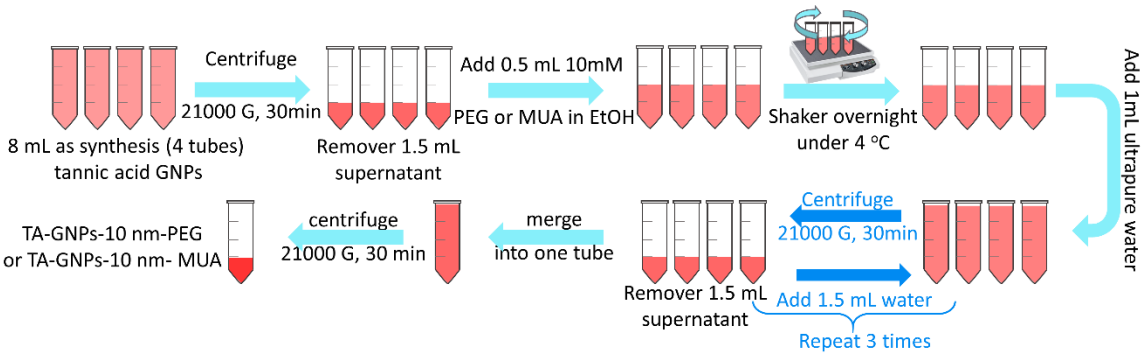

Figure 4.7 Schematic flow chart to show surface ligand (PEG or MUA) exchange for Tannic acid GNPs.

2.3 Decoration of the silica surface with GNPs

To build the covalent bridge between GNPs and silica helices, as shown in Figure 4.8, carboxylic acid groups of GNPs should be activated before they are put in contact with amine group on the modified surface of silica helices (Even if silica helices included

twisted ribbons and helical ribbons, in the section we only worked on twisted ribbons, but keep using the general name silica helices or nanohelices). The activation of the -COOH was done following well-established published process [34, 35] : 1-Ethyl-3-(3-dimethylaminopropyl) -carbodiimide (EDC) and N-hydroxysuccinimide (NHS) are the typical molecules to activate -COOH. Various doses of EDC and NHS were used in different systems. These nanoparticles possess large surface area as compared to its volume and the surface free energy is much higher than the bulk free energy[36, 37, 38] Therefore, by changing the chemical environment in solution, nanoparticles tend to aggregate easily.

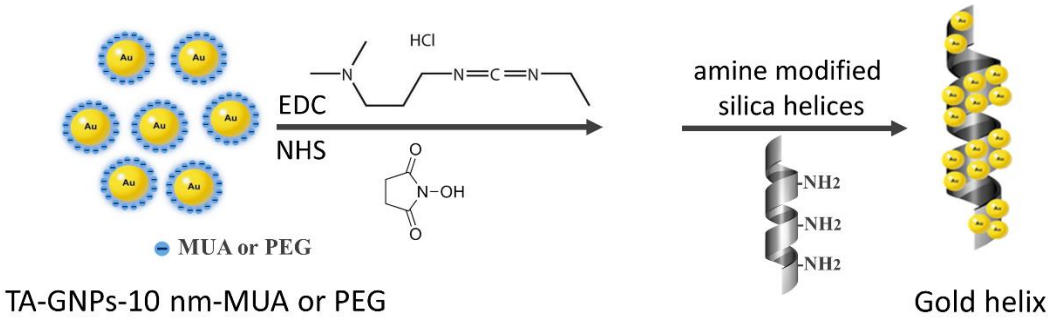

Figure 4.8 Schematic reaction of the formation of Gold helix by covalent bond.

To control the aggregation of GNPs during the -COOH activation, different conditions were optimized. Since the active intermediate formed by EDC reaction is unstable and readily hydrolyzed by water, this competing reaction with water can cleave the active intermediate to regenerate the carboxyl group[39, 40].To prevent rapid hydrolysis of the active intermediate, NHS is added to form a more stable intermediate that reacts slowly with the primary amines to form a stable amide bond. In this work, first the suitable solvent to dissolve EDC and NHS was compared between ethanol and ultrapure water. Then, fresh EDC/NHS solution and EDC/NHS solution aged 2 hours under 4 ^{o}C in EtOH or water were used for the reaction and compared in terms of GNPs aggregation. As shown in table 4.1, the suspension of TA-GNPs-10 nm-PEG in the four conditions are investigated, and globally, aged EDC/NHS water solution turn out to be the best condition to avoid the aggregations of GNPs.

EDC/NHS	12 mM/ 60 mM			
Solvent	EtOH		H_2O	
Solution aging	Fresh solution	Solution aged	Fresh solution	Solution aged
Results	☺☹☺☹	☹☹☹	☹☹☺	☺☺☺

Table 4.1 EDC/NHS solution to activate the carboxylic group on GNPs surface. (The number of faces represented the number of reactions performed)

After the proper activation solution was chosen, the activation duration (1 h to 16 h) and the reaction temperature (4 °C or 25 °C) were optimized (Table 4.2). The coverage homogeneity of the GNPs on the silica helices surface was investigated by TEM images and compared with the CD spectra of the suspension. More detailed results will be discussed in 2.4 section.

EDC/NHS	12 mM/ 60 mM					
Reaction time	1h	2h	3h	4h	5h	16h
T=4 °C	☹	☹	☹ ℹ	☹	☺ ℹ	☺
T=25 °C	☹	☹☺	☹☺ ℹ	☹	☹ ℹ	☹

Table 4.2 Covalent bond conditions study: temperature and reaction time. ℹ marked the conditions that will be discussed in this thesis .

The suitable -COOH activation solution is 12mM EDC and 60mM NHS water solution aged 5 hours under 4 °C. After merging the activation solution with prepared TA-GNPs-10 nm-PEG, with volume ratio 1:1, mixture should be kept on the shaker for 6 hours in 4 °C and washed with centrifugation (Figure 4.9). Next, 50µL of 0.6 mg/mL nanohelices-NH_2 was added to 0.5mL of activated GNPs-PEG. The mixture was then placed 10 min in a sonication bath kept at 20°C for at least one day. Samples are then washed 5 times by centrifugation (15 min, 2000 G) with EtOH, until the supernatant remains transparent. With a slow centrifuge speed (< 3000 G), free GNPs which precipitate at 21000 G, would stay in supernatant during the washing while the GNP grafted on silica helices (gold helix) would precipitate. By washing, the unreactive molecules and excess GNPs can be removed, and final gold helix could be dispersed in water, or ethanol, or the mixture of the two.

Solvent can be changed by centrifuging (15min 2000G), removing the supernatant, and adding new solvent. The final samples were kept in 20 ˚C.

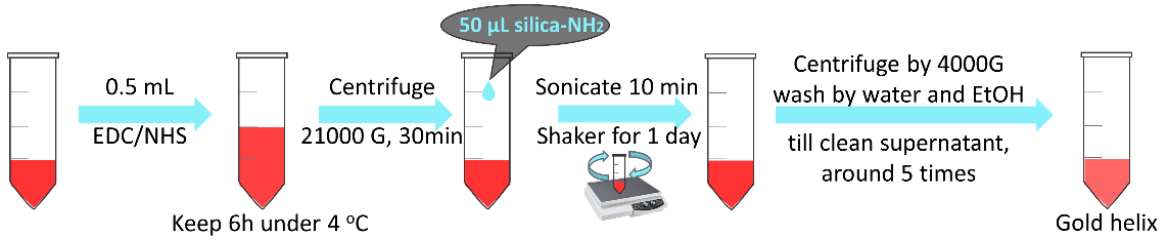

Figure 4.9 Schematic process to form gold helix with covalent bond through activating carboxylic group on the surface ligand (PEG or MUA).

2.4 Characterizations of the Gold helices

2.4.1 Characterizations of GNPs

As presented just before, GNPs with 10 nm diameter were synthesized with tannic acid and tri-sodium citrate, then underwent the ligand exchange by MUA. EDC/NHS solution was added into GNPs solution to activate the -COOH group. Optimal activation of ECD/NHS solution was aged 2 hours under 4 ºC with water as solvent, and optimized reaction temperature and duration are 4 ºC and 5 hours, to activate -COOH group without inducing GNPs aggregation. During the whole process, UV-visible spectra (Figure 4.10) were performed to indicate the absorbance of GNPs.

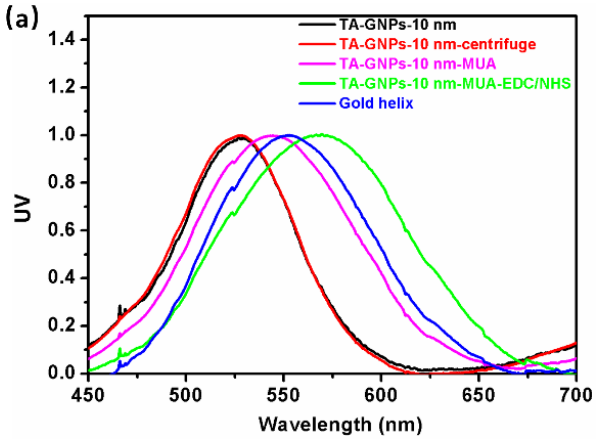

Figure 4.10 (a)UV spectra of as synthesized TA-GNPs, concentration TA-GNPs by centrifuge, TA-GNPs-10 nm- MUA, TA-GNPs-10 nm- MUA-EDC/NHS, and gold helix.

The original TA-GNPs-10 nm suspension absorbed in 528 nm with a red color, and the absorbance peak position did not shift after concentrating the solution by 4 times by

centrifugation denotated as TA-GNPs-10 nm-centrifuge. The gold colloid absorbed in larger wavelength (545 nm) after ligand exchange with MUA: even with optimal activation solution aged EDC/NHS in water, GNPs showed a red shift from 545 to 570 nm due to aggregation with color varying from red to fuchsia. However, after the addition of amine modified silica helices, absorbance peak of GNPs in Gold helices shifted into 553 nm, due to re-dispersion of GNPs. In this work, when the EDC/NHS was added, EDC reacted carboxylic acid and resulted in an active NHS-ester. By mixing amine modified silica helices, peptide bond between amine group and activated carboxyl group (NHS-ester) in organic solvent or water could be formed.

2.4.2 Characterizations of Gold helix

Gold helix formed by covalent bonds are characterized with TEM and CD spectra. Here, four cases which are labeled by red "ⓘ" in Table 4.3 are discussed as representative situations. The four conditions were EDC/NHS reaction at 1/ 4 ^{o}C-3h, 2/ 4°C-5h, 3/ 25°C-3h and 4/ 25°C-5h, and named respectively Gold helix m-n, in which m is temperature and n is reaction time. The figure 4.11 presents the representative TEM images observed in each condition.

From the Figure 4.11 (a), TEM images for Gold helix 25 ^{o}C-3h, we observe that nanoparticles are attached inhomogeneously to the silica substrate alternating thick and multilayered grafting of GNPs, and empty silica surface whereas for the Gold helix 25 ^{o}C-5h, very thick layer of GNPs are observed for which GNPs are heavily aggregated. It is difficult to distinguish the helical morphologies of the silica template. When the activation temperature was lowered to 4 ^{o}C as in Figure 4.11 (c) and (d), less aggregation was observed. For the Gold helix 4^{o}C-3h (Figure 4.11 (c)), silica twisted ribbons were not fully covered by GNPs, and bare surface of the silica helices are visible. Gold helix 4 ^{o}C-5h in Figure 4.11 (d) showed that GNPs grafted on silica twisted ribbon were distributed homogenously without agglomeration (width of Gold helix around 30 nm), which probably represent the most efficient chiral arranged and covalently grafted GNPs.

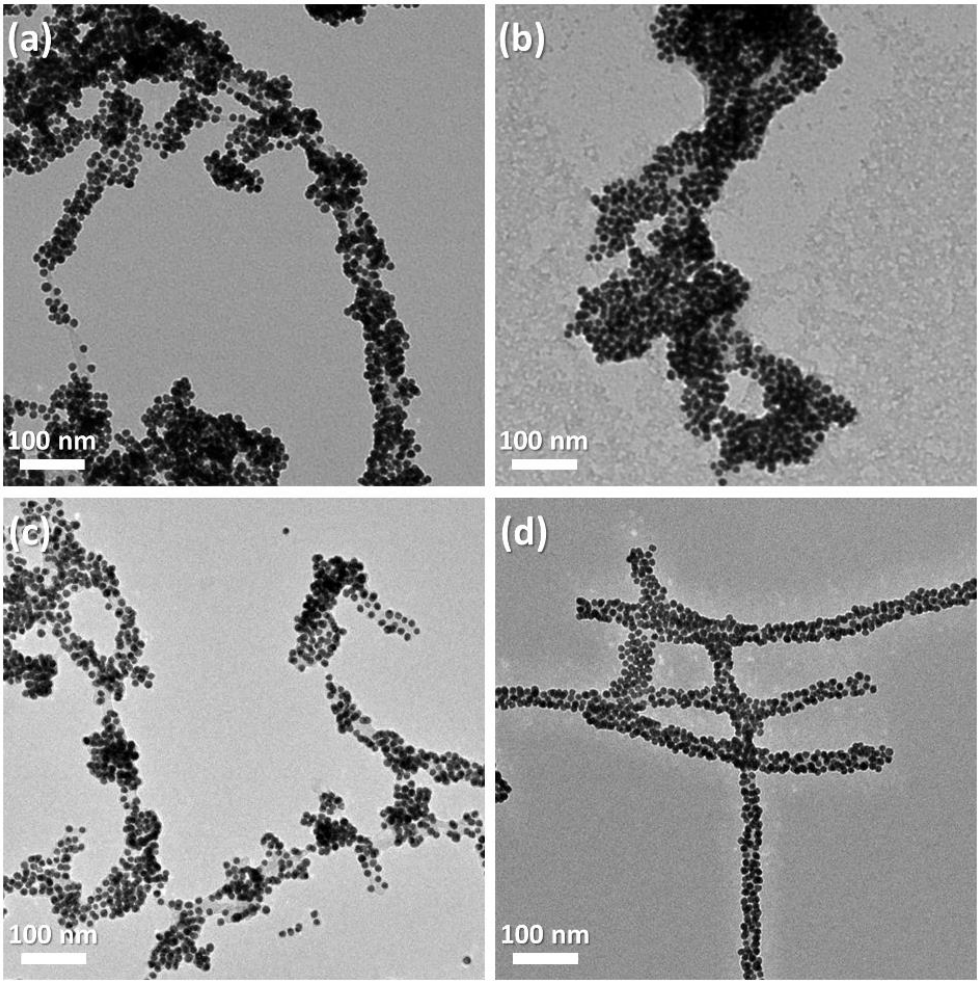

Figure 4.11 TEM images of Gold helix obtained under (a) Gold helix 25 ºC-3h, (b) Gold helix 25 ºC-5h, (c) Gold helix 4 ºC-3h and (d) Gold helix 4 ºC-5h, respectively.

To confirm the covalent bond between the acidic group of the ligands stabilizing the GNPs and silica-NH_2 surface, FT-IR measurements were performed (Figure 4.12 (a)). The black line corresponds to the Gold helix for which the GNPs and silica helices are electrostatically bound and the red one to the covalent binding. In both cases, peaks at 1710 cm^{-1} are observed corresponding to the υ(C=O) of COOH group, whereas new peaks appear for the covalently bound gold helix at 1740 cm^{-1} υ_{as}(NHS-ester C=O), 1760 cm^{-1} υ_{as}(anhydride C=O), 1820 cm^{-1} υ_{s}(anhydride C=O) indicated the active carboxylic group of EDC/NHS even after washing of the sample.[41,42] A shoulder at 1650 cm^{-1} corresponds to the vibration of amide I stretching mode of υ(C=O),[43] and the peak at 1560 cm^{-1} corresponds to N-H bend vibration of amide II.

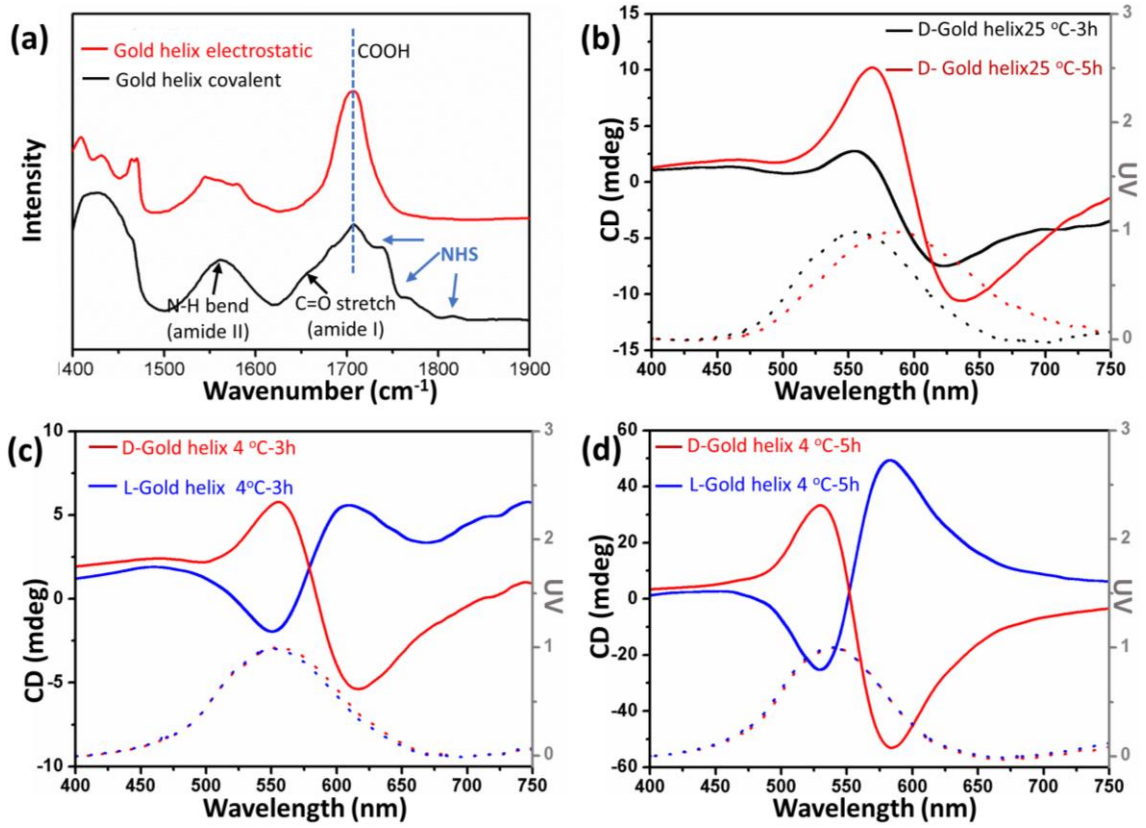

Figure 4.12 IR spectra of Gold helix (a) and CD spectra normalized by UV spectra of D-Gold helix under (b) 25 ºC-3h and 25 ºC-5h. CD spectra normalized by UV spectra of both L and D-Gold helix under (c) 4 ºC-3h and (d) 4 ºC-5h.

CD spectra for D-Goldhelix were normalized by UV absorbance, as shown in Figure 4.12 (b), comparing two reaction times 3h and 5h at 25°C and corresponding TEM are in Figure 4.11 (a) and (b). The CD spectra shown in Figure 4.11 (c) and (d) compare D-Goldhelix vs L-Goldhelix for the reaction times 3h and 5h respectively. It is clearly seen that in spite of the aggregation of GNPs, CD spectra showed that Gold helix absorb with opposite signs for left and right circular polarized lights from 450 to 750 nm. Figure 4.12 (c) are CD and UV spectra of Gold helix 4ºC-3h, corresponding TEM Figure 4.11(c). UV spectra peaks were at 552 nm, and CD spectra showed opposite signal for L and D helix. For the optimal condition Gold helix 4ºC-5h (Figure 4.11(d), TEM image), CD spectra showed higher intensity than 3h samples, and their absorbance peaks were at 545 cm^{-1}. After various trails and characterizations, we could conclude that longer the reaction time (5h), better the grafting and more GNPs were attached on the silica surface, furthermore,

with low temperature (4°C), we could decrease the quantity of the GNPs non-organized aggregation.

2.4.3 Influence of the silica nanohelix morphology

To adjust the CD spectra of Gold helix, silica twisted ribbons with different dimensions were synthesized. As discussed in chapter 3, depending on the aging time or enantiomeric excess (ee) of Gemini tartrate, various chiral morphologies with tunable pitch and width could be obtained. Here, gemini Tartrate with ee=60%, 80% and 90% were studied. The transcription procedures for 60% 80% and 90% twisted ribbons are same as pure enantiomer twisted ribbons, except for the washing steps, where "soft start" and "soft stop" mode of the centrifuge had to be applied. Indeed, for low ee, the organic multi-bilayers self-assembly becomes larger and thicker, therefore, the distance between the two silica walls after the transcription becomes large compared to the silica walls thickness, making these structures much more fragile. Silica twisted ribbons with different dimensions were obtained after the transcription of organic Gemini Tartrate self-assemblies with ee=60% and ee=80% aging 2 days, as shown in Figure 4.13(a) and (b). The morphologies of twisted ribbons are much more heterogeneous than the ones with ee=100%, and the pitches of two samples calculated by statistics are 498.86 ± 354.71 nm and 199.16 ± 45.83 nm for 60% and 80% respectively. With 2d aging time, Gemini Tartrate with ee = 90%, self-assembled into helical ribbons with pitch 64.57 ± 8.2 nm as Figure 4.13 (c).

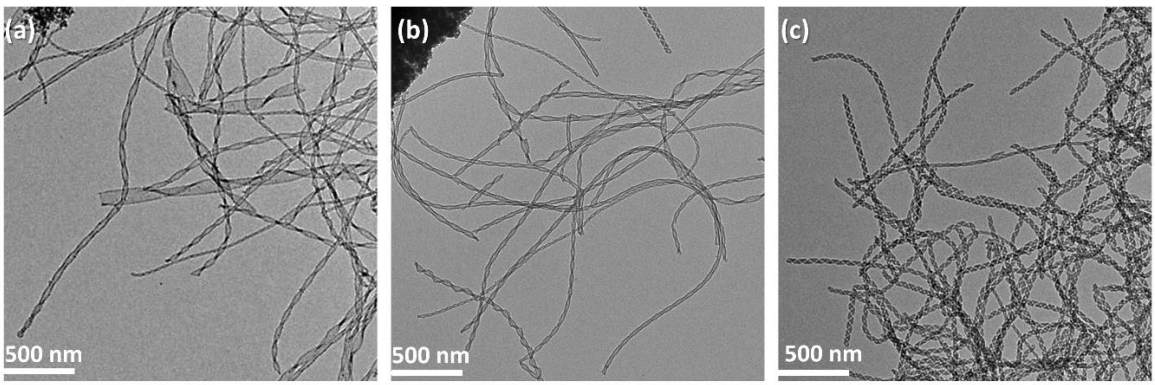

Figure 4.13 TEM images silica twisted ribbons obtained from (a) ee = 60%, (b) ee = 80% and (c) ee = 90% Gemini tartrate.

GNPs are grafted on the silica surface covalently, as shown in Figure 4.14. From the images (a), (b) and (c), well-defined big twisted ribbons fully covered by GNPs can be prepared. However, as shown in Figure 4.14 (d) and (e), the presence of much smaller pitch helices also co-existed for Gold helix-60% and Gold helix-80% respectively, revealing the much higher heterogeneity of the helical dimensions. The morphologies of Gold helix 90% as presented in Figure 4.14(c) and (f) were more homogeneous than 60% and 80%.

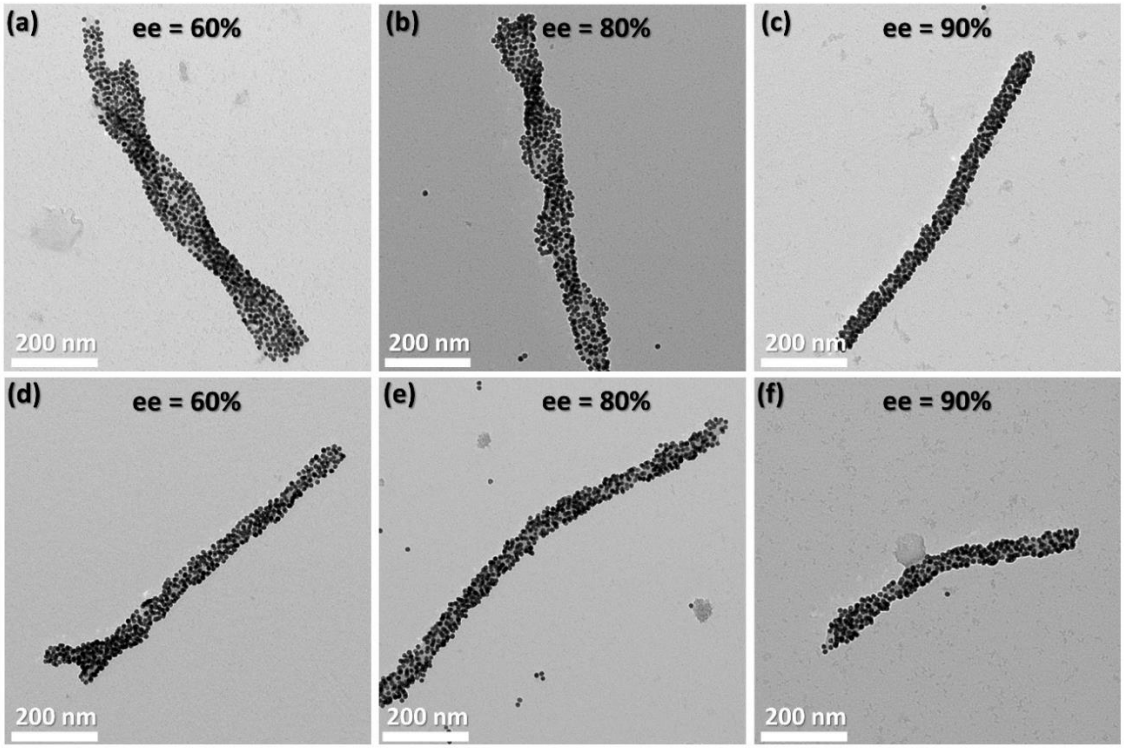

Figure 4.14 TEM images of Gold helix, GNPs grafted on big silica twisted ribbons, the original organic Gemini tartrate are (a),(d) ee = 60%, (b),(e) ee = 80% and (c),(f) ee = 90%.

Although CD and UV measurements were performed for these Goldhelices with ee = 60% and 80%, the results were not conclusive in terms of reproducibility. There can be several reasons for this: 1) The dimensions of twisted ribbons with ee ＜ 0.8 16-2-16 gemini tartrate are heterogeneous. 2) Larger silica twisted ribbons are more fragile than the small ones, and they can be broken easily with washing steps. 3) Large Goldhelices (Figure 4.14 a) precipitated more easily than the small ones (Figure 4.14 d), which may result in the CD measurements only representing the small Goldhelices.

3. Chiroptical studies

CD spectrum is measured as the differential absorbance of left and right circularly polarized light, which represent two possible spin angular momentum states for a photon. Basically, CD is used to detect whether the objects have asymmetric absorption.

3.1 Analysis of chiral signals of Gold helix.

Electronic circular dichroism is defined as the difference

$$\Delta A = A^l - A^r \qquad (1)$$

where A^l and A^r are the absorptions of left and right circularly polarized light. For historical reasons, the output of CD instruments is usually measured as ellipticity θ (in mdeg), related to CD through $\Delta\theta$ (mdeg) = 32982 ΔA.[44] In analogy to Beer-Lambert law, one can define a molar quantity

$$\Delta\varepsilon = \varepsilon^l - \varepsilon^r = \frac{\Delta A}{\mathrm{c{\cdot}L}} \qquad (2)$$

which is dependent of concentration *c*, expressed in mol/L, and of pathlength *L*, expressed in cm.

The definition of equation (1) tells us that *CD* can be measured only in correspondence to absorption bands. It is worth observing that *CD* is a signed quantity, because, ε^l may be smaller or larger than ε^r (and consequently A^l and A^r); it is easy to show that for each absorption band, the *CD* signals of two enantiomers have opposite signs.

Normalized optical activity of chiral system can be defined through the g factor[45]:

$$\mathrm{g} = \frac{\Delta\varepsilon}{\varepsilon} = \frac{\varepsilon^l - \varepsilon^r}{\varepsilon} = \frac{A^l - A^r}{A} = \frac{\Delta\theta}{32982A} \qquad (3)$$

where, ε^l and ε^r are the molar absorption coefficients for left and right polarized light, $\Delta\varepsilon$ and ε are the molar circular dichroism and molar absorptivity, A is the absorbance of non-polarized light (equivalent with the average of A^l and A^r). The dimensionless g-factor allow us to compare the chiroptical properties of various sample independently of the concentration.

CD spectra of three groups of Goldhelices Gold helix were measured (Figure 4.12), from which $\Delta\theta$ and *A* could be read directly, and their g-factors are calculated by equation (3).

G factors for left-Gold helix 25 ^{o}C-3h, left-Gold helix 25 ^{o}C-5h, right and left -Gold helix 4 ^{o}C-3h, and right and left -Gold helix 4 ^{o}C-5h were calculated in Table 4.3. The corresponding TEM images are shown in Figure 4.11 and the CD spectra in Figure 4.12. The ideal sample preparation conditions were the samples L-Gold helix 4 ^{o}C-5h and D-Gold helix-4 ^{o}C-5h, where GNPs are grafted on the silica surface homogenously and distributed uniformly without aggregation. G factors were 2.6×10^{-3} and 2.3×10^{-3} for right- and left-Gold helix respectively, which are 10 times higher than the Goldhelices with electrostatic binding[24] (3×10^{-4}) from our previous report, and the literatures.[46]

Temperature	**25 ^{o}C**		**4 ^{o}C**	
Reaction time	3h	5h	3h	5h
Handedness	left	left	right / left	right / left
g-factor	3.13×10^{-4}	6.25×10^{-4}	$2.30\times10^{-4}/3.39\times10^{-4}$	$2.61\times10^{-3}/2.27\times10^{-3}$

Table 4.3 Gold helix g-factor calculated from the CD spectra in Figure 4.12.

3.2 Optical studies on the isotropic 2D material

The main advantage of the covalent Gold helices regarding the electrostatic one is its stability both in aqueous and organic solvent. The samples can be dried on different surfaces while keeping the GNPs organization on the helix surface. Therefore, simple drop-casting of Gold helix solution on the glass can lead to isotropic 2D materials. In this work, we studied two surface density coverage: (1) 10 µL D-Gold helix suspension in EtOH was deposited on the glass and dried (low density sample). (2) The deposition presented in (1) is repeated 5 times (waiting for the complete sample drying each time) (high density sample). CD measurements (Figure 4.16), and SEM images (Figure 4.17 a b and d c) are utilized to characterize these two materials.

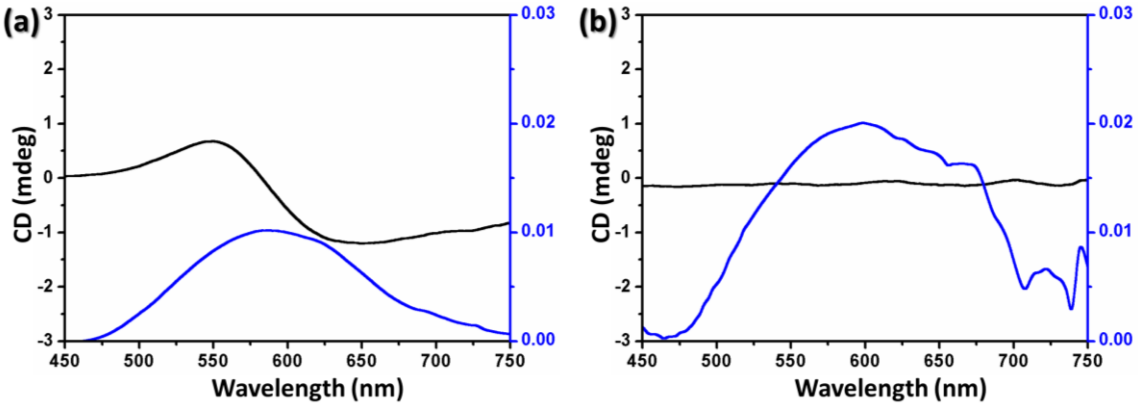

Figure 4.16 CD spectra and UV spectra of isotropic 2D Gold helix with low concentration (a), and high concentration(b).

CD spectra of 1 drop vs 5 drops deposition of Goldhelix on a surface are shown in Figure 4.16. 1-time deposition sample after drying showed the same CD pattern as the Goldhelices in suspension, and g-factor didn't show any variation. However, for the 5 times deposition sample, Figure 4.16 (b), no CD signal was detected. In spite of UV spectra (Figure 4.16 grey line) which showed the red shift from 560 nm (low concentration) to 600 nm (high concentration).

To investigate the difference of the Gold helix morphology features between the two samples, SEM images of these samples are shown in Figure 4.17.

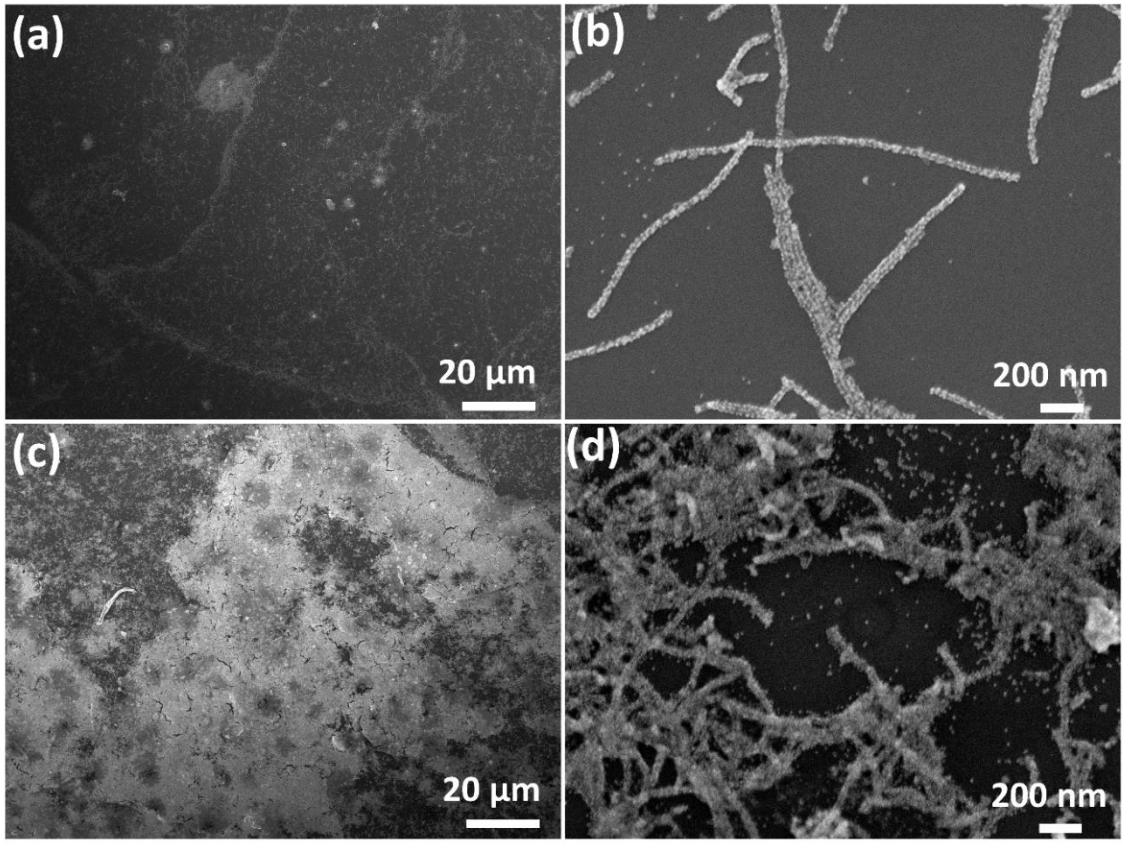

Figure 4.17 SEM images of isotropic 2D Gold helix with low concentration (a), (b) and high concentration (c), (d).

SEM under different magnifications are performed to observe the morphologies of nanoobjects in these two samples. We can clearly observe that in low concentration Figure 4.17 (a) and (b) (high resolution SEM), individual elongated objects are deposited on the glass surface and the GNPs are densely attached on the silica surface whereas in high concentration Figure 4.17 (c) and (d) these nanoobjects are merged to form island-like aggregations, the Gold helices are entangled and overlapped with each other. This observation is coherent with the UV absorbance shift to 600 nm observed in Figure 4.16 (b) which can be induced by the aggregation of the Goldhelices implying a coupling of the GNPs between the different helices. Indeed, the chiral response of Gold helix came from the chiral arrangement of GNPs, and the plasmonic effect between closing GNPs (Figure 4.18 a and c). When the distance of GNPs from two helices are too far to have SPR effect, as indicated by the green dash line in Figure 4.18 (c), only the information on the interaction between the GNPs from the same helix can be defined. However, when two Gold helices touch with each other, SPR could happen between the GNPs attached on different helices.

When this aggregation was excessive, like in Figure 4.17 (c) and Figure 4.18 (b), the SPR between GNPs from different helices counteracted SPR between GNPs from one helix, which is almost equivalent to a free GNPs, as red arrows showing in Figure 4.18 (d).

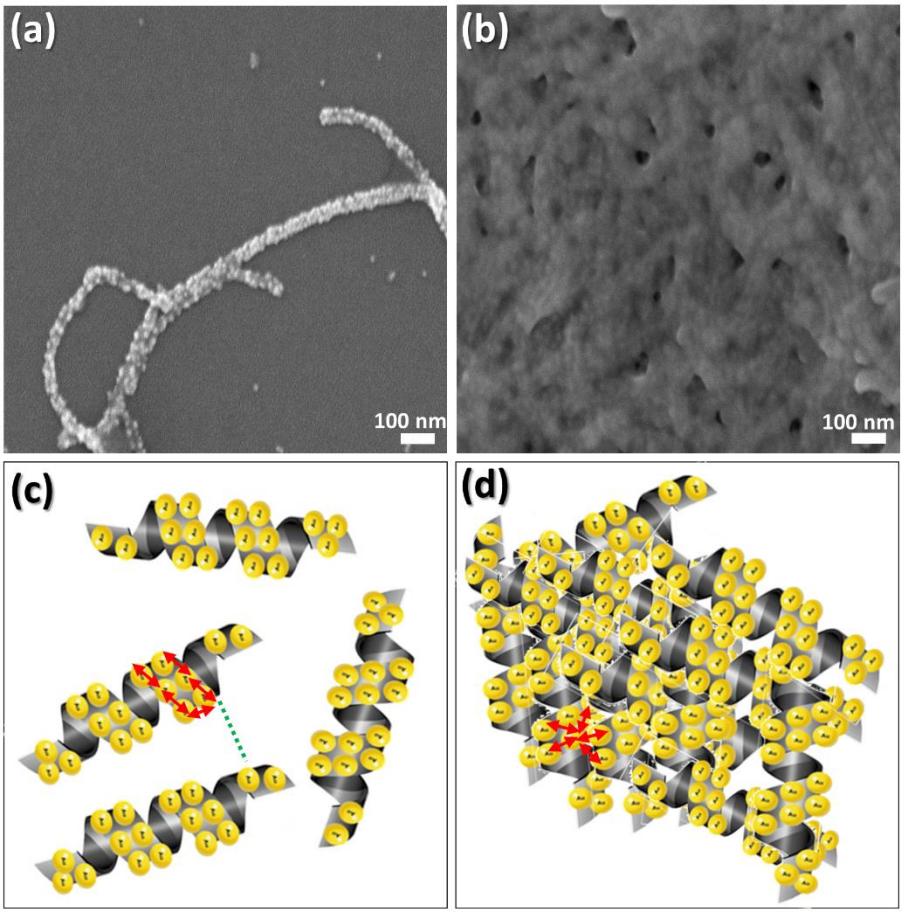

Figure 4.18 SEM images isotropic 2D Gold helix with low concentration (a) and high concentration (b) in under ultra-high resolution. (c) and (d) are schematic Goldhelix for (a) and (b), respectively. The red arrows in (c) and (d)show the possible plasmon resonance between GNPs, and the green dash line in (c) indicates the distance between particles from two helices are too far to have SPR effect.

4. Conclusion

In this chapter, Goldhelices are prepared with covalent bond between silica nanohelices and GNPs. This strong link induces a real increase of the g-factor 10 times compared to the Goldhelices made via electrostatic interactions. This value is also very high compared to the chiroptical activity reported in literature for helicoidal organization of GNPs. The covalent bond between silica nanohelices and GNP also lead to more homogeneous coverage, and finally to the increase of the g factor. With various enantiomer

excess of Gemini tartrate, we tried to tune the morphology of the Goldhelices. Unfortunately, the results on the chiroptical properties were not conclusive, probably because of the strong heterogeneity and the lack of reproducibility. If this point could be improved, the chiroptical results would maybe be more interesting. Finally, the Goldhelices were deposited on 2D substrates. Thanks to the covalent bond, we could prepare 2D isotropic Gold helices surfaces, that kept same chiroptical property as the ones in suspension. However, the aggregations of Gold helix are formed when large amount of Gold helices is deposited on the confined area, which leads to the loss of chiral response.

References

1. M.-C. Daniel and D. Astruc, Gold nanoparticles: assembly, supramolecular chemistry, quantum-size-related properties, and applications toward biology, Catalysis, and Nanotechnology, Chem. Rev., 2004, 104, 293-246.

2. D.A. Weitz and M. Oliveria, Fractal structures formed by kinetic aggregation of aqueous gold collois, Phys. Rev. Lett., 1984, 52(16),1433-1436.

3. Y. Zhang, W. Chu, A. D. Foroushani, H. Wang, D. Li, J. Liu, C. J. Barrow, X. Wang and W. Yang, New gold nanostructures for sensor applications: a review, 2014, 7, 5169-5201.

4. L. Dykmana and N. Khlebtsov, Gold nanoparticles in biomedical applications: recent advances and perspectives, Chem. Sco. Rev., 2012, 41, 2256-2282.

5. S. Gong, W. Schwalb, Y. Wang, Y. Chen, Y. Tang, Y. Si, B. Shirinzadeh and W. Cheng, A wearable and highly sensitive pressure sensor with ultrathin gold nanowires, Nature, 2014, 5, 3132.

6. M. Haggui, M. Dridi, J. Plain, S. Marguet, H. Perez, G. C. Schatz, G. P. Wiederrecht, S. K. Gray and R. Bachelot, Spatial confinement of electromagnetic hot and cold spots in gold nanocubes, ACS Nano, 2012, 6(2), 1299-1307.

7. S. Sengupta and X. Shi, Recent advances in asymmetric gold catalysis, ChemCatChem, 2010, 2, 609-619.

8. Z. Han, H. Xiao, X. Chen and L. Gong, Consecutive intramolecular hydroamination/asymmetric transfer hydrogenation under relay catalysis of an achiral gold complex/chiral Bronsted acid binary system, J. Am. Chem. Soc., 2009, 131, 9182-9183.

9. J. K. Gansel, M. Thiel, M. S. Rill, M. Decker, K. Bade, V. Saile, G. von Freymann, S. Linden and M. Wegener, Gold helix photonic metamaterial as broadband circular polarizer, Science, 2009, 5947(325): 1513-1515.

10. F. Zhu, X. Li, Y. Li, M. Yan and S. Liu, Enantioselective circular dichroism sensing of cysteine and glutathione with gold nanorods, Anal. Chem., 2014, 87, 357-361.

11. J. Nan and X. Yan, A circular dichroism probe for l-cysteine based on the self-assembly of chiral complex nanoparticles, Chem. Eur. J., 2010, 16, 423-427.

12. W. Liu, Z. Zhu, K. Deng, Z. Li, Y. Zhou, H. Qiu, Y. Gao, S. Che and Z. Tang, Gold nanorod@chiral mesoporous silica core-shell nanoparticles with unique optical properties, J. Am. Chem. Soc., 2013, 135, 9659-9664.

13. P. W. K. Rothemund, Folding DNA to create nanoscale shapes and patterns, Nature, 2006, 440, 297-302.

14. S. Douglas, H. Dietz, T. Liedl, B. Hogberg, F. Graf and W. M. Shih, Self-assembly of DNA into nanoscale three-dimensional shapes, Nature, 2009, 459, 414-418.

15. A. Kuzyk, R. Schreiber, Z. Fan, G. Pardatscher, E. Roller, A. Hogele, F. C. Simmel, A. O. Govorov and T. Liedl, DNA-based self-assembly of chiral plasmonic nanostructures with tailored optical response, Nature, 2012, 483, 311-314.

16. Z. Fan and A. O. Govorov, Plasmonic circular dichroism of chiral metal nanoparticle assemblies, Nano Lett., 2010, 10(7), 2580-2587.

17. W. Yan, et al., Self-assembly of chiral nanoparticle pyramids with strong R/S optical activity, J. Am. Chem. Soc., 2012, 134, 15114-15121.

18. Z. Fan, L. Xu, C. Xu, W. Ma, H. Kuang, L. Wang and N. A. Kotov, Chiral nanocrystals: plasmonic spectra and circular dichroism, Nano Lett., 2012, 12, 3283-3289.

19. C. Gautier and T. Burgi, Chiral inversion of gold nanoparticles, J. Am. Chem. Soc, 2008, 130, 7077-7084.

20. A. Guerrero-Martinez, B. Auguie, J. L. Alonso-Gomez, Z. Dzolic, S. Gomez-Grana, M. Zinic, M. Magdalena Cid and L. M. Liz-Marzan, Intense optical activity from three-dimensional chiral ordering of plasmonic nanoantennas, Angew. Chem. Int. Ed, 2011, 50, 5499-5503.

21. H. Qi, K. E. Shopsowitz, W. Y. Hamad and M. J. MacLachlan, Chiral nematic assemblies of silver nanoparticles in mesoporous silica thin films, J. Am. Chem. Soi., 2011, 133, 3728-3731.

22. Q. Zhang, J. Gu, L. Zhang and J. Lin, Diverse chiral assemblies of nanoparticles directed by achiral block copolymers via nanochannel confinement, Nanoscale, 2019, 11, 474-484.

23. T. Delclos, C. Aime, E. Pouget, A. Brizard, I. Huc, M. Delville and R. Oda, Individualized silica nanohelices and nanotubes: tuning inorganic nanostructures using lipidic self-assemblies, Nano lett., 2008, 8(7), 1929-1935.

24. J. Cheng, G. Le Saux, J. Gao, T. Buffeteau, Y. Battie, P. Barois, V. Ponsinet, M. Delville, O. Ersen, E. Pouget and R. Oda, Gold helix: gold nanoparticles forming 3D helical superstructures with controlled morphology and strong chiroptical property, ACS Nano, 2017, 11, 3806-3818.

25. K. Sugiyasu, S. Tamaru, M. Takeuchi, D. Berthier, I. Huc, R. Oda and S. Shinkai, Double helical silica fibrils by sol-gel transcription of chiral aggregates of gemini surfactants, Chem. Commun., 2002, 1212-1213.

26. Y. Ono, K. Nakashima, M. Sano, Y. Kanekiyo, K. Inoue, S. Shinkai, M. Sano and J. Hojo, Organic gels are useful as a template for the preparation of hollow fiber silica, Chem. Commun., 1998, 14, 1477-1478.

27. T. Delclos, C. Aime, E. Pouget, A. Brizard, I. Huc, M. Delville and R. Oda, Individualized silica nanohelices and nanotubes: tuning inorganic nanostructures using lipidic self-assemblies, Nano lett., 2008, 8(7), 1929-1935.

28. Y. Okazaki, J. Cheng, D. Dedovets, G. Kemper, M. Delville, M. Durrieu, H. Hihara, M. Takafuji, E. Pouget and R. Oda, Chiral colloids: homogeneous suspension of individualized SiO_2 helical and twisted nanoribbons, ACS Nano, 2014, 8(7), 6863-6872.

29. E. Grineval, J.-M. Basset, F. Lefebvre, A novel approach to prepare well-defined silica-supported polyoxometalate species by reaction with a chlorinated support, Inorg. Chem., 2013, 902192.

30. R. Anwander, C. Palm, J. Stelzer, O. Groeger and E. Engelhardt, Silazane-silylation of mesoporous silicates: towards tailor-made support materials, Stud. Surf. Sci. Catal., 1998, 117, 135-142.

31. T. H. Galow, A. K. Boal and V. M. Rotello, A building block approach to mixed-colloid systems through electrostatic self-organization, Adv. Mater., 2000, 12, 576-579.

32. R. Tamoto, S. Lecomte, S. Si, S. Moldovan, O. Ersen, M. Delville and R. Oda, Gold nanoparticle deposition on silica nanohelices: A new controllable 3D substrate in aqueous suspension for optical sensing, J. Phy. Chem. C, 2012, 116(43), 23143-23152.

33. H. Muhlpfordt, The preparation of colloidal gold particles using tannic acid as an additional reducing agent, Experientia, 1982, 38, 1127-1128.

34. C. Wang, Q. Yan, H. Liu, X. Zhou and S. Xiao, Different EDC/NHS activation mechanisms between PAA and PMAA brushes and the following amidation reactions, Langmuir, 2011, 27, 12058-12068.

35. S. Sam, L. Touahir, J. S. Andresa, P. Allongue, J.-N. Chazalviel, A. C. Gouget-Laemmel, C. Henry de Villeneuve, A. Moraillon, F. Ozanam, N. Gabouze and S. Djebbar, Semiquantitative study of the EDC/NHS activation of acid terminal groups at modified porous silicon surfaces, Langmuir, 2010, 26(2), 809-814.

36. E. M. Hotze, T. Phenrat and G. V. Lowry, Nanoparticle aggregation: challenges to understanding transport and reactivity in the environment, J. Environ. Qual., 2009, 39, 1909-1924.

37. J. H. Adair, Colloidal lessons learned for dispersion of nanosized particulate suspension, Techna Group Srl., 2005, 93-145.

38. W. Luo and W. Hu, Gibbs free energy, surface stress and melting point of nanoparticle, Physica B, 2013, 425, 90-94.

39. Microsphere coupling-two-step EDC/sulfo NHS covalent coupling procedure for estapor carboxyl-modified dyed microspheres, Merck Millipore, AN1260EN00_MM.

40. C. Wang, Q. Yan, H. B. Liu, X. H. Zhou and S. J. Xiao, Different EDC/NHS avtivation mechanisms between PAA and PMAA brushed and the following amidation reaction, Langmuir, 2011, 27, 10258-12068.

41. B. L. Frey and R.M. Corn, Covalent attachment and derivatization of poly(l-lysine) monolayers on gold surfaces as characterized by polarization−modulation FT-IR spectroscopy, Anal. Chem., 1996, 68(18), 3187-3193.

42 . S. Xiao, S. Brunner and M. Wieland, Reactions of surface amines with heterobifunctional cross-linkers bearing both succinimidyl ester and maleimide for grafting biomolecules, J. Phys. Chem. B, 2004, 108(42), 16508-16517.

43. D. Lin-Vien, N. Colthup, W. Fateley and J. Grasselli, The handbook of infrared and roman characteristic frequencies of organic molecules, Academic press: San Diego, 1991.

44. An introduction to circular dichroism spectroscopy: https://www.chem.uci.edu/~dmitryf/manuals/Fundamentals/CD%20spectroscopy.pdf

45. N. Berova, L. Di Bari and G. Pescitelli, Application of electronic circular dichroism in configurational and conformational analysis of organic compounds, Chem. Soc. Rev., 2007, 36, 914-931.

46. N. L. Sharma, Nondipole optical scattering from liquids and nanoparticles, Phys. Rev. Lett., 2007, 98(21), 217402.

Chapter 5. Hierarchical assembly of helices towards a novel chiral material for optics

Contents

1. Introduction

Controlled alignment of nanoobjects is one key prerequisite in materials science. In this chapter, we present how the individual chiral elements (silica helices and Goldhelices), shown in Chapter 4 can be hierarchically organized into 2D or 3D materials. Three driving forces are the main factors inducing organization in the numerous possible assembly techniques[1,2]: shear force, evaporation (entropy), and mechanical stretching. Sometimes, external forces such as magnetic or electrical fields, or mechanical stretching,[3] can be applied to induce the organization of nano components. The Langmuir-Blodgett[4] technique can sometimes be applied to align molecules or nanoobjects if they have a preferential polarity. Among all of these methods, we have tested three techniques: Grazing Incident Spraying (GIS) (shear forces), dip-coating (evaporation forces) and evaporation guided inside microfluidic channels (evaporation forces). We have tried to organize the silica helices with these three techniques in order to span different organization possibilities and apply them to the Goldhelices in a second step. Because of lack of time, only the GIS has been transferred to the Goldhelices.

The work with these three alignment techniques has been performed by myself under the supervision of three collaborators in different laboratories: Institut Charles Sadron (*Dr. Matthias Pauly* and *Dr. Gero Decher*, **GIS**), Institut de Chimie de la Matière Condensée de Bordeaux (ICMCB, *Dr. Glenna L. Drisko*, **Dip-coating**) and the Laboratory of the Future/CNRS-Solvay-Univ. Bordeaux (*Dr. Jacques Leng*, **Microfluidics**). In this chapter, theoretical calculation of helice deposition density through the dip-coating technique performed by *David Gonzalez-Rodriguez* (Institut Jean Barriol, Université de Lorraine). Mueller matrix ellipsometry measurements of Goldhelices and related calculations were developed by *Yann Battie* (Insititut Jean Barriol, Université de Lorraine).

2. Microfluidics

2.1 Overview of the organization *via* microfluidics

Microfluidics is the science and technology of systems that process or manipulate small (10^{-9} to 10^{-18} liters) amounts of fluids, using channels with dimensions of tens to

hundreds of micrometers. Microfluidics has been able to exploit certain fundamental differences between the physical properties of fluids moving in large channels and those travelling through micrometer-scale channels.[5, 6, 7] It offers new capabilities in the control of molecular concentrations through space and time.[8] There are microchannels that serve as pipes, and other structures that form valves,[9] mixers, [10] and pumps,[11] all of which are essential elements to microchemical factories on a chip. Microfluidic technologies can be used to align fiber-like materials. P. Lee et al.[12] reported the alignment of collagen fibers by microfluidics, and A. D. Van der Meer[13] aligned actin filaments in endothelia cells with a microfluidic assay. In these systems, liquid flow generated shear in the microchannels with controllable flow rates, which induced collage fiber or actin filament alignment parallel to the channel.

In this thesis, a microfluidic evaporator without an outlet was used to align the silica helices. Solvent evaporation through membranes is the only factor that drives the alignment of silica helices.

2.2 Alignment of silica helices *via* microfluidics

A microfluidic evaporator was fabricated as described in the literature[14] and the design of the evaporator was described in the Chapter 2. The dimensions of the channels are 15 μm in height, 80 μm in width and 5000 μm length. The suspension of nanoobjects are manually injected by syringe, and during continuously filling with the solution, ethanol evaporates through the thin PDMS membrane (Figure 5.1). This evaporation lowered the pressure of the solution in the channel, which brought compensating flow filling in the channels. More and more nanoobjects accumulate in the channel, and this is similar to concentration at the boundary of a drying droplet,[15] generating motion through convective flows and shear in the concentration zone. The thickness of the PDMS membrane and the dimensions of the channels are important factors that affect evaporation.

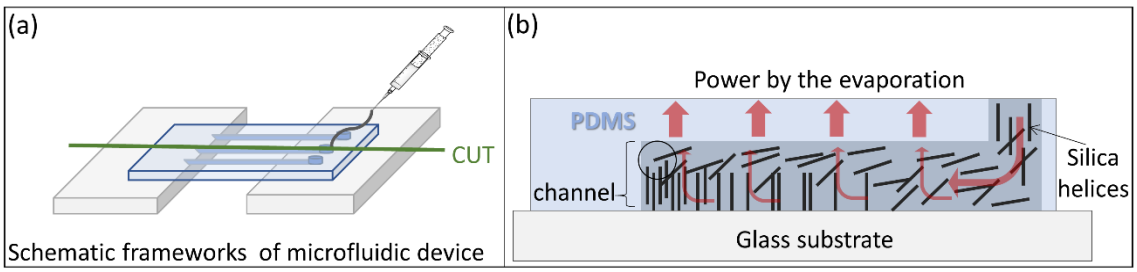

Figure 5.1 (a) Schematic framework of a microfluidic evaporator, and (b) cross view of one channel (green line in a), in which liquid flow and evaporation are marked by red arrows.

As a preliminary test, silica spherical nanoparticle suspensions in ethanol were injected in the channels. Figure 5.2 shows SEM images of compacted silica nanoparticles under different magnifications. Rectangular blocks consisting of silica nanoparticles formed, and densely assembled silica sphere particles packed in the confinement of the extremity of the channel (Figure 5.2 b and c). In Figure 5.2 (b), a flat surface made of silica spherical particles is observed, where silica particles are packed tightly. Figure 5.2 (c) shows the edge of the condensed materials, and we conclude that compact silica is confined by the microfluidic channels.

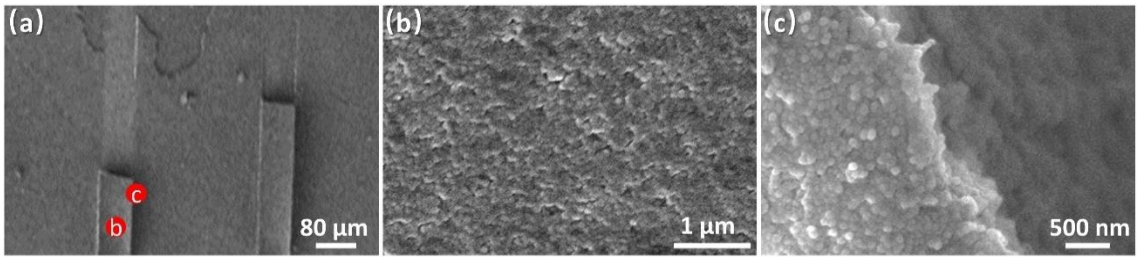

Figure 5.2 SEM images of silica spherical particles assembled by microfluidics at low (a) and high (b), (c) magnifications. (b) and (c) are the magnified images of the red dots indicated in (a).

Silica helices dispersed in ethanol were injected into the microfluidic channels. Figure 5.3 (a) shows that the silica helices were densely assembled within the PDMS channels. Picture 5.3 (b) showed the silica helices outside the dense area, where fiber like materials could be found, which indicated a random distribution of silica helices. However, the magnified SEM image corresponding to position (c) shows that at the end of the channel only dots are observed, which may be attributed to the tips of the helices (Figure 5.3 c). The observation suggests that the silica helices were perpendicularly orientated to the PDMS membrane as illustrated in Figure 5.4.

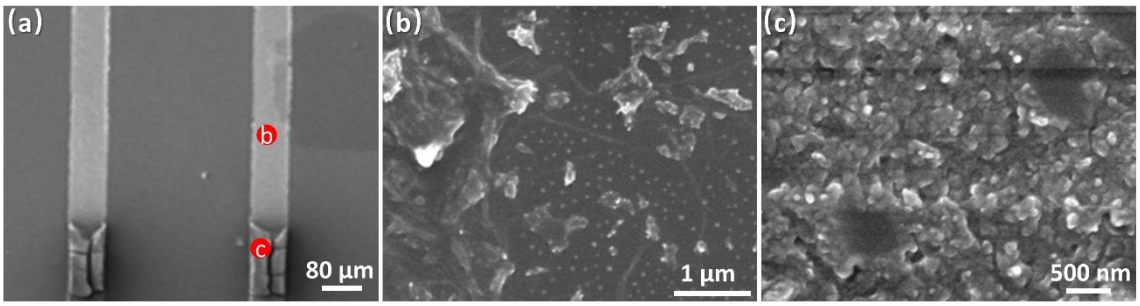

Figure 5.3 SEM images of silica helices assembled by microfluidics at low (a) and high (b), (c) magnifications. (b) and (c) are the magnified images of the red dots indicated in (a).

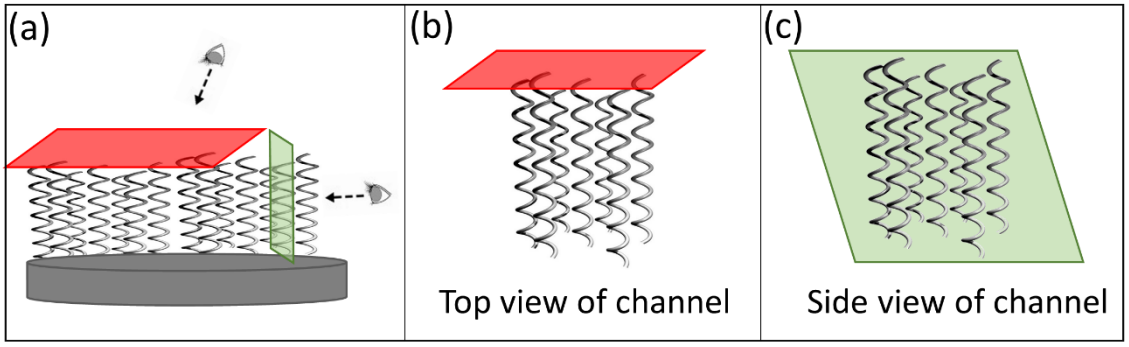

Figure 5.4 (a) Scheme of aligned silica helices on the substrate, top view (b) and side view (c) of the oriented silica helice forest.

Further observation and investigations are required to confirm this orientation and figure out the mechanism of this alignment. Particularly, a cross sectional view would confirm these preliminary results. Because of the complexity of the process and a lack of time, I did not study deeper these structures even if this dense packing would be particularly interesting and original.

3. Dip-coating

3.1 Dip-coating technique

Dip-coating does not require heavily sophisticated and expensive equipment or a pre-treatment of substrates and is achieved simply by withdrawing the substrates under controlled speed. Dip-coating has been applied to many industrial fields, e.g. in the preparation of ceramics, films,[16] and hybrid materials[17]. Since an early study by Schunk, Hurd and Brinker 20 years ago,[18] the mechanistic of this technique still continues to intrigue researchers. During evaporation, complex interactions are present between the

solutes, solution and the surrounding environment at the interface as well as in the bulk, affected by various conditions including chamber temperature and humidity, solution concentration, surface tension, viscosity and withdrawal speed. When this occurs in the presence of spherical particles, the particles are concentrated at the drying line by convective transport driven by evaporation, and then tightly packed due to interparticle capillary forces.[19, 20, 21] Not only do nanoparticles become pinned to the surface by the meniscus, but the meniscus also becomes pinned to the surface by nanoparticles. At low speeds (Figure 5.5 a), the meniscus becomes stretched as the drying line slowly moves farther away from the bulk solution as the substrate is withdrawn. As long as the meniscus is pinned to the drying line, more particles can accumulate in the drying zone, leading to a higher concentration of particles than that of the bulk solution. At some point, the meniscus is so stretched that it overcomes the particle pinning forces and quickly jumps to its expected position, where it is pinned again by a fresh set of deposited particles. This process is repeated and is called the stick-slip phenomenon and can be used to produce regular and controllably spaced linear arrays of particles.[22] However, at high speeds (Figure 5.5 b), there is no stick-slip phenomenon, and evaporation dominates over capillary feeding, driving recirculation currents in what we call the draining regime.

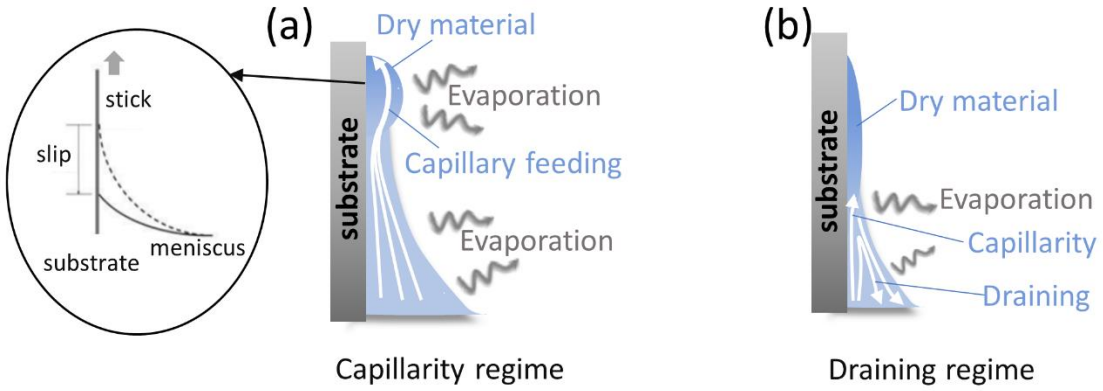

Figure 5.5 Schematic illustration of dip-coating at low and fast withdrawal speeds corresponding to capillarity regime (a) and draining regime (b).

Spheres or small aspect ratio particles can roll more easily than non-round objects with large aspect ratio and thus it is relatively easy to process them into dense assemblies. Particle-substrate and particle-particle electrostatic interaction repulsions and van der

Waals interaction forces balance can prevent tight particle packing. The movement of the suspensions of particles with more complex shapes are plagued by more complex interparticle interactions and higher drag forces along the substrate, substantially increasing the difficulty of obtaining well-organized mono- or multilayered structures. Once evaporation thins the meniscus to the thickness of the nano-object diameter, the objects can no longer significantly diffuse or rotate and can only slide closer to or away from nearby objects. Also, the convective vs shear gradient forces can induce orientations of nano-particles parallel and perpendicular to the contact line (meniscus).[16,20,23,24] Finally, the physical-chemistry properties of the solution (surface tension, viscosity, pH, etc.), as well as the physical experimental parameters like the temperature and the withdrawal speed, can all play a crucial role in surface patterning. These forces can control the formation of nematic-like phases via entropy gain in the concentrated and confined zones,[25] as it has been shown with carbon nanotubes,[26] ZnO nanorods,[27] gold nanorods[28] or biological filaments.[16,23]

3.2 Alignment of silica helices via dip-coating

In this section, evaporation-induced self-assembly of silica helices is addressed by dip-coating. Because it is well known that this technique is affected by the solution properties (viscosity, colloidal stability, colloidal concentration, etc.) and the evaporation rate, this convective assembly of silica helices is studied by examining the effect of polymer additives, silica helix concentration, withdrawal speed and chamber temperature. These different parameters are studied and optimized to accurately control the nanohelices deposition density, macroscopic organization and nanometric nematic order alignment. For all the experiments, the silica helices are suspended in a mixture of ethanol/isopropanol (1:1).

3.2.1 Polymer additives

Polymer additives, which modify the surface tension of the solution, the viscosity and also dispersibility of nanoobjects, were used to optimize helix assembly. Silica nanohelices suspensions were dip-coated onto a silicon substrate, with and without polymer additives. Anionic polyacrylic acid (PAA) and cationic polyethyleneimine (PEI) were the two linear polyelectrolytes used in this study.

The suspensions of silica nanohelices, silica nanohelices with PEI and silica nanohelices with PAA were characterized by dynamic light scattering (DLS) technique. DLS can be used to determine the size distribution of small particles in suspension and data analysis process by DLS calculation only suits spherical particles. Since the mobilities of round particles and fiber-like elongated nanoobjects are different, the size distribution of silica helices (listed in table 5.1) may not be the real values. However, only the suspension in presence of PAA gives nanometric values, suggesting that the helices are better dispersed than in the two other suspensions. This observation is confirmed by the laser power adjustment before the DLS measurements: to reach the necessary amount of 2000 count rate for the DLS measurements, the laser power has to be increased for the silica helix / PAA solution, suggesting a lower scattering than the two other solutions, and so suggesting a better dispersion.

	Size distribution estimated by DLS	Laser Power
Helices	3147.69 nm, 5482.21 nm, 6013.35 nm	46.32%
Helices with PEI	3966.37 nm, 4350.65 nm	45.40%
Helices with PAA	342.09 nm, 653.52 nm, 1725.63 nm, 3147.69 nm	57.70%

Table 5.1 The suspension of silica helices, silica helices with PEI and silica helices with PAA characterized with DLS, and corresponding laser power was indicated.

The stability of the starting colloidal suspensions is of huge importance to the dip-coating process. The homogeneity of the coated surfaces is directly influenced by the presence/absence of the polymer in the suspension: in the absence of polyelectrolyte (Figure 5.6 a), the dip-coating conditions applied here led to a sparse and inhomogeneous helix deposition. The addition of PEI increases the density of helix surface coverage compared to suspensions with no polyelectrolyte, probably due to a lower evaporation rate. However, the helices are still heterogeneously distributed and randomly oriented (Figure 5.6 b). Interestingly, in the presence of the anionic PAA on the other hand, the helices are

well oriented parallel to each other (Figure 5.6 c). All further experiments were conducted with the addition of PAA polyelectrolyte.

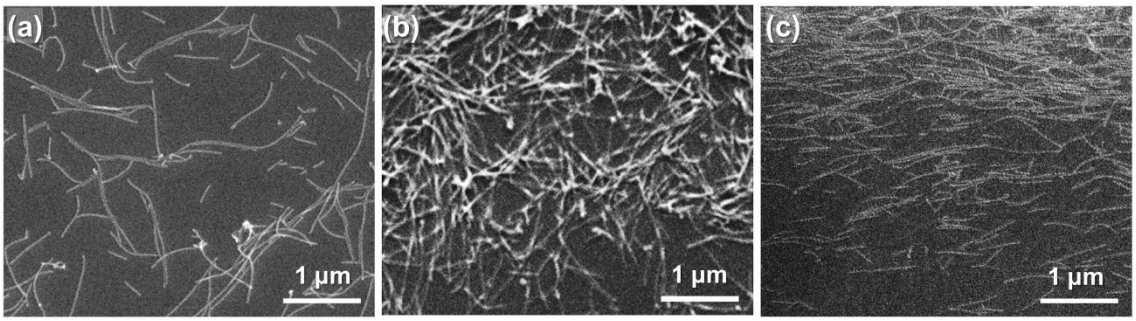

Figure 5.6 Scanning electron microscope (SEM) images for the assemblies of silica helices with (a) no polyelectrolyte, (b) PEI and (c) PAA.

The effect of the mass ratio of SiO_2: PAA on the helix assembly was investigated from 1:5 to 1:20. For each ratio, a clear stick-slip phenomenon appears where periodic helix-rich bands, the stick regions, alternate with helix-poor areas, the slip regions. In the stick regions, the nanohelices align perpendicularly to the withdrawal direction, i.e., parallel to the meniscus (Figure 5.7) showing nematic-like phase organization. Increasing the PAA concentration enhances the width of the stick region and the helix concentration in these zones (Figure 5.7).

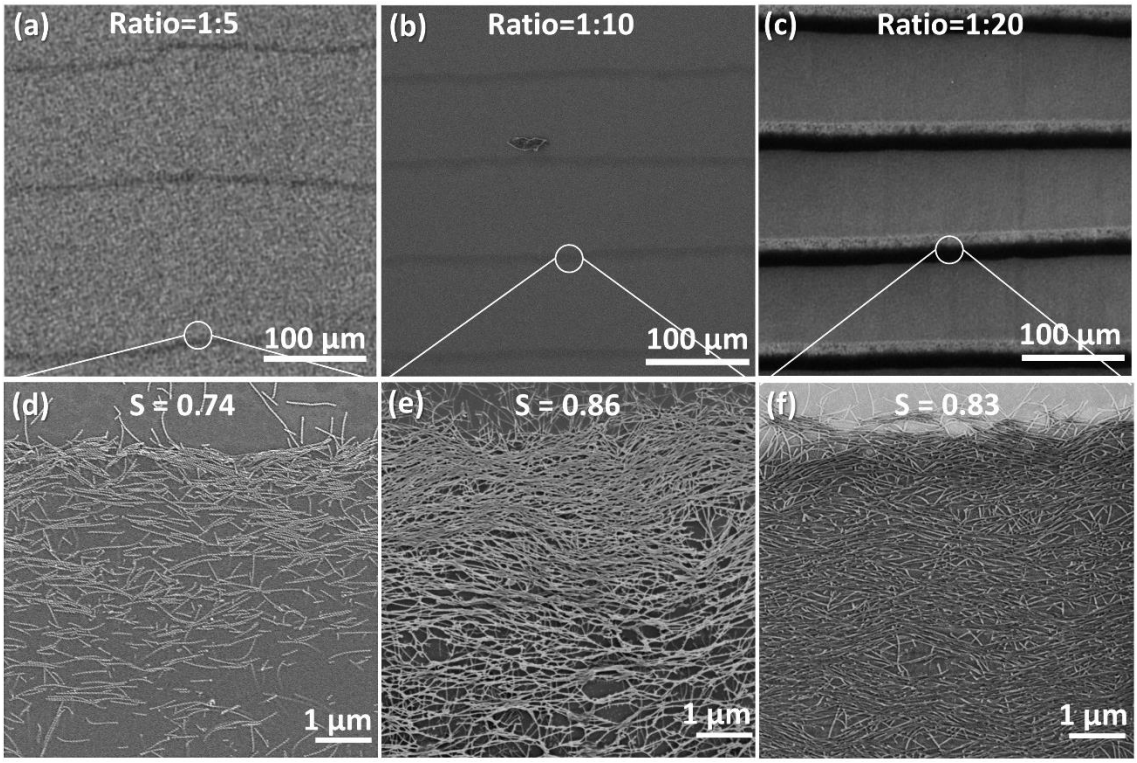

Figure 5.7 SEM images of the dip-coated samples with a SiO_2: PAA ratio of (a) 1:5, (b) 1:10 and (c) 1:20. The images (d)-(f) show higher magnification of the stick regions of (a)-(c).

The alignment of the silica nanohelices within the stick bands can be evaluated using the order parameters *S*, *S* is average value of *s*, which is defined as:[29]

$$s = 2cos^2\theta - 1$$

where, θ is the angle between the main direction and each individual helix direction. If *S*=1, it means all the helix are aligned in horizontal direction. If *S*=0, there is no alignment. S increases from 0.40 in the absence of PAA to a maximum of 0.86 for a mass ratio of SiO_2: PAA of 1:10. This optimum SiO_2: PAA ratio of 1:10 was used for the further experiments in this study.

3.2.2 Silica nanohelices concentration

Stick-slip pattern formed through dip-coating were studied with different concentrations of the nanohelices suspensions from 0.1 mg/mL to 1 mg/mL. The samples observed by polarized optical microscopy in the reflection mode show a black background corresponding to the slip regions and light lines corresponding to the stick regions (Figure 5.8). Both the pitch between two stick regions and the width and the thickness of the stick

regions increase with increasing silica concentration. In parallel, atomic force microscopy (AFM) was used to accurately measure the width and the thickness of the stick regions (Figure 5.10 b-c). The width as well as the thickness of the stick region increase with silica concentration. Due to the higher helix concentration in solution, more helices are deposited during drying. The meniscus is then probably pinned longer by the more significant quantity of helices at the drying line resulting in a bigger jump to its normal position upon unpinning.

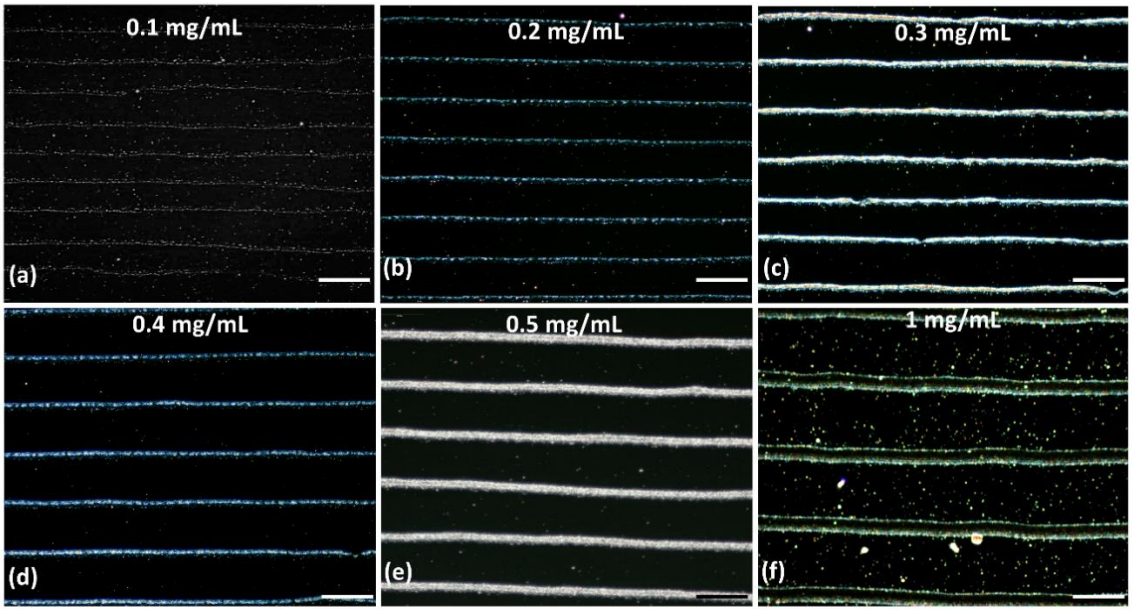

Figure 5.8 Reflection mode polarized optical microscopy images of substrates prepared using a silica concentration ranging from 0.1 to 1 mg/mL. The SiO_2: PAA ratio used was 1:10, the withdrawal speed was 10 µm/s and the temperature of the chamber was 25 °C. Scale bars represent 100 µm.

At slow withdrawal rate, silica helices deposition is driven by evaporative transport in the meniscus, by a similar mechanism as that previously described for spherical particles.[30, 31] The simulation of this evaporation process was done by the collaborator *David Gonzalez-Rodriguez* (LCP-A2MC laboratory, Université de Lorraine) in terms of thickness and width of the stick line *vs* silica concentrations. In the presence of helices, the meniscus becomes pinned (Figure 5.9 b). The distance between the pinning point and the substrate's surface is denoted h_p. This distance h_p increases with time, as a result of helix deposition. The slower the withdrawal rate, the more helices can be deposited and the larger is the helix stick region. The motion of the substrate as it is withdrawn stretches the meniscus. Due to capillary-induced curvature, the meniscus eventually touches the surface of the

substrate and breaks up (Figure 4c). The two resulting menisci rapidly retract to recover their static shape with a contact angle θ_c (Figure 4d). The upper and lower menisci continue to retract over time due to evaporation. The motion of the receding contact line during evaporation will tend to align the nanohelices in the direction of the horizontal band, showing nematic-like phase organization.

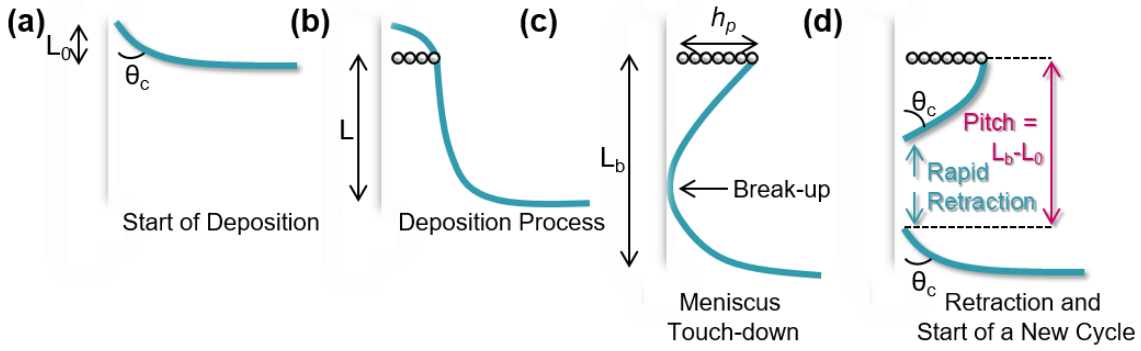

Figure 5.9 Conceptualization of the horizontal strip formation mechanism. (A) The stick zone deposition starts. (b) Intermediate stage. (c) The meniscus touches the substrate, breaking up and ending deposition in the current stick zone. (d) After meniscus break-up, rapid retraction occurs, which contributes to the pitch between stick zones.

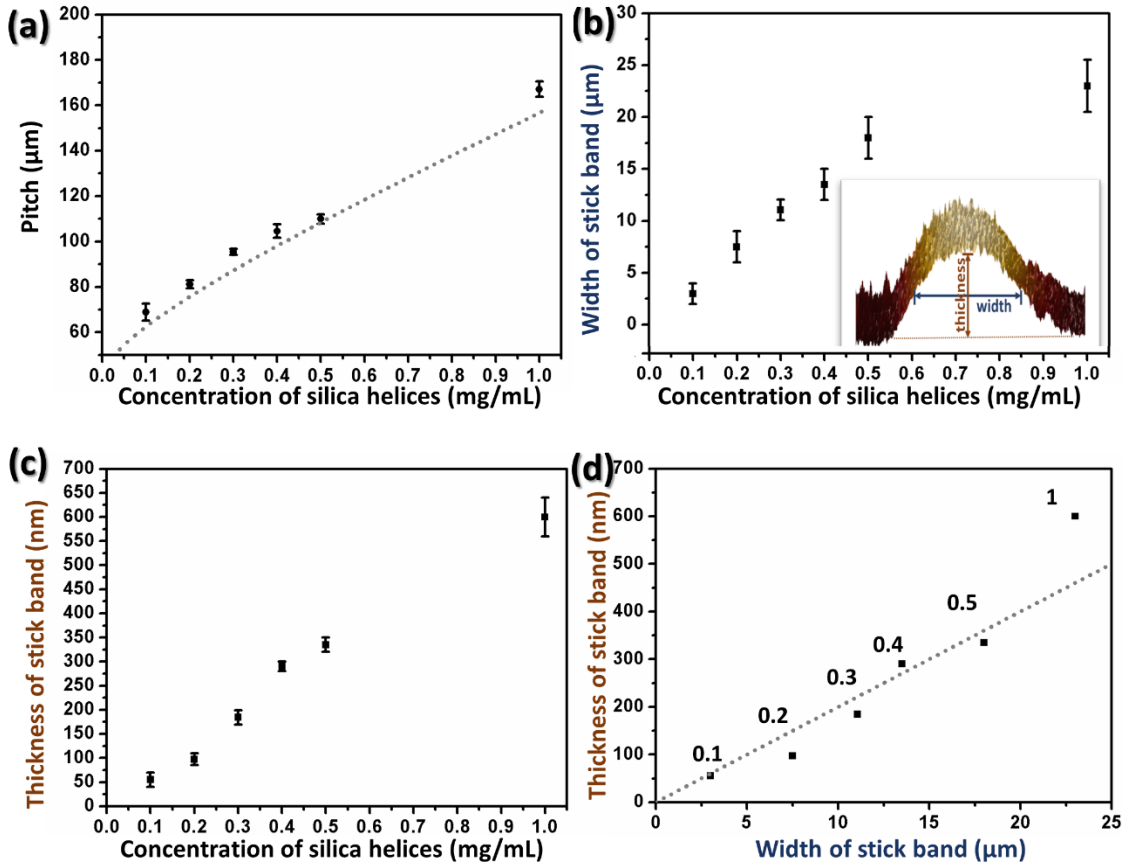

Figure 5.10 (a) Stick-slip pitch vs helix concentration, measured from the optical microscopy images. (b) Stick width vs helix concentration measured using AFM (5 measurements for each point). The inset is an image of the AFM side view of one stick line, showing the definition of width and thickness of the stick regions for a silica concentration of 0.4 mg/mL. The inset is an AFM image of one stick line, showing the definition of width and thickness of the stick region. (c) Stick thickness vs helix concentration (5 measurements for each point). (d) Stick thickness vs stick width measured using AFM images for all the studied concentrations. The gray dotted lines show the theoretical predictions of evaporative transport model in (a) and (d).

For the study of the following parameters, the silica helix concentration was fixed at 0.4 mg/mL as it allows a nice stick-slip phenomenon with high helix concentration in the stick regions, and the solution concentration is largely sufficient in order to achieve a good coverage.

3.2.3 Withdrawal speed

Numerous reports show that during dip-coating the withdrawal speed is closely related to the drag forces and the evaporation conditions strongly affect the film thickness.[32] We studied the effect of the withdrawal speed between 2.5 and 30 000 µm/s

on the film formed by deposition and orientation of silica helices. Orientation was quantified by an order parameter, as described previously. The deposition density is defined as the percentage of the surface covered by helices divided by the total surface when the deposition is homogenous. With the binarized SEM Image (as Figure 5.11 shown), the deposition is calculated by:

$$\textit{Helix deposition} = \textit{Pixels of helices/Total pixels} \qquad (1)$$

where the pixels of helices and total pixels can be read from the Image-J software.

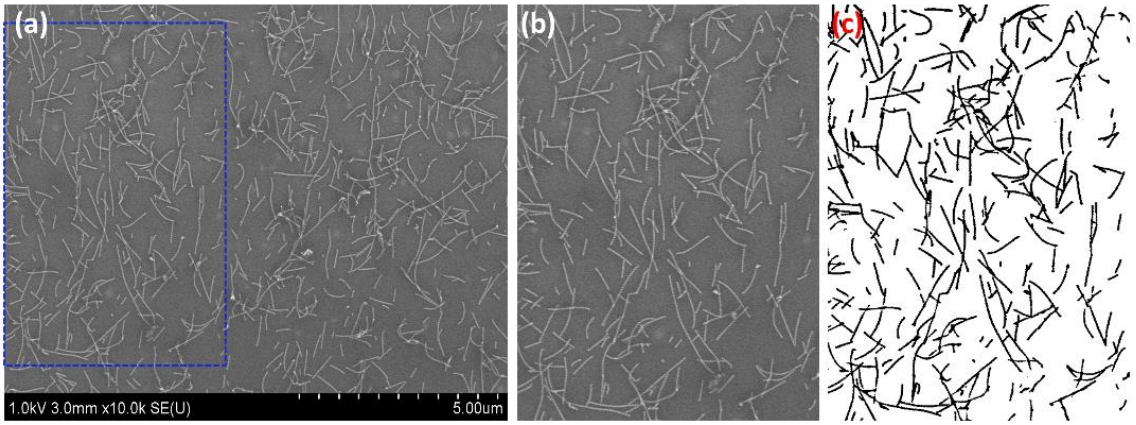

Figure 5.11 (a) Raw SEM image of 0.4 mg/mL silica helices with 30 µm/s withdrawal speed. (b) Selected working area (corresponding to the blue square in a). (c) Binary treated image from (b).

On the other hand, with the stick-slip phenomenon, the deposition is heterogeneous. The ratio between the width of the stick lines and the spacing between two lines is therefore considered, and deposition is calculated by:

$$\textit{Helix deposition} = \textit{Slip}_{\textit{helix deposition}} \times W_{slip}\% + \textit{Stick}_{\textit{helix deposition}} \times W_{stick}\% \qquad (2)$$

where $W_{slip}\% = W_{slip} / (W_{slip} + W_{stick}) \times 100\%$, and $W_{stick}\% = W_{stick} / (W_{slip} + W_{stick}) \times 100\%$, in which W_{slip} and W_{stick} are the width of slip regime and stick regime respectively, and can be calculated from AFM images directly. $Silp_{\text{ helix deposition}}$ is helix deposition in slip regime, which is normally a monolayer and can be calculated according to equation (1) with the pixels. $Stick_{\text{ helix deposition}}$ is defined as:

$$\textit{Stick}_{\textit{ helix deposition}} = (T_{stick}/T_{helices}) \times (\textit{Pixels of helices/ Total pixels}) \qquad (3)$$

where T_{stick} indicates thickness of the stick regime, $T_{helices}$ is thickness of one helix (26 nm). Because the thickness of the stick can be as high as 400 nm, the density deposition of these samples can be higher than 100%.

Figure 5.12 shows the density and the orientation of silica helices surfaces in the capillary regime (withdrawal speed is less than 30 µm/s, blue background) and in the draining regime (withdrawal speed is faster than 100 µm/s, red background).

In the capillary regime, we observed the stick-slip phenomenon (Figure 5.12 a-b). The slower the withdrawal rate, the more helices are deposited and the larger and denser the helix stick regions are. The helix density decreases with increasing speed until the draining regime is reached at 30 µm/s where randomly distributed and monolayer helices replace the stick-slip regions. Helix deposition decreased dramatically from 700% at a withdrawal speed of 2.5 µm/s to 13% at a speed of 30 µm/s. This sparse deposition density remains until 100 µm/s. Above 1000 µm/s the draining regime is reached (Figure 5.12, red). The helix deposition density rises again with increasing speed.

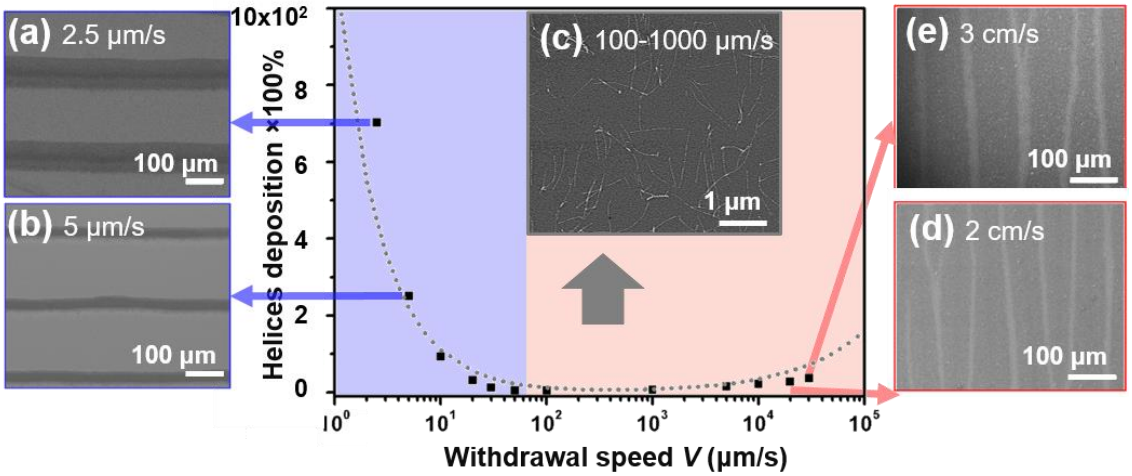

Figure 5.12 Helix deposition vs withdrawal speed, with SEM images at various withdrawal speeds between 2.5-30 000 µm/s. The SiO_2: PAA ratio is 1:10, the silica concentration is 0.4 mg/mL and the chamber temperature is 25 °C. Dot lines are theoretical predictions of the deposition density.

There are two regions of higher particle deposition density, which can be explained by the presence of two physical regimes, governed by evaporative transport and by advective transport, respectively. Slow withdrawal rates correspond to the evaporative transport regime (blue in Figure 5.12), where film thickness increases with slower speeds.

Fast withdrawal rates correspond to the advection regime (red in Figure 5.12), where film thickness increases with faster speeds. In both regimes, well-organized bands appear: horizontal ones in the evaporative transport regime due to the stick-slip phenomenon (periodic helix-rich bands, the stick regions, alternate with helix-poor areas, the slip regions); vertical ones in the advection regime (Figure 5.13). The orientation of the helices in the bands is analyzed by Image-J as shown in the color scheme in Figure 5.13 (g): light blue indicates an orientation of 0°, the horizontal direction, where red indicates ±90°, the vertical direction. The alignment of silica helices is visualized with the color map, and the order parameter *S* can be calculated using the same method as previously described in section of polymer additives.

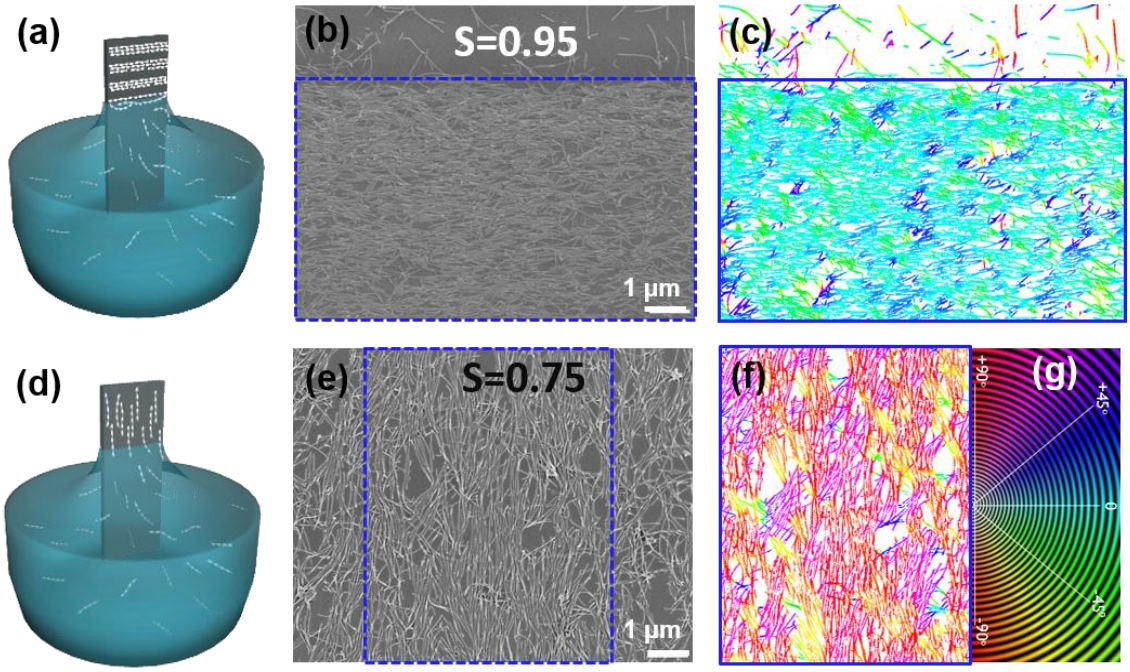

Figure 5.13 (a-c) The horizontal and (d-f) the vertical alignment (a, d) scheme, (b, e) SEM image, and (c, f) orientation analysis. The colloidal solution is SiO_2: PAA=1:10, the silica concentration is 0.4 mg/mL, the chamber temperature is 25 ºC and the withdrawal speed is either (a-c) 10 µm/s or (d-f) 3000 µm/s. (g) is the legend for the colors shown in (c) and (f), with respect to various angles.

A high order parameter *S* between 0.85-0.95 in the horizontal orientation was obtained inside the stick regions for the evaporative transport regime. The SEM image in Figure 5.13 (b) details the border of a slip and stick region, demonstrating the horizontal orientation of the helices in the stick bands. At an intermediate speed (30-1000 µm/s), the order parameter is very low (0.2-0.3), indicating a mostly random orientation (Figure 5.12

c) with a slight alignment preference for 90°, suggesting that helices are subjected to higher shear, but without enough time to fully align. At a withdrawal speed ranging from 5000 µm/s to 30000 µm/s, the deposition density increases with a preferential alignment of 90° (parallel to the withdrawal shear) with an average order parameter *S* of 0.75 (Figure 5.13 2d and 2e).

The topological differences observed between the capillary and draining modes have already been observed and theoretically studied.[22] Faustini et al.[33] proposed two independent models for the capillary and draining regimes of film formation. In the capillary regime, material is deposited at the drying line and the drying line is continuously fed by the capillary rise of the meniscus during solvent evaporation. This can justify the very high density of helices within the stick regions. The capillary forces due to the meniscus evaporation, as well as the entropy gain when elongated objects are aligned, explain the almost perfect alignment of the nanohelices inside the stick regions. On the other hand, in the draining regime no accumulation of particles is expected; only helices present prior to evaporation will be deposited, so the thicker the meniscus the more material is deposited. This is why very high withdrawal speeds induce a higher deposition density. The remarkable switch in the band direction from the capillary to the draining regime has been observed for spherical nanoparticles deposited in the capillary regime by changing the temperature, but not by changing the withdrawal speed.[34]

As in the metaphor of the log driver controlling the movement of logs in a waterway, logs in a stream move parallel to the current when unobstructed and then turn perpendicularly if pinned on one side. In the present case, we believe that not only are the nanohelices pinned in the meniscus in the capillary regime, but the convective flow inside the meniscus induces this orientation. In the draining mode, a gravity driven shear can induce such bands parallel to the withdrawal direction and the entropy gained by the alignment of the helices further enhances this effect. However, very few examples are known of such bands forming in the draining regime because of shear force.[35, 36] The elongated shape of the nanohelices probably is the origin behind such band formation while spherical particles don't exhibit this phenomenon at the same condition.

3.2.4 Theoretical model prediction of deposition density

The density data vs withdrawal rate in Figure 5.9 can be described by a theoretical model developed again by *David Gonzalez-Rodriguez*. The two competing particle transport mechanisms can be quantified as follows:

$$Q_a \approx c\, h\, V \qquad (1)$$

$$Q_e \approx c\, l_c V_e \qquad (2)$$

Here Q_a is the nanohelix transport rate towards the liquid meniscus due to advection of particles into the Landau-Levich film driven by substrate motion. This advective transport rate increases with the withdrawal speed V and is proportional to the particle concentration c and to the thickness of the Landau-Levich film h. Q_e is the nanohelix transport rate towards the meniscus due to evaporation, and V_e is the evaporation speed. The typical length over which evaporation contributes to particle deposition scales as the capillary length l_c, the typical size of the meniscus, as this will be the typical size of the flow recirculation region. The number of particles deposited per unit surface of the plate, which is denoted ρ_P, can be estimated by:

$$\rho_P = \frac{Q_a+Q_e}{V} \approx c\, l_c Ca^{2/3} + c l_c \frac{V_e}{V} = c\, l_c \left[\left(\frac{\mu V}{\gamma}\right)^{2/3} + \frac{V_e}{V}\right] \qquad (3)$$

where ρ_P is the particle deposition density, Q_a is the advective transport rate, Q_e is the evaporative transport rate and V is the withdrawal rate of the substrate. The variable c is the particle concentration in solution, l_c is the capillary length or typical size of the meniscus, and C_a is the capillary number. $C_a = \mu V/\gamma$; where $\mu \approx 10^{-3}$ Pa.s is the dynamic viscosity of ethanol and $\gamma \approx 20$ mN/m is the surface tension coefficient of ethanol. With a density $\rho \approx 800$ kg/m^3, the capillary length of ethanol at 25 °C is estimated to be $l_c \approx 1.6$ mm. The evaporation rate of ethanol at 25 °C is estimated from published data[37] to be the order of V_e = 0.2 μm/s.

This model reproduces the experimental observation in Figure 5.12 (see the fit plotted in dashed line, where the predicted ρ_P has been scaled by a proportionality constant to fit the data). At low withdrawal speeds, evaporation at the meniscus creates the dominant

flux of suspended particles. For V < 50 μm/s, particle deposition is inversely proportional to V, as it is dominated by liquid evaporation. As the plate is withdrawn faster, the plate spends less time in contact with the meniscus, where evaporation-driven deposition occurs. Thus, particle deposition density decreased dramatically from 700% at a withdrawal speed of 2.5 μm/s to 13% at a speed of 30 μm/s. For V > 1000 μm/s, the dominant deposition mechanism becomes advection, where particle transport is driven by the motion of the substrate. Advection increases with the thickness of the Landau-Levich film, $\rho_P \approx V^{2/3}$. In the intermediate regime, 50 < V < 1000 μm/s, both evaporation-induced transport and advection are weak, and particle deposition density reaches its minimum. As described in previous studies,[38,39] there is a transition occurring from evaporative to advective transport which corresponds to the condition $Q_e = Q_a$. By balancing equations (1) and (2) and by considering the current experimental conditions, we obtain a critical speed: $V_{crit} = {V_e}^{2/5} \approx 300\ \mu m/s$. This result is consistent with the recorded data presented in Figure 5.12.

3.2.5 Temperature effect

Temperature is critical to convective evaporation, since temperature affected the physical properties of the solution and evaporation speed. The solution temperature was initially fixed at 25°C, while the chamber temperature was set to 25°C, 35°C and 55°C, respectively inducing gradients of temperature (Figure 5.14). Low magnification SEM images show that the stick-slip phenomenon is still present, but with an increase in the temperature difference between the solution and the chamber temperature, the lines become wavy and diffuse. At higher magnification, swirling helix patterns are observed. The helices remain aligned parallel to their neighbors but follow a swirling motion indicating the presence of complex flow patterns during drying, when there is a relatively large difference between the solution temperature and the chamber temperature. Moreover, the swirling is more intense at the end of the stick regime than at the beginning. Logically, there will be a temperature gradient, where the solution will be warmer at the drying line and at the air-liquid interface. The surface tension is lower for hot solvents than for cold solvents, thus the hot solvent moves towards the cooler zones (Figure 5.14, scheme).

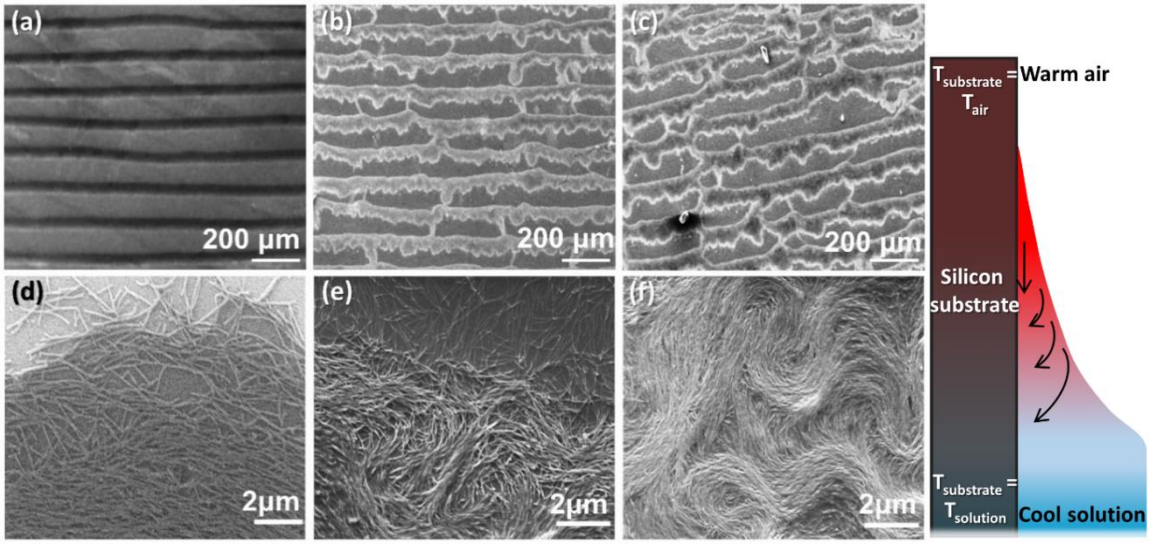

Figure 5.14 SEM images of helices deposited on silicon substrates when the chamber temperature is (a,d) 25, (b,e) 35, and (c,f) 55ºC, at (a-c) low and (d-f) high magnification. The SiO_2: PAA ratio is 1:10, the silica concentration is 0.4 mg/mL and the withdrawal speed is 10 µm/s.

The silicon substrate and the solution in the meniscus are both apt to contain temperature gradients. We can assume that when the meniscus is first pinned, its temperature is near that of the bulk solution. The longer the meniscus is pinned, the more time it has to develop a temperature gradient as the drying line heats to the temperature of the chamber. As the meniscus is stretched, it becomes thinner and heats more quickly. The Marangoni effect, where a mass transfer occurs along an interface due to a gradient of surface tension, is known to generate different patterns, as it has been observed using tungsten nanorods[40] or polystyrene nanoparticles[41]. Although we have a mixture of two alcohols, isopropanol and ethanol have similar surface tensions. However, surface tension is dependent on temperature, and thus by establishing a thermal gradient within the solution, the Bénard-Marangoni effect (also called thermo-capillary convection) should be observable.[42] Indeed, we can assume that the substrate, which has been plunged into the solution for some time, is at the same temperature as the solution (Figure 5.14, scheme). Thus, as the liquid flows from hot to cold due to surface tension forces, the helices move from cold zones to hot zones to conserve mass. By drying, the swirling motion generated is kept at the surface of the substrate. Such effect can be easily observed thanks to the elongated shape and the semi-flexibility of the helices.

3.3 Conclusions

In conclusion, we have shown that large surfaces can be covered with organized silica nanohelices with very good control in terms of pattern, deposition density and object orientation. Different parameters (polymer additives, nano-object concentration, withdrawal speed and temperature) were optimized in order to control this organization. Thick bands can be obtained perpendicular to the withdrawal direction with a controlled periodicity and a nematic alignment inside each band when working in the capillary mode. Less dense bands can be obtained parallel to the withdrawal direction in the draining mode, also showing a good nematic order. Finally, swirling patterns can be created when temperature gradients occur, creating circular currents at the drying line.

4. Grazing Incident Spraying (GIS)

4.1 Grazing Incidence Spray techniques

Recently Gero Decher's group has shown the possibility of coupling the GIS technique with the layer-by-layer (LbL) technique developed 20 years ago[43], allowing the creation of multilayer films with anisotropic nanoobjects aligned in each layer. They developed this first to organize cellulose nanofibrils,[44] but this technique has been used for several systems, like gold nanorods[45] and silver nanowires[46]. The LbL method is based on the electrostatic affinity between positively and negatively charged polyelectrolytes. The films are formed by deposition of alternating layers of oppositely charged materials with washing steps in between. The process, which is extremely simple, is depicted in Figure 5.15 for the case of polyanion-polycation deposition on a positively charged surface.

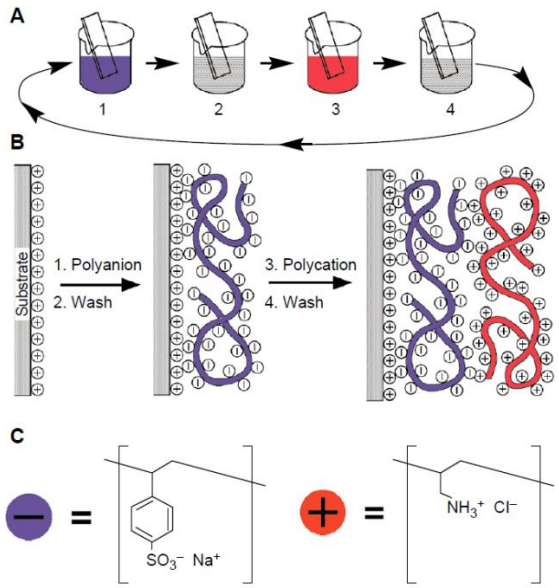

Figure 5.15 (A) Schematic of the film deposition process using slides and beakers. Steps 1 and 3 represent the adsorption of a polyanion and polycation, respectively, and steps 2 and 4 are washing steps. (B) Simplified molecular picture of the first two adsorption steps, depicting film deposition starting with a positively charged substrate. (C) Chemical structures of two typical polyelectrolytes, the sodium salt of poly(styrene sulfonate) and poly(allylamine hydrochloride). [6]

Strong electrostatic attraction occurs between a charged surface and an oppositely charged molecule in solution. In principle, the adsorption of molecules carrying more than one equal charge allows for charge reversal on the surface, which has two important consequences: (i) repulsion of equally charged molecules and thus self-regulation of the adsorption and restriction to a single layer, and (ii) the ability of an oppositely charged molecule to be adsorbed in a second step on top of the first one. Cyclic repetition of both adsorption steps leads to the formation of multilayer structures.

The GIS technique presents particular advantages regarding the organization over a large area: allowance of multilayers with independent orientations and the possibility to control the density of the deposited objects. In the present work an alteration of layers composed of silica helices or Goldhelices with polymer layers will be performed. The polymer layers can be composed of only one layer or alternating polyelectrolytes to increase the thickness of the polymer layer, and therefore the distance between helix films.

For the GIS techniques, five typical parameters need to be optimized to create aligned thin films: air flow, liquid flow rate, nozzle angle, the distance between the nozzle

and the substrate and spray time. Spray time is optimized first with the silica helices for a good alignment and controlled density and then optimized with the Goldhelices in terms of spray time, suspension solvent and substrate functionalization. The experimental scheme of the device is shown in Figure 5.16, in which the suspension of silica helices and Goldhelices are injected into the spray jet and deposited on the substrate through spray.

The substrate can be glass, quartz or a silicon wafer, as long as the surface is flat and treated properly. In order to have a good deposition of the nanoobjects, the surface is covered by a polymer layer. In this work, both the silica helices and the Goldhelices are negatively charged, therefore, the cationic polymer on the substrate facilitate their deposition. Polyethylenimine (PEI) was used.

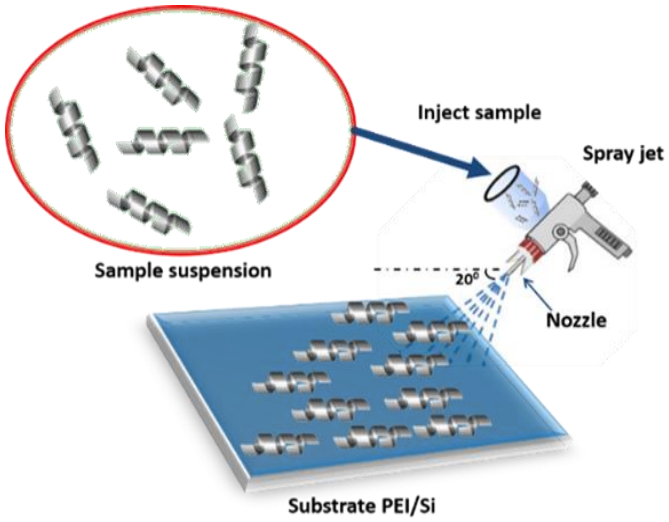

Figure 5.16 Schematic illustration of helixes aligning on the PEI/glass substrate using the GIS technique.

4.2 Alignment of silica helices *via* GIS

Spray solution:

5 mg/L silica helix suspension in a mixture of ethanol and isopropanol (1:1).

Substrate pre-treatment:

2.5 cm×2.5 cm glass pieces are used as substrates. The surface is treated with an oxygen plasma for 3 minutes, sprayed with a PEI solution during 6 s, sprayed with milli-Q water during 10 s and dried with compressed air.

Spray parameters:

An air flow rate of 30 L/min, a liquid flow rate of 1 mL/min, a nozzle angle of 15°, a distance between the nozzle and the substrate of 0.5 cm, and a spray time between 15 to 300 s was applied.

The surfaces obtained with different spray times were observed by SEM. In order to evaluate the surface coverage density and the orientation distribution, all the images are treated with the Image-J software as detailed in Figure 5.17: the original picture (a) is transformed into a binary image (b). From the binary image, the deposition density is calculated by the ratio of the black pixels to the total pixels (black and white). Still from the binary image, the orientation of each helix can be labeled thanks to the Orientation J plugin (c).[29] The color varies according to the angle between the horizontal direction and the helix direction (d). For example, when the angle is 0, which means the helix is in horizontal direction, the helix is light blue. From this image, the 2D nematic order parameter *S* is the average of the *s*, which can be calculated:

$$s = 2cos^2\theta - 1$$

where, θ is the angle between the main direction and each individual helix direction. If *S*=1, all helices are aligned in a single direction. If *S*=0, there is no alignment.

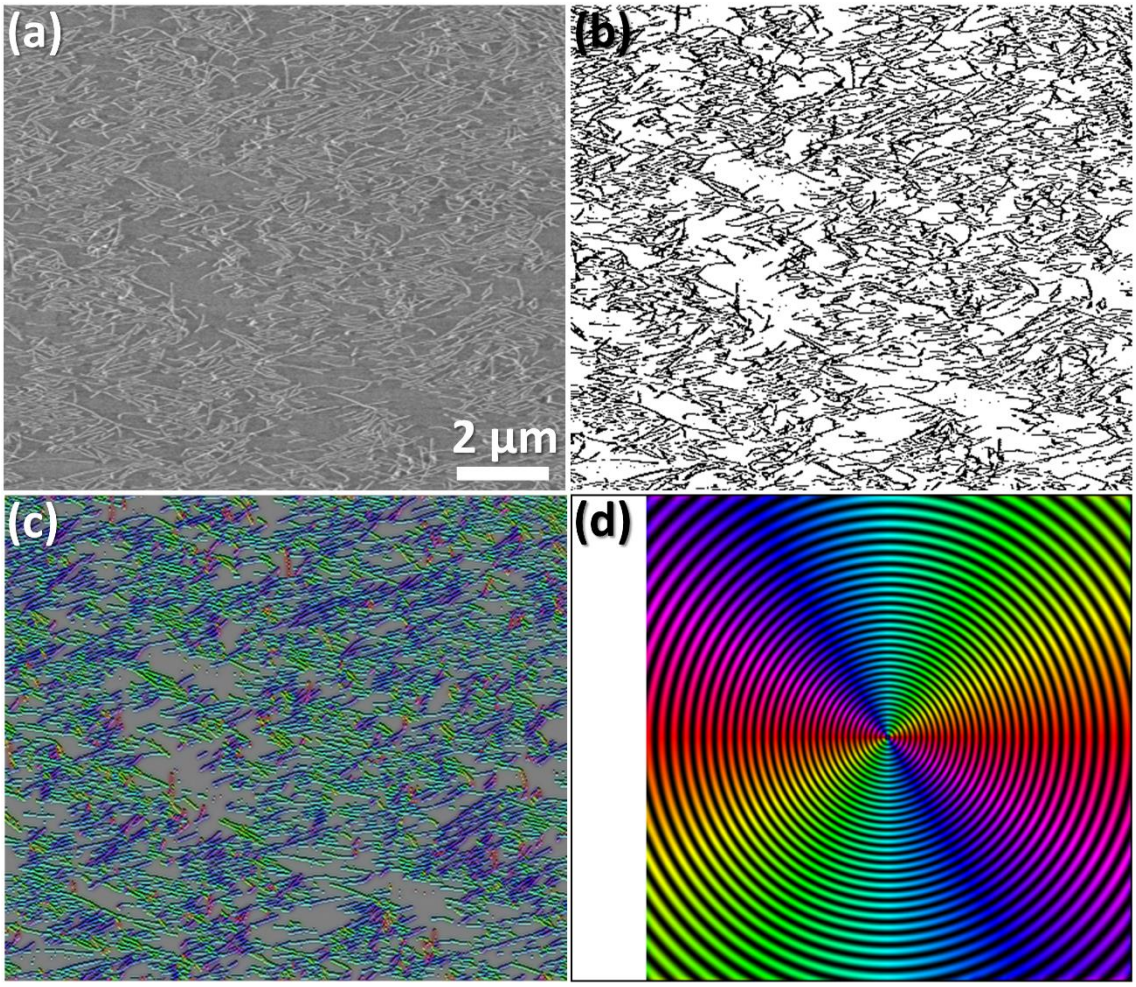

Figure 5.17 SEM images (a) of a typical sample obtained by GIS technique, binary treated SEM (b), and color labeled orientation images (c) based on the color map (d) corresponding to the angle between the helix and the horizontal direction.

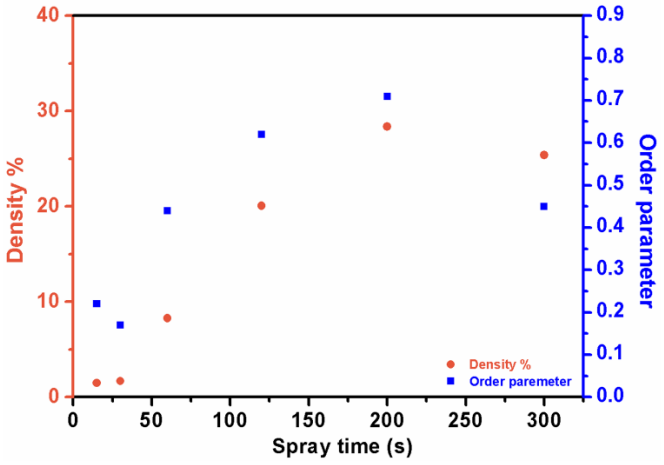

Figure 5.18 Relation of spray time and density, order parameter of silica helix on the glass substrate with various spray time.

The deposition density and the order parameter have been calculated for all the spray times studied from 15s to 300s, and are reported on the graph in Figure 5.18. Up to 200s, with increasing spray time, more materials are deposited on the substrate. The reason is that even if the spray flow has the effect of blowing the nanoobjects away, the affinity between substrate and nanoobjects plays a more important role. When the spray time is longer than 200s, the density decreases instead of remaining unchanged. When the amount of silica helix on the substrate reached a saturation and the spray continued, the new silica helices arriving at the surface collided with the already deposited silica helices. Then when the continuous collision occurred with same area, the silica helices can be removed from the surface. Interestingly, the order parameter follows the same trend, reaching a maximum at 200s. Therefore, optimal spray time is important, not only for preserving the materials but also to having a high deposition density with optimized alignment.

4.3 Alignment of Goldhelices *via* GIS

Spray solution:

To control the concentration of the Goldhelices suspensions, UV absorption at 560 nm is used and controlled at 0.067 (concentration of silica is about 4.5 mg/L).

Substrate pre-treatment:

2.5 cm×2.5 cm glass pieces are used as substrates. The surface is treated by oxygen plasma for 3 minutes, PEI solution is sprayed during 6s, milli-Q water is sprayed during 10s and dried with compressed air.

Spray parameter:

Four parameters have been compared (Table 5.2): the spray time, the nature of the polymer layer (Figure 5.19), the nozzle angle and the nozzle distance. Between Spray A and B, more Goldhelices were deposited on the substrate after 400 s and the deposition density increased from 6.4% (200 s) to 8.7% (400 s). Since poly(allylamine hydrochloride) (PAH) and PEI both are positively charged polymer, they were applied to the support for the Goldhelices, and PEI showed a better deposition (Spray B and C). The orientation of Goldhelices were the same, with an order parameter among spray A, B and C of around

0.4. But the deposition density of Goldhelices was limited to 8.7%. A different incident angle was performed in Spray D. There was an improvement in Goldhelice deposition (16.4% spray D) but with a decreasing in the order parameter (0.3). To improve the alignment, the distance between the nozzle and the substrate was adjusted in Spray E. Finally, we have the optimal condition (spray E): air flow rate 30 L/min, liquid flow rate 1 mL/min, nozzle angle 10^{o}, distance between the nozzle and substrate 0.5 cm, spray time 400 s, giving a deposition density of 21.5 % and an order parameter of 0.64.

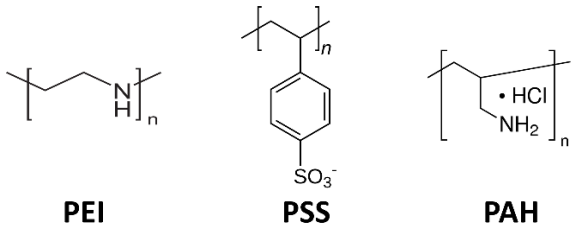

Figure 5.19 chemical structure of PEI PSS and PAH

Sample name	substrate	Angle	distance	Solvent	Spray time	Deposition density	Order parameter
Spray A	PEI	15	1cm	water	200 s	6.4 %	0.41
Spray B	PEI	15	1cm	water	400 s	8.7 %	0.42
Spray C	PEI/PSS/ PAH	15	1cm	water	400 s	8.1 %	0.41
Spray D	PEI	10	1 cm	water	400 s	16.4 %	0.32
Spray E	PEI	10	0.5 cm	water	400 s	21.5 %	0.64
Spray F	PEI	10	0.5 cm	ethanol	400 s	13.2 %	0.42

Table 5.2 Trial spray parameters for gold helix alignment by GIS technique.

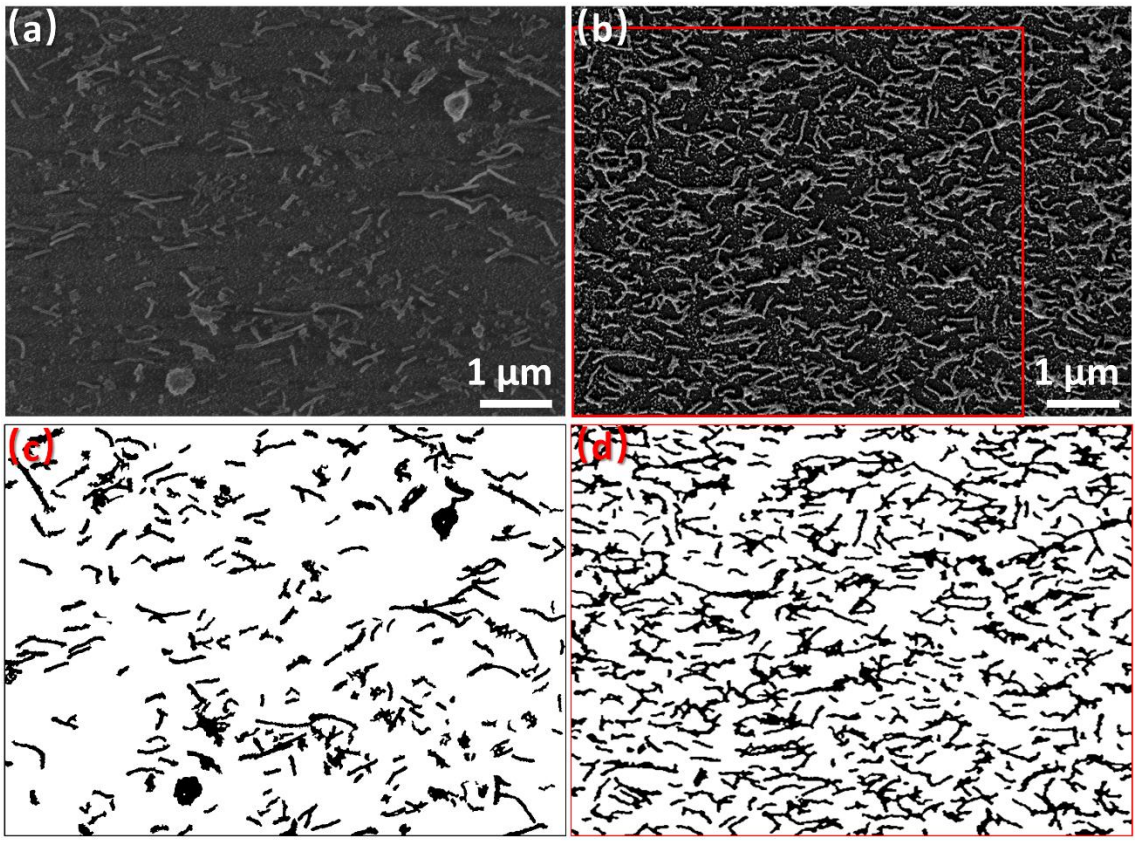

Figure 5.20 SEM images of *Spray-ethanol-1 layer* (a) and *Spray-water-1 layer* (b). (c,d) are the binary image and orientation image with color of (b), treated by Image-J.

As the Goldhelices are stable in both ethanol and water, the GIS was performed with these two suspensions (Spray E and F). Comparing Figure 5.20 (a) and (b), we could find that with different solvents (ethanol and water) the deposition of Goldhelice suspensions are different: higher density can be reached with the water suspension. Coverages calculated from the binary images are 13.2 % and 21.5 % for ethanol and water and order parameters are 0.42 and 0.64 respectively. In summary with the same spray parameters, the Goldhelices dispersed in water can be deposited on the substrate with higher density and order parameters. In further experiments, I disperse the Goldhelices in water.

4.4 Formation of multilayers of Goldhelices

In order to increase the chiroptical response of the samples and to evaluate the 3D packing of the Goldhelices, multilayer samples have been prepared by spraying polymer

multilayers in between the Goldhelices layers, using the LbL technique (Figure 5.21). In detail, after 400 s spraying time, one layer of PEI is deposited so a second layer of Goldhelices can be deposited thanks to the affinity of the Goldhelices for the PEI.

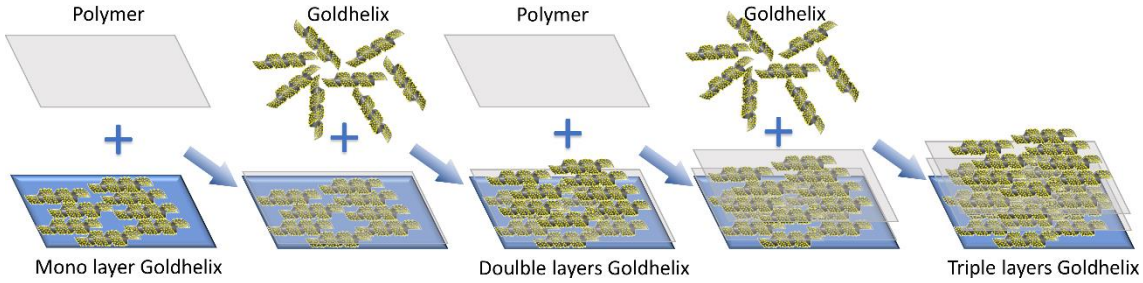

Figure 5.21 Scheme to prepare multilayers Goldhelices: first a monolayer of Goldhelices was obtained, followed by a polymer layer (PEI or PEI-[PSS-PAH]$_n$-PSS-PEI, larger n, thicker polymer between two layers of Goldhelices), and a second layer of Goldhelices was sprayed on the polymer. Multilayer Goldhelices can be prepared by repeating the spraying of polymer and Goldhelices.

To adjust the thickness of the gap between the Goldhelice layers, multilayers of anionic (PEI or PAH) and cationic (Poly(styrenesulfonate) were deposited. The PSS, structure shown in Figure 5.19, polymer can be sprayed, for example, PEI-[PSS-PAH]$_n$-PSS-PEI (n can be any positive integer). By alternating the spraying of cationic (PAH) and anionic (PSS) polymers, the thickness of the polymer layer can be controlled effectively. It is important that the last sprayed layer is PEI to have an affinity with the negatively charged Goldhelices. The spray samples are marked as Spray-Solvent-m layer/layers-P$_n$, m being the number of Goldhelices layers and n being the number of -[PSS-PAH]- pairs. Note that, when n equals 0, the polymer layer is 1, i.e. only a layer of PEI is sprayed between two Goldhelices layers. When n is not 0, the polymer layer equals to 2n+3. The thickness of the gold helix and polymer gap are characterized by cross section SEM. Multilayers of Goldhelices were prepared with different polymer thicknesses as listed in Table 5.3.

Sample name	Suspension	Spray time	Spray layer	Polymer layer
Spray-water-3 layers-P0	H_2O	400 s × 3	3	≈ 1-2 nm
Spray-water-3 layers-P5	H_2O	400 s × 3	3	≈ 20-26 nm
Spray-water-3 layers-P15	H_2O	400 s × 3	3	≈ 50-60 nm

Table 5.3 Several D-gold helix dispersion conditions and spray parameters.

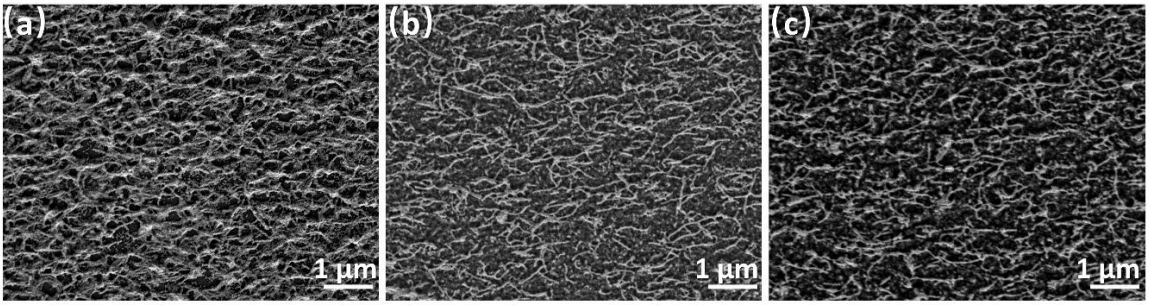

Figure 5.22 SEM images of *Spray-water-3 layers-P0* (a), *Spray-water-3 layers-P5* (b), and *Spray-water-3 layers-P15* (c).

In the SEM images, we can observe an orientation of the Goldhelices in the three samples. In Figure 5.22 (a), even if there is one layer of PEI, which allowed the deposition of multilayers of Goldhelices, the layer separation is not thick enough to visually separate the Goldhelix layers by SEM. The high magnification image (Figure-5.23(e)) showed aggregation of gold clusters, in which we could not distinguish the individual helices. It is therefore impossible to calculate the order parameter of this sample, but one can assume that the orientation within each layer should be close to the one measured with thicker polymer layers. Indeed, with thicker polymer separation we still could manage to calculate the order parameter in *Spray-water-3 layers-P5*, and *Spray-water-3 layers-P15* (Figure 5.22 (b) and (c)), even if the background is not clear, giving $S = 0.64$ and 0.72 respectively.

To measure the polymer layer thickness, cross sections of the samples are observed in SEM. Figure 5.23 (a) to (c) are the representative cross section SEM images of *Spray-water-1-layer, Spray-water-3 layers-P0 and Spray-water-3 layers -P15,* in which the dots indicate GNPs and dark gray zones are the polymer. Only one thin layer of GNPs is shown in picture (a), and a thicker layer of GNPs in Figure 5.23 (b). Because one layer of PEI is too thin to be visible for *Spray-water-3 layers-P0,* only dot piles are observed. For *Spray-water-3 layers-P15*, GNPs are deposited on three layers separately, and the thickness of the gap is 56 ± 8 nm. The discontinuity of the GNPs in Figure 5.22 (c) resulted from the thick and wrinkled polymer layer. Figure 5.23 (d) to (f) correspond to the top view of the same samples. In the monolayer (Figure 5.23 d), we could observe Goldhelices oriented in the horizontal direction with some free GNPs surrounding the Goldhelices. Some of the free GNPs are probably torn off the helix surface due to the shear forces and the others are synthetic residues (remaining GNPs after washing). The quantity of these isolated GNPs is

very low regarding the GNPs attached on the helix surfaces so they should not interact in the chiroptical study results. Actually, since *Spray-water-3 layers-P15* and *Spray-water-3 layers-P5* have similar SEM images (Figure 5.22 b and c), we only showed *Spray-water-3 layers-P15* under high magnification. Figure 5.23(f) representing multilayer Goldhelices with the thick gaps.

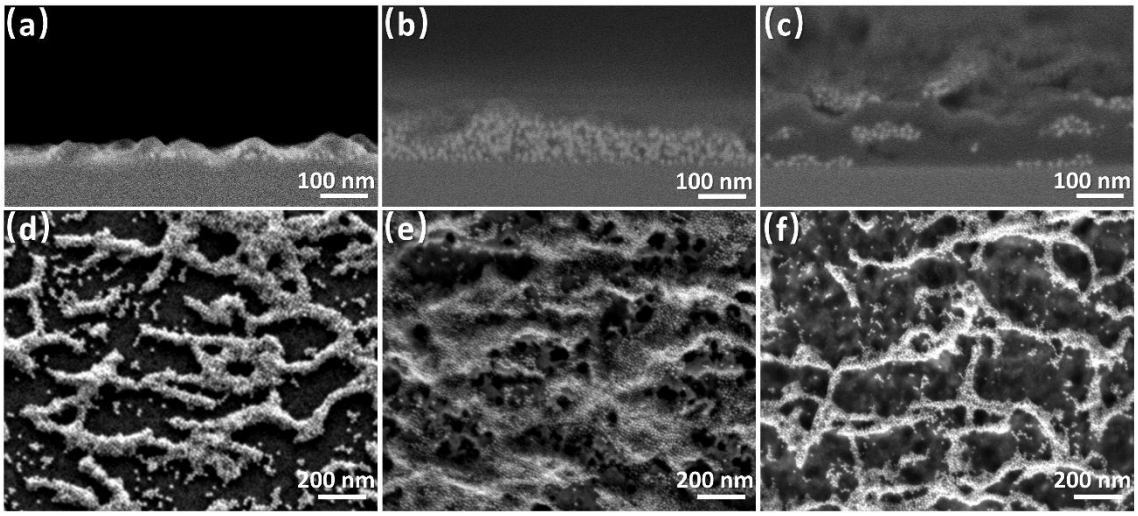

Figure 5.23 SEM images in cross section and high magnification of *Spray-water-1 layer* (a) and (d), *Spray-water-3 layers-P0* (b) and (e), *Spray-water-3 layers-P15* (c) and (f).

4.5 Optical property characterizations of Goldhelice films

Optical properties of the Goldhelices films are evaluated by Mueller matrix polarimetry by using a phase modulation ellipsometer (UVISEL, Horiba). These experiments and calculations were done by *Yann Battie* (Université de Lorraine). As this system only generates linear polarization, the phase modulation ellipsometer only measured 12 elements of the Mueller matrix so only the first three columns of the Mueller matrix are accessible (Figure 5.24). The other elements can be deduced by considering the symmetry of the Mueller matrix in the non-depolarizing structure.[47] According to Azzam et al., [48] the linear dichroism, linear birefringence, circular dichroism and circular birefringence can be directly deduced from the measured Mueller matrix M (as descripted in Chapter 2). And matrix L is obtained based on the transform of $M = e^{L}$, then L can be written as:

$$L = \begin{bmatrix} 0 & -LD & -LD' & CD \\ -LD & 0 & CB & LB' \\ -LD' & -CB & 0 & -LB \\ CD & -LB' & LB & 0 \end{bmatrix}$$

where CB, CD, LB and LD are circular birefringence (CB), circular dichroism (CD), linear birefringence (LB) and linear dichroism (LD). As an example, we show the Mueller matrix measured for the *Spray-water-3 layers-P15* sample.

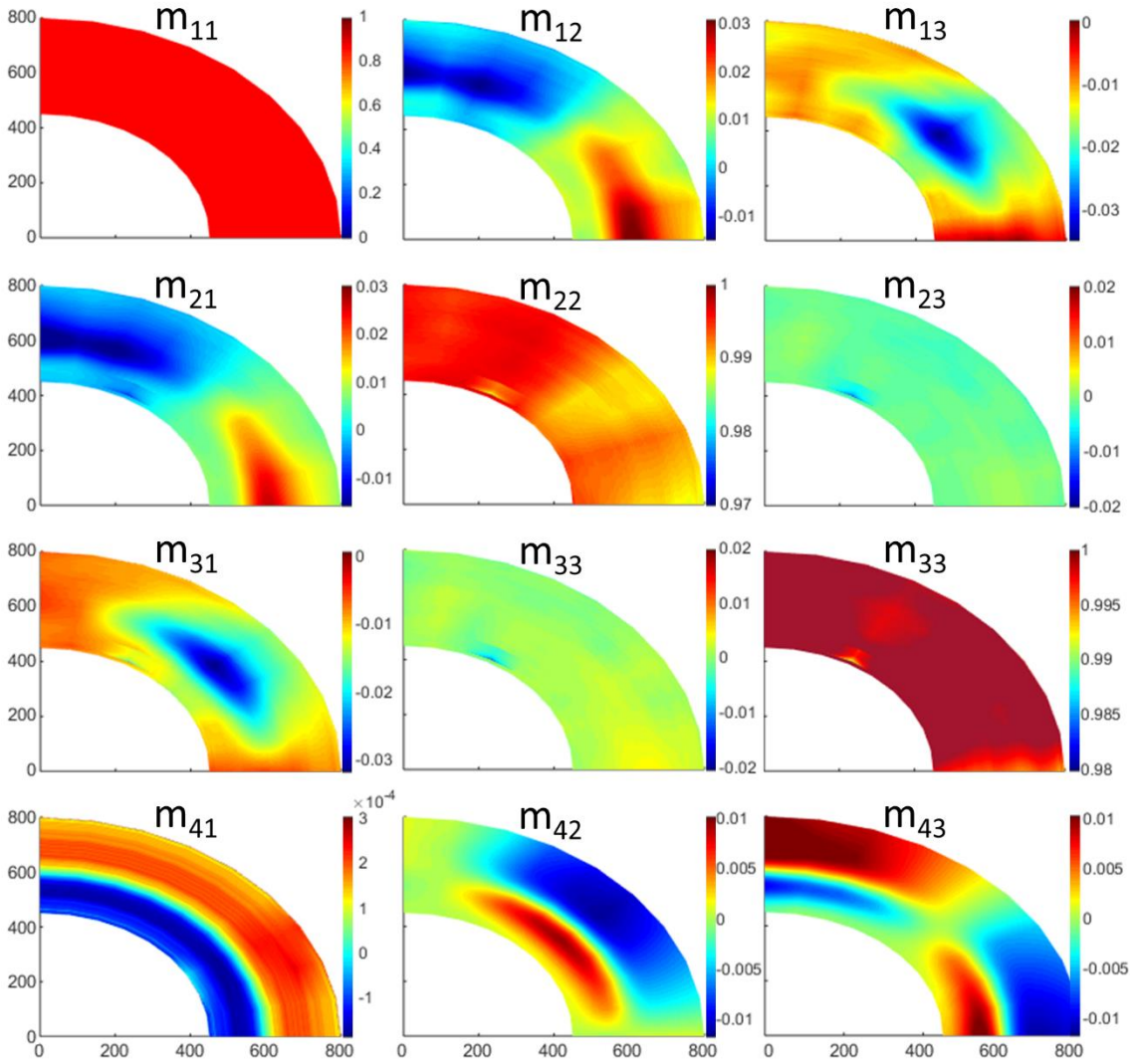

Figure 5.24 Partial Mueller matrix of oriented Goldhelices films. The radial coordinates are the wavelength and the polar angle represents the sample azimuth angle.

The diagonal elements of the Mueller matrix of oriented Goldhelices films are close to 1 (m_{11}, m_{22}, m_{33}). The term m_{41} value is strongly related to the CD. The m_{32} and m_{23} elements, associated to the CB, are equal to 0. The Mueller matrix elements m_{12}, m_{21}, m_{13},

m_{31}, m_{42} and m_{43} depend on the sample orientation, revealing the Goldhelice orientation. The m_{12} and m_{13} elements are close to the m_{21} and m_{31} elements, respectively. In addition, the m_{13}, m_{31}, m_{42} are close to 0 for an azimuth angle of 0° and 90°. Being related to the linear dichroism and linear birefringence, these terms reveal the orientation of the Goldhelices. m_{41} is related to circular dichroism, while m_{12} is the linear dichroism between the x axis (perpendicular to the helix) and y axis (along the helix). As m_{41} is smaller than m_{12}, we conclude that the LD takes precedence over the CD and that the main linear polarization direction is parallel to the main helix axis. So we can consider that this film mainly changes linear polarization and the material exhibits linear anisotropy. If we neglect the circular dichroism, this film is a uniaxial material with an optical axis parallel to the helix axis.

The Mueller matrices of the different samples allow us to precisely distinguish between linear and circular optical effects. As expected, all the samples prepared by GIS show some linear dichroism due to the highly oriented Goldhelices whereas the non-oriented ones do not. This confirms the preferential orientation observed in SEM but also the coupling between the GNPs in the main helix axis direction. In particular, the circular dichroism can be extracted without the linear dichroism effects. Goldhelices suspension in water had a g factor of 4.0×10^{-3}. Monolayer and multilayers of Goldhelices were prepared by GIS technique and g factors of 4.3×10^{-3}, 1.3×10^{-3}, 1.8×10^{-3}, and 4.4×10^{-3} for *Spray-water-1 layer*, *Spray-water-3 layers-P0*, *Spray-water-3 layers-P5*, and *Spray-water-3 layers-P15* (as listed in Table 5.4). Regarding the bulk suspension and the monolayer oriented sample, the same g-factor value is observed, confirming that the general chirality is not at all affected by the drying and the alignment of the samples. Interestingly, the g-factor decreases considerably for the oriented sample when the layers are separated by a 1 nm (*Spray-water-3 layers-P0*) polymer spacer. The g-factor increases a little bit when the Goldhelices layers are separated by a 12 nm (*Spray-water-3 layers-P5)* spacer and recover the same value as for the monolayer samples when they are separated by a 56 nm (*Spray-water-3 layers-P15*) polymer spacer. These specificities are discussed in the next paragraph.

4.6 Comparison between the oriented and non-oriented Goldhelix films

In Chapter 4, randomly deposited Goldhelices samples were described, with monolayer film, the g factor of the non-oriented Goldhelices is the same as the bulk solution (Table 5.4). However, in the non-oriented multilayer samples as described in end of Chapter 4, the Goldhelices are very close to each other, and thus the GNPs do not only interact with the other GNPs of the same helix but also with the GNPs grafted on the neighboring Goldhelices (as shown in Figure 5.25 b). However, instead of directly depositing one drop above another, one thick layer of polymer is placed on the monolayer Goldhelices, then the second layer of Goldhelices is deposited on the polymer. In the end, multilayers of Goldhelices with gaps between Goldhelices can be prepared and g-factor of Goldhelices is around 3.7×10^{-3}, which is comparable with the bulk suspension chiroptical property (4.0×10^{-3}).

Sample	**Non-oriented Goldhelices**				**Oriented Goldhelices**			
	Bulk	Monolayer	Multilayers Gap		Monolayer	Multilayers (3 layers) Gap		
			0 nm	56 nm		1 nm	22 nm	56 nm
LD	0	0	0	0	0.038	0.051	0.035	0.045
g-factor (10^{-3})	4.0	4.3	0	3.7	4.3	1.3	1.8	4.4

Table 5.4 LD and CD intensity of various Goldhelices film (non-oriented, oriented, monolayer, and multilayers).

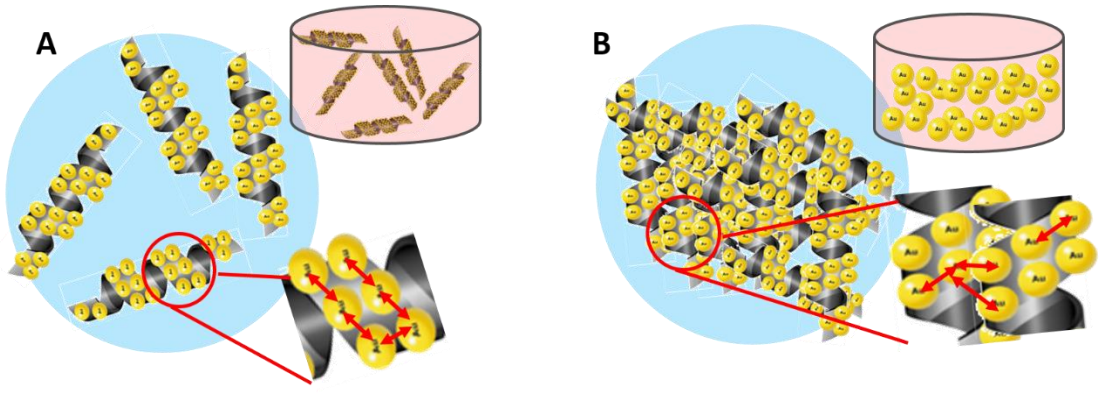

Figure 5.25 The red arrows in (a) and (b) show the possible surface plasmon resonance (SPR) between GNPs. In the case of (a) distance between particles from two helices are too far to have SPR effect, and in (b), the GNPs from two helices generate SPR where is similar with free particles.

For the oriented monolayer sample, the Goldhelices were deposited on the substrate with 22% surface coverage, and the GNPs only couples with the ones on the same helix (distance of the two helices are too far apart, as Figure 5.25 a). For multilayer orientated samples with a 1 nm spacer layer, the average distance between the Goldhelices is larger than for the non-oriented multilayer samples, and thus some CD is observed. But the distance is not large enough to avoid the interactions of GNPs from layers, which is the reason why the g factor of *Spray-water-3 layers-P0* is smaller than the bulk suspension. When the spacer thickness is increased, the average distance between the Goldhelices increases and the individual (chiral) character of the Goldhelices is recovered, leading to a chiroptical activity similar to that of the monolayer (*Spray-water-3 layers-P15*) and the bulk suspension.

Comparing the non-orientated Goldhelices, the aligned Goldhelices films exhibit multi-anisotropy. To evaluate the main effect of the film on the polarization of light, we define the following anisotropic coefficients:

$$\alpha = \frac{LD^2}{LD^2 + LD'^2 + CD^2}$$

$$\beta = \frac{LD'^2}{LD^2 + LD'^2 + CD^2}$$

$$\gamma = \frac{CD^2}{LD^2 + LD'^2 + CD^2}$$

where, LD and CD are horizontal linear dichroism and circular dichroism, LD' is the linear dichroism along the ± 45° axis. Anisotropic coefficients can be viewed as the relative proportion of horizontal linear anisotropy, 45° linear anisotropy or circular anisotropy of the film. These coefficients respect the following sum rules:

$$\alpha + \beta + \gamma = 1$$

Thus, the anisotropic coefficients of the films calculated for each wavelength and azimuth angle can be represented in a ternary plot (Figure 5.26).

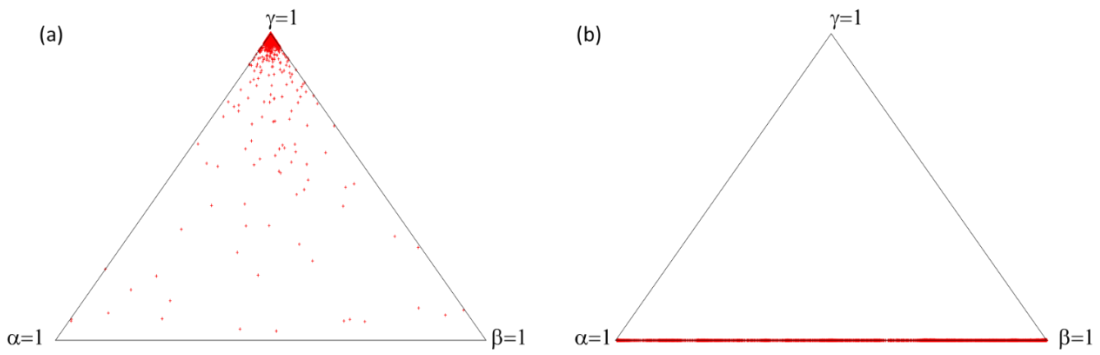

Figure 5.26 Ternary plots to show the proportion of *α*, β and γ for non-orientated Goldhelices(a) and orientated Goldhelices (b).

All measurements are located close to γ =1 for non-oriented Goldhelices, confirming that this film only exhibits circular dichroism. In other words, the unpolarized light which passed through this film tended to be circularly polarized. On the contrary, the coefficient γ of aligned Goldhelix film is negligible compared to α and β . Unpolarized light which passes through this film tends to be linearly polarized.

4.7 Conclusion

In summary, 2D aligned silica helices and Goldhelice materials can be prepared by the GIS technique with a high *S* at 0.71 and 0.72. With the Mueller matrix polarimetry, linear dichroism and circular dichroism can be measured separately. Due to the orientational arrangement through spray, linear dichroism and linear birefringence properties were observed in the aligned samples. In terms of circular dichroism, the g-factor is calculated to evaluate the chirality. A similar g factor is shared by the bulk suspension, the monolayer aligned sample, and multilayer aligned sample with a polymer thickness of 56 nm. The g-factor value decreases considerably for the oriented sample when the layers are separated by a 1 nm and 12 nm polymer spacer.

The chirality of GNPs originates from the helical alignment. When the plasmonic interaction of GNPs form an electromagnetic boundary, and with the helical alignment of GNPs, they give a chiral response at their absorption wavelength. If the distance between two Goldhelices are too close, this plasmonic interaction not only occurs with GNPs on the same helix, but also between the GNPs from two neighboring helices, which decreases this helical boundary effect. This suggestion is also confirmed by the fact that the multilayer

non-oriented sample can recover a 3.7×10^{-3} g value when the layers are separated by a thick polymer, while the g factors are 0 and 4.04×10^{-3} for the multilayer non-oriented sample and bulk suspension.

Non-oriented or oriented Goldhelices can be used as building blocks for circular or linear polarizers, respectively. Moreover, by controlling the number of layers of Goldhelices, the intensity of these properties can be controlled.

5. Summary and Perspectives

5.1 Summary

The three techniques are compared in Table 5.4:

	Techniques	**Microfluidic**	**Dip-coating**	**GIS**
	Alignment	Perpendicular to substrate	Parallel to substrate	Parallel to substrate
	Characterization	SEM with cross section	SEM	SEM
Advantage	Operation	Preparation of evaporator chip is complexed	Device is well developed.	Device is well developed.
Advantage	Density control	Only high concentration	*via* speed	via multilayer spray
Advantage	Large area	Limited by the chip	yes	yes
disadvantage	Specific receiving surface	No requirement	Specific surface	Specific surface
disadvantage	Materials cost	low	low	high

Table 5.5 Summary of microfluidics, dip-coating and GIS techniques.

In general, microfluidics is the only technique that allows helices to align vertically, but the complex preparation process is time consuming. Dip-coating is a technique that has been previously well developed; it offers well-oriented silica helice films with small

material consumption. The GIS techniques has no requirement of the substrate, materials, and the density of the aligned nanoobjects can be controlled by spray time and multilayers. High material costs is the only drawback of this technique, as compared to microfluidics and dip-coating. Depending on the final properties needed with the helices developed (not only the Goldhelices), the optimization of these three techniques will be extremely important for the development of novel functional materials.

5.2 Perspectives

5.2.1 Materials with hierarchical chirality *via* GIS technique

A multilayers Goldhelice film could be fabricated by GIS techniques while preserving the chiral property. To tune the chirality of the material, a hierarchical helix can be imagined by creating a certain angle between the main orientations of the two layers, as shown in Figure 5.27. Then right-handed Goldhelices may give different properties when they are sprayed in the right helix and left helix direction. The angle between the two layers is probably a key factor to tune the chirality of the system.

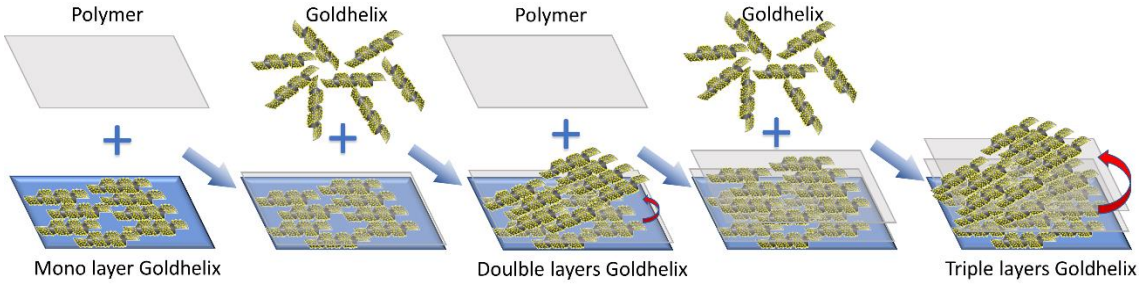

Figure 5.27 Scheme to prepare multilayer Goldhelices, at first a monolayer of Goldhelices was obtained, then followed with a polymer layer, and a second layer of Goldhelices is sprayed on the polymer in a different direction. An angle can be created between the two layers, and a third layer is sprayed by generating the angle between the second layer and third layer.

5.2.2 Aligned Goldhelices *via* Dip-coating

Dip-coating could be developed to align Goldhelices, which are dispersed in water or ethanol with high withdrawal speed. When working in the capillary regime, normally the multilayer Goldhelices may be aligned in a compact way, which will lead to a loss in the chiral optical property. Only with high withdrawal speed, the alignment in the draining regime is promising, and a monolayer of aligned Goldhelices is expected by adjusting the speed and concentration of the suspension.

5.2.3 Aligned Silica helices and Goldhelices *via* Microfluidics

With the evaporation of the solvent, and high concentration of the nanoobjects at the end of the channel, oriented silica helices are probably obtained. Further investigations concerning the observations using cross-sectional views are needed. On the other hand, silica suspensions with polymer are planned to be injected into the microfluidic evaporator, and orientated hybrid structures are promising in terms of better mechanical properties.

References

1. M. Kwiat, S. Cohen, A. Pevzner and F. Patolsky, Large-scale ordered 1D-nanomaterials arrays: Assembly or not?, Nano Today, 2013, 8, 677-6940.

2. J. Liu, H. Liang and S. Yu, Macroscopic-scale assembled nanowire thin films and their functionalities, Chem. Rev., 2012, 112, 4770-4799.

3. H. Zhang and A. I. Cooper, Aligned porous structures by directional freezing, Adv. Mater., 2007, 19, 1529-1533.

4. M.C. Petty, Langmuir-Blodgett Films: an introduction, Cambridge University Press, 1996.

5. H. A. Stone, A. D. Stroock and A. Ajdari, Engineering flows in small devices: microfluidics toward a lab-on-a-chip, Annu. Rev. Fluid Mech., 2004, 36, 381-411.

6. T. M. Squires, Microfluidics: Fluid physics at the nanoliter scale, Rev. Mod. Phys., 2005, 77, 977-1026.

7. D. J. Beebe, G. A. Mensing and G. M. Walker, Physics and applications of microfluidics in biology, Annu. Rev. Biomed. Eng., 2002, 4, 261-286.

8. G. M. Whitesides, The origins and the future of microfluidics, Nature, 2006, 442, 368-373.

9. D. B. Weibel, M. Kruithof, S. Potenta, S. K. Sia, A. Lee and G. M. Whitesides, Torque-actuated valves for microfluidics, Anal. Chem., 2005, 77, 4726-4733.

10. P. Garstecki, M. A. Fischbach and G. M. Whitesides, Design for mixing using bubbles in branched microfluidic channels, Appl. Phys. Lett., 2005, 86, 244108.

11. D. J. Laser and J. G. Santiago, A review of micropumps, J. Micromech. Microeng., 2004, 14, R35-64.

12. P. Lee, R. Lin, J. Moon and L. P. Lee, Microfluidic alignment of collagen fibers for in vitro cell culture, Biomed. Microdevices, 2006, 8, 35-41.

13. A. D. Van der Meer, A. A. Poot, J. Feijen and I. Vermes, Analyzing shear stress-induced aligment of actin filaments in endothelial cells with a microfluidic assay, Biomicrofluidics, 2010, 4, 011103.

14. J. Leng, B. Lonetti, P. Tabeling, M. Joanicot and A. Ajdari, Microevaporators for kinetic exploration of phase diagrams, Phy. Rev. Lett., 2006, 96 (8), 084503.

15. F. Clement and J. Leng, Evaporation of liquids and solutions in confined geometry, Langmuir, 2004, 20(16), 6538-6541.

16. Y. Lu, R. Ganguli, C. A. Drewien, M. T. Anderson, C. J. Brinker, W. Gong, Y. Guo, H. Soyez, B. Dunn, M. H. Huang and J. I. Zink, Continuous formation of supported cubic and hexagonal mesoporous films by sol-gel dip-coating, Nature, 1997, 389, 364-368.

17. M. Jokinen, M. Patsi, H. Rahiala, T. Peltola, M. Ritala and J. B. Rosenholm, Influence of sol and surface properties on in vitro bioactivity of sol-gel-derived TiO_2 and TiO_2-SiO_2 films deposited by dip-coating method, J. Boimed. Mater. Res., 1998, 42, 295-302.

18. P. R. Schunk, A. J. Hurd and J. F. Brinker, Free-meniscus coating processes, In liquid film coating, Springer, Dordrecht, 1997, Chapter 13, 673-708.

19. A. S. Dimitrov and K. Nagayama, Continuous convective assembling of fine particles into two-dimensional arrays on solid surfaces, Langmuir, 1996, 12 (5), 1303-1311.

20. N. D. Denkov, O. Velev, P. Kralchevski, I. Ivanov, H. Yoshimura and K. Nagayama, Mechanism of formation of two-dimensional crystals from latex particles on substrate, Langmuir, 1992, 8, 3183-3190.

21. B. Prevo and O. Velev, In evaporative self-assembly of ordered complex structure, World scientific, 2012, Chapter 3, 109-155.

22. J. Huang, R. Fan, S. Connor and P. Yang, One-step patterning of aligned nanowire arrays by programmed dip coating, Angew. Chem. Int. Ed., 2007, 46, 2414-2417.

23. D. M. Kuncicky, R. R. Naik and O. D. Velev, Rapid deposition and long-range alignment of nanocoatings and arrays of electrically conductive wires from tabacco mosaic virus, Small, 2006, 12 (2), 1462-1466.

24. C. Farcau, H. Moreira, B. Viallet, J. Grisolia and L. Ressier, Tunable conductive nanoparticle wire arrays fabricated by convective self-assembly on nonpatterned substrates, ACS Nano, 2010, 4, 7275-7282.

25. Dann Frenkel, Order through entropy, Nat. Mater., 2015, 14, 9-12.

26. H. Shimoda, S. J. Oh, H. Z. Geng, R. J. Walker, X. B. Zhang, L. E. McNeil and O. Zhou, Self-assembly of carbon nanotubes, Adv. Mater., 2002, 12, 899-901.

27. S. P. Wargacki, B. Pate and R. A. Vaia, Fabrication of 2D ordered films of tobacco mosaic virus (TMV): processing morphology correlations for convective assembly, Langmuir, 2008, 24(10), 5439-5444.

28. P. Li, Y. Li, Z. Zhou, S. Tang, X. Yu, S. Xiao, Z. Wu, Q. Xiao, Y. Zhao, H. Wang and P. K. Chu, Evaporative self-assembly of gold nanorods into macroscopic 3D plasmonic superlattice arrays, Adv. Mater., 2016, 28, 2511-2517.

29. R. Rezakhaniha, Experimental investigation of collagen waviness and orientation in the arterial adventitia using confocal laser scanning microscopy, Biomech. Model Mechanobiol., 2012, 11, 467-473.

30. S. Watanabe, K. Inukai, S. Mizuta and M. T. Miyahara, Mechanism for stripe pattern formation on hydrophilic surfaces by using convective self-assembly, Langmuir, 2009, 25, 7287-7295

31. N.C. Kaplan, N. Wu, S. Mandre, J. Aizenberg and L. Mahadevan, Dynamics of evaporative colloidal patterning, Phys. Fluids, 2015, 27, 092105.

32. S. Roland, D. Gaspard, R. E. Prud'homme and C. G. Bazuin, Morphology evolution in slowly dip-coated supramolecular PS-b-P4VP thin films, Macromolecules, 2012, 45 (13), 5463-5476.

33. M. Faustini, B. Louis, P. A. Albouy, M. Kuemmel and D. Grosso, Preparation of sol-gel films by dip-coating in extreme conditions, J. Phys. Chem. C, 2010, 114 (17), 7637-7645.

34. C. Farcau, H. Moreira, B. Viallet, J. Grisolia and L. Ressier, Tunable conductive nanoparticle wire arrays fabricated by convective self-assembly on nonpatterned substrates, ACS Nano, 2010, 4(12), 7275-7282.

35. A. M. Cazabat, F. Heslot, S. M. Troian and P. Carles, Fingering instability of thin spreading films driven by temperature gradients, Nature, 1990, 346, 824-826.

36. A. Deblais, R. Harich, A. Colin and H. Kellay, Taming contact line instability for pattern formation, Nat. Commun., 2016, 7, 12458.

37. H. E. Hofmann, Evaporation rates of organic liquids, Ind. Eng. Chem., 1932, 24(2): 135-140.

38. M. Le Berre, Y. Chen and D. Baigl, From convective assembly to Landau-Levich deposition of multilayered phospholipid films of controlled thickness, Langmuir, 2009, 25(5), 2554-2557.

39. R. Srikantharajah, T. Schindler, I. Landwehr, S. Romeis, T. Unruh and W. Peukert, From evaporation-induced self-assembly to shear-induced alignment, Nanoscale, 2016, 8, 19882.

40. A. Yella, M. N. Tahir, S. Meuer, R. Zentel, R. Berger, M. Panthofer and W. Tremel, Synthesis, characterization, and hierarchical organization of tungsten oxide nanorods : spreading driven by Maragoni flow, J. Am. Chem. Soc., 2009, 131(48), 17566-17575.

41. Y. Cai and B. Z. Newby, Marangoni flow-induced self-assembly of hexagonal and stripelike nanoparticle patterns, J. Am. Chem. Soc., 2008, 130 (19), 6067-6077.

42. A. Karbalaei, R. Kumar and H. J. Cho, Thermocapillarity in microfluidics- a review, Micromachines, 2016, 7, 13.

43. G. Decher, Fuzzy nanoassemblies: toward layered polymeric multicomposites, Science, 1997, 277, 1232-1237.

44. R. Blell, X. Lin, T. Lindstrom, M. Ankerfors, M. Pauly, O. Felix and G. Decher, Generating in-plane orientational order in multilayer films prepared by spray-assisted layer-by-layer assembly, ACS Nano, 2017, 11, 84-94.

45. S. Sekar, V. Lemaire, H. Hu, G. Decher and M. Pauly, Anisotropic optical and conductive properties of oriented 1D-nanoparticle thin films made by spray-assisted self-assembly, Faraday Discuss., 2016, 191, 373-389.

46. H. Hu, M. Pauly, O. Felix and G. Decher, Spray-assisted alignment of Layer-by-Layer assembled silver nanowires: a general approach for the preparation of highly anisotropic nano-composite films, Nanoscale, 2017, 9, 1307-1314.

47. O. Arteaga and R. Ossikovski, Complete mueller matrix from a partial polarimetry experiments: the 12-element case, J. Opt. Soc. Am. A, 2019, 36 (3), 416-427.

48. R. M. A. Azzam, Propagation of partially polarized light through anisotropic media with or without depolarization: a differential 4 × 4 matrix calculus, J. Opt.Am., 1978, 68 (12), 1756-1767.

General Conclusions

Manufacturing materials that interact with visible light in a controllable way is challenging, as it must be structured on a scale smaller than the wavelength of the exciting electromagnetic field.

This thesis aims to design and fabricate gold chiral nanomaterials through bottom up strategies. Since the GNPs have a surface plasmon resonance in the range of 500-600 nm, chirality can then be expressed in this frequency range. To fulfill this goal, the work presented in this thesis consists of three parts: 1) Chiral superstructures of organic assemblies are employed as the templates for inorganic helical structures *(Chapter 3)*; 2) Plasmonic GNPs are covalently grafted to the helical structures, with chiral absorption expressed in the visible range *(Chapter 4)*; 3) Three different techniques, that is, microfluidics, dip-coating and grazing incident spray are applied to align the chiral nano-helices. The macroscopic materials obtained by these techniques present significant steps for the further applications *(Chapter 5)*.

In Chapter 1, I present the classification of different types of chirality omnipresent in our word. Firstly, I describe how chirality is transmitted and amplified from chiral molecules to chiral supramolecular structures, and from organic to inorganic structures using bottom-up methods. Secondly, several factors bringing chirality to plasmonic materials are described and classified. Finally, various techniques to align nanoobjects are introduced. The use of the ensemble of these interdisciplinary approaches can lead not only to the design of chiral nanomaterials, but also to the fabrication of macroscopic materials for applications.

In Chapter 2, a detailed description of the research design is introduced. At first, the morphology of the organic helical structure is studied, then the synthesis of inorganic helical structures, such as silica helices and Goldhelices, is developed, and the finally three techniques are used to the obtain 3D materials and organize the inorganic helices. All the characterization techniques are introduced, which are attributed to two groups: microscopy and spectroscopy.

In Chapter 3, the self-assembly process of 16-2-16 gemini tartrate is studied. With the various ee 16-2-16 gemini tartrate, there are two types of evolution in terms of helice morphologies. For ee > 0.9, a double bilayer structure transformed from twisted to helical

ribbons with time. For ee < 0.8, only twisted ribbons can be formed, and with time the width and pitch of twisted ribbons increase proportionally, which led to larger twisted ribbons. In general, the evolution of the morphologies of the self-assemblies of 16-2-16 gemini tartrate for the same ee depends on the concentration of the gemini, the higher the concentration, the faster the evolution. The final morphology at equilibrium is the same for all the concentrations and depends on the enantiomeric excess of the 16-2-16 gemini tartrate.

In Chapter 4, we describe how to fabricate the silica nanohelices with GNPs grafted to their surfaces (Goldhelices). Silica nanohelices are synthesized through the sol-gel process using organic self-assemblies of 16-2-16 gemini tartrate surfactant as templates. GNPs with 10 nm diameters are synthesized and grafted covalently to the silica helical structures. The GNP grafting method can be expanded to other NPs as long as the surface includes proper chemical affinity.

In Chapter 5, I show how to create 2D materials by aligning silica helices on surfaces. Such procedures were carried out using microfluidics, dip-coating, and the GIS technique. For the alignment of Goldhelices, the GIS technique allows us to obtain multilayers of Goldhelice films. This technique has no requirement for the substrate or materials. The density of the aligned nanoobjects can be controlled by spray time and a multilayer approach. Dip-coating allowed us to create well-oriented silica helice films with small material consumption with tunable pattering. Microfluidics, on the other hand is the only technique that allows helices to align vertically, but the complex preparation process is time consuming. Non-oriented or oriented Goldhelices can be used as a building blocks for circular or linear polarizers. The Goldhelices deposited randomly on 2D surfaces keep the same chiroptical properties as Goldhelices in suspension. Moreover, by controlling the number of layers of Goldhelices, the intensity of these properties can be controlled. The alignment techniques used in this thesis can also be applied to other elongated materials.

In summary, the purpose of this thesis is to design and achieve nanomaterials with chiroptical properties in the visible range through bottom-up synthesis approaches. Despite the complex manipulation processes, we have obtained stable and macroscopic materials consisting of Goldhelices, which show chiroptical properties in the visible range.

Furthermore, we can control their orientation leading to novel optical properties, which gives a promising approach towards applications, such as ultra-thin quarter wave plates, chiral sensing in the visible range and electromagnetic nanodevices. Compared to other plasmonic chiral nanomaterials, our system opens a totally new perspective towards chiral control. Instead of the chiral ligands typically used to induce chirality, the only chiral source of the Goldhelices is the helical geometry of the template. The chiroptical properties can be controlled by several parameters such as silica-GNPs interactions (electrostatic bond or covalent bond), diameters of the GNPs, and the hierarchical orientation of the Goldhelices. The recurrent challenges in the bottom-up approaches in nanoscience towards applications are their scalability in terms of the production quantities, but also to deal with the problem of how to create larger materials with controlled organization. The three alignment techniques in this thesis pave the way towards fabricating macroscopic materials from nanoobject suspensions.